Ontwikkeling van een 2.5D kwantitatieve elektromagnetische beeldvormingstechniek voor de visualisatie van verborgen objecten met behulp van millimetergolven

A 2.5D Electromagnetic Quantitative Inverse Scattering Technique to Visualize Concealed Objects Using Millimeter Waves

Sara Van den Bulcke

Promotor: prof. dr. ir. A. Franchois
Proefschrift ingediend tot het behalen van de graad van
Doctor in de Ingenieurswetenschappen: Elektrotechniek

Vakgroep Informatietechnologie
Voorzitter: prof. dr. ir. D. De Zutter
Faculteit Ingenieurswetenschappen
Academiejaar 2009 - 2010

UNIVERSITEIT GENT

ISBN 978-90-8578-336-7
NUR 928, 959
Wettelijk depot: D/2010/10.500/12

A 2.5D Electromagnetic Quantitative Inverse Scattering Technique to Visualize Concealed Objects using Millimeter Waves

Sara Van den Bulcke

Dissertation submitted to obtain the academic degree of
Doctor of Electrical Engineering

Publicly defended at Ghent University on 18/03/2010

Supervisor:

prof. dr. ir. A. Franchois
Electromagnetics group
Department of Information Technology
Faculty of Engineering
Ghent University
Sint-Pietersnieuwstraat 41
B-9000 Ghent, Belgium
http://emweb.intec.ugent.be

Members of the examining board:

prof. dr. ir. D. De Zutter (chairman)	Ghent University, Belgium
prof. dr. ir. H. Rogier (secretary)	Ghent University, Belgium
prof. dr. ir. A. Franchois (supervisor)	Ghent University, Belgium
prof. dr. ir. A. Pizurica	Ghent University, Belgium
prof. dr. ir. J. Stiens	Vrije Universiteit Brussel, Belgium
prof. dr. ir. A. Litman	Institut Fresnel, France

FACULTEIT INGENIEURSWETENSCHAPPEN

INTEC

UNIVERSITEIT GENT

Dankwoord

Zo, hier zijn we dan aangekomen: de laatste schrijfdag van mijn doctoraat. Na alle wetenschappelijke tekst, word ik geacht ik hier nu iets literairs tevoorschijn te toveren. Zoals het een echte burgie siert, heb ik het hier dan ook niet gemakkelijk mee. En met een aantal taalkundigen in de familie ligt de lat onmiddellijk een stuk hoger. Maar met wat Leonard Cohen en Mariza in de oren, een theetje bij de hand en de eerste voorjaarszon in het gezicht moet dit wel vlotten. Bovendien wordt het stilaan tijd dat dit schrijven afgerond geraakt, mijn groeiende buik maakt dat ik steeds moeilijker tot bij het toetsenbord geraak...

Toen ik hier in september 2005 de eerste keer op 'de gang' kwam, kon ik me nog niet goed voorstellen hoe dat doctoreren zou verlopen. Het is zoals met vele dingen in het leven (studierichting kiezen, trouwen, kinderen krijgen,...), je volgt je intuïtie, begint aan iets en pas als je er helemaal in ondergedompeld bent, ontdek je echt wat het allemaal inhoudt. Sommige periodes lijkt het wel of alle dagen hetzelfde zijn, je bent iets aan het bedenken of uitwerken en de tijd vliegt voorbij voor je het goed en wel beseft. Maar die stabiele periodes worden op de meest onvoorspelbare momenten afgewisseld door de klassieke ups and downs. Ineens passen alle kleine radertjes in elkaar en komt er een mooi resultaat tevoorschijn of heb je 'het licht gezien'. Op zulke dagen kan zelfs de lege koffiekan of papier dat vastzit in de printer je dag niet meer verpesten. Op andere momenten denk je dat je die bug in je programma waar je al dagen naar zoekt nooit gaat vinden en zakt je de moed wel eens in de schoenen. Gelukkig zijn er dan je familie, vrienden en collega's die je aandacht even afleiden, zodat je oog toch nog op die ene bug valt. En zo vlogen die vier jaar voorbij... Veel vrienden en familie hebben me de afgelopen jaren gevraagd: "Maar wat doe je nu eigenlijk op den unief?" Ik beken: ik ben er niet steeds in geslaagd om hierop een bevredigend antwoord te geven. Ik hoop dit met voorliggend boek en de presentatie op mijn openbare verdediging een beetje goed te maken.

Nu ik zo terugkijk op de voorbije jaren zijn er best wel veel dingen gebeurd op 'de gang'. Oude bekenden zijn vertrokken, nieuwe gezichten zijn verschenen en oude rotten in het vak verzekerden de continuïteit. Mijn promoter, Ann, bedank ik om me de kans te geven dit doctoraatsavontuur te starten en me de vrijheid te geven om verschillende onderzoekspistes te bewandelen. Gedurende de jaren heeft ze mijn wetenschappelijke schrijverskwaliteiten aangescherpt. Bovendien waren de gesprekjes over de kinderen een aangename afleiding van de soms ietwat droge wetenschappelijke kost. Daniël wens ik te bedanken voor zijn goede zorgen, de snelle opvolging van mijn schrijfsels en zijn motiverende woorden. Onder de categorie 'oude rotten' vallen

ook Hendrik en Isabelle. Isabelle is onze wegwijzer in het administratieve doolhof en helpt graag met alle praktische zaken. Hendrik slaagt er steeds in de middagpauzes in de Brug op te vrolijken met al dan niet geslaagde mopjes. Mensen gaan er vaak vanuit dat burgies alles weten over computers. Ik vrees echter dat in dit vakgebied mijn vrouw-zijn primeert boven het burgieschap. Daarom ben ik dan ook Jan, Bert en Kristien (nochtans ook op en top vrouw) van harte dankbaar voor hun computerkennis. In de hogere echelons van de universiteitsstructuur wens ik ook de vakgroepvoorzitters te bedanken: Prof. Lagasse en Prof. De Zutter.
In "den bureau" is Luc een vaste waarde. Onze praatjes over de kinderen en ecologisch bouwen/verbouwen waren talrijk. Wanneer ik het allemaal eens even beu was, kon ik ook met mijn gezaag bij Luc terecht. Bedankt! Bram en Tom vallen onder de categorie "verdwenen oude bekenden", zij konden me steeds overdonderen met hun programmeertalent en hebben me zo ook veel bijgeleerd. De overkant van mijn bureau is de voorbije jaren verschillende keren van gezicht veranderd. Eerst was er Peter, met wie het zeker aangenaam werken was. Zijn enthousiasme voor boeken, films en cultuur was vaak erg aanstekelijk. The last two years, Mari occupies the chair in front of me. This elegant Italian lady doubled the feminine population in our office and gave me the opportunity to have some classical woman-talk during the day. In dit academiejaar kwam ook Pieter erbij: zeker een waardevolle aanwinst. Het internationale karakter van onze werkplek werd nog meer aangedikt door de komst van Weigang Wei. Weigang, thank you for giving me a brief introduction to the Chinese habits. This made me realize even more that we, Europeans, take a lot of things for granted and have a relatively easy and comfortable life for which we should be grateful. Jürgen was mijn vaste reisgezel op conferentie. Uren hebben we daar gezellig zitten babbelen (als we geen boek aan het lezen waren). Bovendien leidde hij me binnen in de wereld van de inverse problemen. Wanneer ik weer maar eens met een wiskundig, computertechnisch, Matlab- of latech- gerelateerd ei zat, kon ik steeds bij Jan, Ignace, Joris, Kristof en Thomas terecht. Ook alle andere collega's wil ik bedanken voor hun grote en kleine bijdragen tot mijn doctoraat, de werksfeer, de momenten van ontspanning.

Door al dat "gestudeer en gedoctoreer" zou een mens al eens vergeten hoe het er in de echte wereld aan toe gaat. Om ons daarvoor te behoeden zijn er gelukkig onze familie en vrienden. Johannes bedank ik als vaste side-kick tijdens onze studietijd. Ondertussen zijn we getrouwd en fiere ouder en hebben we het allebei wat drukker gekregen. Toch geniet ik steeds van de gezellige momenten samen met Tine en de kroost. Ook Wouter en Annelies zijn vaak van de partij. Vroeger kookten de vrouwen vaak samen terwijl de mannen hun wekelijkse kilometers liepen. Door kinderen, bouw- en verbouw perikelen zijn die wekelijkse Bourgondische uitspattingen wat op de achtergrond geraakt, maar als het er dan toch nog eens van komt, zijn de porties steevast te groot en is het lekker genieten.
Nooit was ik mijn studententijd doorgekomen zonder de scouts. Er ging zoveel (soms teveel) tijd naar de scouts dat er vaak weinig tijd over was om me echt zorgen te maken in mijn studies, al durfde ik me dat in de examentijd wel eens te beklagen. Ondertussen

liggen die wilde jaren al enige tijd achter ons, maar nog steeds geniet ik van de gezellige compagnie van de vele vrienden die ik aan die scoutsjaren overgehouden heb. Nu we volgende zomer in Lokeren gaan wonen, ben ik zeer blij dat Ben zijn vrienden daar ook mijn goede vrienden zijn geworden. Onze kennismaking begon als een schuchtere ”hallo” in de Okapi, bij de Nolle leerden we elkaar beter kennen en nu, met de kinderen erbij, spreken we al eens vaker overdag af. Straks staan we samen aan de scoutspoort op onze kleine ravotters te wachten!

Mama en papa, jullie zijn steeds een grote ruggensteun. Ik ben fier jullie dochter te zijn en dit boek draag ik dan ook graag aan jullie op. Velen hebben ons de laatste maanden geplaagd: ”Hoe hebben jullie dit nu weer geflikt? Je eerste (misselijke) maanden van de zwangerschap laten samenvallen met het schrijven van dit boek, en dat dan nog tegelijkertijd met Ben! Je doctoraat verdedigen met een bolle buik en verhuizen wanneer je bevalling wordt voorzien?” De laatste maanden waren inderdaad drukke tijden. Daarom bedank ik jullie, ouders, samen met Veerle, Wouter en de hele schoonfamilie voor jullie goede zorgen. We kunnen altijd op jullie rekenen.

Arne, kleine grote man, ik weet dat jij met evenveel enthousiasme door dit boek zal bladeren als door je beestenboekjes. Wanneer we na een dag werken en nadenken al eens afgestompt thuiskomen, vrolijk jij ons steeds op met je gebabbel. Kleine broer of zus hebben we nog niet echt goed leren kennen, maar die kleine en grote schopjes op de meest onverwachte momenten tijdens de dag, waren alvast een mooie afleiding tijdens het schrijven. Welkom kleine spruit!

De naam ’Ben’ is hier al een aantal keer gevallen. Het is echter niet zomaar een naam, maar de naam van mijn grote liefde. Ben, zonder jou was dit boek er zeker niet gekomen. Ik ben niet altijd even zeker van mezelf, maar jij leerde me de afgelopen jaren wat zelfvertrouwen betekent. Ook wanneer ik het doctoreren even niet meer zag zitten, had jij steeds peptalk klaar. Wanneer ik je nu bezig zie met Arne, straal ik van trots. Ik ben zo fier op mijn mannen!

En zo heb ik onverwacht weer maar eens het cliché bevestigd dat vrouwen taterkonten zijn. Ik hoop dan ook dat jullie nog de moed overhouden om eens in de rest van dit boek rond te neuzen. Succes!

Sara Van den Bulcke
Gent, 18/03/2010

Contents

Samenvatting

In dit doctoraat wordt een kwantitatieve elektromagnetische beeldvormingstechniek ontwikkeld om verborgen objecten te karakteriseren met behulp van millimetergolven. De term elektromagnetische beeldvorming omvat een reeks technieken die informatie proberen te achterhalen over bepaalde objecten uitgaande van de wijze waarop ze elektromagnetische straling verstrooien. Men spreekt van elektromagnetische inverse verstrooiing wanneer het object belicht wordt met gekende elektromagnetische golven, in dit doctoraat opeenvolgend invallend vanuit meerdere richtingen, en de corresponderende verstrooide velden - meerbepaald de elektrische veldvector - expliciet opgemeten worden in een aantal waarnemingspunten. Die opgemeten data wordt dan gebruikt om de vorm, afmetingen, locatie en elektromagnetische materiaalparameters (de complexe permittiviteit) van het ongekende object met behulp van een numeriek algoritme te reconstrueren. Wanneer, zoals in dit doctoraatsonderzoek, de inherente materiaalparameters van het object numeriek in kaart worden gebracht, spreekt men van een kwantitatieve beeldvormingstechniek.

De laatste decennia werd veel onderzoek verricht naar kwantitatieve beeldvorming met behulp van microgolfstraling, met als meest gekende toepassingen medische beeldvorming en het niet-destructief testen van materialen. In dit doctoraat maken we echter gebruik van millimetergolven, met een typische golflengte tussen één millimeter en één centimeter. Dit komt overeen met relatief hoge frequenties (30 tot 300 GHz). Het gebruik van dit type golven voor beeldvorming is vrij recent en volgt uit de sterk toegenomen interesse voor de ontwikkeling van beveiligingstoepassingen. Millimetergolven hebben namelijk de interessante eigenschap dat ze gemakkelijk door kledij dringen maar wel gereflecteerd worden door het menselijk lichaam. Dat maakt ze bijzonder geschikt om verborgen objecten onder kledij te detecteren. De meeste praktische toepassingen, zoals de body scanners die momenteel verschijnen op verschillende grote luchthavens, zijn echter geen kwantitatieve maar kwalitatieve beeldvormingstoepassingen: ze kunnen enkel benaderend de vorm en positie van een verborgen object bepalen maar ze geven geen informatie over de materiaalparameters. In dit doctoraat hebben we onderzocht hoe millimetergolven gebruikt kunnen worden in het kader van kwantitatieve beeldvorming.

De keuze voor millimetergolven heeft echter een grote invloed op de numerieke implementatie van de kwantitatieve beeldvormingstechniek. Doordat de golflengte zo klein is, zijn de objecten (bijvoorbeeld een mes of ander wapen) zeer groot ten

opzichte van de golflengte, wat bij de numerieke implementatie leidt tot zeer grote verstrooiingsproblemen met een groot geheugengebruik en lange rekentijden. Een andere consequentie van de keuze voor millimetergolven is het type belichting dat gebruikt wordt. Typisch gedragen millimetergolven zich zoals een Gaussbundel, bijgevolg heeft het invallende elektromagnetische veld eindige afmetingen (een 94 GHz bundel heeft bijvoorbeeld een doormeter van 1.6 cm), dit in tegenstelling tot een vlakke golf of dipoolbronnen bij microgolfbeeldvorming. Doordat een groot object slechts gedeeltelijk belicht wordt door die Gaussbundel, kunnen we een belangrijke veronderstelling maken die de grootte van het verstrooiingsprobleem sterk zal beperken. We veronderstellen namelijk dat het object een cilindrisch karakter heeft en dus oneindig lang is in een bepaalde richting. Bijgevolg volstaat het om enkel de dwarse doorsnede van het object te beschouwen, hetgeen een twee-dimensionale ruimtelijke discretisatie mogelijk maakt. De invallende Gaussbundel heeft echter eindige afmetingen en moet dus wel volledig in drie dimensies beschreven worden. Op die manier komen we tot wat algemeen een twee-en-een-half-dimensionale (2.5D) aanpak wordt genoemd: objecten worden in twee dimensies behandeld, elektromagnetische velden in drie dimensies. Voor de detectie van verborgen objecten op het menselijk lichaam is deze 2.5D aanpak zeker gerechtvaardigd: we kunnen bijvoorbeeld de buik benaderen door een oneindig lange inhomogene cilinder aangezien zijn karakteristieken niet drastisch veranderen over een afstand van slechts enkele centimeters (het gebied dat belicht wordt door de Gaussbundel) in de lengterichting.

Het elektromagnetische inverse verstrooiingsprobleem is niet-lineair, daarom wordt het gewoonlijk iteratief opgelost als een optimalisatievraagstuk waarin de objectparameters de onbekenden zijn. Men begint met een initiële gok voor de objectparameters en gebruikt dan een numeriek verstrooiingsmodel om het bijhorende verstrooide elektrisch veld te berekenen. Dit wordt dan vergeleken met het opgemeten verstrooide elektrisch veld. Uitgaande van deze vergelijking worden dan de objectparameters aangepast. Deze procedure wordt herhaald tot de gesimuleerde verstrooide velden voldoende overeenkomen met de opgemeten velden. Voor de praktische implementatie wordt gewerkt met een grid van pixels dat het ongekende object omvat. De waarden van de complexe permittiviteit in alle pixels van het grid zijn de onbekenden in het optimalisatievraagstuk. Dit doctoraat bestaat uit twee delen, het eerste deel beschrijft het numeriek verstrooiingsmodel, het tweede deel behandelt het optimalisatievraagstuk.

Het numeriek verstrooiingsmodel wordt gewoonlijk de voorwaartse simulator genoemd. Dit model berekent de verstrooide velden voor een gegeven permittiviteitsprofiel, belicht met gekende invallende elektromagnetische golven. Voor elke wijziging aan het permittiviteitsprofiel tijdens de optimalisatie moet dit verstrooiingsmodel gevalueerd worden. Daarom is een snelle en efficiënte implementatie essentieel. In dit doctoraat wordt gewerkt met een volume-integraalformulering van het verstrooiingsprobleem, dit betekent dat de verstrooiers in het model gediscretiseerd worden op een rooster van cellen, in tegenstelling tot de randintegraalbenadering waarin enkel de

randen van objecten gediscretiseerd worden. In elke cel van het rooster worden dan de drie componenten van de verstrooide elektrische veldvector bepaald door de volume-integraalvergelijking (VIE) iteratief op te lossen. Doordat wij echter in de 2.5D benadering werken, kunnen we niet zomaar de gekende 3D volume-integraalvergelijking gebruiken, maar is deze geherformuleerd naar een 2.5D versie. Dit gebeurt door alle drie-dimensionale grootheden (de elektromagnetische velden) te Fouriertransformeren langsheen de onveranderlijke richting van de verstrooiers, bijvoorbeeld de z-richting in een Cartesiaans assenstelsel. Op die manier krijgen de veldcomponenten, in plaats van een (x,y,z)-afhankelijkheid, een (x,y,k_z)-afhankelijkheid waarbij k_z de spectrale component genoemd wordt. Door deze één-dimensionale spatiale Fouriertransformatie is de 3D VIE herschreven in de vorm van een set van 2D VIE's, één voor elke spectrale component. Na het oplossen van alle 2D VIE's, worden de oplossingen gecombineerd door middel van de inverse één-dimensionale spatiale Fourier transformatie tot het gezochte drie-dimensionale verstrooide veld.

De rekentijd wordt aanzienlijk beperkt door een iteratie bij het oplossen van een VIE te versnellen door gebruik te maken van snelle Fourier transformaties (FFT's). In dit doctoraat worden alle berekeningen in het numeriek verstrooiingsmodel multithreaded uitgevoerd, wat betekent dat zij verdeeld worden over verschillende processoren binnen één machine, die dan elk een deel van het werk doen. Verder beperken we ook de rekentijd door te zorgen voor een goede beginschatting voor het veld op het grid, deze beginschatting wordt bepaald als een lineaire combinatie van een aantal voorgaande oplossingen voor gelijkaardige configuraties. Deze techniek wordt *marching-on* genoemd.

Naast het numerieke verstrooiingsmodel is er ook een numeriek model nodig om de invallende elektromagnetische velden te beschrijven. In het geval van een vlakke golf als belichting is zo een model vrij evident, hetgeen echter niet het geval is voor een Gaussbundel. In de literatuur zijn verschillende modellen terug te vinden om een drie-dimensionale Gaussbundel te implementeren. Wij hebben deze technieken vertaald naar de overeenkomstige 2.5D versie. Het meest efficiënte model is gebaseerd op de complexe bron formulering, maar dan toegepast voor de 2.5D benadering. Speciale aandacht is besteed aan het selecteren van een zo laag mogelijk aantal spectrale componenten om de Gaussbundel accuraat te beschrijven, aangezien het aantal op te lossen VIE's gelijk is aan het aantal spectrale componenten in de beschrijving van het invallende veld.

Het numerieke verstrooiingsmodel is gevalideerd door verstrooide velden voor een aantal cirkelvormige homogene en stuksgewijs homogene testcilinders te vergelijken met de bijhorende analytische oplossing, dit zowel voor loodrecht als scheef invallende vlakke golven. Om te verifiëren of de gesimuleerde verstrooide velden ook correct zijn in het geval van Gaussbundel belichting, vergelijken we met gesimuleerde velden bekomen met volledig 3D numerieke verstrooiingsmodellen. Bovendien tonen we aan dat de beperking tot oneindig lange cilindervormige objecten in de 2.5D benadering kan afgezwakt worden tot *voldoende lange* cilinders bij belichting met

Gaussbundels: de objecten dienen minimaal dubbel zo lang te zijn als de grootte van het belichte gebied. Ter illustratie van de toepassing om verborgen objecten op het menselijke lichaam te detecteren is de verstrooiing aan een eenvoudig model voor de buik bestudeerd. Aangezien millimetergolven niet ver doordringen in het lichaam is het niet nodig om het volledige inwendige accuraat te modelleren. Daarom nemen we enkel een laag kledij, een huidlaag en een onderhuidse vetlaag in rekening. Er is een duidelijke invloed op het elektrisch veld wanneer er tussen de kledij en de huid een klein object wordt geplaatst. Bovendien tonen deze simulaties zeer goed de voordelen van de 2.5D benadering aan: door de grote afmetingen van het lichaam en de relatief hoge permittiviteitswaarden ervan, is het aantal onbekenden zeer groot, wat een volledige drie-dimensionale simulatie zo goed als onmogelijk maakt.

Aangezien in de praktijk de inputdata voor het inverse verstrooiingsprobleem opgemeten verstrooide velden zijn, gaan we ook na in hoever de gesimuleerde verstrooide velden overeenkomen met de experimenteel opgemeten equivalenten. We hebben daartoe beschikking van twee sets van opgemeten velden: de Vrije Universiteit Brussel stelde veldamplitudes opgemeten voor een homogene teflon cilinder belicht door een loodrecht invallende Gaussbundel ter beschikking, terwijl het Institut Fresnel in Marseille amplitude en fasemetingen deed voor vlakke golven die scheef invallen op een inhomogene cilinder. Uit beide vergelijkingen blijkt dat het ontwikkelde numerieke verstrooiingsmodel inderdaad in staat is om het gedrag van verstrooide velden accuraat te beschrijven.

Het tweede deel van dit proefschrift gaat over het optimalisatieprobleem gekoppeld met de inverse beeldvorming. Hierin wordt het verschil tussen opgemeten en gesimuleerde verstrooide velden geminimaliseerd door het iteratief aanpassen van het gediscretiseerde permittiviteitsprofiel. De methode die wij toepassen is een Gauss-Newton optimalisatie gecombineerd met een lijnoptimalisatie. Als maat voor het verschil tussen opgemeten en gesimuleerde velden wordt een kleinste-kwadraten data fit kostfunctie gebruikt, waaraan een regularisatieterm is toegevoegd. Deze extra term dient bijgevoegd te worden omdat het inverse verstrooiingsprobleem slecht gesteld is. Dit komt tot uiting doordat grote perturbaties (vaak met een hoge spatiale frequentie) in het permittiviteitsprofiel slechts aanleiding geven tot kleine perturbaties in de verstrooide velden. Die kleine veranderingen kunnen gecamoufleerd raken wanneer de data vervuild zijn met ruis. Perturbaties in de verstrooide velden kunnen aldus het gereconstrueerde permittiviteitsprofiel degraderen. Het afremmen van ongewenste variaties in het permittiviteitsprofiel gebeurt door een regularisatiemethode toe te passen. De regularisatiemethode introduceert *a-priori* informatie in de kostfunctie om het verlies aan informatie door ruis te compenseren en zo ongewenste veranderingen van het permittiviteitsprofiel in te dijken. Binnen het Gauss-Newton schema is er voorts een uitdrukking nodig voor de afgeleiden van het verstrooide veld naar de permittiviteitsonbekenden. In dit doctoraat worden hiervoor analytische uitdrukkingen geformuleerd binnen de 2.5D benadering.

Aanvankelijk worden in dit doctoraat twee bestaande regularisatiemethodes toegepast. De eerste methode is een spatiale regularisatietechniek en wordt ”multiplicative smoothing” regularisatie genoemd. In dit geval legt de toegevoegde a-priori informatie op dat het gezochte permittiviteitsprofiel vrij glad is, dus sterke lokale variaties van de permittiviteit worden afgestraft. Deze regularisatie voegt de gladheidsrestrictie multiplicatief toe aan de data fit term. De tweede regularisatiemethode is niet spatiaal, maar veronderstelt dat het permittiviteitsprofiel bestaat uit een klein aantal discrete waarden, die echter niet op voorhand moeten gekend zijn. Bijgevolg is dit type regularisatie ideaal om stuksgewijs homogene objecten te reconstrueren. Deze methode wordt de ”stepwise relaxed value picking” regularisatie genoemd. Deze twee regularisatiemethodes hebben ons geïnspireerd tot de ontwikkeling van een nieuwe methode, die we de ”stepwise relaxed object smoothed value picking” regularisatie noemen. Net zoals de stepwise relaxed value picking regularisatie, bevoordeelt deze nieuwe methode stuksgewijs homogene objecten door de complexe permittiviteitswaarden te groeperen in het complexe vlak rond een aantal referentiewaarden, die ook zelf deel uitmaken van het optimalisatieproces. Het verschil met de voornoemde regularisatietechniek is dat er bovendien binnen de homogene gebieden, die verschijnen tijdens de optimalisatie, gladheid van de permittiviteit wordt opgelegd. Op die manier worden een spatiale en een niet-spatiale techniek efficiënt gecombineerd. Deze nieuwe methode resulteert vaak in een langere berekeningsduur, maar is vooral nuttig wanneer de gewone ”stepwise relaxed value picking” regularisatie aanleiding geeft tot artefacten in de reconstructie.

Om de kwantitatieve inverse verstrooiingstechniek, voorgesteld in dit proefschrift, te valideren maken we gebruik van experimentele data. Aangezien er nog geen millimetergolf amplitude- en fase-data beschikbaar zijn voor de inversiegemeenschap, gebeurt deze validatie voor microgolven. Het Institut Fresnel in Marseille heeft een publiek toegankelijke twee-dimensionale databank met verstrooiingsmetingen aan inhomogene cilinders, belicht door vlakke golven. Wij hebben drie objecten uit deze databank gereconstrueerd door gebruik te maken van TM- en TE- gepolariseerde velden en door de drie verschillende regularisatietechnieken toe te passen. Daaruit blijkt dat de nieuwe stepwise relaxed object smoothed value picking regularisatie de beste reglarisatiemethode is voor dit type objecten aangezien die een bijna perfecte reconstructie oplevert.

Om aan te tonen dat de reconstructietechniek ook veelbelovend is bij millimetergolffrequenties maken we gebruik van synthetische meetdata. Dit zijn verstrooide velden die gegenereerd zijn door het numerieke verstrooiingsmodel en waaraan witte Gaussische ruis is toegevoegd om het effect van meetruis te simuleren. We hebben een vergelijking gemaakt tussen de reconstructiekwaliteit bij een belichting met vlakke golven enerzijds en Gaussbundels anderzijds. Daarbij is vastgesteld dat, alhoewel de simulaties met Gaussbundels langer duren, het totale aantal iteraties in het optimalisatieschema gelijk is voor beide types velden. De reconstructie met Gaussbundels vertoont iets meer lokale schommelingen in het permittiviteitsprofiel.

Als sluitstuk van dit werk is een eerste poging gedaan om een millimetergolf-beeldvormingstechniek voor de detectie van verborgen objecten onder kledij te simuleren. Daarvoor maken we gebruik van het vereenvoudigde buikmodel dat reeds eerder werd vermeld. Door de enorme afmetingen van het geheel zijn we echter verplicht om dit model nog verder te vereenvoudigen, om het aantal spectrale componenten in de beschrijving van de Gaussbundel sterk te beperken en om ook het aantal invalsrichtingen van de belichting sterk te limiteren. Ondanks al deze vereenvoudigingen en beperkingen, duurt één enkele iteratie in het optimalisatieschema (toepassen van de Gauss-Newton optimalisatie met lijnoptimalisatie) tussen de 15 en 27 uur. Bovendien maakt de buik een rondomrond belichting van het verborgen object onmogelijk, wat de informatie in de meetdata nog meer beperkt en dus de reconstructie bemoeilijkt. Na ongeveer vijf rekendagen en zes iteraties verschijnt het verborgen object met de juiste afmetingen op de correcte positie en ligt de bijhorende waarde voor de permittiviteit vrij dicht bij de eigenlijke waarden. Dit is een ideaal voorbeeld om de mogelijkheden van kwantitatieve millimetergolf beeldvorming te illustreren, maar toont ook aan waar de beperkingen van deze methode momenteel liggen.

Summary

In this doctoral thesis, a quantitative electromagnetic imaging technique is developed to detect hidden objects using millimeter waves. The term 'electromagnetic imaging' describes a number of techniques that try to extract information about certain objects, based on how they scatter electromagnetic radiation. When electromagnetic inverse scattering is considered, the object is illuminated with known electromagnetic waves from different directions and the corresponding scattered fields are measured in a number of receiver points. The measured data is then used to reconstruct the shape, dimensions, location and the electromagnetic material parameters (the complex permittivity) of the unknown object. When – as in this work – the numerical values of the material parameters of the unknown object are determined, one speaks about a quantitative imaging technique.

During the last two decades, quantitative imaging techniques have been studied extensively for microwave radiation, for applications in medical imaging and non-destructive testing. In this PhD work however, we use millimeter waves. These waves have a wavelength between one millimeter and one centimeter, corresponding to relatively high frequencies (30 to 300 GHz). The interest in millimeter waves has recently grown within the imaging research community thanks to its possible use in security applications. Indeed, one of the most interesting properties of millimeter waves is that they easily penetrate clothing but reflect on the human body. This makes them perfectly suitable to detect weapons or explosives hidden under clothing. However, most of the practical applications, as the body scanners which are currently used at different international airports, are not quantitative but qualitative imaging applications. They can only approximately determine the shape and position of the hidden object, but are not capable of defining the material parameters. In this PhD work, we have studied how millimeter waves can be used in the framework of a quantitative imaging technique.

The choice for millimeter waves largely complicates the numerical implementation of the quantitative imaging technique. Indeed, the considered objects are very large compared to the small wavelength, which results in very large scattering problems to be computed. This leads to massive memory consumptions and extremely large simulation times. Another consequence of the chosen wavelength is that the type of illumination is typically a Gaussian beam, contrary to the plane waves and dipole sources which are typically used in the microwave imaging community. However,

since the beam illuminates a spatially limited region, the size of the scattering problem can be reduced drastically by assuming that all objects are cylindrical and infinitely long in one dimension. Consequently, it is sufficient to only account for the cross section of the object, which makes a two-dimensional spatial discretization possible. The incident Gaussian beam however has to maintain its full three-dimensional nature in the numerical description. In this way we come to a-two-and-a-half-dimensional approach, where all objects are treated in two dimensions and all electromagnetic field quantities are treated in three dimensions. This 2.5D approach is justified for the detection of a concealed object on the human body when, on a centimeter space scale, the geometric and material parameters of the object and torso do not drastically change in the elongated direction.

With the quantitative inverse scattering problem, the unknown permittivity profile is related to the scattered field data in a non-linear way. Therefore, it is generally solved iteratively as an optimization problem in which the object parameters are the unknowns. One starts with an initial guess for the object parameters and then uses a numerical scattering model to determine the corresponding scattered field. In a next step, the computed scattered field is compared to the measured scattered field. From this comparison, more suitable object parameters are obtained. This procedure is repeated until the simulated scattered field is sufficiently close to the measured scattered field. In the practical implementation, a grid of pixels is used which contains the unknown objects. The complex values of the permittivity in all pixels of the considered grid are the unknowns in the optimization problem. This PhD work contains two parts: a first part describes the numerical scattering model, while a second part deals with the described optimization problem.

The numerical scattering model is usually called the forward solver. This model computes the scattered field starting from a given permittivity profile and a known electromagnetic illumination. This scattering model needs to be solved for each different permittivity profile during the optimization process. Therefore, a fast and efficient implementation is indispensable. In this PhD, we use a volume integral approach to solve the scattering problem. Here, the scatterers are discretized on a regular grid of cells. This is in contrast to boundary integral methods where only the boundaries of a piecewise homogeneous object are discretized. In each cell of the grid, the three components of the total field are determined by solving the volume integral equation (VIE) iteratively. However, since we apply the 2.5D approach, we do not use the well-known 3D VIE, but revert to a reformulated 2.5D expression. This is done by Fourier transforming all 3D electromagnetic quantities along the elongated direction of the scatterers, for instance along the z-axis of a Cartesian coordinate system. In this way, all field components have an (x,y,k_z)-dependency instead of a (x,y,z)-dependency, where k_z is the spectral component. By performing this one-dimensional Fourier transform, the 3D VIE is rewritten as a set of 2D VIEs, one for each spectral component. After solving all 2D VIEs, the corresponding scattered field solutions are

combined to the wanted 3D scattered field by performing a one-dimensional inverse Fourier transform.

The computation time, required to solve the VIEs is dramatically reduced by applying fast Fourier transforms. In this PhD, all computations are implemented using multithreaded commands. Hence, the computations are performed by different processors within one machine. Furthermore, the computational time is decreased by proposing a well chosen initial guess for the total field at the start of the solution process for each VIE. This initial guess is determined as a linear combination of previous total field solutions for similar configurations. This is known as the marching-on technique.

Besides the numerical scattering model, a model is required to describe the incident electromagnetic field. While such a model is straightforward for a plane wave illumination, this is not the case for a Gaussian beam illumination. Literature describes different models to implement 3D Gaussian beams. We have reformulated these descriptions to fit the 2.5D approach. The most efficient model is based on the complex source formulation, applied to the 2.5D approach. Special attention is devoted to limit the number of spectral components needed to describe the Gaussian beam accurately, since one has to solve the same number of VIEs.

The numerical scattering model is validated by comparing simulated scattered fields on circular homogeneous and piecewise homogeneous cylinders with their corresponding analytical solution as well for perpendicularly incident plane waves as for obliquely incident waves. To verify the validity of the model in case of Gaussian beam illumination, we have compared our simulation results with simulation results obtained from full 3D numerical scattering models. Moreover, we demonstrate that the limitation to infinitely long cylindrical objects in the 2.5D approach can be weakened to sufficiently long cylinders when a Gaussian beam illumination is considered: the object length should be minimal double in size compared to the illuminated area. To illustrate the feasibility of detecting hidden objects on the human body, the electromagnetic scattering on a simplified human body model is considered. Since millimeter waves do not have a significant penetration depth in the human body, the interiors are not needed to be fully described. Therefore, we only account for a layer of clothing, skin and underlying fat. There is a significant influence on the electromagnetic waves when a small object is placed between the clothing and the skin. Furthermore, these simulations show the direct advantages of the 2.5D approach: due to the large dimensions of the human body and the relatively high corresponding permittivity values, the number of unknowns is very large, which makes a full 3D simulation up to now unfeasible.

In practice, the input data of the inverse scattering problem are measured scattered fields. Therefore we also investigate how well simulated scattered fields correspond to experimentally measured equivalents. We had access to two sets of measured scattered fields: the Vrije Universiteit Brussel performed field amplitude measurements on an homogeneous teflon cylinder, illuminated by a perpendicularly incident Gaussian

beam, while the Institut Fresnel in Marseille performed amplitude and phase measurements for plane wave illumination obliquely incident on an inhomogeneous cylinder. Both comparisons show that the developed numerical scattering model is perfectly capable to describe the scattered fields accurately.

The second part of this PhD work deals with the optimization technique to solve the inverse scattering problem. Here, the difference between measured and simulated scattered fields is minimized by iteratively adapting the discretized permittivity profile. The method we use is a Gauss-Newton optimization combined with a line search. As a measure for the difference between the measured and the simulated fields, a least squares data cost function with an additional regularization term is considered. This extra term is required since the inverse scattering problem is ill-posed. This ill-posedness for instance manifests itself when large differences in the permittivity profile (often with a high spatial frequency) only result in small changes in the scattered fields. These small changes can get obscured when the data is polluted with noise. These perturbations in the scattered fields can degrade the reconstructed permittivity profile. Regularization methods weaken the unwanted variations in the permittivity profile by introducing a-priori known information in the optimization problem to compensate the loss of information due to the noise. Furthermore, the Gauss-Newton scheme needs the derivatives of the scattered fields with respect to the permittivity unknowns. In this PhD work, an analytical expression is derived for the 2.5D approach.

Two existing regularization methods are applied in this PhD. The first method is a spatial regularization technique, called multiplicative smoothing regularization. In this case, a priori knowledge of a smooth permittivity profile is introduced in the optimization problem. Hence, large local variations of the permittivity are suppressed. This regularization adds the smoothing restriction multiplicatively to the data fit term. The second regularization method is not spatial, but assumes that the permittivity profile consists of a small number of discrete values which are not known in advance. Consequently, this type of regularization is suited to reconstruct piecewise homogeneous objects. This method is called the stepwise relaxed value picking regularization. Both regularization methods inspired us to formulate a new regularization method which we called the stepwise relaxed object smoothed value picking regularization technique. Similar to the stepwise relaxed value picking regularization, this new method favors piecewise homogeneous objects by grouping the complex permittivity values in the complex plane around an unknown number of reference values, which are also part of the optimization process. Similar to the multiplicative smoothing regularization, smoothness is enforced, but only within the homogeneous domains which appear during the optimization. In this way, a spatial and non-spatial technique are efficiently combined. This new regularization technique often has a longer simulation time, but is especially useful when the original stepwise relaxed value picking regularization leads to artifacts in the reconstructed profile.

To validate the quantitative inverse scattering technique, presented in this PhD work, we have used experimental data. Since no amplitude and phase data in the mil-

limeter wave range is available in the inversion community, we revert to microwave measurements. The Institut Fresnel in Marseille provides a public database with 2D scattering measurements on inhomogeneous cylinders under a plane wave illumination. We have reconstructed three objects from this database illuminated by TM and TE polarized fields. Here, we applied the three different regularization techniques described above. From the simulations, it is clear that the new stepwise relaxed object smoothed value picking regularization is the best type of regularization method since it results in almost perfect reconstructions.

To demonstrate that the proposed reconstruction technique is also perfectly applicable at millimeter wave frequencies, we use synthetic data. These are scattered fields which are generated by the numerical scattering model with added white Gaussian noise to mimic the effect of measurement noise. We have compared the quality of the reconstructions for a plane wave illumination on the one hand and for a Gaussian beam on the other hand. Here, it is concluded that the total number of iterations in the optimization scheme is identical for both types of field, although simulation times for Gaussian beam illumination are larger. The reconstructions with Gaussian beams show some more local fluctuations in the permittivity profile. To conclude the presented PhD work, a first attempt is made to simulate a millimeter wave imaging technique for the detection of hidden objects under clothing. Therefore we use the simplified human body model which is mentioned earlier. Due to the extremely large dimensions we are however obliged to further simplify the used model, to reduce the number of spectral components and to limit the number of illumination directions. Despite all these simplifications and limitations, one single iteration in the optimization scheme (applying the Gauss-Newton optimization with line search) still lasts between 15 and 27 hours. Moreover, the human body makes all round illumination of the hidden object impossible, which limits the information content of the measurement data even more and complicates the reconstruction. After about five days of computing and 6 iterations, the hidden object appears at the correct position and with the right dimensions. The corresponding permittivity value fairly agrees with the actual value. This is a good example to illustrate the possibilities of quantitative millimeter wave imaging, but it also shows the present limitations of the presented method.

List of Abbreviations

2D	Two-Dimensional
3D	Three-Dimensional
2.5D	Two-and-a-half-Dimensional
BEM	Boundary Element Method
BICGSTAB	Bi-Conjugate Gradient
BIE	Boundary Integral Equation
CG	Conjugate Gradient
CPU	Central Processing unit
CSB	Complex Source Beam
CSIE	Contrast Source Integral Equation
DFT	Discrete Fourier Transform
EIT	Electrical Impedance Tomography
FDE	The FoamDielExt target
FDI	The FoamDielInt target
FDTD	Finite Difference Time Domain
FFT	Fast Fourier Transform
GBscal	Scalar Gaussian Beam
GBvect	Vectorial Gaussian Beam
GHz	Gigahertz
GLMT	Generalized Lorenz and Mie Theorem
LHS	Left Hand Side
LS	Least Squares
NRMSE	Normalized Root Mean Square Error
MHz	Megahertz
MoM	Method of Moments
MS	Multiplicative Smoothing
PWE	Plane Wave Expansion
RHS	Right Hand Side
SRVP	Stepwise Relaxed Value Picking
TD	The TwinDiel target
TE	Transverse Electric
TFQMR	Transpose-Free Quasi-Minimal Residual
TM	Transverse Magnetic
VIE	Volume Integral Equation
VP	Value Picking
mm-wave	Millimeter wave

List of Symbols

Vectors and matrices

Vectors of general dimension are denoted by boldface lower case letters. Matrices of general dimensions as well as electromagnetic field vectors and dyadics are denoted by boldface upper case letters.

$\mathbf{r}$	The position vector in two dimensions
$\boldsymbol{\rho}$	The position vector in three dimensions
$\mathbf{u}_x$	A unit vector in the positive x-direction
$\mathbf{u}_y$	A unit vector in the positive y-direction
$\mathbf{u}_z$	A unit vector in the positive z-direction
$\mathbf{I}$	The 3×3 unit matrix

Operations on vectors and matrices and related concepts

$(\ldots)^*$	Complex conjugate
$(\ldots)^T$	Transpose
$(\ldots)^H$	Conjugate transpose
$\widehat{\ldots}$	Fourier transformed quantity (w.r.t. the z-coordinate)
$\|\ldots\|$	The L^2 norm, i.e. $\|\mathbf{u}\|^2 = \mathbf{u}^H\mathbf{u}$ for a vector $\mathbf{u}$
u_n	n-th element of the general vector $\mathbf{u}$
$A_{n,m}$	(n,m)-th element of the general matrix $\mathbf{A}$
$\cdot$	scalar (inner) product of two vectors, e.g. $\mathbf{u}_x \cdot \mathbf{u}_y$

Electromagnetic symbols

ε_0	The permittivity of vacuum
μ_0	The permeability of vacuum
ε	The complex permittivity
ε'	The real part of the complex permittivity
ε''	The imaginary part of the complex permittivity
ε_r	The complex relative permittivity
f	The frequency
ω	The angular frequency ($\omega = 2\pi f$)

λ_0	The free space wavelength
λ_{cyl}	Wavelength inside a dielectric cylinder
σ	The conductivity
k_0	The free space wave number $k_0 = j\omega\sqrt{\varepsilon_0\mu_0}$
χ	The permittivity contrast
$(\ldots)_0$	Subscript to indicate a property of vacuum
$\mathbf{E}$	The total electric field vector
$\mathbf{E}^{\mathrm{i}}$	The incident electric field vector
$\mathbf{E}^{\mathrm{s}}$	The scattered electric field vector
$\mathbf{H}$	The magnetic field vector
$\mathbf{D}$	The electric flux density vector
$\mathbf{J}$	The electric current density vector
$\mathbf{J}^{\mathrm{i}}$	The applied current density vector
ρ	The charge density
$\mathbf{J}^{\mathrm{s}}$	The contrast current density vector
$\mathbf{A}^{\mathrm{s}}$	The vector potential
G	The Green function of free space
$\mathcal{G}^{\mathcal{V}}$	Green operator acting on a vector function with support $\mathcal{V}$
$\widehat{\mathbf{G}}$	The Green dyadic of free space
$\widehat{\mathbf{G}}_{\mathrm{inh}}$	The Green dyadic in an inhomogeneous background medium

Symbols related to the incident field

$\mathbf{u}_{pol}$	Polarization vector of the incident field
$\mathbf{u}^{\mathrm{i}}$	Propagation direction of the incident field
$\mathbf{k}^{\mathrm{i}}$	Propagation vector of the incident field, $\mathbf{k}^{\mathrm{i}} = k_0\mathbf{u}^{\mathrm{i}}$
A	Amplitude of the incident field
θ^{i}	Elevation angle of the incident field
$\boldsymbol{\rho}_0$	Beam waist center of a Gaussian beam
w_0	Beam waist radius of a Gaussian beam
b_0	Beam collimation distance of a Gaussian beam
k_z	Spectral component of the incident field
k_c	Central spectral component of a Gaussian beam, $k_c = k_0\mathbf{u}^{\mathrm{i}} \cdot \mathbf{u}_z$
$s(\mathbf{r})$	Complex distance from the real point $\mathbf{r}$ to a complex source point $\boldsymbol{\rho}_c$

Symbols related to the forward scattering problem

$\varepsilon_{k,l}$	The relative permittivity of cell (k,l)
$\chi_{k,l}$	The permittivity contrast of cell (k,l)
Δ	The grid size of the forward problem grid, also denoted as Δ_{fw}
N^s	Number of forward problem cells in the x-direction
M^s	Number of forward problem cells in the y-direction
$\mathbf{D}^{\text{init}}$	Initial guess for the electric flux density vector
$\mathcal{S}$	Cross-section of an infinitely long dielectric cylinder
$\mathcal{D}$	The computational domain, also named investigation domain
$\mathbf{r}_{n,m}^{(0)}$	Center point of cell (n,m), given by $\mathbf{r}_{n,m}^{(0)} = (n\Delta,\ m\Delta)$
$\psi^{(p)}(\mathbf{r})$	Scalar basis function, used in the testing and expansion procedure of the discretization scheme
$\widehat{E}^{\text{i}}_{p;k,l}$	Expansion coefficient for the incident electric field component p, corresponding to cell (k,l)
$\widehat{d}_{p;k,l}$	Expansion coefficient for the electric flux density component p, corresponding to cell (k,l)
$\widehat{a}_{p;k,l}$	Expansion coefficient for the vector potential component p, corresponding to cell (k,l)
$g_{n,m}$	Discretized Green's function, corresponding to cell (n,m)
$\mathbf{r}_R$	Receiver position, also denoted as detector point

Symbols related to the inverse scattering problem

N^{ε}	The number of permittivity unknowns
Δ_{ε}	The grid size of the reconstruction grid
N^x	Number of inverse problem cells in the x-direction
N^y	Number of inverse problem cells in the y-direction
$\Phi_{k,l}$	A 2D pulse function which is 1 in cell (k,l) of the reconstruction grid and zero elsewhere
$\boldsymbol{\varepsilon}$	The N^{ε}-dimensional vector containing the permittivity unknowns ε_{ν}
N^A	The number of antenna positions
$\mathbf{r}^A$	The position vector for an antenna
N^T	The number of transmitting antenna positions
$\mathbf{r}_t^A$	The position vector for a transmitting antenna
$\mathbf{u}_{t,p}^A$	The polarization vector of the incident field, generated by an antenna in position $\mathbf{r}_t^A$
N^P	The number of different polarizations for incident fields generated from antenna positions $\mathbf{r}_t^A$

N^I	The total number of illuminations
N_t^R	The number of receiving antenna positions, corresponding to illumination t
$\mathbf{r}_r^A$	The position vector for a receiving antenna
$\mathbf{u}_{r,p}^A$	The polarization vector of the receiving antenna positioned in $\mathbf{r}_r^A$
$\mathbf{e}^{\text{meas}}$	Data vector containing the measured scattered fields
N^D	Length of the data vector $\mathbf{e}^{\text{meas}}$
$\mathbf{e}^{\text{scat}}(\boldsymbol{\varepsilon})$	Vector containing the simulated scattered fields for the permittivity profile $\boldsymbol{\varepsilon}$
$\mathcal{F}^{LS}$	The data fit cost function
$\mathcal{F}^{\mathcal{MS}}$	The cost function with multiplicative smoothing regularization
α	Regularization parameter for multiplicative smoothing regularization
$\mathcal{F}^{\mathcal{R}}$	The smoothing regularizing function
$\mathcal{N}^{\mathcal{R}}$	A normalization constant for multiplicative smoothing regularization
$\mathcal{F}^{\mathcal{VP}}$	The cost function with stepwise relaxed value picking regularization
P	The number of VP values used in stepwise relaxed value picking regularization
γ	Regularization parameter for stepwise relaxed value picking regularization
$\mathcal{F}^{\mathcal{P}}$	The VP regularizing function with P VP values
$\mathbf{c}$	Vector containing all VP values used in stepwise relaxed value picking regularization, except the background permittivity
f^P	The P-dimensional choice function in stepwise relaxed value picking regularization
$\mathcal{F}^{\mathcal{SROSVP}}$	The cost function with stepwise relaxed object smoothed value picking regularization
ζ	Regularization parameter for object smoothed part of $\mathcal{F}^{\mathcal{SROSVP}}$
$\mathcal{F}^{\mathcal{OS}}$	The object smoothed regularizing function
$\Delta\boldsymbol{\varepsilon}$	Update direction for the permittivity vector
$\mathbf{g}$	A (complex) gradient vector
$\mathbf{H}$	A (complex) Hessian matrix
$\mathbf{g}^{\mathcal{LS}}$	Gradient vector for the data fit cost function
$\mathbf{H}^{\mathcal{LS}}$	Hessian matrix for the data fit cost function
$\mathbf{J}$	The Jacobian matrix of the scattered field vector with respect to the permittivity unknowns
Σ_k^{reg}	Matrix containing second order derivatives of the regularizing part of the cost function

Ω^{reg}	Vector containing first order derivatives of the regularizing part of the cost function
λ^{reg}	Trade-off parameter used in the construction of the permittivity correction $\Delta\boldsymbol{\varepsilon}$
T^N	The noise level

Special functions

J_n	n-th order Bessel function of the first kind
Y_n	n-th order Bessel function of the second kind
$H_n^{(1)}$	n-th order Hankel function of the first kind

Miscellaneous

j	The imaginary unit, $j = \sqrt{-1}$
s	Seconds
t	Time variable
∞	Infinity

List of Publications

Articles in international journals

- S. Van den Bulcke and A. Franchois, "A full-wave 2.5D volume integral equation solver for 3D millimeter-wave scattering by large inhomogeneous 2D objects," *IEEE Transactions on Antennas and Propagation*, vol. 57, no. 2, pp. 535-545, Feb. 2009.
- S. Van den Bulcke, L. Zhang, A. Franchois, J. M. Geffrin and J. Stiens, "Plane wave and Gaussian beam scattering by long dielectric cylinders: 2.5D simulations versus measurements," *International Journal of Infrared and Millimeter Waves*, vol. 29, no. 11, pp. 1038-1047, Nov. 2008.

Articles in conference proceedings

- S. Van den Bulcke, A. Franchois, L. Zhang, and J. Stiens, "A 2.5D BiCGS-FFT forward solver to model scattering in a mm-wave imaging system," *Proceedings of the Mediteranean Microwave Symposium (MMS 2006)*, Genova, Italy, Sept. 19-21, 2006, pp. 277-280.
- S. Van den Bulcke, A. Franchois, L. Zhang, and J. Stiens, "Modeling a millimeter wave imaging system with a 2.5D BICGS-FFT volume integral equation technique," *Proceedings of the European Conference on Antennas and Propagation (EUCAP 2006)*, Nice, France, Nov. 6-10, 2006, (Proceedings available on CD-ROM), ISBN 92-9092-937-5.
- S. Van den Bulcke and A. Franchois, "A 2.5D solver to model scattering of long dielectric cylinders in an active millimeter wave imaging system," *Proceedings of the 23rd Annual Review of Progress in Applied Computational Electromagnetics (ACES 2007)*, Verona, Italy, March 19-23, 2007, pp. 1223-1229. Invited.
- S. Van den Bulcke and A. Franchois, "2.5D solver for 3D scattering by a large 2D inhomogeneous object," *Proceedings of the International Symposium on Electromagnetic Theory (EMTS 2007)*, Ottawa, ON, Canada, July 26-28, 2007.
- S. Van den Bulcke and A. Franchois, "Modelling 3D mm-wave scattering from human body under Gaussian beam illumination with a 2.5D VIE solver," *Proceedings of the 24rd Annual Review of Progress in Applied Computational Electromagnetics (ACES 2008)*, Niagara Falls, Canada, March 30 - April 4, 2008, pp. 63-67.

- S. Van den Bulcke, A. Franchois, J.M. Geffrin, L. Zhang, and J. Stiens, "3D scattering by large inhomogeneous 2D objects: Validation of a full-wave 2.5D VIE solver with millimeter wave Gaussian beam and microwave experiments," *Proceedings of the Progress in Electromagnetics Research Symposium (PIERS 2008)*, Boston, USA, July 2-6, 2008.
- S. Van den Bulcke and A. Franchois, "Quantitative millimeter wave imaging of 2.5D inhomogeneous objects," *International Conference on Electromagnetics in Advanced Applications (ICEAA 2009)*, Torino, Italy, Sept. 14-18, 2009, pp. 86-89.

Conference Abstracts

- S. Van den Bulcke and A. Franchois, "An exact 2.5D BiCGS-FFT forward solver to model electromagnetic scattering in an active millimeter wave imaging system," In *Proceedings of the 7th FirW Ph.D. Symposium*, Faculty of Engineering, Ghent, Belgium, Nov. 29, 2006, CD-ROM.
- S. Van den Bulcke and A. Franchois, "Validation of a full-wave 2.5D VIE solver with millimeter-wave Gaussian beam and microwave experiments," In *Proceedings of the URSI Forum*, Brussels, Belgium, May 30, 2008, CD-ROM.
- S. Van den Bulcke and A. Franchois, "2.5D microwave inversion of dielectric objects using Value Picking regularization," In *Proceedings of the Workshop on Electromagnetic Inverse Problems*, School of Mathematics, University of Manchester, Manchester, UK, June 15-18, 2009, 2p.

Scientific Award

- Laureate presentation award at the 7th FirW Ph.D. Symposium, Faculty of Engineering, Ghent, Belgium, Nov. 29, 2006.

A 2.5D Electromagnetic Quantitative Inverse Scattering Technique to Visualize Concealed Objects using Millimeter Waves

CHAPTER 1

General introduction

1.1. Situation

In this doctoral thesis, a quantitative electromagnetic imaging technique is developed to detect hidden objects using millimeter waves.

The term *electromagnetic imaging* describes a number of techniques that try to extract information about unknown objects, based on their electromagnetic behavior. Such techniques are widely used in many different scientific domains. Geologists use them to resolve different layers in soil or to estimate the size of magma chambers in volcanos [1]. Rich geologists (sponsored by the oil industry) combine them with seismic and acoustic methods to detect new oil supplies without performing the expensive test drilling of boreholes [2]. For health care, electromagnetic imaging techniques are of interest to detect breast cancer [3, 4, 5] or prostate cancer [6, 7], to monitor ventilation in chronic pulmonary diseases [8, 9] or to study the behavior of the heart [10]. Other applications are the localization of neurological defects in the brain from EEG measurements [11] and the prevention of cot death [12, 13]. Non-destructive testing techniques are developed to detect cracks in solid materials [14] or to localize metal bars in reinforced concrete [15, 16].

Electromagnetic imaging techniques which are based on the use of electromagnetic *waves* are denoted as *inverse scattering methods*, contrary to e.g. the Electrical Impedance Tomography (EIT) imaging techniques [6, 9, 17]. Inverse scattering methods try to extract information about an object, based on how it scatters electromagnetic radiation. In this extraction procedure, often called *the inverse scattering problem*, an object is illuminated with known electromagnetic waves, e.g. from different directions, and the corresponding scattered fields are measured in a number of receiver points. The measured data is then used to reconstruct the shape, dimensions, location and electromagnetic material parameters – in this PhD the complex permittivity profile – of the unknown object.

The wide range of methods to solve an inverse scattering problem can roughly be classified in two classes, depending on the type of information they extract from the measurements. The first class contains the *qualitative* methods. Examples are radar imaging [18, 19], diffraction tomography [20, 21, 22], the Linear Sampling method [23, 24]. These methods provide approximate information on properties as reflectivity, induced currents: this only gives some idea of the shape, location and number of objects. Qualitative methods use a linear or linearized model to relate the data and the reconstruction parameters, which makes them quite fast compared to the second class, the *quantitative* methods. Quantitative algorithms provide detailed information on the intrinsic electromagnetic material properties of an object since they relate the data and the reconstruction parameters exactly. This requires the solution of a system of non-linear equations, instead of a linear or linearized version. Due to this non-linearity, it is common to apply an iterative optimization procedure. The focus of this PhD work lies entirely on the quantitative inverse problem.

Quantitative inverse scattering methods have been studied widely in the microwave frequency range [25,26,27,28,29,30,31,32]. They are mainly used for medical imaging [5, 33, 34, 35, 36, 37] and non destructive testing of materials [38, 39]. In this PhD work however, we use millimeter waves. These waves have a wavelength between one millimeter and one centimeter, corresponding to relatively high frequencies (30 to 300 GHz) in the electromagnetic spectrum.

The interest in millimeter waves recently has grown in the imaging research community thanks to its possible use in security applications [40, 41, 42, 43, 44, 45], although the application range is much wider [46,47]. One of the most interesting properties of millimeter waves is that they easily penetrate clothing but reflect on the human body. This makes them perfectly suitable to detect weapons or explosives hidden under clothing. X-rays offer no alternative to millimeter waves for this type of application due to their ionizing nature and metal detectors fail at detecting non-metallic hidden objects. However, most of the practical applications, such as the body scanners which are currently installed at different international airports, are not quantitative but qualitative imaging applications. In 2005, an SBO-IWT research project, funded by the Flemish government, was initiated by the Vrije Universiteit Brussel (VUB) as a cooperation between different universities (among which the department of Information Technology of Ghent University) to develop a qualitative millimeter wave imaging system for concealed object detection based on [48]. In this PhD work, we have studied how millimeter waves can be used in the framework of a quantitative inverse scattering technique.

The choice for millimeter waves largely complicates the numerical implementation of the quantitative inverse scattering technique for concealed object detection. Indeed, the considered objects tend to be very large compared to the wavelength. Therefore, full-wave three-dimensional computations as in [29, 35, 49, 50, 51] are hardly feasible, since these methods result in a large amount of unknowns and thus a big memory consumption and long simulation times. Another consequence of the chosen

wavelength is that the type of illumination is usually a highly directive Gaussian beam, contrary to the more uniform plane wave-like illuminations, which are typically used in the microwave imaging community. The fully vectorial three-dimensional nature of the Gaussian beam illumination forbids the use of a purely two-dimensional scattering model [52, 53, 54]. However, since the beam illuminates a spatially limited region, the size of the scattering problem can be reduced drastically by assuming that all objects are cylindrical and infinitely long in one dimension. Consequently, it is sufficient to only account for the cross section of the object, which makes a two-dimensional spatial discretization possible. The incident Gaussian beam however has to maintain its full three-dimensional nature in the numerical description. In this way we come to a two-and-a-half-dimensional (2.5D) approach, where all objects are treated in two dimensions and all electromagnetic field quantities are treated in three dimensions. This 2.5D approach is justified for the detection of a concealed object on the human body when, on a centimeter space scale, the geometric and material parameters of the object and torso do not drastically change in the elongated direction.

1.2. Description of the problem

With the quantitative inverse scattering problem, the unknown permittivity profile is related to the scattered field data in a non-linear way. Therefore, it is usually solved iteratively as an optimization problem in which the object parameters – in this PhD the complex permittivity – are the unknowns.

A major constituent of the quantitative inverse scattering problem is the numerical scattering model, which computes the scattered fields that correspond to a given set of object parameters and a given illumination. Generally, the input of a model is called the *model parameters*, its output is denoted as the *data*. The evaluation of a numerical scattering model for a given set of object parameters is often denoted as the *forward scattering problem*, where the term *forward* indicates that the model parameters are known, but the data need to be determined, see Fig. 1.1.

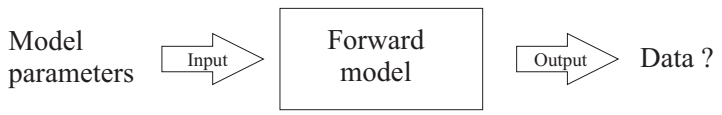

Figure 1.1: Flowchart of the forward problem.

In quantitative inverse scattering applications however, the model output (the data) is at hand, while the model parameters are of interest. Since one works the other way around, this procedure is called *the inverse problem*. An example of an iterative procedure to solve the inverse problem is shown in Fig. 1.2. One starts with an initial guess for the model parameters and then uses the forward model to determine the

corresponding scattered field data. In a next step, the computed scattered field data are compared to the measured scattered field data. From this comparison, more suitable model parameters are obtained. This procedure is repeated until the simulated scattered field is sufficiently close to the measured scattered field.

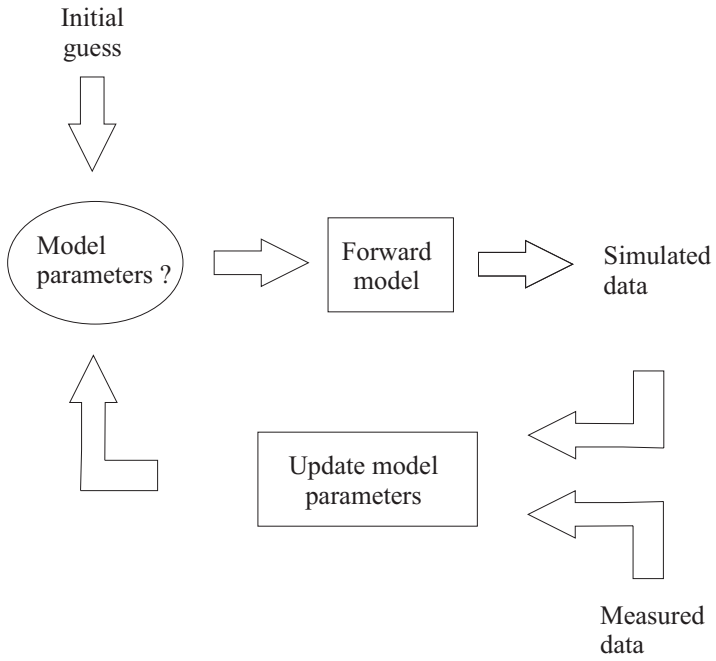

Figure 1.2: Flowchart of solving the inverse problem.

In the practical implementation, a grid of pixels is used which contains the unknown object. The complex values of the permittivity in all pixels of the considered grid are the unknowns in the optimization problem. This approach to reconstruct objects is denoted a *pixel based* optimization scheme.

This PhD work contains two parts: a first part describes the forward scattering problem, while a second part deals with the inverse scattering problem.

1.2.1 The forward problem: evaluating the numerical scattering model

The numerical scattering model computes the scattered field starting from a given permittivity profile and a known electromagnetic plane wave or Gaussian beam illumination. This forward problem needs to be solved for each permittivity profile during the optimization process. Therefore, a fast and efficient implementation is indispensable.

In literature, techniques have been presented to determine the three-dimensional scattered fields of an infinitely long homogeneous cylinder, with circular or elliptic

cross-section, that is illuminated by a plane wave [55]. These so-called *analytic solutions* do not discretize the scattering object. Gouesbet [56] extended this theory to the case of an arbitrary shaped incident beam within the framework of the Generalized Lorenz and Mie Theorem and based on the variable separation method. However, these techniques cannot handle inhomogeneous cylinders with arbitrary cross-section, which strongly limits the range of possible scattering configurations. Furthermore, the capability of simulating inhomogeneous cylinders is necessary when a forward solver is to be included in a quantitative pixel-based inversion scheme. Therefore, in this PhD work, we do not use the analytic solutions and their extensions to Gaussian beam illumination to solve the forward problem.

Existing numerical 2.5D schemes were particularly designed to interpret experimental data from ground penetrating radars in a geophysical context, see e.g. [1] and for submarine imaging, see e.g. [57]. In these applications, three-dimensional low frequency excitations induce scattered fields that are interpreted in a numerical inversion scheme to reveal buried objects (e.g. pipe lines), different ground layers (e.g. gas fields), etc. Different numerical techniques have been used in 2.5D forward problem schemes. In [58], the Boundary Element Method (BEM) is adopted to compute the scattered fields. The computational domain is restricted to be piecewise homogeneous enabling to discretize only the boundaries. When the number of objects is increasing, a BEM no longer offers an advantage compared to volume discretization schemes. In [59], an improved Finite Difference Time Domain (FDTD) scheme is presented. The method reduces the number of finite difference cells but (as all FDTD schemes) needs absorbing boundary conditions such as perfectly matched layers to simulate free space. This is also the case for a Finite Element Method (FEM), which is often chosen for its flexible meshing capability. In [2], a Volume Integral Equation (VIE) approach is adopted. The computational domain is discretized using identical cells as in the FDTD method, but the interactions between the cells are described using integral equations. Open boundary problems are naturally handled in this approach avoiding the use of absorbing boundary conditions. Building on the existing experience in the research group, this PhD work applies a VIE approach to allow for strongly inhomogeneous scattering objects.

Within the *volume* integral equation approach, the scatterer is discretized on a regular grid of cells. This is in contrast to boundary integral equation (BIE) methods where only the boundaries of a piecewise homogeneous object are discretized [51]. In each cell of the grid, the three components of the total field are determined by solving the VIE iteratively. However, since we apply the 2.5D assumption, we do not use the well-known 3D VIE, but revert to a reformulated 2.5D expression. This is done by Fourier transforming all 3D electromagnetic quantities along the elongated direction of the scatterers, for instance along the z-axis of a Cartesian coordinate system. In this way, all field components have an (x, y, k_z)-dependency instead of a (x, y, z)-dependency, where k_z is the spectral component. By performing this one dimensional Fourier transform, the 3D VIE is rewritten as a set of 2D VIEs, one for each spectral

component. After solving all 2D VIEs, the corresponding scattered field solutions are combined to the desired 3D scattered field by performing a one dimensional inverse Fourier transform.

The computation time, required to solve the VIEs is dramatically reduced by applying fast Fourier transforms. In this PhD, all computations are implemented using multithreaded commands. Hence, the computations are performed by different processors within one machine. Furthermore, the computational time is decreased by proposing a well chosen initial guess for the total field at the start of the solution process for each VIE. This initial guess is determined as a linear combination of previous total field solutions for similar configurations. This is known as the marching-on technique [60, 61].

Besides the numerical scattering model, a model is required to describe the incident electromagnetic field. While such a model is straightforward for a plane wave illumination, this is not the case for a Gaussian beam illumination. Literature describes different models to implement 3D Gaussian beams [62, 63, 64]. We have reformulated these descriptions to fit the 2.5D approach. The most efficient model is based on the complex source formulation [63, 64], applied to the 2.5D approach. Special attention is devoted to limit the number of spectral components needed to describe the Gaussian beam accurately, since one has to solve the same number of VIEs. Furthermore, in the case of a Gaussian beam illumination, we demonstrate that the object does not have to be *infinitely* long, as long as its extent is somewhat larger than the size of the illuminated region and its electromagnetic permittivity is invariant along this extent. We refer to such objects as *quasi two-dimensional objects*.

1.2.2 The inverse problem: estimating the model parameters

In the inverse scattering problem, the difference between measured and simulated scattered fields is minimized by iteratively adapting the discretized permittivity profile. The method we use is a Gauss-Newton optimization combined with a line search [65]. The computational efficiency of a Gauss-Newton scheme is improved when an analytical expression is available for the derivatives of the scattered fields with respect to the permittivity unknowns. In this PhD work, such expressions are derived for the 2.5D approach.

This inverse problem is *ill-posed*, which means that existence, uniqueness and stability of a solution (convergence to the solution) cannot be guaranteed simultaneously [66]. To complicate matters even further, the electromagnetic inverse problem is also *non-linear*, e.g. doubling the model parameters does not lead to a doubled scattered field. In the following, it is illustrated how the ill-posedness and non-linearity can be tackled.

- **non-linearity**:
  If the experimental scattering data are collected in the data vector $\mathbf{e}^{\text{meas}}$ and the simulated scattered field data are collected in the vector $\mathbf{e}^{\text{scat}}(\boldsymbol{\varepsilon}(\boldsymbol{\rho}))$, the inverse

problem tries to solve

$$\mathbf{e}^{\text{meas}} = \mathbf{e}^{\text{scat}}(\varepsilon(\boldsymbol{\rho})) \tag{1.1}$$

for the permittivity profile $\varepsilon(\boldsymbol{\rho})$. Here, $\mathbf{e}^{\text{scat}}(\varepsilon(\boldsymbol{\rho}))$ represents the forward problem, evaluated for $\varepsilon(\boldsymbol{\rho})$, with $\boldsymbol{\rho} = (x, y, z)$ the position vector. Due to its non-linearity, the quantitative inverse scattering problem is solved in an iterative way.

- **existence**:
  Measurements are hardly ever performed in ideal circumstances, usually the measurement data will be corrupted by measurement noise. Furthermore, the numerical implementation of the forward model also introduces noise (as a consequence of discretization, some approximations, ...) Due to these effects it is almost impossible to find a profile $\varepsilon(\boldsymbol{\rho})$ that yields an exact data fit (1.1). Therefore, this exact data fit is replaced by the minimization of a least squares data fit:

$$||\mathbf{e}^{\text{meas}} - \mathbf{e}^{\text{scat}}(\varepsilon(\boldsymbol{\rho}))||^2 \tag{1.2}$$

- **non-uniqueness**:
  Problems with non-uniqueness result from another characteristic of the inverse problem: there are only a limited number of degrees of freedom in the measured field data (the information content of the data is limited). The permittivity profile however can have a large amount of degrees of freedom. Therefore, different permittivity profiles can minimize the least squares data fit (1.2). The solution to this problem is to provide as much non-redundant data as possible.

- **stability**:
  The stability problem is a consequence of the fact that the computed scattered fields are not very sensitive to changes in the permittivity profile. Large differences in the permittivity profile (often with a high spatial frequency) only result in small changes in the scattered fields. These small perturbations in the scattered fields can get obscured when the data is polluted with noise, which can degrade the reconstructed permittivity profile. So, information is lost due to noise on the measured and simulated data. The usual way to cope with this is to apply a proper regularization to the inverse problem to weaken unwanted variations in the permittivity profile. A-priori information thus is added to the inverse problem to compensate for this loss of information. Examples of such a-priori information are the assumptions that there are no big jumps in the permittivity profile (smooth object), or that there are only a limited number of distinct permittivity values in the profile (piecewise homogeneous object). This additional information also diminishes the effect of non-uniqueness since it also reduces the number of degrees of freedom for the permittivity profile.

Two existing regularization methods are applied in this PhD. The first method is a spatial regularization technique, called multiplicative smoothing regularization [67]. In this case, a priori knowledge of a smooth permittivity profile is introduced in the optimization problem. Hence, large local variations of the permittivity are suppressed. This regularization adds the smoothing restriction multiplicatively to the data fit term. The second regularization method is not spatial, but assumes that the permittivity profile consists of a small number of discrete values which are not known in advance. Consequently, this type of regularization is suited to reconstruct piecewise homogeneous objects. This method is called the stepwise relaxed value picking regularization [67, 68]. Both regularization methods inspired us to formulate a new regularization method which we called the stepwise relaxed object smoothed value picking regularization technique. Similar to the stepwise relaxed value picking regularization, this new method favors piecewise homogeneous objects by grouping the complex permittivity values in the complex plane around an unknown number of reference values, which are also part of the optimization process. Similar to the multiplicative smoothing regularization, smoothness is enforced, but only within the homogeneous domains that appear during the optimization. In this way, a spatial and non-spatial technique are efficiently combined. This new regularization technique often has a longer simulation time, but is especially useful when the original stepwise relaxed value picking regularization leads to artifacts in the reconstructed profile.

1.3. Overview of the PhD work

The first part of this PhD work deals with the 2.5D forward solver. The implementation is detailed in Chapter 2. The first step is a proper discretization of the contrast source integral equation after conversion to the 2.5-dimensional case, yielding multiple linear sets of equations to be solved. The next step is to use an iterative method (a Biconjugate Gradient iterative solver) to solve these systems and combine it with accelerating techniques (e. g. the Fast Fourier Transform method and marching-on techniques) to speed-up the solution process.

Chapter 3 describes the incident fields in detail. Two different types of illuminations are studied: plane waves and Gaussian beams. Different models are studied for the implementation of a Gaussian beam illumination.

The forward solver is validated for many different test cases: by comparing simulations to analytic solutions and to results of fully three-dimensional numerical solvers, also developed at the department of Information Technology [51, 69]. This extensive validation is presented in Chapter 4 and in [70]. As an illustration for the concealed weapon detection applications, a body scattering example is also simulated.

The last chapter in the forward problem part of this PhD work, Chapter 5, is devoted to the comparison of obtained numerical results to experimentally measured fields. Measurements have been performed at the LAMI-ETRO department of Vrije

Universiteit Brussel (VUB) and at the Institut Fresnel in Marseille. Results of this comparison with experimental results are presented in [71].

The second part of this PhD work is devoted to the 2.5-dimensional electromagnetic inverse scattering problem. Chapter 6 describes the implementation details: the global configuration, the updating process for the complex permittivity, different definitions of cost functions and regularization strategies.

To validate the proposed quantitative inverse scattering technique, we use experimental data. Since no amplitude and phase data in the millimeter wave range is available in the inversion community, we revert to microwave measurements. The Institut Fresnel in Marseille provides a public database with 2D scattering measurements on inhomogeneous cylinders under a plane wave illumination. Chapter 7 presents reconstructions of these objects, for different regularization strategies.

Chapter 8 presents reconstructions from synthetic data in the millimeter wave range. On the one hand, we compare reconstructions for a plane wave illumination to reconstructions for a Gaussian beam illumination. On the other hand, a first attempt is made to simulate a millimeter wave imaging technique for the detection of hidden objects under clothing.

The last chapter of this PhD work contains the conclusion and proposes some interesting further research topics.

Bibliography

[1] L. Tabarovsky, M. Goldman, M. Rabinovich, and K. Strack, "2.5-D modeling in electromagnetic methods of geophysics," *Journal of Applied Geophysics*, vol. 35, no. 4, pp. 261–284, Oct. 1996.

[2] A. Abubakar, P. van den Berg, and T. Habashy, "An integral equation approach for 2.5-dimensional forward and inverse electromagnetic scattering," *Geophysical Journal International*, vol. 165, no. 3, pp. 744–762, June 2006.

[3] J. De Zaeytijd and A. Franchois, "3D quantitative microwave imaging with a regularized gauss-newton method for breast cancer detection," in *The 24rd Annual Review of Progress in Applied Computational Electromagnetics (ACES 2008)*, Niagara Falls, Canada, 2008, pp. 467–472.

[4] M. Zhao, J. Shea, S. Hagness, D. van der Weide, B. Van Veen, and T. Varghese, "Numerical study of microwave scattering in breast tissue via coupled dielectric and elastic contrast," *IEEE Antennas and Wireless Propagation Letters*, vol. 7, pp. 247–250, 2008.

[5] N. Irishina, M. Moscoso, and O. Dorn, "Microwave imaging for early breast cancer detection using a shape-based strategy," *IEEE Transactions on Biomedical Imaging*, vol. 56, no. 4, pp. 1143–1153, April 2009.

[6] R. Halter, A. Schned, J. Heaney, A. Hartov, S. Schutz, and K. Paulsen, "Electrical impedance spectroscopy of benign and malignant prostatic tissues," *Journal of Urology*, vol. 179, no. 4, pp. 1580–1586, April 2008.

[7] A. Tubaro, C. De Nunzio, A. Trucchi, A. Stoppacciaro, and L. Miano, "The electromagnetic detection of prostate cancer: Evaluation of diagnostic accuracy," *Urology*, vol. 72, no. 2, pp. 340–344, August 2008.

[8] S. Egot-Lemaire, J. Pijanka, J. Sule-Suso, and S. Semenov, "Dielectric spectroscopy of normal and malignant lung cells at ultra high frequencies," *Physics in Medicine and Biology*, vol. 54, no. 8, pp. 2341–2357, April 2009.

[9] G. Hahn, J. Dittmar, A. Just, and G. Hellige, "Improvements in the image quality of ventilatory tomograms by electrical impedance tomography," *Physiological Measurement*, vol. 29, no. 6, pp. S51–S61, June 2008.

[10] S. Semenov, V. Posukh, A. Bulyshev, T. Williams, Y. Sizov, P. Repin, A. Souvorov, and A. Navarov, "Microwave tomographic imaging of the heart in intact swine," *Journal of Electromagnetic Waves and Applications*, vol. 20, no. 7, pp. 873–890, 2006.

[11] G. Crevecoeur, H. Hallez, L. Dupr, R. Van de Walle, P. Boon, and I. Lemahieu, "Validation of the two-level approach for the solution of the EEG inverse prob-

lem in an anisotropic realistic head model," *IEEE Transactions on Magnetics*, vol. 45, no. 3, pp. 1670–1673, March 2009.

[12] A. Taktak, P. Record, R. Gadd, and P. Rolfe, "Practical factors in neonatal lung imaging using electrical impedance tomography," *Medical and Biological Engineering and Computing*, vol. 33, no. 2, pp. 202–205, March 1995.

[13] T. Tidswell, R. Bayford, J. Wyatt, and D. Holder, "Functional imaging of neonatal evoked responses with electrical impedance tomography," *Neuroimage*, vol. 13, no. 6, pp. S1268–S1268, June 2001.

[14] W. Park and D. Lesselier, "MUSIC-type imaging of a thin penetrable inclusion from its multi-static response matrix," *Inverse Problems*, vol. 25, no. 7, July 2009.

[15] A. Franchois, P. Lewyllie, and L. Taerwe, "2-D near-field SAR non-destructive testing of rebars in a concrete wall," *International Journal of Applied Electromagnetics and Mechanics*, vol. 19, no. 1-4, pp. 333–338, 2004.

[16] S. Van Damme, A. Franchois, D. De Zutter, and L. Taerwe, "Nondestructive determination of the steel fiber content in concrete slabs with an open-ended coaxial probe," *IEEE Transactions on Geoscience and Remote Sensing*, vol. 42, no. 11, pp. 2511–2521, November 2004.

[17] D. Barber and B. Brown, "Applied potential tomography (review article)," *Journal of Physics E: Scientific Instruments*, vol. 17, 1984.

[18] T. Hansen and P. Johansen, "Inversion scheme for ground penetrating radar that takes into account the planar air-soil interface," *IEEE Transactions on Geoscience and Remote Sensing*, vol. 38, no. 1, pp. 496–506, 2000.

[19] C. Leuschen and R. Plumb, "A matched-filter-based reverse-time migration algorithm for ground-penetrating radar," *IEEE Transactions on Geoscience and Remote Sensing*, vol. 39, no. 5, pp. 929–936, 2001.

[20] A. Devaney, "A filtered backpropagation algorithm for diffraction tomography," *ultrasonic Imaging*, vol. 4, no. 4, pp. 336–350, 1982.

[21] J. Bolomey, L. Jofre, C. Pichot, G. Peronnet, and M. Solaimani, "Microwave diffraction tomography for biomedical applications," *IEEE Transactions on Microwave Theory and Techniques*, vol. 30, no. 11, pp. 1998–2000, 1982.

[22] W. Tabbara, B. Duchêne, C. Pichot, D. Lesselier, L. Chommeloux, and N. Joachimowicz, "Diffraction tomography: contribution to the analysis of some applications in microwaves and ultrasonics," *Inverse Problems*, vol. 4, no. 2, pp. 305–331, 1988.

[23] D. Colton and P. Monk, "A linear sampling method for the detection of leukemia using microwaves," *SIAM Journal on Applied Mathematics*, vol. 58, no. 3, pp. 926–941, 1998.

[24] D. Colton, H. Haddar, and M. Piana, "The linear sampling method in inverse electromagnetic scattering theory," *Inverse Problems*, vol. 19, pp. S105–S137, 2003.

[25] W. Chew and Y. Wang, "Reconstruction of two-dimensional permittivity distribution using the distorted born iterative method," *IEEE Transactions on Medical Imaging*, vol. 9, no. 2, pp. 218–225, 1990.

[26] N. Joachimowicz, C. Pichot, and J. Hugonin, "Inverse scattering: An iterative numerical method for electromagnetic imaging," *IEEE Transactions on Antennas and Propagation*, vol. 39, no. 12, pp. 1742–1752, 1991.

[27] S. Caorsi, A. Massa, and M. Pastorino, "A computational technique based on a real-coded genetic algorithm for microwave imaging purposes," *IEEE Transactions on Geoscience and Remote Sensing*, vol. 38, no. 4, pp. 1697–1708, July 2000.

[28] T. Cui, W. Chew, A. Aydiner, and S. Chen, "Inverse scattering of two-dimensional dielectric objects buried in a lossy earth using the distorted born iterative method," *IEEE Transactions on Geoscience and Remote Sensing*, vol. 39, no. 2, pp. 339–345, 2001.

[29] G. Franceschini, D. Franceschini, and A. Massa, "Full-vectorial three-dimensional microwave imaging through the iterative multiscaling strategy - a preliminary assessment," *IEEE Transactions on Geoscience and Remote Sensing Letters*, vol. 2, no. 4, pp. 428–432, 2005.

[30] T. Takenaka, H. Zhou, and T. Tanaka, "Inverse scattering for a three-dimensional object in the time domain," *Journal of the Optical Society of America A*, vol. 20, no. 10, pp. 1867–1874, 2003.

[31] A. Franchois and C. Pichot, "Microwave imaging - complex permittivity reconstruction with a levenberg-marquardt method," *IEEE Transactions on Antennas and Propagation*, vol. 45, no. 2, pp. 203–215, Feb. 1997.

[32] O. Feron, B. Duchene, and A. Mohammad-Djafari, "Microwave imaging of inhomogeneous objects made of a finite number of dielectric and conductive materials from experimental data," *Inverse Problems*, vol. 21, no. 6, pp. S95–S115, 2005.

[33] A. Abubakar, P. van den Berg, and J. Mallorqui, "Imaging of biomedical data using a multiplicative regularized contrast source inversion method," *IEEE Transactions on Microwave Theory and Techniques*, vol. 50, no. 7, pp. 1761–1770, 2002.

[34] P. Mojabi and J. LoVetri, "Microwave biomedical imaging using the multiplicative regularized gauss-newton inversion," *IEEE Antennas and Wireless Propagation Letters*, vol. 8, pp. 645–648, 2009.

[35] Z. Zhang and Q. Liu, "Three-dimensional nonlinear image reconstruction for microwave biomedical imaging," *IEEE Transactions on Biomedical Engineering*, vol. 51, no. 3, pp. 544–548, 2004.

[36] T. Rubaek, P. Meaney, P. Meincke, and K. Paulsen, "Nonlinear microwave imaging for breast-cancer screening using gauss-newton's method and the CGLS inversion algorithm," *IEEE Transactions on Antennas and Propagation*, vol. 55, no. 8, pp. 2320–2331, 2007.

[37] P. Meaney, M. Fanning, D. Li, S. Poplack, and K. Paulsen, "A clinical prototype for active microwave imaging of the breast," *IEEE Transactions on Microwave Theory and Techniques*, vol. 48, no. 11, pp. 1841–1853, 2000.

[38] D. Álvarez , O. Dorn, N. Irishina, and M. Moscoso, "Crack reconstruction using a level-set strategy," *Journal of Computational Physics*, vol. 228, no. 16, pp. 5710–5721, 2009.

[39] U. Hasar, "Non-destructive testing of hardened cement specimens at microwave frequencies using a simple free-space method," *NDT & E International*, vol. 42, no. 6, pp. 550–557, 2009.

[40] D. Sheen, D. Mc Makin, and T. Hall, "Three-dimensional millimeter-wave imaging for concealed weapon detection," *IEEE Transactions on Microwave Theory and Techniques*, vol. 49, no. 9, pp. 1581–1592, Sept. 2001.

[41] K. Langenberg, K. Mayer, and C. Sklarczyk, "Wave field imaging for homeland security," in *Proceedings of the International URSI EMTS Commission B - Electromagnetic Theory Symposium*, Ottawa, Canada, 2007.

[42] N. Farhat and W. Guard, "Millimeter wave holographic imaging of concealed weapons," *Proceedings of the IEEE*, vol. 59, pp. 1383–1384, 1971.

[43] D. M. Makin, D. Sheen, H. Collins, T. Hall, and R. Severtsen, "Wideband, millimeter-wave, holographic weapons surveillance system," *Proceedings of the SPIE European Symposium on Optics for Environmental and Public Safety*, vol. 2511, pp. 131–141, 1995.

[44] D. Sheen, D. Mc Makin, H. Collins, T. Hall, and R. Severtsen, "Concealed explosive detection on personnel using a wideband holographic millimeter-wave imaging system," *Proceedings of the SPIE International Symposium on Aerospace /Defense Sensing, Simulation, and Controls*, vol. 2755, pp. 503–513, 1996.

[45] H. Chen, S. Lee, R. Rao, M. Slamani, and P. Varshney, "Imaging for concealed weapon detection," *IEEE Signal Processing magazine*, vol. 22, no. 2, pp. 52–61, 2005.

[46] J. Lovberg, R. Chou, and C. Martin, "Real-time millimeter-wave imaging radiometer for avionic synthetic vision," *Proceedings of the SPIE - The International Society for Optical Engineering*, vol. 2220, 1994.

[47] P. Hsu, B. Deng, J. Wang, C. Domier, and N. Luhmann, "Millimeter-wave imaging array development for microwave reflectometry and ECE imaging," *Review of Scientific Instruments*, vol. 72, pp. 364–367, 2001.

[48] L. Volkov and J. Stiens, "Systems and methods for millimeter and sub-millimeter wave imaging," U.S Patent 6 777 684, Aug., 2004.

[49] P. Zwamborn and P. van den Berg, "The three-dimensional weak form of the conjugate gradient FFT method for solving scattering problems," *IEEE Transactions on Microwave Theory and Techniques*, vol. 40, no. 9, pp. 1757–1766, Sept. 1992.

[50] J. De Zaeytijd, I. Bogaert, and A. Franchois, "An efficient hybrid MLFMA-FFT solver for the volume integral equation in case of sparse 3-D inhomogeneous dielectric scatterers," *Journal of Computational Physics*, vol. 227, no. 14, pp. 7052–7068, July 2008.

[51] J. Peeters, J. Fostier, F. Olyslager, and D. De Zutter, "New parallel approaches for fast multipole solvers," in *Proceedings of the second European Conference on Antennas and Propagation*, Edinburgh, UK, 2007, pp. 1–5.

[52] J. Richmond, "Scattering by a dielectric cylinder of arbitrary cross section shape," *IEEE Transactions on Antennas and Propagation*, vol. 13, no. 3, pp. 334–341, May 1965.

[53] P. Zwamborn and P. van den Berg, "A weak form of the conjugate gradient FFT method for two-dimensional TE scattering problems," *IEEE Transactions on Microwave Theory and Techniques*, vol. 39, no. 6, pp. 953–960, June 1991.

[54] A. Tijhuis, K. Belkebir, and A. Litman, "Theoretical and computational aspects of 2-D inverse profiling," *IEEE Transactions on Geoscience and Remote Sensing*, vol. 39, no. 6, pp. 1316–1330, June 2001.

[55] C. Bohren and D. Huffman, *Absorption and scattering of light by small particles*. Wiley, 1983.

[56] G. Gouesbet, "Interaction between an infinite cylinder and an arbitrary-shaped beam," *Applied Optics*, vol. 36, no. 18, pp. 4292–4304, 1997.

[57] M. Everett and R. Edwards, "Transient marine electromagnetics: the 2.5-D forward problem," *Geophysical Journal International*, vol. 113, no. 3, pp. 545–561, 1993.

[58] E. Ngakosso, A. Straub, M. Saillard, and P. Vincent, "Electromagnetic 2.5-dimensional forward modelling with boundary integral formulation," *Geophysical Journal International*, vol. 135, no. 3, pp. 1028–1044, Dec. 1998.

[59] G. Zhao and Q. Liu, "The 2.5-D multidomain pseudospectral time-domain algorithm," *IEEE Transactions on Antennas and Propagation*, vol. 51, no. 3, pp. 619 – 627, March 2003.

[60] A. Tijhuis, M. van Beurden, and P. Zwamborn, "Iterative solution of field problems with a varying physical parameter," *Elektrik, Turkish Journal of Electrical Engineering & Computer Sciences*, vol. 10, no. 2, pp. 163–183, 2002.

[61] Z. Peng and A. Tijhuis, "Transient scattering by a lossy dielectric cylinder: Marching-on-in-frequency approach," *Journal of Electromagnetic Waves and Applications*, vol. 7, no. 5, pp. 739–763, 1993.

[62] P. Goldsmith, *Quasioptical Systems: Gaussian Beam Quasioptical Propagation and Applications*. New York: IEEE Press / Chapman and Hall Publishers Series on Microwave Technology and RF, 1997.

[63] E. Heyman and L. Felsen, "Gaussian beam and pulsed beam dynamics: complex-source and complex-spectrum formulations within and beyond paraxial asymptotics," *Journal of the Optical Society of America A*, vol. 18, no. 7, pp. 1588–1611, July 2001.

[64] I. Lindell, *Advanced Field Theory*. Helsinki, Finland: Helsinki University of Technology, 2000.

[65] R. Fletcher, *Practical Methods of Optimization*. New York: John Wiley, 1990.

[66] J. Hadamard, "Sur les problèmes aux derivéés partielles et leur signification physique," *Princeton University Bulletin*, 1902.

[67] J. De Zaeytijd and A. Franchois, "3D quantitative microwave imaging from measured data with multiplicative smoothing and value picking regularization," *Inverse Problems*, vol. 25, no. 2, p. 024004, Feb. 2009.

[68] J. De Zaeytijd, A. Franchois, and J. Geffrin, "A new value picking regularization strategy – application to the 3D electromagnetic inverse scattering problem," *IEEE Transactions on Antennas and Propagation*, vol. 57, no. 4, pp. 1133–1149, April 2009.

[69] P. Lewyllie, A. Franchois, C. Eyraud, and J.M. Geffrin, "Testing a 3D BCGS-FFT solver against experimental data," in *Proceedings of the 9th International Conference on Electromagnetics in Advanced Applications (ICEAA 2005)*, Torino, Italy, Sept. 2005, pp. 421–424.

[70] S. Van den Bulcke and A. Franchois, "A full-wave 2.5D volume integral equation solver for 3D millimeter-wave scattering by large inhomogeneous 2D objects," *IEEE Transactions on Antennas and Propagation*, vol. 57, no. 2, pp. 535–545, Feb. 2009.

[71] S. Van den Bulcke, L. Zhang, A. Franchois, J. Geffrin, and J. Stiens, "Plane wave and gaussian beam scattering by long dielectric cylinders: 2.5D simulations versus measurements," *International Journal of Infrared and Millimeter Waves*, vol. 29, no. 11, pp. 1038–1047, Nov. 2008.

PART I

THE FORWARD PROBLEM

CHAPTER 2

Solving the forward problem

2.1. Introduction

The forward problem consists of determining the scattered fields that correspond to a given permittivity profile of an object and some set of incident fields (multi-view illumination). The forward solver presented in this chapter is developed to be part of a quantitative imaging scheme. Hence, it should be able to simulate completely inhomogeneous objects. Therefore, a volume integral equation (*VIE*) scheme is selected. The integral equation formulation implicitly accounts for the appropriate boundary conditions by means of the Green's function, whereas with a differential equation formulation (Finite Element Method, Finite Difference Time Domain method,) the boundary conditions need to be imposed explicitly.

Since the forward solver is intended to be used in the millimeter wave range (small wavelength compared to object dimensions) computations can hardly be done in a fully three-dimensional fashion, as already stated in Chapter 1. Therefore, a 2.5-dimensional (2.5D) technique is adopted: the fields maintain their three-dimensional character but the objects are restricted to be long inhomogeneous, possibly lossy, dielectric cylinders with invariant electromagnetic properties along their axis. Due to this assumption, it is sufficient to only discretize the two-dimensional cross-section of the scattering objects, which strongly reduces the number of unknowns.

The 2.5D forward problem is expanded into a number of two-dimensional problems by performing a spatial Fourier transform of all fields along the invariant z-direction. Each spectral Fourier component then corresponds to a particular two-dimensional problem, that is formulated as a contrast source integral equation in terms of the Fourier transformed electric fields. The different two-dimensional problems only depend on the transverse spatial variable $\mathbf{r}$. The Method of Moments is applied to convert each two-dimensional problem to a linear set of equations, which is solved with a fast iterative technique. After an inverse Fourier transformation, the different

two-dimensional solutions are recombined to obtain the full three-dimensional scattered field.

Zwamborn et al. [1, 2] determined a contrast source integral equation in terms of a vector potential for the purely two-dimensional and three-dimensional cases. In this work, we follow the same approach to derive and discretize a set of contrast source integral equations for the 2.5D case. All this is discussed in the following sections of this chapter.

2.2. Configuration

We assume that the scatterer is isotropic, dielectric (non-magnetic) and embedded in free space (with permittivity ε_0 and permeability μ_0), and that it can be inhomogeneous. In the 2.5D assumption, the complex permittivity profile $\varepsilon(\mathbf{r})$ of an object is denoted as a function of the transverse two-dimensional position coordinate $\mathbf{r}$. It is a combination of the (real) relative dielectric permittivity $\varepsilon_r'(\mathbf{r})$ and the conductivity $\sigma(\mathbf{r})$:

$$\varepsilon(\mathbf{r}) = \varepsilon_0\varepsilon_r(\mathbf{r}) = \varepsilon'(\mathbf{r}) + j\varepsilon''(\mathbf{r}) = \varepsilon_0\varepsilon_r'(\mathbf{r}) + j\frac{\sigma(\mathbf{r})}{\omega}, \tag{2.1}$$

where we have omitted the angular frequency (ω) dependency in the various profiles. The arbitrarily shaped cross-section of a dielectric cylinder is represented by $\mathcal{S}$. The axis of the cylinder is aligned with the z-axis of a three-dimensional cartesian coordinate system $\boldsymbol{\rho} = \mathbf{r} + z\mathbf{u}_z$, where $\mathbf{r} = x\mathbf{u}_x + y\mathbf{u}_y$ defines the position in the xy-plane, see Fig. 2.1.

All simulations are restricted to a single frequency and a time-dependence $e^{-j\omega t}$ is assumed for all field related quantities. Hence, the (time-harmonic) incident electric field (with three-dimensional character) can be denoted with the complex vector

$$\begin{aligned}\mathbf{E}^{\mathrm{i}}(\mathbf{r},z) &= E_1^{\mathrm{i}}(\mathbf{r},z)\mathbf{u}_x + E_2^{\mathrm{i}}(\mathbf{r},z)\mathbf{u}_y + E_3^{\mathrm{i}}(\mathbf{r},z)\mathbf{u}_z \\ &= [E_1^{\mathrm{i}}(\mathbf{r},z), E_2^{\mathrm{i}}(\mathbf{r},z), E_3^{\mathrm{i}}(\mathbf{r},z)].\end{aligned} \tag{2.2}$$

The superscript 'i' indicates the incident field, the superscript 's' represents the scattered field. The total field (without superscript) is defined as the sum of incident and scattered field:

$$\begin{aligned}\mathbf{E}(\mathbf{r},z) &= [E_1(\mathbf{r},z), E_2(\mathbf{r},z), E_3(\mathbf{r},z)] \\ &= \mathbf{E}^{\mathrm{i}}(\mathbf{r},z) + \mathbf{E}^{\mathrm{s}}(\mathbf{r},z).\end{aligned} \tag{2.3}$$

2.3. Towards a set of Contrast Source Integral Equations

The derivation of the set of contrast source integral equations starts from the Maxwell equations in the frequency domain for the three-dimensional total fields in a two-

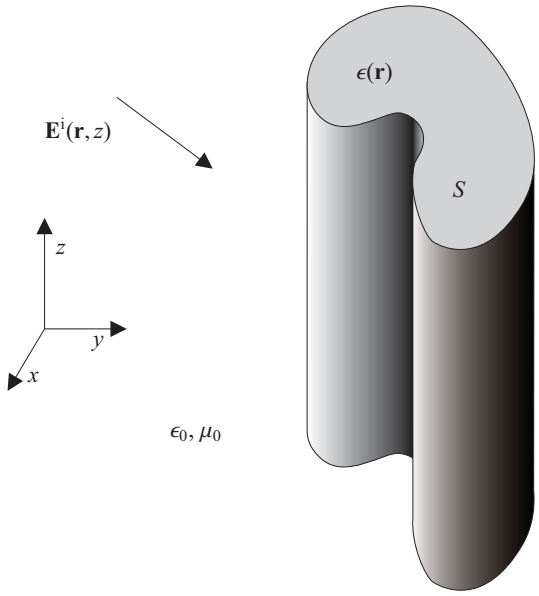

Figure 2.1: 2.5D Configuration.

dimensional isotropic inhomogeneous dielectric medium (characterized by $\varepsilon(\mathbf{r})$):

$$\nabla \times \mathbf{E}(\mathbf{r},z) = j\omega\mu_0 \mathbf{H}(\mathbf{r},z) \tag{2.4a}$$

$$\nabla \times \mathbf{H}(\mathbf{r},z) = \mathbf{J}^{\mathrm{i}}(\mathbf{r},z) - j\omega\varepsilon(\mathbf{r})\mathbf{E}(\mathbf{r},z) \tag{2.4b}$$

$$\nabla \cdot (\varepsilon(\mathbf{r})\mathbf{E}(\mathbf{r},z)) = \rho^{\mathrm{i}}(\mathbf{r},z) \tag{2.4c}$$

$$\mu_0 \nabla \cdot \mathbf{H}(\mathbf{r},z) = 0 \tag{2.4d}$$

with $\nabla = (\frac{\partial}{\partial x}, \frac{\partial}{\partial y}, \frac{\partial}{\partial z})$ and $\mathbf{H}(\mathbf{r},z)$ the total magnetic field. $\mathbf{J}^{\mathrm{i}}(\mathbf{r},z)$ is an applied source current density and $\rho^{\mathrm{i}}(\mathbf{r},z)$ the corresponding charge density.

By performing a Fourier transform of the electromagnetic fields along the z-direction, the 2.5-dimensional forward problem transforms into a set of two-dimensional problems. This spatial Fourier transform (denoted with a " $\widehat{\ }$ " superscript) is defined as

$$\widehat{g}(\mathbf{r},k_z) = \int_{-\infty}^{\infty} g(\mathbf{r},z) e^{-jk_z z} \mathrm{d}z \tag{2.5}$$

and its inverse transform as

$$g(\mathbf{r},z) = \frac{1}{2\pi} \int_{-\infty}^{\infty} \widehat{g}(\mathbf{r},k_z) e^{jk_z z} \mathrm{d}k_z. \tag{2.6}$$

The spatial Fourier transform (2.5) of the Maxwell equations (2.4) yields the transformed equations:

$$\widehat{\nabla} \times \widehat{\mathbf{E}}(\mathbf{r}, k_z) = j\omega\mu_0 \widehat{\mathbf{H}}(\mathbf{r}, k_z) \tag{2.7a}$$

$$\widehat{\nabla} \times \widehat{\mathbf{H}}(\mathbf{r}, k_z) = \widehat{\mathbf{J}}^{\mathrm{i}}(\mathbf{r}, k_z) - j\omega\varepsilon(\mathbf{r})\widehat{\mathbf{E}}(\mathbf{r}, k_z) \tag{2.7b}$$

$$\widehat{\nabla} \cdot \Big(\varepsilon(\mathbf{r})\widehat{\mathbf{E}}(\mathbf{r}, k_z)\Big) = \widehat{\rho}^{\mathrm{i}}(\mathbf{r}, k_z) \tag{2.7c}$$

$$\mu_0 \widehat{\nabla} \cdot \widehat{\mathbf{H}}(\mathbf{r}, k_z) = 0 \tag{2.7d}$$

where, following (2.6), $\widehat{\nabla} = (\frac{\partial}{\partial x}, \frac{\partial}{\partial y}, jk_z)$. In (2.7), $\widehat{\mathbf{J}}^{\mathrm{i}}(\mathbf{r}, k_z)$ is the applied current density that generates the incident field $\widehat{\mathbf{E}}^{\mathrm{i}}(\mathbf{r}, k_z)$ and $\widehat{\rho}^{\mathrm{i}}(\mathbf{r}, k_z)$ is the charge density that corresponds to $\widehat{\mathbf{J}}^{\mathrm{i}}(\mathbf{r}, k_z)$.
Before deriving the set of two-dimensional contrast source integral equations, the term *contrast source* is introduced.

2.3.1 Definition of a contrast source

The Fourier transformed Maxwell equations (2.7) can be reformulated in terms of sources in a homogeneous free space medium:

$$\widehat{\nabla} \times \widehat{\mathbf{E}}(\mathbf{r}, k_z) = j\omega\mu_0 \widehat{\mathbf{H}}(\mathbf{r}, k_z) \tag{2.8a}$$

$$\widehat{\nabla} \times \widehat{\mathbf{H}}(\mathbf{r}, k_z) = \widehat{\mathbf{J}}^{\mathrm{i}}(\mathbf{r}, k_z) - j\omega\left(\varepsilon(\mathbf{r}) - \varepsilon_0\right)\widehat{\mathbf{E}}(\mathbf{r}, k_z) - j\omega\varepsilon_0\widehat{\mathbf{E}}(\mathbf{r}, k_z) \tag{2.8b}$$

$$\varepsilon_0 \widehat{\nabla} \cdot \widehat{\mathbf{E}}(\mathbf{r}, k_z) = \widehat{\rho}^{\mathrm{i}}(\mathbf{r}, k_z) + \frac{1}{j\omega}\widehat{\nabla} \cdot \Big[-j\omega\left(\varepsilon(\mathbf{r}) - \varepsilon_0\right)\widehat{\mathbf{E}}(\mathbf{r}, k_z)\Big] \tag{2.8c}$$

$$\mu_0 \widehat{\nabla} \cdot \widehat{\mathbf{H}}(\mathbf{r}, k_z) = 0 \tag{2.8d}$$

Furthermore, the law of charge conservation is given by

$$\widehat{\rho}(\mathbf{r}, k_z) = \frac{1}{j\omega}\widehat{\nabla} \cdot \widehat{\mathbf{J}}(\mathbf{r}, k_z). \tag{2.9}$$

If this law is combined with equations (2.8), it can be seen that a solution $(\widehat{\mathbf{E}}(\mathbf{r}, k_z), \widehat{\mathbf{H}}(\mathbf{r}, k_z))$ of Maxwell's equations (2.7), is also a solution for the Maxwell's equations formulated for free space (2.8), where a source current density is introduced:

$$\widehat{\mathbf{J}}^{\mathrm{s}}(\mathbf{r}, k_z) = -j\omega\left(\varepsilon(\mathbf{r}) - \varepsilon_0\right)\widehat{\mathbf{E}}(\mathbf{r}, k_z). \tag{2.10}$$

In what follows, the electric flux density

$$\begin{aligned} \widehat{\mathbf{D}}(\mathbf{r}, k_z) &= [\widehat{D_1}(\mathbf{r}, k_z), \widehat{D_2}(\mathbf{r}, k_z), \widehat{D_3}(\mathbf{r}, k_z)] \\ &= \varepsilon(\mathbf{r})\widehat{\mathbf{E}}(\mathbf{r}, k_z) \end{aligned} \tag{2.11}$$

is chosen as the unknown field rather than the total field $\widehat{\mathbf{E}}(\mathbf{r},k_z)$, in accordance with [1]. Hence, the source current density (2.10) can be rewritten as

$$\begin{aligned}\widehat{\mathbf{J}}^{\mathrm{s}}(\mathbf{r},k_z) &= -j\omega\frac{[\varepsilon(\mathbf{r})-\varepsilon_0]}{\varepsilon(\mathbf{r})}\widehat{\mathbf{D}}(\mathbf{r},k_z)\\ &= -j\omega\chi(\mathbf{r})\widehat{\mathbf{D}}(\mathbf{r},k_z).\end{aligned} \tag{2.12}$$

The quantity $\chi(\mathbf{r})$ is the normalized permittivity contrast function and differs from zero only in the object with support $\mathcal{S}$. Hence, the additional source current density $\widehat{\mathbf{J}}^{\mathrm{s}}(\mathbf{r},k_z)$ is called the *contrast current* density.
From the linearity of the fields with respect to the sources in the Maxwell equations (2.8), it follows that the incident field $\widehat{\mathbf{E}}^{\mathrm{i}}(\mathbf{r},k_z)$ satisfies

$$\widehat{\nabla}\times\widehat{\mathbf{E}}^{\mathrm{i}}(\mathbf{r},k_z) = j\omega\mu_0\widehat{\mathbf{H}}^{\mathrm{i}}(\mathbf{r},k_z) \tag{2.13a}$$

$$\widehat{\nabla}\times\widehat{\mathbf{H}}^{\mathrm{i}}(\mathbf{r},k_z) = \widehat{\mathbf{J}}^{\mathrm{i}}(\mathbf{r},k_z) - j\omega\varepsilon_0\widehat{\mathbf{E}}^{\mathrm{i}}(\mathbf{r},k_z) \tag{2.13b}$$

$$\varepsilon_0\widehat{\nabla}\cdot\widehat{\mathbf{E}}^{\mathrm{i}}(\mathbf{r},k_z) = \widehat{\rho}^{\mathrm{i}}(\mathbf{r},k_z) \tag{2.13c}$$

$$\mu_0\widehat{\nabla}\cdot\widehat{\mathbf{H}}^{\mathrm{i}}(\mathbf{r},k_z) = 0 \tag{2.13d}$$

and the scattered field $\widehat{\mathbf{E}}^{\mathrm{s}}(\mathbf{r},k_z)$ satisfies

$$\widehat{\nabla}\times\widehat{\mathbf{E}}^{\mathrm{s}}(\mathbf{r},k_z) = j\omega\mu_0\widehat{\mathbf{H}}^{\mathrm{s}}(\mathbf{r},k_z) \tag{2.14a}$$

$$\widehat{\nabla}\times\widehat{\mathbf{H}}^{\mathrm{s}}(\mathbf{r},k_z) = -j\omega\chi(\mathbf{r})\widehat{\mathbf{D}}(\mathbf{r},k_z) - j\omega\varepsilon_0\widehat{\mathbf{E}}^{\mathrm{s}}(\mathbf{r},k_z) \tag{2.14b}$$

$$\varepsilon_0\widehat{\nabla}\cdot\widehat{\mathbf{E}}^{\mathrm{s}}(\mathbf{r},k_z) = \frac{1}{j\omega}\widehat{\nabla}\cdot\Big[-j\omega\chi(\mathbf{r})\widehat{\mathbf{D}}(\mathbf{r},k_z)\Big] \tag{2.14c}$$

$$\mu_0\widehat{\nabla}\cdot\widehat{\mathbf{H}}^{\mathrm{s}}(\mathbf{r},k_z) = 0 \tag{2.14d}$$

These equations give rise to the contrast source integral equation when the scattered field is expressed in terms of a vector potential.

2.3.2 Scattered field in terms of a vector potential

Equations (2.14) are solved with the aid of a vector potential $\widehat{\mathbf{A}}^{\mathrm{s}}(\mathbf{r},k_z)$, defined as

$$\widehat{\mathbf{H}}^{\mathrm{s}}(\mathbf{r},k_z) = -j\omega\varepsilon_0\widehat{\nabla}\times\widehat{\mathbf{A}}^{\mathrm{s}}(\mathbf{r},k_z). \tag{2.15}$$

First, a Helmholtz equation is derived for this vector potential [3]. Therefore, (2.15) is substituted in (2.14a) yielding

$$\widehat{\nabla}\times\Big(\widehat{\mathbf{E}}^{\mathrm{s}}(\mathbf{r},k_z) - k_0^2\widehat{\mathbf{A}}^{\mathrm{s}}(\mathbf{r},k_z)\Big) = 0, \tag{2.16}$$

with $k_0^2 = \omega^2 \varepsilon_0 \mu_0$. Equation (2.16) implies that $\widehat{\mathbf{E}}^{\mathrm{s}}(\mathbf{r}, k_z) - k_0^2 \widehat{\mathbf{A}}^{\mathrm{s}}(\mathbf{r}, k_z)$ can be derived from a scalar potential. Hence, we write

$$\widehat{\mathbf{E}}^{\mathrm{s}}(\mathbf{r}, k_z) = k_0^2 \widehat{\mathbf{A}}^{\mathrm{s}}(\mathbf{r}, k_z) + \nabla\phi. \tag{2.17}$$

Insertion of (2.15) and (2.17) in (2.14b) yields

$$\widehat{\nabla}^2 \widehat{\mathbf{A}}^{\mathrm{s}}(\mathbf{r}, k_z) + k_0^2 \widehat{\mathbf{A}}^{\mathrm{s}}(\mathbf{r}, k_z) = -\frac{\chi(\mathbf{r}) \widehat{\mathbf{D}}(\mathbf{r}, k_z)}{\varepsilon_0} + \left(\widehat{\nabla} \left(\widehat{\nabla} \cdot \widehat{\mathbf{A}}^{\mathrm{s}}(\mathbf{r}, k_z) \right) - \widehat{\nabla}\phi \right). \tag{2.18}$$

Applying the Lorenz gauge condition

$$\widehat{\nabla} \cdot \widehat{\mathbf{A}}^{\mathrm{s}}(\mathbf{r}, k_z) - \phi = 0 \tag{2.19}$$

finally yields the Helmholtz equation for the vector potential:

$$\widehat{\nabla}^2 \widehat{\mathbf{A}}^{\mathrm{s}}(\mathbf{r}, k_z) + k_0^2 \widehat{\mathbf{A}}^{\mathrm{s}}(\mathbf{r}, k_z) = -\frac{\chi(\mathbf{r}) \widehat{\mathbf{D}}(\mathbf{r}, k_z)}{\varepsilon_0}. \tag{2.20}$$

The solution of this equation is given by

$$\widehat{\mathbf{A}}^{\mathrm{s}}(\mathbf{r}, k_z) = \frac{1}{\varepsilon_0} \int_{\mathcal{S}} \widehat{G}(\mathbf{r}, \mathbf{r}'; k_z) \chi(\mathbf{r}') \widehat{\mathbf{D}}(\mathbf{r}', k_z) \mathrm{d}\mathbf{r}', \tag{2.21}$$

where the integration is limited to the object domain $\mathcal{S}$, since the contrast $\chi(\mathbf{r})$ only differs there from zero. The 2D Green's function $\widehat{G}(\mathbf{r}, \mathbf{r}'; k_z)$ is the solution of the Helmholtz equation

$$\widehat{\nabla}^2 \widehat{G}(\mathbf{r}, \mathbf{r}'; k_z) + k_0^2 \widehat{G}(\mathbf{r}, \mathbf{r}'; k_z) = -\delta(\mathbf{r}') \tag{2.22}$$

or, since $\widehat{\nabla}^2 = \nabla_{2D}^2 - k_z^2$ and $\nabla_{2D}^2 = (\frac{\partial}{\partial x}, \frac{\partial}{\partial y})$, of

$$\nabla_{2D}^2 \widehat{G}(\mathbf{r}, \mathbf{r}'; k_z) + (k_0^2 - k_z^2) \widehat{G}(\mathbf{r}, \mathbf{r}'; k_z) = -\delta(\mathbf{r}'). \tag{2.23}$$

It is given by

$$\widehat{G}(\mathbf{r}, \mathbf{r}'; k_z) = \frac{j}{4} H_0^{(1)} \left(\sqrt{k_0^2 - k_z^2}\, |\mathbf{r} - \mathbf{r}'| \right). \tag{2.24}$$

and corresponds to the 2D Green's function of homogeneous space with relative permittivity $\varepsilon_r = 1 - k_z^2 / k_0^2$.

The second step consists of expressing the scattered field in terms of the vector potential. Therefore, the Lorenz gauge condition (2.19) is inserted in (2.17) yielding

$$\widehat{\mathbf{E}}^{\mathrm{s}}(\mathbf{r}, k_z) = \left(k_0^2 \mathbf{I} + \widehat{\nabla}\widehat{\nabla} \right) \cdot \widehat{\mathbf{A}}^{\mathrm{s}}(\mathbf{r}, k_z), \tag{2.25}$$

where $\mathbf{I}$ is the 3×3 identity dyadic.

2.3.3 Set of Contrast Source Integral Equations

The contrast source integral equation (CSIE) for a given spectral component k_z is now obtained in terms of the electric flux density $\widehat{\mathbf{D}}(\mathbf{r},k_z)$ by substituting (2.25), together with (2.11), into (2.3):

$$\widehat{\mathbf{E}}^{\mathrm{i}}(\mathbf{r},k_z) = \frac{\widehat{\mathbf{D}}(\mathbf{r},k_z)}{\varepsilon(\mathbf{r})} - \left(k_0^2\mathbf{I} + \widehat{\nabla}\widehat{\nabla}\right)\cdot\widehat{\mathbf{A}}^{\mathrm{s}}(\mathbf{r},k_z), \tag{2.26}$$

where the vector potential $\widehat{\mathbf{A}}^{\mathrm{s}}(\mathbf{r},k_z)$ is given by (2.21).

Figure 2.2 shows the 2.5D forward model for a given permittivity $\varepsilon(\mathbf{r})$ and incident field $\mathbf{E}^{\mathrm{i}}(\mathbf{r},z)$ as a set of contrast source integral equations (2.26) with varying k_z. First, a Fourier transform is performed on the incident field $\mathbf{E}^{\mathrm{i}}(\mathbf{r},z)$. Every spectral component corresponds to a particular 2D forward problem (2.26) which is then solved for the unknown electric flux density $\widehat{\mathbf{D}}(\mathbf{r},k_z)$. Next, the corresponding scattered fields $\widehat{\mathbf{E}}^{\mathrm{s}}(\mathbf{r},k_z)$ are combined, yielding the final three-dimensional scattered field after an inverse Fourier transform.

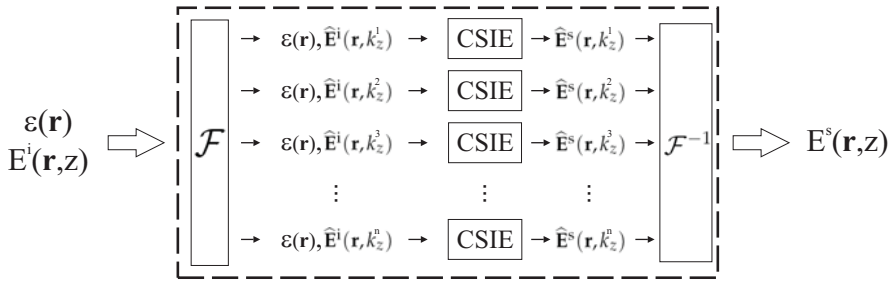

Figure 2.2: Forward model.

The number of spectral components k_z, and hence the number of forward problems, depends on the type of incident field. In this PhD work, plane waves and Gaussian beams are used. The Fourier transformation of a plane wave only yields one spectral component, more particularly the projection of the propagation vector $\mathbf{k}$ on the z-axis. The Fourier transformation of a Gaussian beam is also Gaussian, hence its spectrum is concentrated around the projection of the beam propagation vector $\mathbf{k}$ on the z-axis, which restricts the number of 2D problems to be solved. These incident fields are thoroughly discussed in Chapter 3.

Figure 2.3 illustrates the iterative solution of the CSIE (2.26), where the grey box represents one *CSIE*-block from Fig. 2.2. First, one takes an initial guess for the electric flux density $\widehat{\mathbf{D}}(\mathbf{r},k_z) = \widehat{\mathbf{D}}_{\mathrm{init}}(\mathbf{r},k_z)$ within $\mathcal{S}$. Next, the corresponding vector potential $\widehat{\mathbf{A}}^{\mathrm{s}}(\mathbf{r},k_z)$ is computed based on formula (2.21). Both electric flux density and vector potential are then plugged into the right hand side (*RHS*) of equation (2.26). This RHS is compared to the known left hand side (*LHS*), i.e. the incident field $\widehat{\mathbf{E}}^{\mathrm{i}}(\mathbf{r},k_z)$

within $\mathcal{S}$. If the difference between RHS and LHS is sufficiently small (i.e. smaller than a predefined treshold), it is assumed that the current value for $\widehat{\mathbf{D}}(\mathbf{r},k_z)$ is the solution. If not, a new guess for the electric flux density $\widehat{\mathbf{D}}(\mathbf{r},k_z) = \widehat{\mathbf{D}}'(\mathbf{r},k_z)$ is made by the Biconjugate Gradient iterative routine [4] and the process starts all over again. Once the solution for $\widehat{\mathbf{D}}(\mathbf{r},k_z)$ is obtained, the corresponding total field can be computed from (2.11). The scattered field within $\mathcal{S}$ immediately follows from (2.11), while the scattered field on the detectors is computed with (2.21) and (2.25).

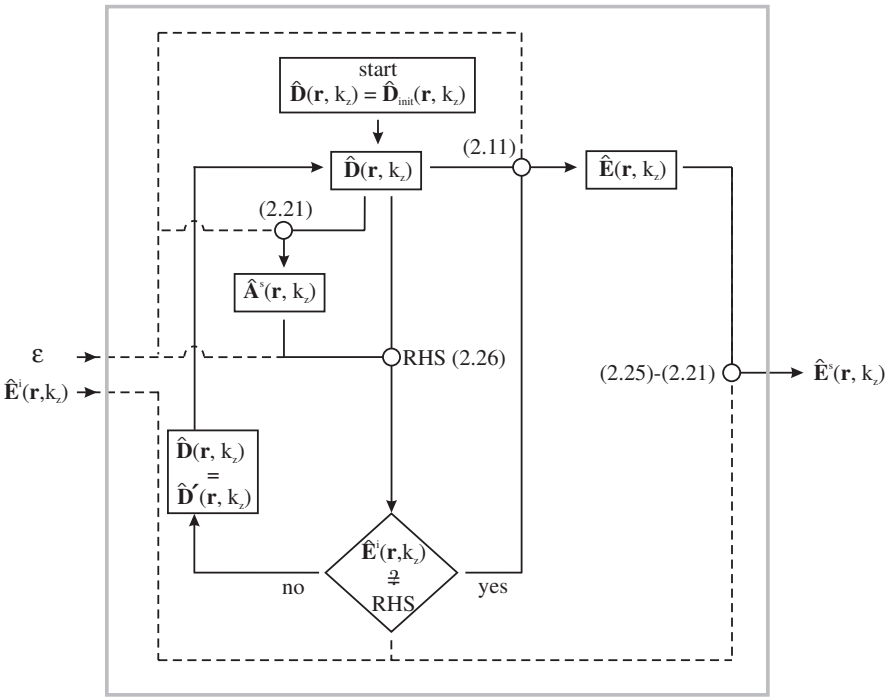

Figure 2.3: CSIE model.

The contrast source integral equation (2.26) takes the following form for each component individually:

$$\begin{aligned}\widehat{E}_1^{\mathrm{i}}(\mathbf{r},k_z) =& \frac{\widehat{D}_1(\mathbf{r},k_z)}{\varepsilon(\mathbf{r})} - k_0^2\widehat{A}_1^{\mathrm{s}}(\mathbf{r},k_z) \\ &- \frac{\partial^2}{\partial x^2}\widehat{A}_1^{\mathrm{s}}(\mathbf{r},k_z) - \frac{\partial^2}{\partial x\partial y}\widehat{A}_2^{\mathrm{s}}(\mathbf{r},k_z) - jk_z\frac{\partial}{\partial x}\widehat{A}_3^{\mathrm{s}}(\mathbf{r},k_z), \qquad (2.27a)\\ \widehat{E}_2^{\mathrm{i}}(\mathbf{r},k_z) =& \frac{\widehat{D}_2(\mathbf{r},k_z)}{\varepsilon(\mathbf{r})} - k_0^2\widehat{A}_2^{\mathrm{s}}(\mathbf{r},k_z) \\ &- \frac{\partial^2}{\partial x\partial y}\widehat{A}_1^{\mathrm{s}}(\mathbf{r},k_z) - \frac{\partial^2}{\partial y^2}\widehat{A}_2^{\mathrm{s}}(\mathbf{r},k_z) - jk_z\frac{\partial}{\partial y}\widehat{A}_3^{\mathrm{s}}(\mathbf{r},k_z), \qquad (2.27b)\\ \widehat{E}_3^{\mathrm{i}}(\mathbf{r},k_z) =& \frac{\widehat{D}_3(\mathbf{r},k_z)}{\varepsilon(\mathbf{r})} - k_0^2\widehat{A}_3^{\mathrm{s}}(\mathbf{r},k_z) \\ &- jk_z\frac{\partial}{\partial x}\widehat{A}_1^{\mathrm{s}}(\mathbf{r},k_z) - jk_z\frac{\partial}{\partial y}\widehat{A}_2^{\mathrm{s}}(\mathbf{r},k_z) + k_z^2\widehat{A}_3^{\mathrm{s}}(\mathbf{r},k_z), \qquad (2.27c)\end{aligned}$$

where the indices $1,2,3$ denote the x-, y- and z-component respectively.

The CSIE (2.27) for the Fourier transformed field vector $\widehat{\mathbf{D}}(\mathbf{r},k_z)$ differs from the CSIE for the two-dimensional TE field vector in Zwamborn and Van den Berg [1] by the extra terms $\frac{\partial}{\partial x}\widehat{A}_3^{\mathrm{s}}(\mathbf{r},k_z)$ and $\frac{\partial}{\partial y}\widehat{A}_3^{\mathrm{s}}(\mathbf{r},k_z)$ in the first two equations and by the additional third equation.

2.4. Discretization scheme

For every spectral parameter k_z in the incident field, the contrast source integral equation ((2.26) or (2.27)) must be solved numerically, which requires a discretization of the involved quantities.

Since all variables in (2.26) only depend on the transverse spatial variable $\mathbf{r}$, a 2D spatial discretization is applied:

- The permittivity $\varepsilon(\mathbf{r})$ is discretized on a uniform square grid.
- Equation (2.26) is discretized with a Galerkin Method of Moments, whereby the unknown field quantities $\widehat{\mathbf{D}}(\mathbf{r},k_z)$ and $\widehat{\mathbf{A}}^{\mathrm{s}}(\mathbf{r},k_z)$ are expanded in basis functions and equation (2.26) is tested with appropriate testing functions.
- The expression for the vector potential (2.21) is discretized in a way to preserve convolution symmetry.

2.4.1 Discretization grids

In this PhD work we have extended the 2D Galerkin Method of Moments discretization presented in [1] to the 2.5D case. Consider a rectangular computational domain $\mathcal{D}$, which completely includes the support S of the scatterer and which is uniformly meshed in $N_s \times M_s$ square cells with edge size Δ and with center points

$\mathbf{r}_{n,m}^{(0)} = (n\Delta,\ m\Delta)$, with $n = 0 \ldots N_s - 1, m = 0 \ldots M_s - 1$, see Fig. 2.4. In each cell, the complex permittivity and contrast are assumed to be constant with values $\varepsilon_{n,m}$ and $\chi_{n,m}$, respectively.

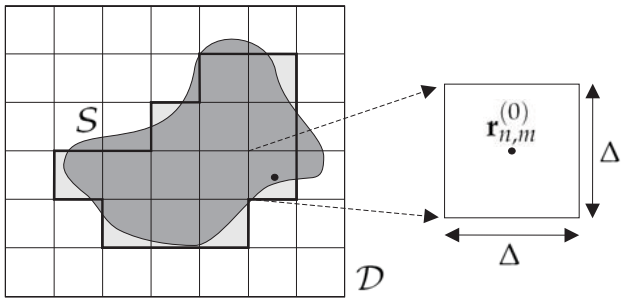

Figure 2.4: Discretization within the computational domain $\mathcal{D}$ of an object with cross-sectional shape $\mathcal{S}$ into square cells with center $\mathbf{r}_{n,m}^{(0)}$ and edge size Δ.

Furthermore, three staggered grids are introduced, see Fig. 2.5:

$$\begin{aligned} \mathbf{r}_{n,m}^{(1)} &= [(n-\frac{1}{2})\Delta,\ m\Delta], \\ \mathbf{r}_{n,m}^{(2)} &= [n\Delta,\ (m-\frac{1}{2})\Delta], \\ \mathbf{r}_{n,m}^{(3)} &= [n\Delta, m\Delta]. \end{aligned} \tag{2.28}$$

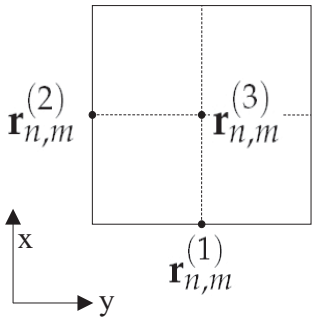

Figure 2.5: Center points of staggered grids, as defined in (2.28).

2.4.2 Discretization of the Contrast Source Integral Equation

The CSIE is tested by multiplying the equations for the x-, y- and z- component in (2.27) with scalar functions $\psi^{(p)}(\mathbf{r}^{(p)}_{n,m}-\mathbf{r})$ for $n=0\ldots N_s-1, m=0\ldots M_s-1$ and where $p=1,2,3$ denotes the x-, y- and z-component respectively. Afterwards, these products are integrated over the computational domain $\mathcal{D}$. For the x-component, for example, this testing procedure yields

$$\begin{aligned}\int_{\mathcal{D}} \widehat{E}^{\mathrm{i}}_1(\mathbf{r},k_z)\psi^{(1)}(\mathbf{r}^{(1)}_{n,m}-\mathbf{r})\mathrm{d}\mathbf{r} &= \int_{\mathcal{D}} \frac{\widehat{D}_1(\mathbf{r},k_z)}{\varepsilon(\mathbf{r})}\psi^{(1)}(\mathbf{r}^{(1)}_{n,m}-\mathbf{r})\mathrm{d}\mathbf{r}\\ &- k_0^2\int_{\mathcal{D}} \widehat{A}^{\mathrm{s}}_1(\mathbf{r},k_z)\psi^{(1)}(\mathbf{r}^{(1)}_{n,m}-\mathbf{r})\mathrm{d}\mathbf{r} - \int_{\mathcal{D}} \frac{\partial^2}{\partial x^2}\widehat{A}^{\mathrm{s}}_1(\mathbf{r},k_z)\psi^{(1)}(\mathbf{r}^{(1)}_{n,m}-\mathbf{r})\mathrm{d}\mathbf{r}\\ &- \int_{\mathcal{D}} \frac{\partial^2}{\partial x\partial y}\widehat{A}^{\mathrm{s}}_2(\mathbf{r},k_z)\psi^{(1)}(\mathbf{r}^{(1)}_{n,m}-\mathbf{r})\mathrm{d}\mathbf{r} - jk_z\int_{\mathcal{D}} \frac{\partial}{\partial x}\widehat{A}^{\mathrm{s}}_3(\mathbf{r},k_z)\psi^{(1)}(\mathbf{r}^{(1)}_{n,m}-\mathbf{r})\mathrm{d}\mathbf{r}.\end{aligned}$$

The next step is to expand every component p of all field quantities ($\widehat{E}^{\mathrm{i}}_p(\mathbf{r},k_z)$, $\widehat{D}_p(\mathbf{r},k_z)$ and $\widehat{A}^{\mathrm{s}}_p(\mathbf{r},k_z)$) in basis functions $\psi^{(p)}(\mathbf{r}-\mathbf{r}^{(p)}_{k,l})$:

$$\begin{aligned}\widehat{E}^{\mathrm{i}}_p(\mathbf{r},k_z) &= \sum_{k,l}\widehat{E}^{\mathrm{i}}_{p;k,l}\,\psi^{(p)}(\mathbf{r}-\mathbf{r}^{(p)}_{k,l}),\\ \widehat{D}_p(\mathbf{r},k_z) &= \varepsilon_0\sum_{k,l}\widehat{d}_{p;k,l}\,\psi^{(p)}(\mathbf{r}-\mathbf{r}^{(p)}_{k,l}),\\ \widehat{A}^{\mathrm{s}}_p(\mathbf{r},k_z) &= \sum_{k,l}\widehat{a}_{p;k,l}\,\psi^{(p)}(\mathbf{r}-\mathbf{r}^{(p)}_{k,l}).\end{aligned} \tag{2.29}$$

To simplify the notations, the k_z-dependence of the expansion coefficients $\widehat{E}^{\mathrm{i}}_{p;k,l}, \widehat{d}_{p;k,l}$ and $\widehat{a}_{p;k,l}$ is omitted. In principle, it is not necessary to expand also the vector potential since this introduces small inaccuracies, but it yields a considerable acceleration for each iteration [1, 2].
Now, the expanded fields are introduced in the tested CSIE. This leads to the set of equations, in which the coefficients $\widehat{d}_{p;k,l}$ are the unknowns:

$$
\begin{aligned}
\sum_{k,l}\widehat{E}^{\mathrm{i}}_{1;k,l}v^{(1)}(\mathbf{r}^{(1)}_{k,l},\mathbf{r}^{(1)}_{n,m}) &= \sum_{k,l}\widehat{d}_{1;k,l}u^{(1)}(\mathbf{r}^{(1)}_{k,l},\mathbf{r}^{(1)}_{n,m}) - k_0^2\sum_{k,l}\widehat{a}_{1;k,l}v^{(1)}(\mathbf{r}^{(1)}_{k,l},\mathbf{r}^{(1)}_{n,m}) \\
&\quad + \sum_{k,l}\widehat{a}_{1;k,l}w^{(1,1)}(\mathbf{r}^{(1)}_{k,l},\mathbf{r}^{(1)}_{n,m}) + \sum_{k,l}\widehat{a}_{2;k,l}w^{(1,2)}(\mathbf{r}^{(2)}_{k,l},\mathbf{r}^{(1)}_{n,m}) \\
&\quad + jk_z\sum_{k,l}\widehat{a}_{3;k,l}w^{(1,3)}(\mathbf{r}^{(3)}_{k,l},\mathbf{r}^{(1)}_{n,m}) \\
\sum_{k,l}\widehat{E}^{\mathrm{i}}_{2;k,l}v^{(2)}(\mathbf{r}^{(2)}_{k,l},\mathbf{r}^{(2)}_{n,m}) &= \sum_{k,l}\widehat{d}_{2;k,l}u^{(2)}(\mathbf{r}^{(2)}_{k,l},\mathbf{r}^{(2)}_{n,m}) - k_0^2\sum_{k,l}\widehat{a}_{2;k,l}v^{(2)}(\mathbf{r}^{(2)}_{k,l},\mathbf{r}^{(2)}_{n,m}) \\
&\quad + \sum_{k,l}\widehat{a}_{1;k,l}w^{(2,1)}(\mathbf{r}^{(1)}_{k,l},\mathbf{r}^{(2)}_{n,m}) + \sum_{k,l}\widehat{a}_{2;k,l}w^{(2,2)}(\mathbf{r}^{(2)}_{k,l},\mathbf{r}^{(2)}_{n,m}) \\
&\quad + jk_z\sum_{k,l}\widehat{a}_{3;k,l}w^{(2,3)}(\mathbf{r}^{(3)}_{k,l},\mathbf{r}^{(2)}_{n,m}) \\
\sum_{k,l}\widehat{E}^{\mathrm{i}}_{3;k,l}v^{(3)}(\mathbf{r}^{(3)}_{k,l},\mathbf{r}^{(3)}_{n,m}) &= \sum_{k,l}\widehat{d}_{3;k,l}u^{(3)}(\mathbf{r}^{(3)}_{k,l},\mathbf{r}^{(3)}_{n,m}) - (k_0^2-k_z^2)\sum_{k,l}\widehat{a}_{3;k,l}v^{(3)}(\mathbf{r}^{(3)}_{k,l},\mathbf{r}^{(3)}_{n,m}) \\
&\quad - jk_z\sum_{k,l}\widehat{a}_{1;k,l}w^{(3,1)}(\mathbf{r}^{(1)}_{k,l},\mathbf{r}^{(3)}_{n,m}) \\
&\quad - jk_z\sum_{k,l}\widehat{a}_{2;k,l}w^{(3,2)}(\mathbf{r}^{(2)}_{k,l},\mathbf{r}^{(3)}_{n,m}).
\end{aligned}
\tag{2.30}
$$

The functions $u^{(p)}(\mathbf{r}^{(p)}_{k,l},\mathbf{r}^{(p)}_{n,m})$, $v^{(p)}(\mathbf{r}^{(p)}_{k,l},\mathbf{r}^{(p)}_{n,m})$ and $w^{(p,q)}(\mathbf{r}^{(q)}_{k,l},\mathbf{r}^{(p)}_{n,m})$ contain the expansion and testing functions:

$$
\begin{aligned}
u^{(p)}(\mathbf{r}^{(p)}_{k,l},\mathbf{r}^{(p)}_{n,m}) &= \int_{\mathcal{D}}\frac{\varepsilon_0}{\varepsilon(\mathbf{r})}\psi^{(p)}(\mathbf{r}-\mathbf{r}^{(p)}_{k,l})\psi^{(p)}(\mathbf{r}^{(p)}_{n,m}-\mathbf{r})\mathrm{d}\mathbf{r} && p=1,2,3, \\
v^{(p)}(\mathbf{r}^{(p)}_{k,l},\mathbf{r}^{(p)}_{n,m}) &= \int_{\mathcal{D}}\psi^{(p)}(\mathbf{r}-\mathbf{r}^{(p)}_{k,l})\psi^{(p)}(\mathbf{r}^{(p)}_{n,m}-\mathbf{r})\mathrm{d}\mathbf{r} && p=1,2,3, \\
w^{(p,q)}(\mathbf{r}^{(q)}_{k,l},\mathbf{r}^{(p)}_{n,m}) &= \int_{\mathcal{D}}\left(\frac{\partial}{\partial q}\psi^{(q)}(\mathbf{r}-\mathbf{r}^{(q)}_{k,l})\right)\left(\frac{\partial}{\partial p}\psi^{(p)}(\mathbf{r}^{(p)}_{n,m}-\mathbf{r})\right)\mathrm{d}\mathbf{r} && p,q=1,2, \\
w^{(p,3)}(\mathbf{r}^{(3)}_{k,l},\mathbf{r}^{(p)}_{n,m}) &= \int_{\mathcal{D}}\psi^{(3)}(\mathbf{r}-\mathbf{r}^{(3)}_{k,l})\left(\frac{\partial}{\partial p}\psi^{(p)}(\mathbf{r}^{(p)}_{n,m}-\mathbf{r})\right)\mathrm{d}\mathbf{r} && p=1,2, \\
w^{(3,p)}(\mathbf{r}^{(p)}_{k,l},\mathbf{r}^{(3)}_{n,m}) &= \int_{\mathcal{D}}\left(\frac{\partial}{\partial p}\psi^{(p)}(\mathbf{r}-\mathbf{r}^{(p)}_{k,l})\right)\psi^{(3)}(\mathbf{r}^{(3)}_{n,m}-\mathbf{r})\mathrm{d}\mathbf{r} && p=1,2.
\end{aligned}
\tag{2.31}
$$

To maintain the coupling between the field components in (2.30), the derivatives $\frac{\partial}{\partial p}\psi^{(p)}$ in (2.31) for $p=1,2=x,y$ must be non-zero. Therefore, the expansion and testing functions are chosen as [5]

$$
\begin{aligned}
\psi^{(1)}(\mathbf{r}) &= \Lambda(x;2\Delta)\,\Pi(y;\Delta), \\
\psi^{(2)}(\mathbf{r}) &= \Pi(x;\Delta)\,\Lambda(y;2\Delta), \\
\psi^{(3)}(\mathbf{r}) &= \Pi(x;\Delta)\,\Pi(y;\Delta).
\end{aligned}
\tag{2.32}
$$

The basis function $\Lambda(u;2\Delta)$ is a one-dimensional triangle function with support 2Δ:

$$\Lambda(u;2\Delta) = \begin{cases} \frac{u+\Delta}{\Delta} & -\Delta \le u \le 0 \\ \frac{\Delta-u}{\Delta} & 0 \le u \le \Delta \end{cases} \tag{2.33}$$

and $\Pi(u;\Delta)$ is a one-dimensional pulse function with support Δ:

$$\Pi(u;\Delta) = \begin{cases} 0 & u \le -\frac{\Delta}{2} \\ 1 & -\frac{\Delta}{2} \le u \le \frac{\Delta}{2} \\ 0 & u \ge \frac{\Delta}{2} \end{cases}. \tag{2.34}$$

Note that, for this choice of expansion and testing functions, the expansion coefficients in (2.29) satisfy

$$\begin{aligned} \widehat{E}^{\mathrm{i}}_{p;k,l} &= \widehat{E}^{\mathrm{i}}_{p}(\mathbf{r}^{(p)}_{k,l}, k_z), \\ \varepsilon_0 \widehat{d}_{p;k,l} &= \widehat{D}_{p}(\mathbf{r}^{(p)}_{k,l}, k_z), \\ \widehat{a}_{p;k,l} &= \widehat{A}^{\mathrm{s}}_{p}(\mathbf{r}^{(p)}_{k,l}, k_z). \end{aligned} \tag{2.35}$$

Furthermore, the expressions for $u^{(p)}(\mathbf{r}^{(p)}_{k,l}, \mathbf{r}^{(p)}_{n,m})$, $v^{(p)}(\mathbf{r}^{(p)}_{k,l}, \mathbf{r}^{(p)}_{n,m})$ and $w^{(p,q)}(\mathbf{r}^{(q)}_{k,l}, \mathbf{r}^{(p)}_{n,m})$ in (2.31) can be evaluated analytically. This yields the final discretized form of the contrast source integral equation:

$$\begin{aligned} \sum_{k=1}^{3} \widehat{E}^{\mathrm{i}}_{1;n+k-2,m} v_k &= \sum_{k=1}^{3} \widehat{d}_{1;n+k-2,m} u^{(1)}_k + \sum_{k=1}^{3} \widehat{a}_{1;n+k-2,m} c_k \\ &\quad - \sum_{k=1}^{2}\sum_{l=1}^{2} \widehat{a}_{2;n+k-2,m+l-1} w^{(1,2)}_{k,l} - ik_z\Delta\left(\widehat{a}_{3;n,m} - \widehat{a}_{3;n-1,m}\right) \\ \sum_{l=1}^{3} \widehat{E}^{\mathrm{i}}_{2;n,m+l-2} v_l &= \sum_{l=1}^{3} \widehat{d}_{2;n,m+l-2} u^{(2)}_l + \sum_{l=1}^{3} \widehat{a}_{2;n,m+l-2} c_l \\ &\quad - \sum_{k=1}^{2}\sum_{l=1}^{2} \widehat{a}_{1;n+k-1,m+l-2} w^{(2,1)}_{k,l} - ik_z\Delta\left(\widehat{a}_{3;n,m} - \widehat{a}_{3;n,m-1}\right) \\ \Delta^2 \widehat{E}^{\mathrm{i}}_{3;n,m} &= \Delta^2 \frac{1}{\varepsilon_{r;n,m}} \widehat{d}_{3;n,m} - \Delta^2 (k_0^2 - k_z^2) \widehat{a}_{3;n,m} \\ &\quad - ik_z\Delta\left(\widehat{a}_{1;n+1,m} - \widehat{a}_{1;n,m}\right) - ik_z\Delta\left(\widehat{a}_{2;n,m+1} - \widehat{a}_{2;n,m}\right), \end{aligned} \tag{2.36}$$

where c_i, $u_i^{(p)}$, v_i and $w_{i,j}^{(p,q)}$, for $p,q=1,2$ are the i-th and (i,j)-th elements of

$$u^{(1)} = \frac{\Delta^2}{6}\begin{bmatrix} \frac{1}{\varepsilon_{r;n-1,m}} \\ \frac{2}{\varepsilon_{r;n-1,m}} + \frac{2}{\varepsilon_{r;n,m}} \\ \frac{1}{\varepsilon_{r;n,m}} \end{bmatrix}, \qquad u^{(2)} = \frac{\Delta^2}{6}\begin{bmatrix} \frac{1}{\varepsilon_{r;n,m-1}} \\ \frac{2}{\varepsilon_{r;n,m-1}} + \frac{2}{\varepsilon_{r;n,m}} \\ \frac{1}{\varepsilon_{r;n,m}} \end{bmatrix},$$

$$c = -k_0^2\frac{\Delta^2}{6}\begin{bmatrix}1\\4\\1\end{bmatrix} - \begin{bmatrix}1\\-2\\1\end{bmatrix}, \qquad v = \frac{\Delta^2}{6}\begin{bmatrix}1\\4\\1\end{bmatrix},$$

$$w^{(1,2)} = w^{(2,1)} = \begin{bmatrix}1 & -1\\ -1 & 1\end{bmatrix}. \tag{2.37}$$

2.4.3 Discretization of the vector potential expression

For given values of the expansion coefficients $\widehat{d}_{p;n,m}$ of the electric flux density, the expansion coefficients $\widehat{a}_{p;n,m}$ of the vector potential are computed with a discretized version of the vector potential expression (2.21). Therefore, all components $\widehat{D}_p(\mathbf{r},k_z)$ of the electric flux density are replaced by their expansion (2.29) in (2.21). This yields an integration of the contrast multiplied by the basis functions, which is accounted for by introducing three different contrast functions:

$$\begin{aligned} \chi_{n,m}^{(1)} &= \frac{\chi(\mathbf{r}_{n-1,m}^{(0)}) + \chi(\mathbf{r}_{n,m}^{(0)})}{2}, \\ \chi_{n,m}^{(2)} &= \frac{\chi(\mathbf{r}_{n,m-1}^{(0)}) + \chi(\mathbf{r}_{n,m}^{(0)})}{2}, \\ \chi_{n,m}^{(3)} &= \chi(\mathbf{r}_{n,m}^{(0)}). \end{aligned} \tag{2.38}$$

The Green's function $\widehat{G}(\mathbf{r},\mathbf{r}';k_z)$ (2.24) is discretized by integrating it over circular patches with center $\mathbf{r}_{n,m}^{(0)} = (n\Delta,\ m\Delta)$ and radius $\Delta/2$ [6] and then dividing the result by the patch surface [1]:

$$g_{n,m} = \begin{cases} \frac{i}{\Delta\sqrt{k_0^2-k_z^2}} J_1\left(\sqrt{k_0^2-k_z^2}\frac{\Delta}{2}\right) H_0^{(1)}\left(\sqrt{k_0^2-k_z^2}\sqrt{n^2+m^2}\Delta\right) \\ \frac{i}{\Delta\sqrt{k_0^2-k_z^2}}\left(H_1^{(1)}\left(\sqrt{k_0^2-k_z^2}\frac{\Delta}{2}\right) + \frac{4i}{\pi\Delta\sqrt{k_0^2-k_z^2}}\right) & \text{if } n=m=0. \end{cases} \tag{2.39}$$

This way of discretizing the expression for the vector potential (2.21) preserves its convolution symmetry. Therefore, a discrete version of the convolution theorem [7] can be applied to express the vector potential coefficients $\widehat{a}_{p;n,m}$ by means of the two-dimensional Discrete Fourier Transform (DFT)

$$\widehat{a}_{p;n,m} = \Delta^2 DFT^{-1}\left[DFT[g_{n,m}]\ DFT[\chi_{n,m}^{(p)}\widehat{d}_{p;n,m}]\right]. \tag{2.40}$$

Using DFT's to evaluate the vector potential coefficients substantially accelerates the computation of the forward problem.

2.5. Iterative solution of the discretized set of equations

The linear set of equations (2.36) is solved for the unknown electric flux density coefficients $\widehat{d}_{p;n,m}$ with an iterative stabilized biconjugate gradient method (BICGS) [4, 8]. Starting from an initial estimate for $\widehat{d}_{p;n,m}$, e.g. $\widehat{d}_{p;n,m} = 0$, the corresponding values of the vector potential coefficients $\widehat{a}_{p;n,m}$ are computed from (2.40). The RHS of the discretized system (2.36) is evaluated and compared to the known LHS. From this comparison, a better estimate for $\widehat{d}_{p;n,m}$ is derived. This iterative procedure is stopped when the error between RHS and LHS is smaller than a predefined threshold. Since the discretized system (2.36) is solved successively for increasing values of k_z, the total number of iterations can be significantly reduced by choosing the initial estimate for $\widehat{d}_{p;n,m}$ not equal to zero but with a marching-on-in-k_z technique [9]. Once the coefficients $\widehat{d}_{p;n,m}$ are known, all field related quantities (electric flux density, vector potential, total and scattered field) can be characterized in every grid point of the computational domain $\mathcal{D}$.

2.6. From grid to detector

In many applications, and for sure in quantitative imaging, one is only interested in scattered field values in some predefined *detector points* $\mathbf{r}_R$, where $_R$ stands for receiver, lying outside the computational domain $\mathcal{D}$. The scattered field in the detector points $\mathbf{r}_R$ can be computed from the electric flux density coefficients $\widehat{d}_{p;n,m}$ by discretizing the expression

$$\widehat{\mathbf{E}}^{\mathrm{s}}(\mathbf{r}_R, k_z) = \left(k_0^2 \mathbf{I} + \widehat{\nabla}\widehat{\nabla}\right) \cdot \widehat{\mathbf{A}}^{\mathrm{s}}(\mathbf{r}_R, k_z), \tag{2.41}$$

where the vector potential in $\mathbf{r}_R$ is given by

$$\widehat{\mathbf{A}}^{\mathrm{s}}(\mathbf{r}_R, k_z) = \frac{1}{\varepsilon_0} \int_{\mathbf{r}' \in \mathcal{D}} \widehat{G}(\mathbf{r}_R, \mathbf{r}'; k_z) \chi(\mathbf{r}') \widehat{\mathbf{D}}(\mathbf{r}', k_z) \mathrm{d}\mathbf{r}'. \tag{2.42}$$

However, from (2.35), the electric flux density $\widehat{\mathbf{D}}(\mathbf{r}', k_z)$ is known on the staggered grid points (2.28), whereas the contrast is characterized in the center points $\mathbf{r}_{k,l}^{(0)}$ of the cell. To obtain the electric flux density coefficients in the center of the cells, denoted as $\widehat{\mathbf{d}}_{k,l}^{(0)}$, from the values on the staggered grids (2.28), the following approximations

are made:

$$\begin{aligned}\widehat{d}^{(0)}_{1;k,l} &= \frac{\widehat{d}_{1;k,l}+\widehat{d}_{1;k+1,l}}{2},\\ \widehat{d}^{(0)}_{2;k,l} &= \frac{\widehat{d}_{2;k,l}+\widehat{d}_{2;k,l+1}}{2},\\ \widehat{d}^{(0)}_{3;k,l} &= \widehat{d}_{3;k,l}.\end{aligned} \tag{2.43}$$

When the expression for the vector potential (2.42) is inserted in (2.41) and the integral is discretized, the scattered field $\widehat{\mathbf{E}}^{\mathrm{s}}(\mathbf{r}_R,k_z)$ is obtained from the electric flux densities $\widehat{\mathbf{d}}^{(0)}_{k,l}$ through

$$\widehat{\mathbf{E}}^{\mathrm{s}}(\mathbf{r}_R,k_z)=\Delta^2\sum_{k=0}^{N_s}\sum_{l=0}^{M_s}\left((k_0^2\mathbf{I}+\widehat{\nabla}\widehat{\nabla})\,\widehat{G}(\mathbf{r}_R,\mathbf{r}^{(0)}_{k,l};k_z)\right)\cdot\left(\chi_{k,l}\,\widehat{\mathbf{d}}^{(0)}_{k,l}\right). \tag{2.44}$$

Here, the grad-div operation is with respect to the receiver coordinate $\mathbf{r}_R$ in the Green's function

$$\widehat{G}(\mathbf{r}_R,\mathbf{r}^{(0)}_{k,l};k_z)=\frac{j}{4}H_0^{(1)}\left(\sqrt{k_0^2-k_z^2}\,|\mathbf{r}_R-\mathbf{r}^{(0)}_{k,l}|\right) \tag{2.45}$$

and can be evaluated analytically.

When the scattered field $\widehat{\mathbf{E}}^{\mathrm{s}}(\mathbf{r}_R,k_z)$ is computed in the detector points for each spectral component k_z, the final three-dimensional scattered field $\mathbf{E}^{\mathrm{s}}(\mathbf{r}_R,z)$ is obtained by performing the inverse spatial Fourier transformation with respect to k_z

$$\mathbf{E}^{\mathrm{s}}(\mathbf{r}_R,z)=\frac{1}{2\pi}\int_{-\infty}^{+\infty}\widehat{\mathbf{E}}^{\mathrm{s}}(\mathbf{r}_R,k_z)e^{ik_zz}\mathrm{d}k_z. \tag{2.46}$$

Equation (2.46) suggest that the CSIE should be solved for an infinite number of spectral components of the incident field, ranging from $-\infty$ to $+\infty$. In practice, we use a discretized version of (2.46) where a finite number of appropriately chosen k_z values are retained. This will be discussed in Chapter 3.

2.7. Acceleration techniques

In the forward problem, the discretized CSIE (2.36) is solved iteratively. The best way to reduce the computation time of the iterative routine, is reducing the number of iterations itself by making a good initial guess for the electric flux density. In this PhD work, this is done by using two different marching-on techniques.

Furthermore, the computation time for a single iteration is reduced by paying extra attention to a fast and efficient implementation of the computations that are involved. This is even more useful when the forward solver is to be included in an inverse scheme, since in that case the number of CSIE's to be solved increases significantly: there are different CSIE's for every spectral component of every incident field and this

for every update of the permittivity profile. The first step in an iteration is the calculation of the vector potential expansion coefficients (2.40), which is already speeded-up substantially by using DFT's. In this step, the most time consuming computations are the three forward DFT's of the contrast sources, one forward DFT of the Green's matrix and three inverse DFT's to obtain the vector potential coefficients. The second step in an iteration is the right hand side evaluation of the CSIE (2.36), which needs a large amount of multiplications and summations. The third step is the computation of the scattered field in the detector points ((2.44) - (2.46)), involving many Hankel function evaluations and a large amount of multiplications and summations.

Different acceleration techniques are proposed:

- Using multithreaded commands: this speeds up the forward and inverse DFT's, together with the RHS evaluation of the CSIE.
- Accelerating the forward and inverse DFT's when applied to zero padded matrices.
- Performing computations that are common for many RHS evaluations of the CSIE and storing their results in memory in the set-up phase of the algorithm.

"There is no such thing as free lunch", stated Milton Friedman and this principle applies also here. In most cases, no acceleration can be achieved without extra memory consumption. Therefore, once the geometry and incident fields are initialized, an estimation for the memory consumption is made. Based on this memory estimation, we manually tune the different acceleration techniques so that the achieved acceleration is maximal without overriding the memory limit.

2.7.1 Multithreaded commands

A common way to speed up computations is performing them in a parallel way: the computations are spread out over multiple processors on multiple machines, each having their own memory to store results. In such an approach, special attention has to be paid to the communication between all machines [10]. An intermediate solution, which avoids the communication problems between separate machines, is the use of so-called *multithreaded commands* [11]: computations run on multiple processors of one machine, all accessing the same memory.

When the forward solver is used as a scattering simulator, but not as a part of an inverse solver, we use multithreaded versions of standard forward and inverse DFT routines [12]. Since there is a slight overhead, the acceleration factor for the Fourier transforms is somewhat smaller than the number of processors that is used to perform the Fourier transforms. The evaluation of the right hand side of the CSIE in every grid point is also done in a multithreaded manner: all evaluation points are distributed over the available processors and each processor computes the RHS only for the points assigned to it. Since these RHS evaluations are independent of each other, no problems arise with processors that are waiting for results of other processors as input or processors simultaneously trying to write in the same memory location. The principle of

distributing a single forward problem over all cores of a machine is shown in Fig. 2.6 (a).

When the forward solver is included in an inversion algorithm, a parallelization is achieved on a coarser level (see Fig. 2.6 (b)): the forward problems are distributed over all available processors and each forward problem is computed single-threaded by a particular processor. Due to the smaller overhead, this yields the largest acceleration, but it also requires much more memory, since all forward problem related matrices, which differ for each forward problem, are now stored simultaneously (instead of sequentially in one matrix). Therefore, a trade off is made between accelerating the forward problems itself by distributing them over multiple processors and distributing complete forward problems, as in Fig. 2.6(c).

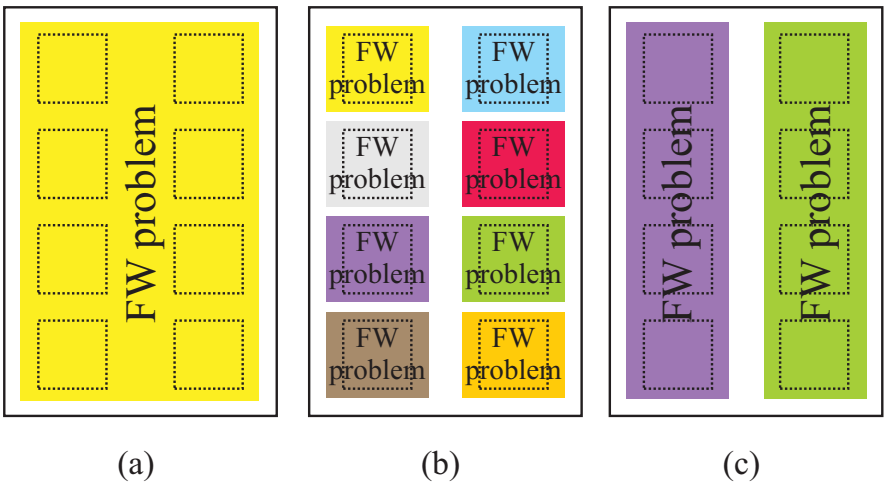

Figure 2.6: Computations are spread out over multiple processors (dotted lines) of a machine to reduce computation time: (a) A single forward problem is multithreaded using all available processors, (b) forward problems of an inverse problem are distributed over different processors and (c) a single forward problem is distributed over half of the available processors, allowing two forward problems to be computed simultaneously.

2.7.2 Accelerated computation of Discrete Fourier Transforms

In Section 2.4.3, it is stated that the vector potential expansion coefficients $\widehat{a}_{p;n,m}$ are computed in a fast way by using two-dimensional forward and inverse discrete Fourier transforms:

$$\widehat{a}_{p;n,m} = \Delta^2 DFT^{-1}\left[DFT[g_{n,m}]\; DFT[\chi^{(p)}_{n,m}\widehat{d}_{p;n,m}]\right].$$

Due to the cyclic nature of the DFT, the $N_s \times M_s$ matrices $g_{n,m}$ and $\chi^{(p)}_{n,m}\widehat{d}_{p;n,m}$ are in fact periodically extended. In order to preserve a correct evaluation of the convolu-

tion product, the contrast source matrix $\chi^{(p)}_{n,m}\widehat{d}_{p;n,m}$ needs to be zero padded prior to applying the DFT. This means that an equal amount of zeros is added in both x- and y- directions, enlarging this matrix to a $2N_s \times 2M_s$ matrix. Furthermore, the matrix containing the Green's function elements $g_{n,m}$ must be constructed in the so called *wrapped around order*, also yielding a $2N_s \times 2M_s$ matrix (without zeros).

For the two-dimensional forward and inverse DFT's of the involved complex matrices, a fast standard two-dimensional routine from the FFTW library [12] can be used. This routine contains two steps: first, $2M_s$ times a one-dimensional Fourier transform of an array of size $2N_s$ in the x-direction, second $2N_s$ times a one-dimensional Fourier transform of an array of size $2M_s$ in the y-direction. As such, it does not exploit the structure of the zero padded contrast source matrix. This is illustrated in Fig. 2.7, where in Fig. 2.7(a) the contrast source matrix is represented as the grey part and the zeros, added after zero padding, as the white part .

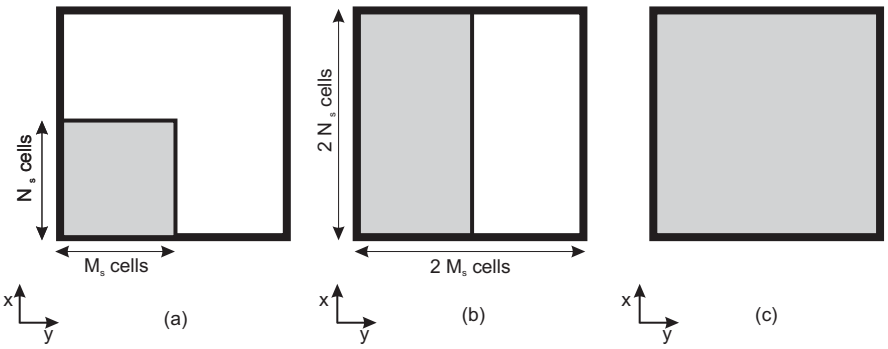

Figure 2.7: Performing a two-dimensional DFT on a $2N_s \times 2M_s$ matrix is a two-step procedure: first, $2M_s$ times a one-dimensional Fourier transform of an array of size $2N_s$ in the x-direction ((a) to (b)) and afterwards $2N_s$ times a one-dimensional Fourier transform of an array of size $2M_s$ in the y-direction ((b) to (c)).

In the first step of the standard 2D DFT routine, M_s one-dimensional DFT's are thus performed on arrays containing only zero elements (the right part of the matrix in Fig. 2.7 (a)). To avoid this, we do not use the standard 2D DFT routine but the fast standard one-dimensional DFT routine from the FFTW library [12] and omit the 1D DFT's on zero arrays. For example, in case of square matrices ($N_s = M_s$), the reduction from $2M_s + 2N_s$ to only $M_s + 2N_s$ one-dimensional DFT's decreases the computational effort by 25%. For the 2D inverse Fourier transform, this two-step scheme is performed in the opposite direction, starting with Fig. 2.7 (c) and ending with Fig. 2.7 (a). Note furthermore that the number of elements in x- and y-direction (N_s and M_s respectively) are rounded up to the nearest appropriate FFT size [12] these standard DFT's routines are optimized for.

2.7.3 Green's function computations in set-up

The vector potential coefficients $\widehat{a}_{p;n,m}$ given by (2.40) have to be updated in each iteration of the forward solver. Since the Green's function matrix $g_{n,m}$ does not depend on the field coefficients $\widehat{d}_{p;n,m}$, it can be evaluated during the initial set-up phase. For a given set of spectral components k_z, the forward DFT's of the matrices $g_{n,m}$ for each k_z thus are stored in memory.

A similar approach is used to accelerate the computation of the scattered field in the detector points (2.44) where the term $(k_0^2\mathbf{I}+\widehat{\nabla}\widehat{\nabla})\ \widehat{G}(\mathbf{r}_R,\mathbf{r}_{k,l}^{(0)};k_z)$ is computed in advance for every spectral component k_z. When the number of unknowns is too large such that the grid-grid and grid-detector Green's function matrices cannot be stored in the available memory, then their elements need to be continuously recalculated.

2.7.4 Marching-on techniques

A common initial guess for the unknowns in the iterative solution of the CSIE (2.36) is the total field equal to zero: all $\widehat{d}_{p;n,m}=0\ (p=1,2,3)$. However, if multiple forward problems are solved for slightly different incident fields (e.g. plane waves with slightly different incident angles), it can be expected that the corresponding field solutions do not differ considerably. Therefore, field solutions from previously solved similar forward problems can be extrapolated to yield a suitable initial guess for the current forward problem. This guess is already close to the final solution and hence reduces the number of iterations considerably without influencing the final result.

Extrapolating previous solutions to determine an initial guess for a similar problem is performed by applying a *marching-on* technique. The only requirement for the method to be efficient is that the total field error which is chosen as the stopping criterion (related to the desired accuracy of the solution) is not much lower than the total field error, that is introduced by the discretization and noise [13]. The most common applications are marching-on-in-frequency, marching-on-in-angle and marching-on-in-shape, where forward problems must be solved at different frequencies, for different angles of incidence or for different scatterer shapes respectively [9, 14].

Marching-on techniques are implemented as follows [9]. First, a linear operator $\mathcal{L}$ is introduced which represents the evaluation of the RHS of the CSIE for the current value of $\widehat{\mathbf{d}}$, where the vector $\widehat{\mathbf{d}}$ contains all components $(p=1,2,3)$ of the electric flux density expansion coefficients $\widehat{d}_{p;n,m}$ in all cells. Similarly, all components of the discretized incident field are collected in the vector $\widehat{\mathbf{e}}^{\mathrm{i}}$. Hence, the CSIE (2.26) can be represented as

$$\widehat{\mathbf{e}}^{\mathrm{i}}=\mathcal{L}\widehat{\mathbf{d}} \tag{2.47}$$

If K previous solutions are taken into account, the initial guess for solving the l-th forward problem is determined as:

$$\widehat{\mathbf{d}}_l^{\text{init}} = \sum_{k=1}^{K} \beta_k \, \widehat{\mathbf{d}}_k \tag{2.48}$$

The extrapolation coefficients β_k are found by minimizing the squared error between LHS and RHS of the CSIE, corresponding to the current (l-th) forward problem:

$$||\mathcal{L}\widehat{\mathbf{d}}_l^{\text{init}} - \widehat{\mathbf{e}}^{\text{i}}{}_l||^2. \tag{2.49}$$

Hence, the linear system of K equations

$$\sum_{k=1}^{K} [\mathcal{L}\,\widehat{\mathbf{d}}_{k'}]^H \mathcal{L}\,\widehat{\mathbf{d}}_k \beta_k = [\mathcal{L}\,\widehat{\mathbf{d}}_{k'}]^H \widehat{\mathbf{e}}^{\text{i}}{}_l \qquad k' = 1 \ldots K \tag{2.50}$$

yields the expansion coefficients β_k. Usually, K is chosen to be 2 or 3 [9].
In this PhD work, forward problems must be solved for a set of spectral components for the case of a Gaussian beam illumination. Furthermore, when the forward solver is embedded in an inversion algorithm, there are multiple incident fields that sequentially illuminate the target. Two different marching-on techniques can therefore be used: marching-on-in-spectral-component and marching-on-in-incident-field, depending on the configuration. For an inverse problem with Gaussian beams as incident fields, the marching-on-in-spectral-component is combined with the marching-on-in-incident field, as shown in Fig. 2.8 with the marching-on-in-spectral-component technique represented as red arrows and the marching-on-in-incident field represented as green arrows. Suppose the Gaussian beams are simulated with n spectral components. For the first spectral component k_z^1 of the first incident field, no previous solutions are available. Therefore, the initial guess for the electric flux density $\widehat{\mathbf{d}}_l^{\text{init}}$ is set to zero. For the second spectral component, one previous solution is taken into account, while for the third spectral components, two solutions can be used in the extrapolation. Further on (for the next $n-3$ spectral components), the three latest solutions are combined. In that way, all CSIE's that correspond to the n spectral components of the first incident field are efficiently solved. Now, the first spectral component of the second incident field is simulated with as initial guess the field solution of the first illumination, at the same spectral component k_z^1. For the following spectral components, the same procedure is adopted as for the marching-on-in-spectral-component of the first incident field. To summarize, marching-on-in-spectral-component is used for simulations corresponding to the same 3D incident field, while the marching-on-in-incident-field is used to generate initial guesses for the first spectral component of 3D incident fields. These marching-on techniques require the storage of previous solutions, this is why for very large problems, the number of previous solutions that are taken into account is reduced, or only one or none of the marching-on techniques is used.

2.8. Conclusion

In this chapter, we have detailed the implementation of the 2.5D forward solver. Since it is developed to be part of a quantitative imaging scheme, it should be able to simulate completely inhomogeneous objects. Hence, a volume integral equation scheme was selected. The well known contrast source integral approach for two- and three-dimensional configurations is in this PhD work reformulated for the 2.5-dimensional case. This 2.5D formulation for the contrast source integral equation is derived from the Maxwell equations by performing a spatial Fourier transform of the electromagnetic fields along the invariant direction of the scatterer. As such, instead of one three-dimensional contrast source integral equation, a set of two-dimensional contrast source integral equations is obtained, one for every spectral component. The discretized version of the integral equation is iteratively solved by applying a Biconjugate gradient method. Since the forward solver is to be included in an inverse one, special attention has been paid to a fast and efficient implementation. We have used multi-threaded commands to speed up computations, accelerated two-dimensional DFT's of zero-padded matrices by omitting one-dimensional DFT's on zero arrays and moved Green's function computations to the set-up phase. Furthermore, a marching-on-in-incident-field and a marching-on-in-spectral-component technique is applied to provide suitable initial guesses for the iterative solution of the CSIE's.

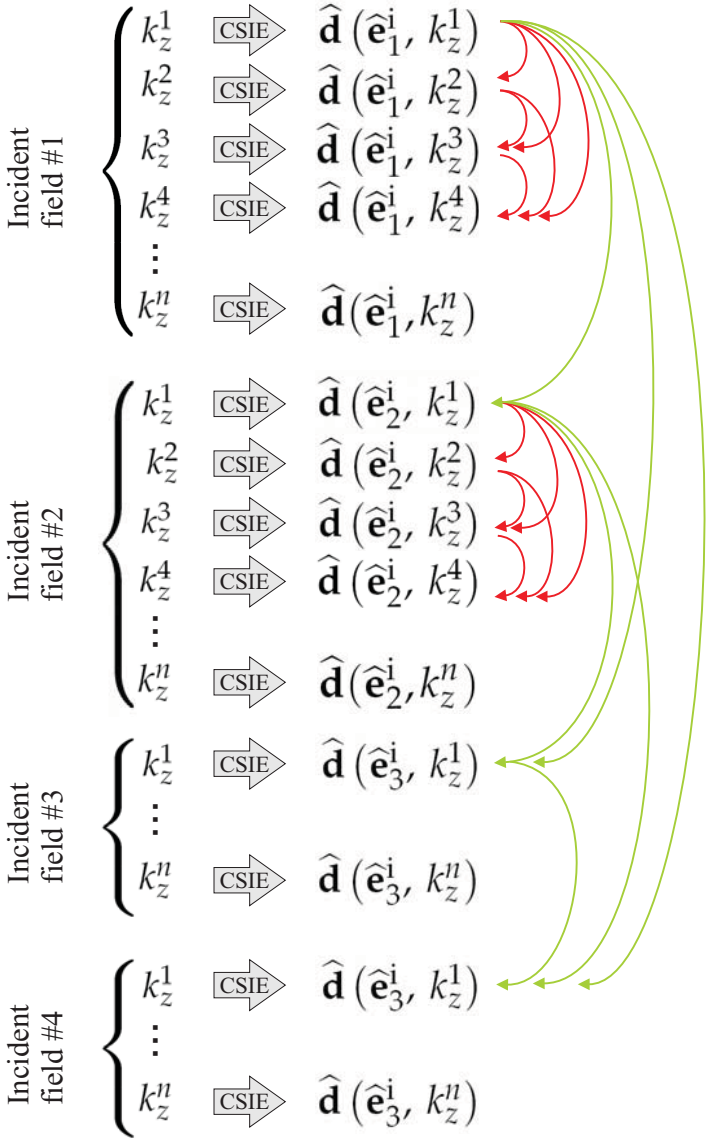

Figure 2.8: Marching-on-in-spectral-component (indicated by red arrows) combined with marching-on-in-incident-field (indicated by green arrows) to derive a suitable initial guess for a next forward problem.

Bibliography

[1] P. Zwamborn and P. van den Berg, "A weak form of the conjugate gradient FFT method for two-dimensional TE scattering problems," *IEEE Transactions on Microwave Theory and Techniques*, vol. 39, no. 6, pp. 953–960, June 1991.

[2] ——, "The three-dimensional weak form of the conjugate gradient FFT method for solving scattering problems," *IEEE Transactions on Microwave Theory and Techniques*, vol. 40, no. 9, pp. 1757–1766, Sept. 1992.

[3] J. Van Bladel, *Electromagnetic Fields, second edition*. New Jersey: Wiley-Interscience: The IEEE press series on electromagnetic wave theory, 2007.

[4] R. da Cunha and T. Hopkins, "PIM 2.0 the parallel iterative methods package for systems of linear equations user's guide (fortran 77 version)," University of Kent Computing Laboratory, Canterbury, UK, Tech. Rep. 1-96*, Jan. 1996.

[5] A. Abubakar, P. van den Berg, and T. Habashy, "An integral equation approach for 2.5-dimensional forward and inverse electromagnetic scattering," *Geophysical Journal International*, vol. 165, no. 3, pp. 744–762, June 2006.

[6] J. Richmond, "Scattering by a dielectric cylinder of arbitrary cross section shape," *IEEE Transactions on Antennas and Propagation*, vol. 13, no. 3, pp. 334–341, May 1965.

[7] W. Press, S. Teukolsky, W. Vetterling, and B. Flannerly, *Numerical recipes in C: the art of scientific computing*. Cambridge University Press, 1995.

[8] H. van der Vorst, "BI-CGSTAB: A fast and smoothly converging variant of BI-CG for the solution of non symmetric linear systems," *SIAM Journal on Scientific and Statistical Computing*, vol. 13, no. 2, pp. 631–644, 1992.

[9] A. Tijhuis, M. van Beurden, and P. Zwamborn, "Iterative solution of field problems with a varying physical parameter," *Elektrik, Turkish Journal of Electrical Engineering & Computer Sciences*, vol. 10, no. 2, pp. 163–183, 2002.

[10] J. Fostier, "Parallel techniques for fast multipole algorithms," Ph.D. dissertation, Ghent University, 2009.

[11] D. Butenhof, *Programming with POSIX(R) Threads*. Addison-Wesley Professional Computing Series, 1997.

[12] M. Frigo and S. Johnson, "FFTW: An adaptive software architecture for the FFT," in *Proceedings of the 1998 IEEE International Conference on Acoustics, Speech and Signal Processing*, Seattle, USA, 1998, pp. 1381–1384.

[13] A. Franchois and A. Tijhuis, "A quasi-newton reconstruction algorithm for a complex microwave imaging scanner environment," *Radio Science*, vol. 38, no. 2, January 2003.

[14] A. Tijhuis, K. Belkebir, and A. Litman, "Theoretical and computational aspects of 2-D inverse profiling," *IEEE Transactions on Geoscience and Remote Sensing*, vol. 39, no. 6, pp. 1316–1330, June 2001.

CHAPTER 3

Incident fields

3.1. Introduction

The main concept of the 2.5-dimensional forward solver introduced in the previous chapter, is the Fourier transformation of the three-dimensional fields in the invariant direction of the simulated cylinders, in the presented PhD work chosen to be the z-direction. When this Fourier transformation is applied to the three-dimensional incident field, a set of two-dimensional incident fields is obtained. Any three-dimensional incident field can be described in this 2.5-dimensional procedure. However, since for every spectral component a particular contrast source integral equation has to be solved, a limited range of spectral components is beneficial. This is not the case for every type of incident field. Therefore, in this PhD work, the incident fields are restricted to be plane waves, which have only one spectral component, or Gaussian beams, which can be described using a limited number of spectral components. Furthermore, in applications for millimeter waves, the incident field typically has a Gaussian beam character. The 2.5-dimensional implementation of a three-dimensional plane wave is straightforward and is discussed in Section 3.2. In Section 3.3, three different models of Gaussian beams are investigated. Besides a model based on a classical scalar formulation, we have adapted the scalar [1, 2] and vectorial [2] three-dimensional complex source beam formulations to the 2.5D case. Furthermore, it is detailed how spectral components are selected.

As a validation, the model for the 2.5D scalar complex source beam formulation is compared to the model based on the classical scalar formulation and the model for the 2.5D vectorial complex source beam formulation is compared to the three-dimensional complex source beam description on which its derivation is based.

3.2. Plane wave illumination

The incident field of a three-dimensional incident plane wave is given by

$$\mathbf{E}^{\mathrm{i}}(\mathbf{r},z) = Ae^{j\mathbf{k}^{\mathrm{i}}\cdot\boldsymbol{\rho}}\mathbf{u}_{pol}, \tag{3.1}$$

where A represents the complex amplitude and $\mathbf{u}_{pol}$ is the three-dimensional polarization vector. The propagation vector $\mathbf{k}^{\mathrm{i}}$ is given by

$$\mathbf{k}^{\mathrm{i}} = k_0\mathbf{u}^{\mathrm{i}}, \tag{3.2}$$

and represents free-space propagation along the $\mathbf{u}^{\mathrm{i}}$-direction. The polarization vector $\mathbf{u}_{pol}$ is orthogonal to the propagation direction, hence $\mathbf{u}^{\mathrm{i}}\cdot\mathbf{u}_{pol} = 0$.
The Fourier transformed incident field (with respect to the z-coordinate) is readily given by

$$\widehat{\mathbf{E}}^{\mathrm{i}}(\mathbf{r},k_z) = Ae^{j\mathbf{k}^{\mathrm{i}}_{\perp}\cdot\mathbf{r}}\mathbf{u}_{pol}, \tag{3.3}$$

where $\mathbf{k}^{\mathrm{i}}_{\perp}$ is the projection of the three-dimensional propagation vector $\mathbf{k}^{\mathrm{i}}$ on the horizontal xy-plane and the spectral component k_z is the projection of $\mathbf{k}^{\mathrm{i}}$ on the z-axis.

3.3. Gaussian beam illumination

In what follows, the 2.5-dimensional implementation of a three-dimensional Gaussian beam illumination is detailed. Such an incident field yields a limited range of spectral components and results in a limited number of contrast source integral equations to be solved.
The general configuration of a Gaussian beam is presented in Fig. 3.1, which defines some of the beam parameters. The beam waist plane is the plane, orthogonal to the propagation direction, where the beam is the most confined. The corresponding smallest radius of the beam is called the beam waist radius. The beam waist plane is a planar equiphase surface. For increasing distances along the propagation direction, the equiphase surfaces become more and more spherical while the beam radius increases. This type of beam is called *Gaussian* because it has a Gaussian profile in the cross-sectional planes, which are orthogonal to the propagation direction.

Two types of describing three-dimensional Gaussian beams can be distinguished: *scalar* beams and *vectorial* beams, shortly denoted as *GBscal* and *GBvect*. Scalar beam models are commonly used, e.g. in optics. In a vectorial wave problem (as in this PhD work), it is common to simply add a polarization vector $\mathbf{u}_{pol}$ to the scalar beam model, here denoted as $E^{\mathrm{i}}_{GBscal}(\mathbf{r},z)$, to construct a three-dimensional vectorial beam. This polarization vector is tangent to the equiphase surface of the beam. Hence, the three-dimensional electric field is given by

$$\mathbf{E}^{\mathrm{i}}_{GBscal}(\mathbf{r},z) = E^{\mathrm{i}}_{GBscal}(\mathbf{r},z)\mathbf{u}_{pol}. \tag{3.4}$$

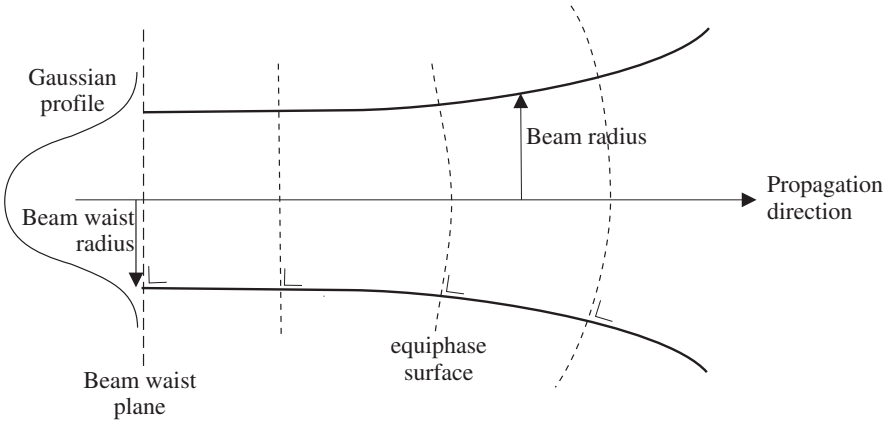

Figure 3.1: Definition of some parameters of a three-dimensional Gaussian beam.

However, this approach (3.4) is only valid in the well collimated region of the beam, where the phase front is planar and orthogonal to the beam propagation direction, see Fig. 3.1. Outside the well collimated region, the equiphase surface becomes spherical and a unique polarization direction can no longer be determined. Hence, a beam as (3.4) is no exact solution to Maxwell's equations. The restriction to well collimated beams is called the *paraxial approximation*. The expressions based on the scalar three-dimensional beam in the paraxial approximation and the reformulation to the 2.5D case are discussed in Section 3.3.1.
A more complex, but fully vectorial Gaussian beam formulation, denoted as $\mathbf{E}^{\mathrm{i}}_{GBvect}(\mathbf{r},z)$, is valid in total space, thus also in the non-collimated region of the Gaussian beam. The analytical expression, together with its reformulation to the 2.5D case, is discussed in Section 3.3.2.

3.3.1 2.5D descriptions based on a 3D scalar Gaussian beam

Two methods to construct a three-dimensional scalar Gaussian beam are considered: a classical formulation [3] and a complex-source beam formulation, as proposed in [1, 2].

Classical formulation for a scalar Gaussian beam

Let us first consider a beam that is propagating along the y-direction, with the beam waist plane located at $y = y_0$. The beam waist radius is w_0 in both x- and z- directions

and the beam center $\boldsymbol{\rho}_0 = \mathbf{r}_0 + z_0\mathbf{u}_z$ is located in the point $x = 0, y = y_0$ and $z = 0$ (hence $\boldsymbol{\rho}_0 = \mathbf{r}_0$).
According to the paraxial approximation formulation [3] the scalar Gaussian beam is then given by

$$E^{\mathrm{i}}_{GBscal}(\mathbf{r},z) = \frac{w_0}{w}\exp\left(-\frac{\xi^2}{w^2} - \frac{jk_0\xi^2}{2R} + j\phi_0\right)\exp\left(jk_0(y-y_0)\right) \tag{3.5}$$

with

$$\begin{aligned}
\xi &= \sqrt{x^2+z^2},\\
b_0 &= \frac{w_0^2 k_0}{2},\\
w &= w_0\sqrt{1+\left(\frac{y-y_0}{b_0}\right)^2},\\
R &= (y-y_0) + \frac{1}{(y-y_0)}\,b_0^2,\\
\phi_0 &= \arctan\left(\frac{y-y_0}{b_0}\right).
\end{aligned}$$

It is common to simply add a polarization vector $\mathbf{u}_{pol}$ (orthogonal to $\mathbf{u}_y$) to the expression for a scalar beam to obtain a three-dimensional incident field

$$\mathbf{E}^{\mathrm{i}}_{GBscal}(\mathbf{r},z) = E^{\mathrm{i}}_{GBscal}(\mathbf{r},z)\mathbf{u}_{pol}. \tag{3.6}$$

In this PhD work, formulation (3.5)-(3.6) is used as a reference to validate the complex-source beam formulation, discussed further, in the collimated region. Since the implementation of a plane wave as incident field is straightforward in the 2.5D solver and easily verified (see Section 4.2), the three-dimensional scalar beam (3.5) is decomposed into plane waves. Such decomposition is beneficial since the Fourier transformation in the z-direction of (3.5) is complicated. Each scalar plane wave of the decomposition is augmented by the vector $\mathbf{u}_{pol}$ and serves as an excitation function in the 2.5D forward problem. Their solutions are combined to the final scattered field, corresponding with the Gaussian beam illumination.

The decomposition of the incident scalar Gaussian beam is shown in Fig. 3.2. Figure 3.2 (a) shows the amplitude of the Gaussian beam (3.5) in the beam waist plane $y = y_0$. To determine the plane wave spectrum, a two-dimensional discrete Fourier transform in the beam waist plane is performed. The result of this operation is a set of N propagation vectors $\mathbf{k}^{\mathrm{i}}_n$ with corresponding complex amplitudes A_n, $n = 1\ldots N$, shown in Fig. 3.2 (b). The propagation vector $\mathbf{k}^{\mathrm{i}}_n$ is defined by

$$\mathbf{k}^{\mathrm{i}}_n = (k^{\mathrm{i}}_{x,n}, \sqrt{k_0^2 - k^{\mathrm{i}2}_{x,n} - k^{\mathrm{i}2}_{z,n}}, k^{\mathrm{i}}_{z,n}), \tag{3.7}$$

see Fig. 3.2 (b). Each plane wave is assigned the polarization vector of the original Gaussian beam. Hence, the three-dimensional Gaussian beam is decomposed into N plane wave functions (3.1)

$$\mathbf{E}^{\mathrm{i}}_{GBscal}(\mathbf{r},z) = \sum_{n=1}^{N} A_n e^{j\mathbf{k}^{\mathrm{i}}_n \cdot \boldsymbol{\rho}} \mathbf{u}_{pol}. \tag{3.8}$$

Note that each scalar plane wave, augmented with $\mathbf{u}_{pol}$, is a mathematical function rather than a vectorial plane wave solution since $\mathbf{u}_{pol}$ is generally not perpendicular to $\mathbf{k}^{\mathrm{i}}_n$. Furthermore, the numerical implementation of the two-dimensional discrete Fourier transform in the beam waist plane has to be performed with care to reduce errors such as aliasing.

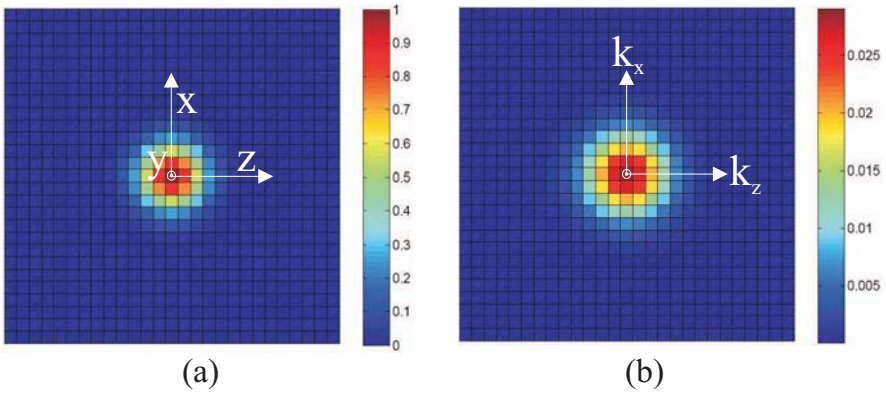

Figure 3.2: (a): Gaussian beam profile in the beam waist plane $y = y_0$. (b): plane wave decomposition of the Gaussian beam. Each cell represents a plane wave, with amplitude $|A|$ represented by the cell's color and propagation vector $\mathbf{k}^{\mathrm{i}}$ defined by its location (k_x, k_z) in the Fourier space plane.

This procedure can be applied to a Gaussian beam propagating in an arbitrary direction. In this case, the plane wave decomposition is still performed in the beam waist plane. Therefore, a local coordinate system is introduced with the xz-plane coinciding with the beam waist plane. Afterwards, the propagation vectors $\mathbf{k}^{\mathrm{i}}_n$ (3.7) are transformed to the global coordinate system.
To limit the number of forward problems, the plane waves with the largest amplitude are selected. This is done by exploiting the fact that the plane wave spectrum of a Gaussian beam is also Gaussian (see Fig. 3.2 (b)) and decreases as $\exp(-k_\xi^2 w_0^2/4)$ for increasing $k_\xi = \sqrt{k_x^2 + k_z^2}$. Now, plane waves with an amplitude smaller than $\exp(-a)$, with a a chosen positive real constant, are neglected, i.e. all plane waves with

$$k_\xi > 2\sqrt{a}/w_0. \tag{3.9}$$

In the case of an orthogonally incident Gaussian beam, the set of forward problem solutions can further be halved by exploiting the symmetry of the contributing plane waves along the z-axis.

Complex source beam formulation for a scalar Gaussian beam

The classical formulation yields a relatively large number of plane wave forward problems and extra difficulties such as aliasing when performing the plane wave decomposition. A formulation which avoids these problems is the complex source beam formulation.
Consider a three-dimensional *scalar* Gaussian beam, propagating along a direction $\mathbf{u}^{\mathrm{i}}$, with beam center in $\boldsymbol{\rho}_0 = \mathbf{r}_0 + z_0\mathbf{u}_z$ and with circular beam waist radius w_0. In the three-dimensional complex-source beam formulation [1, 2], such a beam is obtained by evaluating the three-dimensional Green's function

$$G(\boldsymbol{\rho}) = \frac{\exp\left(-jk_0|\boldsymbol{\rho}|\right)}{4\pi|\boldsymbol{\rho}|} \tag{3.10}$$

with respect to a complex source point $\boldsymbol{\rho}_c = \boldsymbol{\rho}_0 + jb_0\mathbf{u}^{\mathrm{i}}$. This complex source point is a combination of the real source point $\boldsymbol{\rho}_0$ and the beam collimation distance, defined as $b_0 = w_0^2 k_0/2$.

In this PhD work, we have extended this approach to the 2.5D case: the Fourier transformed scalar beam is now obtained by evaluating the 2.5D Green's function

$$\widehat{G}(\mathbf{r},\mathbf{r}';k_z) = \frac{j}{4}H_0^{(1)}\left(\sqrt{k_0^2-k_z^2}\,|\mathbf{r}-\mathbf{r}'|\right), \tag{3.11}$$

with respect to the complex source point $\boldsymbol{\rho}_c = (x_c, y_c, z_c)$. Therefore, a complex distance from a point $\mathbf{r}$ to the complex source point $\boldsymbol{\rho}_c$ is defined as

$$s(\mathbf{r}) = \sqrt{(\mathbf{r}-\boldsymbol{\rho}_c)\cdot(\mathbf{r}-\boldsymbol{\rho}_c)} = \sqrt{(x-x_c)^2+(y-y_c)^2+z_c^2}, \tag{3.12}$$

with $Im\left(s(\mathbf{r})\right) \leq 0$ [1]. This complex distance is used as the argument in the 2.5D Green's function and yields the Fourier transformed scalar Gaussian beam :

$$\widehat{E}^{\mathrm{i}}_{GBscal}(\mathbf{r},k_z) = \frac{j}{4}H_0^{(1)}\left(\sqrt{k_0^2-(k_c-k_z)^2}\,s(\mathbf{r})\right), \tag{3.13}$$

where $k_c = k_0\mathbf{u}^{\mathrm{i}}\cdot\mathbf{u}_z$ is the central spectral component corresponding with the propagation direction. Note that we have shifted the spectral components k_z in (3.13) with a value k_c compared to (3.11). This is intuitively understood as follows. In case of an orthogonally incident Gaussian beam ($\mathbf{u}^{\mathrm{i}} = \mathbf{u}_y$, hence $k_c = 0$), the largest contribution to the beam in (3.13) corresponds to $k_z = 0$, which is the spectral component linked to the propagation direction since $k_0\mathbf{u}_y\cdot\mathbf{u}_z = 0$. All other spectral components k_z will contribute less to the beam since $\widehat{E}^{\mathrm{i}}_{GBscal}(\mathbf{r},k_z\neq 0) < \widehat{E}^{\mathrm{i}}_{GBscal}(\mathbf{r},0)$. This be-

havior must also apply to the obliquely incident beams. Hence, independent of the propagation direction of the beam, the main contribution to the beam should correspond to the spectral component $k_z = k_0 \mathbf{u}^{\mathrm{i}} \cdot \mathbf{u}_z$, which is accounted for by shifting the k_z values with a factor k_c.

The selection procedure for contributing spectral components k_z in a scalar Gaussian beam illumination is identically as the one in the case of a completely vectorial beam, therefore it is simultaneously discussed for both cases in Section 3.3.3, where it is shown that this elegant complex source beam approach yields far less spectral components when compared to the plane wave decomposition of a classically formulated Gaussian beam.

3.3.2 2.5D description of a 3D vectorial Gaussian beam

The previous models for a Gaussian beam are only valid in the collimated region of the beam. Outside this region, the polarization must change according to the local curvature of the phase front. This is the case for a fully vectorial Gaussian beam, which can be constructed by applying a similar approach as for the scalar complex source beam. This fully vectorial formulation is valid inside as well as outside the collimated region.

Whereas a point source in complex space generates a three-dimensional scalar Gaussian beam, a dipole source in complex space generates a three-dimensional vectorial Gaussian beam [2].

If we expand this approach to the 2.5D case, the Fourier transformed vectorial Gaussian beam yields:

$$\widehat{\mathbf{E}}^{\mathrm{i}}_{GBvect}(\mathbf{r}, k_z) = \left(k_0^2 \mathbf{I} + \widehat{\nabla}\widehat{\nabla} \right) \cdot \widehat{E}^{\mathrm{i}}_{GBscal}(\mathbf{r}, k_z) \mathbf{u}_{pol}, \tag{3.14}$$

where $\widehat{E}^{\mathrm{i}}_{GBscal}(\mathbf{r}, k_z)$ is the scalar complex source beam (3.13) and $\mathbf{u}_{pol}$ represents the polarization direction in the beam waist plane. This elegant expression for a vectorial Gaussian beam can be evaluated analytically. However, a set of contributing spectral components k_z still has to be determined. This is discussed in the next section (Section 3.3.3).

At millimeter wave frequencies, the arguments of the 2.5D Green's function (3.13) become very large. Therefore, the Hankel function and its derivatives are evaluated analytically using asymptotic expansions [4]. Furthermore, they are scaled by a factor $\exp(-k_0 b_0)$, which corresponds to a normalization with respect to the field in the real source point $\boldsymbol{\rho}_0$ at the dominating spectral component $k_z = k_c$ (hence, $s(\boldsymbol{\rho}_0) = \sqrt{(\boldsymbol{\rho}_0 - \boldsymbol{\rho}_c) \cdot (\boldsymbol{\rho}_0 - \boldsymbol{\rho}_c)} = -jb_0$). These asymptotic expansions are also necessary when a scalar complex source Gaussian beam (3.13) is implemented.
In the following chapters, Gaussian beams are always implemented as 2.5D dipole sources in complex space.

3.3.3 Spectral decomposition of a Gaussian beam

As mentioned before, a general 3D incident field is incorporated into the 2.5D description by transforming the field along the z-direction. In the case of a scalar or vectorial Gaussian beam illumination, this approach becomes straightforward when using the complex source beam formulation. Indeed, this formulation avoids the Fourier transform in the z-direction in an elegant way since the conversion to the 2.5D case is done by simply substituting the three-dimensional Green's function by its 2.5-dimensional variant. Generating a finite set of spectral components k_z that corresponds to a (scalar or vectorial) complex source Gaussian beam is done in a two-step procedure, shown in Fig. 3.3.

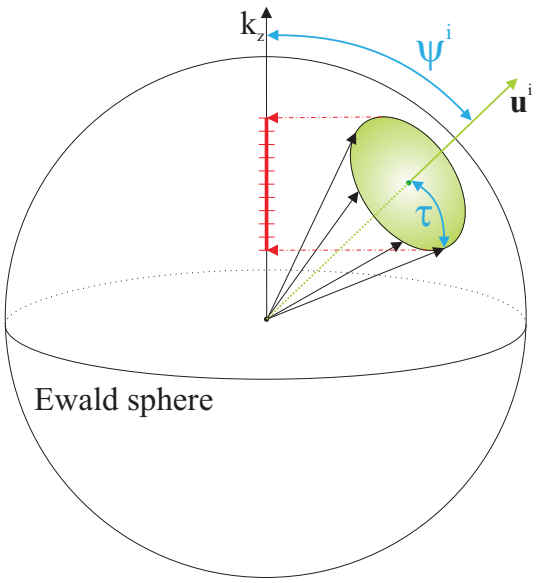

Figure 3.3: Projection of circular patch with contributing propagation vectors on the k_z-axis of the Ewald sphere.

First, upper and lower bounds for k_z need to be determined by neglecting certain spectral components. From the definition of the inverse Fourier transform (2.6), k_z values should be taken from $[-\infty,+\infty]$. This interval can be significantly reduced by neglecting all plane waves with an amplitude smaller than $\exp(-a)$ (with a a chosen positive real constant) from the beam's plane wave spectrum: i.e. all plane waves with $k_\xi > 2\sqrt{a}/w_0$, as in Section 3.3.1. Consequently, all contributing propagation vectors lie within a circular patch with center $k_0\mathbf{u}^{\mathrm{i}}$ and radius $2\sqrt{a}/w_0$ on the Ewald sphere, see Fig. 3.3. Projection of this patch on the k_z-axis yields the interval of spectral com-

ponents k_z which significantly contribute to the 3D Gaussian beam:

$$k_z \in [k_0\, cos(\psi^{\mathrm{i}} + \tau), k_0\, cos(\psi^{\mathrm{i}} - \tau)], \tag{3.15}$$

where $\cos(\psi^{\mathrm{i}}) = \mathbf{u}^{\mathrm{i}} \cdot \mathbf{u}_z$ and $\sin\tau = 2\sqrt{a}/(w_0\, k_0)$.

Second, discrete values for k_z within this interval are determined by applying a Gauss-quadrature formula [4]. These selected spectral components all result in a forward problem to be solved. Hence, when a Q-point Gaussian quadrature formula is used to discretize the Gaussian beam spectrum (3.14), the incident field for the scalar case is written as

$$\mathbf{E}^{\mathrm{i}}_{GBscal}(\mathbf{r}, z) = \frac{1}{2\pi} \sum_{q=1}^{Q} w_q \widehat{E}^{\mathrm{i}}_{GBscal}(\mathbf{r}, k_z^q) \mathbf{u}_{pol} e^{jk_z^q z} \tag{3.16}$$

and for the vectorial case as

$$\mathbf{E}^{\mathrm{i}}_{GBvect}(\mathbf{r}, z) = \frac{1}{2\pi} \sum_{q=1}^{Q} w_q \widehat{\mathbf{E}}^{\mathrm{i}}_{GBvect}(\mathbf{r}, k_z^q) e^{jk_z^q z} \tag{3.17}$$

with

$$\widehat{\mathbf{E}}^{\mathrm{i}}_{GBvect}(\mathbf{r}, k_z^q) = \left(k_0^2 \mathbf{I} + \widehat{\nabla}\widehat{\nabla}\right) \cdot \widehat{E}^{\mathrm{i}}_{GBscal}(\mathbf{r}, k_z^q) \mathbf{u}_{pol}. \tag{3.18}$$

Here, w_q are the Gaussian weights corresponding to the used Gauss quadrature points. Note that in (3.16) the polarization vector is added to the scalar formulation which restricts us to the paraxial approximation and a non-exact solution of the Maxwell's equations.

A similar approach for the selection of spectral components k_z is also possible for the classical formulation of a Gaussian beam ((3.5)-(3.6)) or for more advanced vectorial Gaussian beam formulations beyond the paraxial approximation [5]. In this case, the Fourier transform with respect to the z-coordinate has to be performed explicitly. Due to the complexity of the analytical expression (3.5) and of the expressions in [5], this Fourier transform has to be performed numerically with care and introduces extra errors. From this, it is clear that in the 2.5D description of a Gaussian beam, the use of a complex source beam formulation is strongly recommended.

3.4. Comparison of the scalar Gaussian beam formulations

In this section, both 2.5D implementations for a scalar Gaussian beam under the paraxial approximation (plane wave decomposition of a classically formulated beam and a scalar complex source beam) are compared to a classically formulated three-dimensional scalar Gaussian beam. Furthermore, the scattered fields from a small homogeneous dielectric cylinder, corresponding to both 2.5D scalar beam formulations, are compared.

Consider a three-dimensional TM polarized (i.e. the magnetic field lies in the *xy*-plane, the electric field lies in a plane through the *z*-axis) Gaussian beam illumination, orthogonally or obliquely incident on a scattering cylinder. The corresponding propagation vector $\mathbf{u}^{\mathrm{i}}$ makes an angle θ^{i} with the horizontal *xy*-plane, as in Fig. 3.4 and lies in the vertical *yz*-plane. The scattering object is a dielectric cylinder with relative permittivity $\varepsilon_{r,cyl} = 2$ and radius $a = \lambda_0 = 1$ mm. The Gaussian beam center $\boldsymbol{\rho}_0$ is in the origin and the beam waist radius is $w_0 = 8$ mm. The scattered field is calculated in $K = 51$ detector points with spacing $\lambda_0/10$ on a line parallel to the *x*-axis in $y = 5\lambda_0$. The BICGS tolerance for the iterative solution of the contrast source integral equations is set to 10^{-5} and the discretization cell size is $\Delta = \lambda_0/20$ (the choice for this discretization cell size is discussed in Chapter 4).

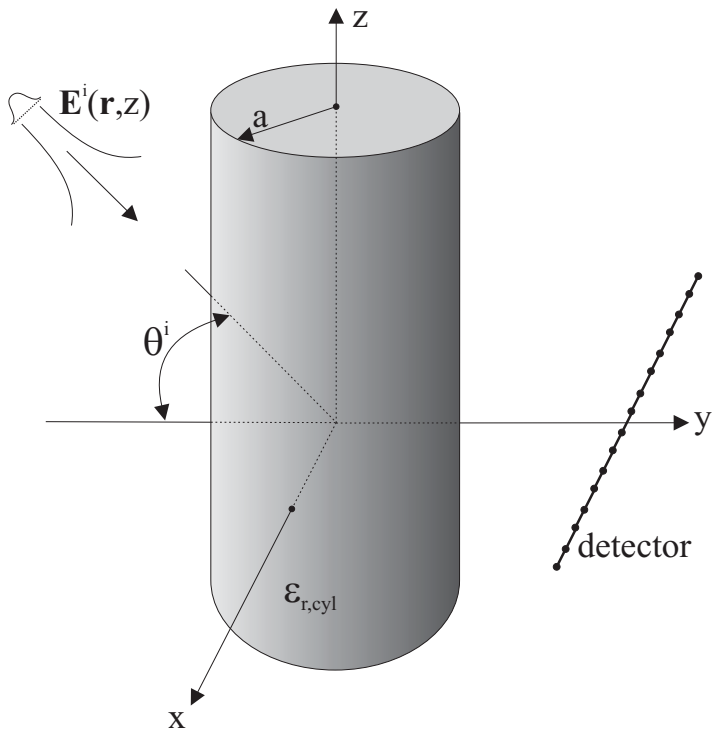

Figure 3.4: Three-dimensional Gaussian beam obliquely incident on a homogeneous circular cylinder.

The incident field is implemented in two ways as presented in Section 3.3.1: on the one hand using an expansion (3.8) into 81 plane waves (yielding 81 CSIE's to be solved) and on the other hand using the complex-source beam formulation (3.16) with 10 quadrature points (yielding 10 CSIE's to be solved). All spectral components with amplitude smaller than $\exp(-5) = 6.7\ 10^{-3}$ are neglected.

For the comparison of the two types of incident fields, a normalized root mean square error (NRMSE) is defined for each component ($p = x,\ y,\ z$) of the *incident* field on the computation grid $\mathcal{D}$ (denoted as *on grid-error*) as

$$NRMSE \quad E^{\mathrm{i}} = \frac{\sqrt{\sum_{k=0}^{N_s-1}\sum_{l=0}^{M_s-1}|E^{\mathrm{i}}_{2.5D,p}(\mathbf{r}^{(p)}_{k,l}) - E^{\mathrm{i}}_{3D,p}(\mathbf{r}^{(p)}_{k,l})|^2}}{\sqrt{\sum_{k=0}^{N_s-1}\sum_{l=0}^{M_s-1}|E^{\mathrm{i}}_{3D,p}(\mathbf{r}^{(p)}_{k,l})|^2}}. \tag{3.19}$$

In (3.19), $E^{\mathrm{i}}_{2.5D,p}(\mathbf{r}^{(p)}_{k,l})$ stands for the p-th component of the incident field obtained by the plane wave expansion (PWE) or by using the complex-source beam (CSB) formula. $E^{\mathrm{i}}_{3D,p}(\mathbf{r}^{(p)}_{k,l})$ is the p-th component of the three-dimensional incident field, computed from the classical three-dimensional Gaussian beam formulation (3.5).

Also, a normalized root mean square error is defined between the *scattered* fields on the computational grid $\mathcal{D}$ as

$$NRMSE \quad E^{\mathrm{s}} = \frac{\sqrt{\sum_{k=0}^{N_s-1}\sum_{l=0}^{M_s-1}|E^{\mathrm{s}}_{CSB,p}(\mathbf{r}^{(p)}_{k,l}) - E^{\mathrm{s}}_{PWE,p}(\mathbf{r}^{(p)}_{k,l})|^2}}{\sqrt{\sum_{k=0}^{N_s-1}\sum_{l=0}^{M_s-1}|E^{\mathrm{s}}_{PWE,p}(\mathbf{r}^{(p)}_{k,l})|^2}}, \tag{3.20}$$

where $E^{\mathrm{s}}_{CSB,p}(\mathbf{r}^{(p)}_{k,l})$ and $E^{\mathrm{s}}_{PWE,p}(\mathbf{r}^{(p)}_{k,l})$ are the p-th component of the scattered fields corresponding to the respective incident field formulations.

First, the propagation direction of the Gaussian beam is along the positive y-axis ($\theta^{\mathrm{i}} = 0^\circ$), hence $E^{\mathrm{i}}_x = E^{\mathrm{i}}_y = 0$. For this test case, no symmetry with respect to the xy-plane is used to reduce the number of forward problems. The scattered fields on the detector points, obtained with both formulations, are compared in Fig. 3.5 and show a very good agreement. Table 3.1 shows that the NRMSE of the z-component of the incident field for both incident field formulations are less than 1%. This shows that enough plane waves and quadrature points were taken into account. Indeed, simulations with 225 instead of 81 plane waves and with 20 instead of 10 quadrature points yield the same NRMSE. The NRMSE of the corresponding scattered field E^{s}_z is of order 10^{-3}. Table 3.1 also shows the total simulation time (including the computation of the scattered field), which is about 9 times larger for the plane wave expansion than for the complex-source point Gaussian beam. The CPU time for the plane wave expansion could be reduced by carefully selecting and combining plane waves with the same k_z values in advance.

Second, the propagation direction of the Gaussian beam makes an angle $\theta^{\mathrm{i}} = 30^\circ$ with the xy-plane, hence $E^{\mathrm{i}}_x = 0$. The scattered fields on the detector points again agree well with each other, as can be seen in Fig. 3.6. Table 3.2 presents the NRMSE of the y- and z-components of the incident field for both incident field formulations, which are again quite small.

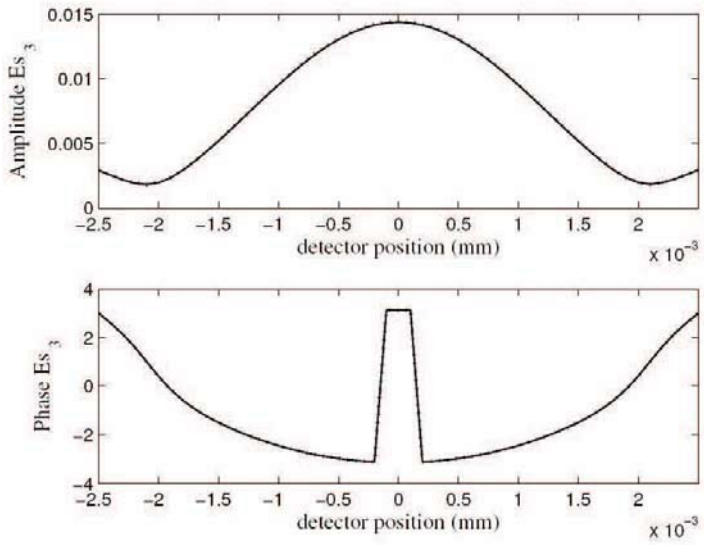

Figure 3.5: Amplitude (top) and phase (bottom) of the z-component of the scattered field for a cylinder with radius λ_0 under a 3D-TM orthogonal Gaussian beam illumination with $\theta^{\mathrm{i}} = 0°$. Solid line: Gaussian beam as Green's function of a complex source point with 10 quadrature points, dotted line: Gaussian beam expanded in 81 plane waves.

Table 3.1: On grid-errors (3.19) and (3.20) and computational effort for the simulations with an orthogonally incident scalar Gaussian beam ($\theta^{\mathrm{i}} = 0°$). *PWE*: plane wave expansion and *CSB*: complex-source Gaussian beam.

	CSB vs. classical 3D	PWE vs. classical 3D	CSB vs. PWE
NRMSE E_z^{i}	$5.9\ 10^{-3}$	$6.4\ 10^{-3}$	$1.0\ 10^{-3}$
NRMSE E_z^{s}	-	-	$9.3\ 10^{-4}$
total CPU time	8 s	70 s	-

Table 3.2: On grid-errors (3.19) and (3.20) and computational effort for the oblique scalar Gaussian beam simulations ($\theta^{\mathrm{i}} = 30°$). *PWE*: plane wave expansion and *CSB*: complex-source Gaussian beam.

	CSB vs. classical 3D	PWE vs. classical 3D	CSB vs. PWE
NRMSE E_y^{i}	$5.0\ 10^{-3}$	$5.6\ 10^{-3}$	$1.2\ 10^{-3}$
NRMSE E_z^{i}	$5.0\ 10^{-3}$	$5.6\ 10^{-3}$	$1.2\ 10^{-3}$
NRMSE E_y^{s}	-	-	$7.2\ 10^{-3}$
NRMSE E_z^{s}	-	-	$4.6\ 10^{-3}$
total CPU time	9 s	77 s	-

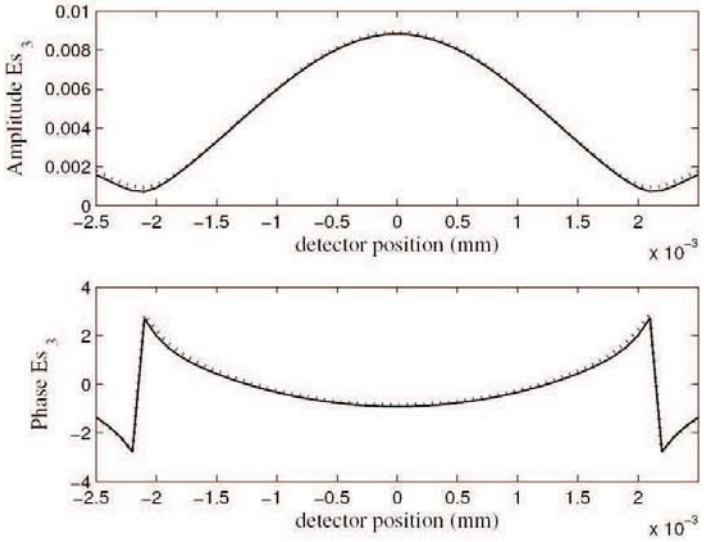

Figure 3.6: Amplitude (top) and phase (bottom) of the z-component of the scattered field for a cylinder with radius λ_0 under a 3D-TM oblique Gaussian beam illumination with $\theta^i = 30°$. Solid line: Gaussian beam as Green's function of complex source point with 10 quadrature points, dotted line: Gaussian beam expanded in 81 plane waves.

3.5. Accuracy study of the 2.5D vectorial complex source beam formulation

For the rest of this PhD work, we have chosen the fully vectorial complex source beam formulation (3.17) with (3.18) and (3.13) as the standard Gaussian beam formulation. In this section, a validation study is performed to evaluate the accuracy of the proposed 2.5D implementation. Therefore, the 2.5D vectorial complex source beam is compared to the 3D vectorial complex source beam [2] on which its implementation is based. The incident field of a 2.5D vectorial complex source beam is also compared to experimentally measured incident fields in Chapter 5.

The 3D Gaussian beam under consideration is an orthogonally or obliquely incident 100 GHz ($\lambda_0 = 3$ mm) beam with a beam waist radius of $w_0 = 8$ mm. This beam configuration is very similar to the experimentally generated beam in Chapter 5. The center of the beam waist plane coincides with the center of the computational domain, hence $z_0 = 0$. Both TM polarization and TE polarization (i.e. with the electric field in the xy-plane) are studied. The 3D incident field that corresponds with the Gaussian beam is calculated on a computational domain $\mathcal{D}$, which contains 48 by 48 cells of size $\lambda_0/20$. The p-th component of the incident field is calculated in the grid points $\mathbf{r}_{k,l}^{(p)}$. The parameter a, which defines the threshold for omitting spectral components on the

Ewald sphere, is set to 5. Hence, all spectral components with amplitude smaller than $\exp(-5) = 6.7\ 10^{-3}$ are neglected.

Also here, a normalized root mean square error is defined between the 3D incident field $\mathbf{E}^{\mathrm{i}}_{2.5D}$, generated within the 2.5D scheme using (3.17), and the directly 3D evaluated incident field $\mathbf{E}^{\mathrm{i}}_{3D}$. Contrary to (3.19), a NRMSE is defined which includes all field components:

$$NRMSE \quad \mathbf{E}^{\mathrm{i}}_{2.5D} = \frac{\sqrt{\sum_{k=0}^{N_s-1}\sum_{l=0}^{M_s-1}\sum_{p=1}^{3}|E^{\mathrm{i}}_{2.5D,p}(\mathbf{r}^{(p)}_{k,l}) - E^{\mathrm{i}}_{3D,p}(\mathbf{r}^{(p)}_{k,l})|^2}}{\sqrt{\sum_{k=0}^{N_s-1}\sum_{l=0}^{M_s-1}\sum_{p=1}^{3}|E^{\mathrm{i}}_{3D,p}(\mathbf{r}^{(p)}_{k,l})|^2}}. \tag{3.21}$$

First, the effect of the number of quadrature points Q in (3.17) is studied. Figure 3.7 shows the NRMSE as a function of Q, in case of TM polarization. The different curves correspond to Gaussian beams with elevation angles θ^{i} (as defined in Fig. 3.4) ranging from 0° (orthogonally incident) to 60°. Since the number of forward problems that need to be solved relates directly to the number of quadrature points, it is essential to choose this number as low as possible. In this case, $Q = 5$ is appropriate and corresponds to a maximal error of 1.1%. In case of a TE-polarized beam, the errors are significantly smaller, as can be seen from Fig. 3.8. Also here, $Q = 5$ is a good choice and corresponds to a maximal error of 0.26%.

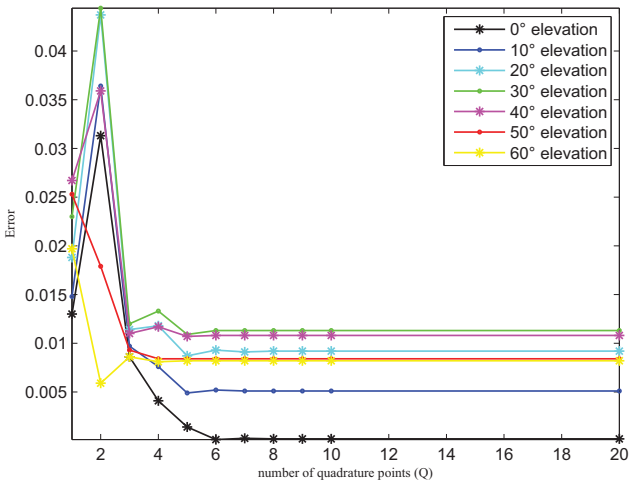

Figure 3.7: NRMSE between a 2.5D formulated TM-polarized complex source Gaussian beam and a directly 3D formulated TM-polarized complex source beam as a function of the number of quadrature points. Different curves correspond to Gaussian beams with different elevation angles.

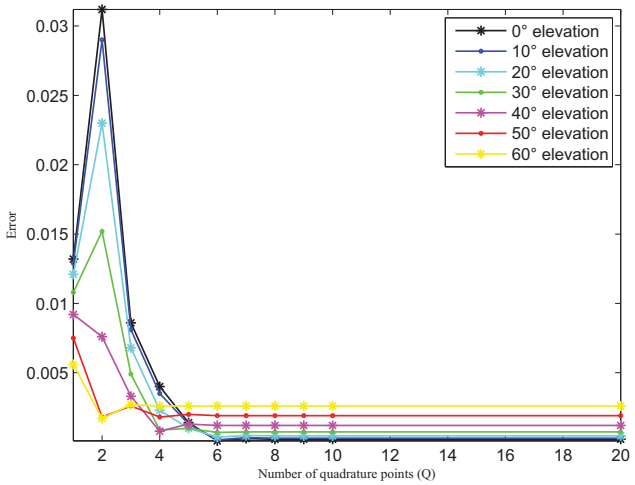

Figure 3.8: NRMSE between a 2.5D formulated TE-polarized complex source Gaussian beam and a directly 3D formulated TE-polarized complex source beam as a function of the number of quadrature points. Different curves correspond to Gaussian beams with different elevation angles.

Second, the effect of the elevation angle θ^i on the NRMSE is investigated. Figures 3.9 and 3.10 show the NRMSE as a function of θ^i for the case of a TM and TE polarized Gaussian beam respectively. It is expected that all curves for different Q converge towards each other for larger elevation angles due to the fact that for larger elevation angles, the circular patch on the Ewald sphere that contains the remaining spectral components is more tilted. Hence, its projection on the k_z axis has a smaller extent and the number of quadrature points to cover this interval is less critical. This behavior is clearly visible in Figs. 3.9 and 3.10. We now focus on the curve for $Q = 5$. Both for TM and TE polarization, orthogonal incident beams ($\theta^i = 0^\circ$) yield the smallest NRMSE. For the TM case, the NRMSE gradually increases towards its maximum of 1.1% for $\theta^i = 30^\circ$. For larger elevation angles the error decreases again and stagnates at around 0.8%. The behavior is slightly different for the TE case: the NRMSE gradually increases towards its maximum of 0.26% for $\theta^i = 60^\circ$.

We conclude that the proposed 2.5D vectorial implementation of a complex source beam (3.17) with (3.18) and (3.13) is an accurate formulation for all elevation angles considered in this work ($0^\circ - 60^\circ$).

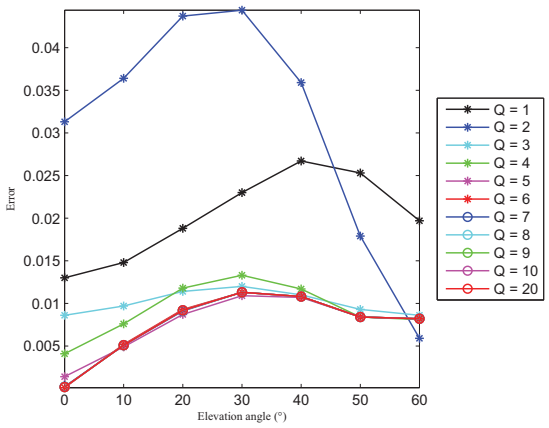

Figure 3.9: NRMSE between a 2.5D formulated TM-polarized complex source Gaussian beam and a directly 3D formulated TM-polarized complex source beam as a function of the elevation angle θ^i. Different curves correspond to 2.5D Gaussian beams implemented using different numbers of quadrature points.

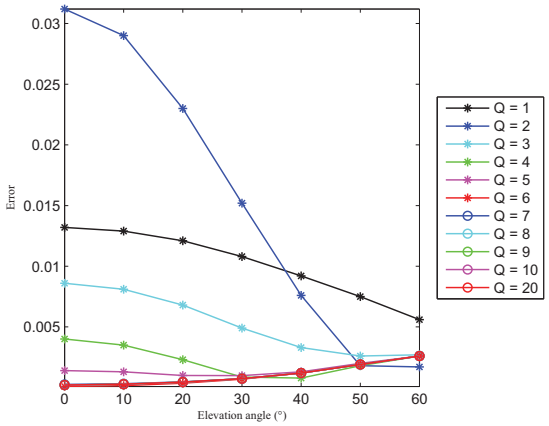

Figure 3.10: NRMSE between a 2.5D formulated TE-polarized complex source Gaussian beam and a directly 3D formulated TE-polarized complex source beam as a function of the elevation angle θ^i. Different curves correspond to 2.5D Gaussian beams implemented using different numbers of quadrature points.

3.6. Conclusion

In this chapter, three different models to implement a Gaussian beam have been studied. In a first model, a polarization vector is added to the classical formulation for a scalar Gaussian beam under the paraxial approximation. Two complications arise when applying this approach. On the one hand, this type of incident field is not an exact solution of Maxwell's equations. On the other hand, an analytical form of the Fourier transformation of this expression to obtain the set of spectral components is not at hand. Since the latter is elegantly overcome by the other two formulations, this classical formulation has only been implemented as a validation case for the other methods by decomposing the Gaussian beam in plane waves.

The second model is based on a scalar complex source beam formulation. Here, the Gaussian beam is obtained as the field generated by a point source in complex space. Still, it is only valid under the paraxial approximation since, also here, a polarization vector is added to the scalar beam. In this PhD work, we have reformulated this approach for the 2.5D case and elegantly avoided the explicit Fourier transformation of the incident field to obtain the spectral components. The contributing spectral components are discretized by inspecting the beam's plane wave spectrum on the Ewald sphere

The third model is the most complete and is the standard implementation for a Gaussian beam within the presented 2.5D forward solver. Here, a dipole source in complex space generates a fully vectorial three-dimensional Gaussian beam. No polarization vector needs to be added which makes it an exact solution of Maxwell's equations. Furthermore, the formulation is valid both inside and outside the well collimated region of the beam. In this PhD work, this approach has been translated to the 2.5-dimensional case. The discretization of the spectral components is performed similarly as for the scalar complex source Gaussian beam formulation.

All three 2.5D Gaussian beam implementations have been validated by constructing the 2.5-dimensional incident fields for every selected spectral component and combining them into a three-dimensional field. Since the first two models are only valid in the paraxial approximation, they are not compared to the third one, but to the corresponding three-dimensional classical formulation, which also has an added fixed polarization vector. Both 2.5D formulations agreed very well with this classical 3D formulation, both for orthogonal *and* oblique incidence. The third, fully vectorial, 2.5D formulation has been compared to the corresponding three-dimensional formulation on which its derivation is based. The NRMSE between the 2.5D beam and the 3D beam has been evaluated for different elevation angles and different numbers of quadrature points (Q) in the discretization of the spectrum. We have concluded that $Q = 5$ is a good choice and limits the NRMSE on the incident field to a maximum of 1.1% in case of TM polarization and to a maximum of 0.26% for TE polarization, both for elevation angles up to 60°.

Bibliography

[1] E. Heyman and L. Felsen, "Gaussian beam and pulsed beam dynamics: complex-source and complex-spectrum formulations within and beyond paraxial asymptotics," *Journal of the Optical Society of America A*, vol. 18, no. 7, pp. 1588–1611, July 2001.

[2] I. Lindell, *Advanced Field Theory*. Helsinki, Finland: Helsinki University of Technology, 2000.

[3] P. Goldsmith, *Quasioptical Systems: Gaussian Beam Quasioptical Propagation and Applications*. New York: IEEE Press / Chapman and Hall Publishers Series on Microwave Technology and RF, 1997.

[4] M. Abramowitz and I. Stegun, *Handbook of Mathematical Functions with Formulas, Graphs, and Mathematical Tables*, ninth dover printing ed. New York: Dover, 1970.

[5] C. Sheppard and S. Saghafi, "Electromagnetic Gaussian beams beyond the paraxial approximation," *Journal of the Optical Society of America A*, vol. 16, no. 6, pp. 1381–1386, 1999.

CHAPTER 4

Validation of the forward solver and case studies

4.1. Introduction

In this chapter, the accuracy of the 2.5D forward solver is examined for different types of incident fields and different scattering objects. All simulations are performed on a machine with two AMD Opteron 270 Quad Core processors.

The first part of this chapter is devoted to the comparison of 2.5D simulation results to *analytic solutions*. These are analytic expressions for the scattered field. We consider: (i) a homogeneous circular dielectric cylinder and (ii) a piecewise-homogeneous multi-layered circular dielectric cylinder under orthogonally and obliquely incident plane wave illuminations. The evaluation of these analytic expressions is computationally demanding, therefore we restrict ourselves to relatively small cylinders with radii of the order of a wavelength.

The second part of this chapter deals with the comparison of 2.5D simulation results to scattered fields obtained with fully three-dimensional forward solvers. The first 3D solver is a *Volume* Integral Equation (VIE) solver [1], whereas the second 3D solver [2] is a parallelized *Boundary* Integral Equation (BIE) solver. Both 3D solvers are also developed in the department of Information Technology.

Furthermore, it will be shown that the scattering from a *finite* dielectric cylinder under three-dimensional Gaussian beam illumination can be modeled within the 2.5D approach. To illustrate this, several 2.5D simulations are compared with data obtained with the aforementioned 3D boundary integral equation solver.

Finally, the applicability of the 2.5D approach to investigate millimeter-wave scattering from concealed objects on the human body is illustrated.

4.2. Comparison to analytic solutions

In this section, simulation results from the 2.5D forward solver are compared to analytic solutions for plane wave scattering at infinitely long circular dielectric cylinders, more in particular homogeneous cylinders and a piecewise homogeneous multilayered cylinder. Two types of polarization are studied: Transverse Magnetic (TM) polarization and Transverse Electric (TE) polarization. Transverse Magnetic indicates that the magnetic field lies in the transverse plane. Hence, the electric field, which is perpendicular to the magnetic field, lies in a plane through the z-axis. With Transverse Electric polarization, the electric field lies in the xy-plane.

A comparison to the analytic solutions is presented for purely two-dimensional configurations, where the plane wave is orthogonally incident on the infinitely long cylinder (hence $k_z = 0$ and $\mathbf{E} = E_3\mathbf{u}_z$ or $\mathbf{E} = E_1\mathbf{u}_x + E_2\mathbf{u}_y$ for a TM- or TE- polarized field respectively), and for three-dimensional field configurations, where the plane wave is obliquely incident.

To determine the accuracy of a simulated scattered electric field, the Normalized Root Mean Square Error (NRMSE) with respect to the analytical solutions is employed. This quantity measures differences between the solution obtained with the 2.5D forward solver and the exact analytical solution in the N detector points. For every component $p = x,\ y,\ z$ of the scattered field, this error is defined as

$$NRMSE(E_p^{\mathrm{s}}) = \frac{\sqrt{\sum_{n=1}^{N} |E_{2.5D,p}^{\mathrm{s}}(n) - E_{exact,p}^{\mathrm{s}}(n)|^2}}{\sqrt{\sum_{n=1}^{N} |E_{exact,p}^{\mathrm{s}}(n)|^2}}. \tag{4.1}$$

4.2.1 Scattering by homogeneous cylinders

2D analytic solution for a TM polarized orthogonally incident plane wave

First, the 2.5D forward solver is validated in a purely two-dimensional configuration. The incident field is a TM-polarized plane wave with unit amplitude, propagating in the y-direction and orthogonally incident on a homogeneous dielectric cylinder with a relative permittivity $\varepsilon_{r,cyl} = 2$ and with radius $a = \lambda_0$, where λ_0 is the free-space wavelength, see Fig. 4.1. In this example, the frequency is chosen to be 300 GHz, corresponding to a free space wavelength of $\lambda_0 = 1$ mm. There are $N = 360$ equidistant measurement points on a circle with radius $b = 20\lambda_0$.

Simulations are performed using four different discretization cell sizes Δ, corresponding to 10, 20, 40 and 80 cells per wavelength $\lambda_{cyl} = \lambda_0/\sqrt{\varepsilon_{r,cyl}}$ inside the cylinder. The BICGS iterations are stopped when the relative error (between left and right hand side of the contrast source integral equation) dropped below a prescribed tolerance.

Figure 4.2 shows the amplitude and phase of the z-component of the scattered field $\mathbf{E}^{\mathrm{s}} = E_3^{\mathrm{s}}\mathbf{u}_z$ for a cell size of $\Delta = \lambda_{cyl}/20$. The 2.5D forward solver (dotted lines) and the analytic solution (solid lines) show an excellent agreement. Table 4.1 gives, as a

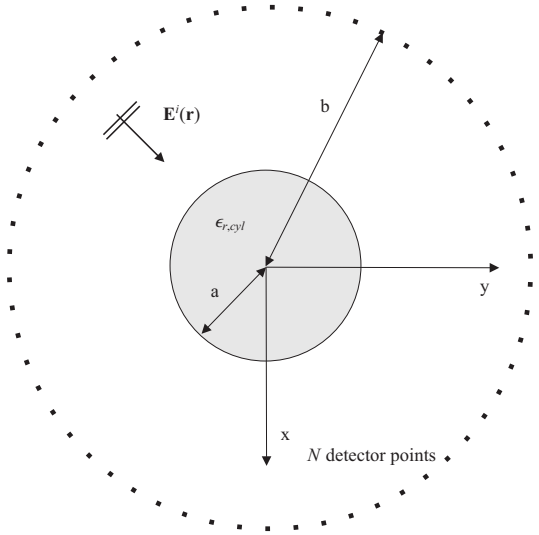

Figure 4.1: Cross-section of an infinitely long homogeneous circular cylinder, illuminated by an orthogonally incident plane wave and surrounded with a circular detector array.

function of the cell size, some simulation parameters and the scattered field error. It is clear that the NRMSE decreases linearly with the cell size Δ and that a size $\Delta < \lambda_{cyl}/20$ is needed to reduce the error to one percent.

A major contribution to the NRMSE in Table 4.1 is due to the discretization in square cells of a circular cylinder, which gives rise to a *staircasing effect* on the edges of the cylinder. This effect can be reduced by taking a very fine discretization grid, as is the case for $\Delta = \lambda_{cyl}/80$, or by explicitly accounting for the presence of edges within cells [3]. Forward solvers based on a Boundary Integral Equation approach suffer less from this effect, since in that case the boundaries between homogeneous regions are discretized with a piecewise linear approximation, allowing a smoother fit to the curved edges. However, a VIE approach with square grid cells is appropriate in this PhD work since we are mainly interested in pixel-based inverse scattering, where the location and shape of edges are a-priori unknown and where, during the reconstructions, the pixels can take on a continuum of permittivity values.

2D analytic solution for a TE polarized orthogonally incident plane wave

For the next validation test, the same configuration as above (Fig. 4.1) is simulated, but now with an orthogonally incident TE-polarized incident field. The plane wave propagates in the y-direction and is polarized along the x-direction.

Again, the four discretization cell sizes Δ, corresponding to 10, 20, 40 and 80 cells per wavelength, are used to discretize the circular cylinder. Figure 4.3 shows the

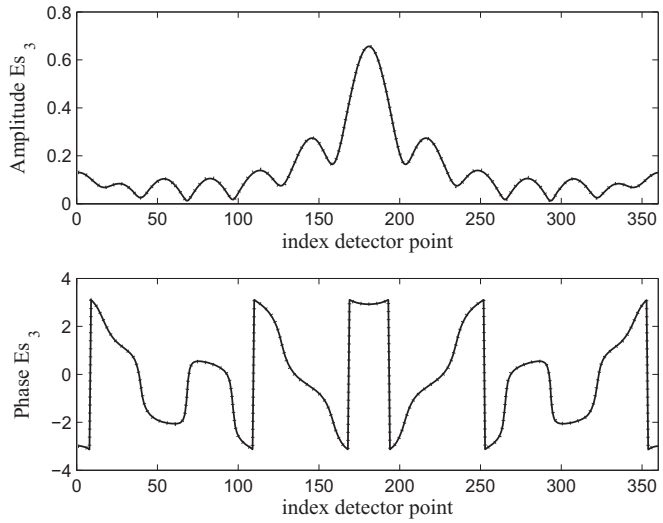

Figure 4.2: Amplitude (top) and phase (bottom) of the 2D-TM scattered field for a cylinder with radius λ_0 and relative permittivity $\varepsilon_{r,cyl} = 2$. Solid line: analytic solution, dotted line: 2.5D solver discretized with 20 cells per λ_{cyl}.

Table 4.1: Parameters for the 2D-TM simulations: discretization cell size, grid dimensions, total number of unknowns, BiCGS tolerance, number of CG iterations, total CPU time and NRMSE of the z-component of the scattered field.

Δ	grid size	# unkn.	tolerance	# it.	CPU time	NRMSE E_3^s
$\lambda_{cyl}/10$	35 x 35	3 675	$1.0\ 10^{-2}$	11	0' 01"	$4.0\ 10^{-2}$
$\lambda_{cyl}/20$	63 x 63	11 907	$1.0\ 10^{-3}$	18	0' 05"	$1.3\ 10^{-2}$
$\lambda_{cyl}/40$	120 x 120	43 200	$1.0\ 10^{-3}$	18	0' 20"	$7.7\ 10^{-3}$
$\lambda_{cyl}/80$	234 x 234	164 268	$1.0\ 10^{-3}$	20	1' 22"	$3.2\ 10^{-3}$

amplitude and phase of the x- and y- components of the scattered field for the cell size $\Delta = \lambda_{cyl}/20$. The 2.5D solver (dotted lines) and the analytic solution (solid lines) again show an excellent agreement. Simulation parameters are presented in Table 4.2. From Table 4.3, it is clear that, also in this case, the NRMSE decreases linearly with the cell size Δ and that a size $\Delta < \lambda_{cyl}/20$ is needed to reduce the error to one percent.

Next, simulations are performed for increasingly larger cylinders (with radii λ_0, $2\lambda_0$, $4\lambda_0$, $6\lambda_0$ and $8\lambda_0$) but with a fixed discretization size $\Delta = \lambda_{cyl}/20$.
Table 4.4 shows the simulation parameters, the NRMSE's can be found in Table 4.5. The largest cylinder (with more than half a million of unknowns) yields an error of less than 5 percent and is solved in 42 minutes. The amplitude and phase of the x- and

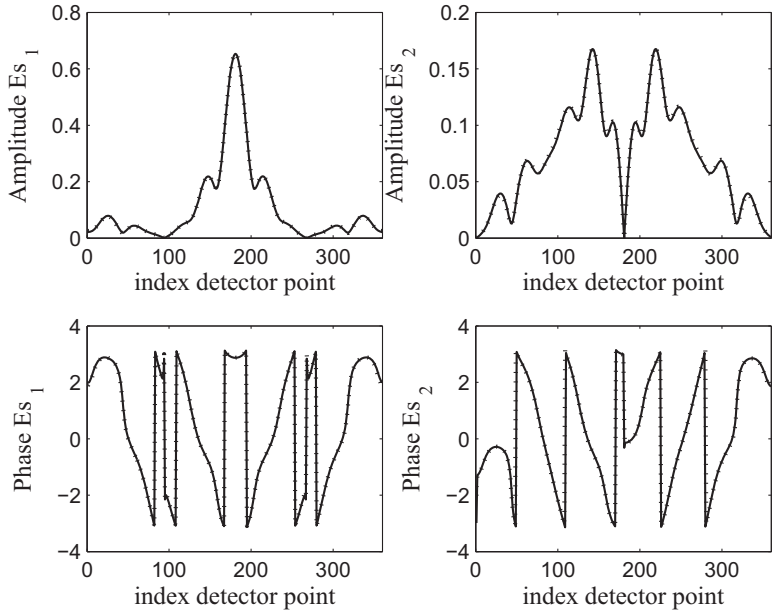

Figure 4.3: Amplitude (top) and phase (bottom) of the *x*- (left) and *y*- (right) components of the 2D-TE scattered field for a cylinder with radius λ_0 and relative permittivity $\varepsilon_{r,cyl} = 2$. Solid line: analytic solution, dotted line: 2.5D solver discretized with 20 cells per λ_{cyl}.

Table 4.2: Parameters for the 2D-TE simulations: discretization cell size, grid dimensions, total number of unknowns, BiCGS tolerance, number of CG iterations, total CPU time.

Δ	grid size	# unkn.	tolerance	# it.	CPU time
$\lambda_{cyl}/10$	35 x 35	3 675	$1.0\ 10^{-3}$	14	0' 01"
$\lambda_{cyl}/20$	63 x 63	11 907	$1.0\ 10^{-3}$	16	0' 05"
$\lambda_{cyl}/40$	120 x 120	43 200	$1.0\ 10^{-3}$	20	0' 21"
$\lambda_{cyl}/80$	234 x 234	164 268	$1.0\ 10^{-2}$	17	1' 25"

Table 4.3: NRMSE for the *x*- and *y*-components of the scattered field for the 2D-TE simulations.

Δ	NRMSE E_1^s	NRMSE E_2^s
$\lambda_{cyl}/10$	$2.4\ 10^{-2}$	$4.8\ 10^{-2}$
$\lambda_{cyl}/20$	$9.3\ 10^{-3}$	$1.4\ 10^{-2}$
$\lambda_{cyl}/40$	$4.8\ 10^{-3}$	$8.3\ 10^{-3}$
$\lambda_{cyl}/80$	$2.3\ 10^{-3}$	$5.1\ 10^{-3}$

y- components of the scattered field, for the largest cylinder, are presented in Fig. 4.4. Again, there is a very good agreement with the analytic solution.

Table 4.4: Parameters for the 2D-TE simulations for increasingly large cylinders: radius, grid dimensions, total number of unknowns, BiCGS tolerance, number of CG iterations, total CPU time.

radius	grid size	# unkn.	tolerance	# it.	CPU time
1 λ_0	63 x 63	11 907	1.0 10^{-3}	16	0' 05"
2 λ_0	120 x 120	43 200	1.0 10^{-3}	61	0' 25"
4 λ_0	234 x 234	164 268	1.0 10^{-3}	293	3' 09"
6 λ_0	350 x 350	367 500	1.0 10^{-3}	943	15' 09"
8 λ_0	462 x 462	640 332	1.0 10^{-3}	1600	42' 01"

Table 4.5: NRMSE of the x- and y- components of the scattered field for the 2D-TE simulations with increasingly large cylinders.

radius	NRMSE E_1^s	NRMSE E_2^s
1 λ_0	9.3 10^{-3}	1.4 10^{-2}
2 λ_0	1.9 10^{-2}	4.6 10^{-2}
4 λ_0	7.8 10^{-2}	1.0 10^{-1}
6 λ_0	4.7 10^{-2}	4.3 10^{-2}
8 λ_0	4.5 10^{-2}	4.5 10^{-2}

3D analytic solution for a TM polarized obliquely incident plane wave

After a purely two-dimensional test, we now validate the numerical results of the 2.5D forward solver for a three-dimensional illumination. Here, the incident field is an obliquely incident TM-polarized plane wave. It has a propagation vector $\mathbf{k}^{\mathrm{i}} = k_0 \mathbf{u}_i$ that makes an elevation angle $\theta^{\mathrm{i}} = 40^\circ$ with the xy-plane (see Fig. 4.5). The only spectral component is given by $k_z^{\mathrm{i}} = k_0 \sin\theta^{\mathrm{i}}$. The frequency is set to 8 GHz, corresponding to a free space wavelength of $\lambda_0 \approx 3.75$ cm.

The scattering object is a homogeneous dielectric cylinder with permittivity $\varepsilon_{r,cyl} = 2$, having a circular cross-section with radius 6 cm. It is discretized using 35 cells per wavelength $\lambda_{cyl} = \lambda_0/\sqrt{\varepsilon_{r,cyl}}$ inside the cylinder to reduce staircasing effects. The scattered field is computed in 100 equidistantly spaced detector points on a circle with radius $r_{detec} = 10$ cm.

Figure 4.6 shows the amplitude and phase of the z-component of the scattered electric field, whereas Fig. 4.7 shows the amplitude and phase of the ϕ-component (in cylindrical coordinates). There is a perfect agreement between the 2.5D results (dotted lines) and the analytical solutions (solid lines).

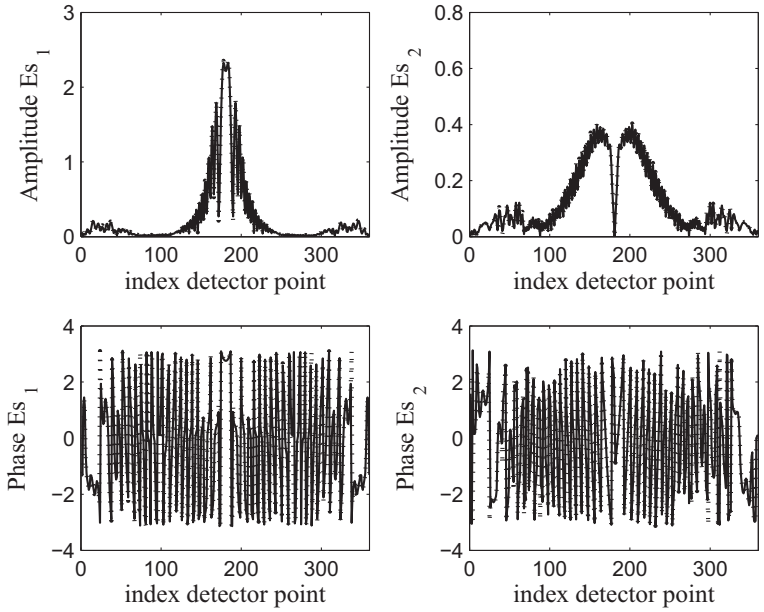

Figure 4.4: Amplitude (top) and phase (bottom) of the *x*- (left) and *y*- (right) components of the 2D-TE scattered field for the cylinder with radius $8\lambda_0$. Solid line: analytic solution, dotted line: 2.5D solver with 20 cells per λ_{cyl}.

4.2.2 Scattering by an inhomogeneous cylinder

Since there are no analytic solutions for scattering by completely inhomogeneous cylinders, the validation for the inhomogeneous case is done for the intermediate case of a piecewise-homogeneous multi-layered dielectric cylinder with circular cross-section.

A four-layered dielectric cylinder (see Fig. 4.8) is illuminated by an obliquely incident TM-polarized plane wave. The layers' radii are set to $r_1 = 12$ cm, $r_2 = 9$ cm, $r_3 = 6$ cm and $r_4 = 3$ cm and the respective relative permittivities are $\varepsilon_{r,1} = 2.0$, $\varepsilon_{r,2} = 2.5$, $\varepsilon_{r,3} = 3.0$ and $\varepsilon_{r,4} = 3.5$. All other simulation settings (frequency, incident field, detector configuration, ...) are the same as in the 3D illumination example of the previous section.

Simulated and analytically computed fields are compared in Fig. 4.9 and Fig. 4.10: Figure 4.9 shows the amplitude and phase of the z-component of the scattered electric field, whereas Fig. 4.10 shows the amplitude and phase of the corresponding ϕ-component. There is once more a perfect agreement between the 2.5D results (dotted lines) and the analytical solutions (solid lines).

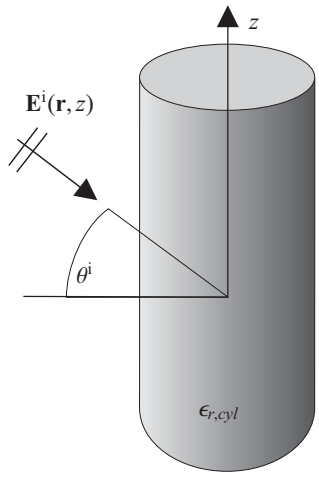

Figure 4.5: Configuration with an obliquely incident TM-polarized plane wave illuminating a homogeneous dielectric cylinder.

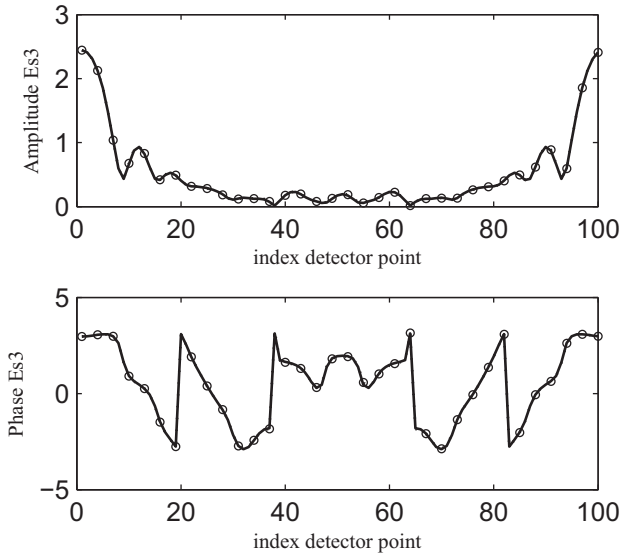

Figure 4.6: Amplitude (top) and phase (bottom) of the z-component (cylindrical coordinate system) of the 3D scattered field for a homogeneous cylinder with radius 0.06 m under oblique TM plane wave illumination with $\theta^{\mathrm{i}} = 40^{\circ}$ at 8 GHz. Solid line: analytical solution, dotted line: 2.5D simulation.

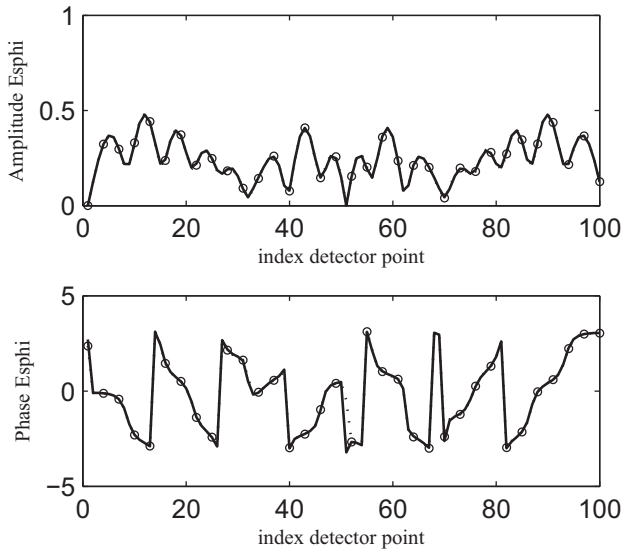

Figure 4.7: Amplitude (top) and phase (bottom) of the ϕ-component (cylindrical coordinate system) of the 3D scattered field for a homogeneous cylinder with radius 0.06 m under oblique TM plane wave illumination with $\theta^{i} = 40^{\circ}$ at 8 GHz. Solid line: analytical solution, dotted line: 2.5D simulation.

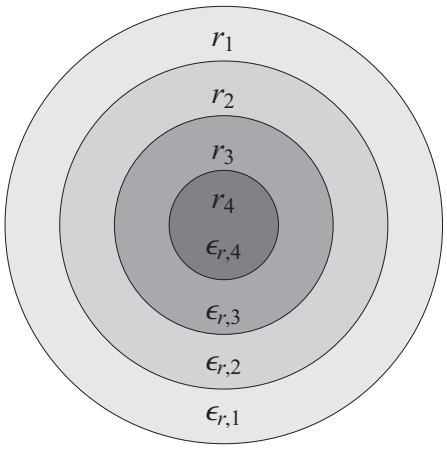

Figure 4.8: Cross-section of the four-layered dielectric cylinder with radii $r_1 = 12$ cm, $r_2 = 9$ cm, $r_3 = 6$ cm and $r_4 = 3$ cm and respective permittivities $\varepsilon_{r,1} = 2.0$, $\varepsilon_{r,2} = 2.5$, $\varepsilon_{r,3} = 3.0$ and $\varepsilon_{r,4} = 3.5$.

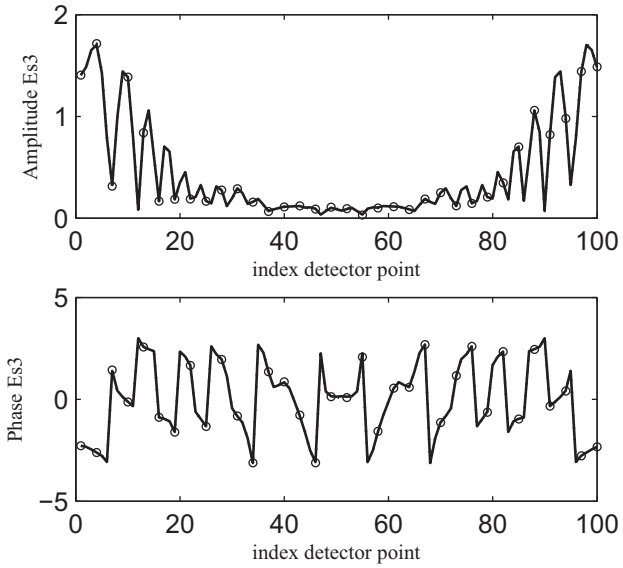

Figure 4.9: Amplitude (top) and phase (bottom) of the z-component (cylindrical coordinate system) of the 3D scattered field for the four-layered dielectric cylinder of Fig. 4.8 under oblique TM plane wave illumination with $\theta^i = 40^\circ$ at 8 GHz. Solid line: analytical solution, dotted line: 2.5D simulation.

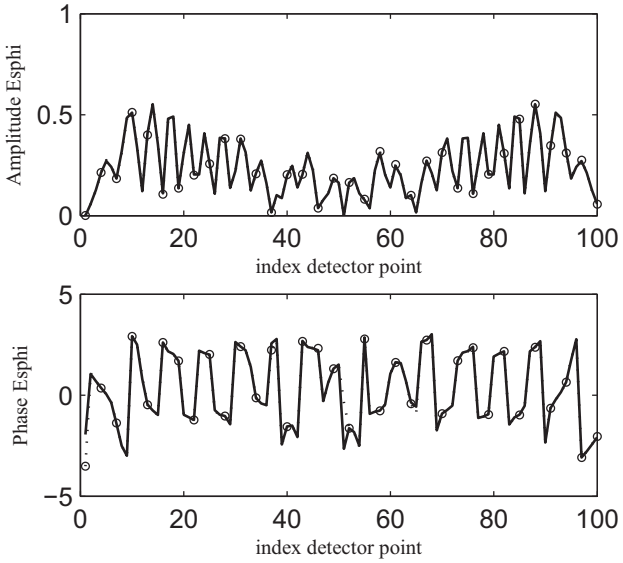

Figure 4.10: Amplitude (top) and phase (bottom) of the ϕ-component (cylindrical coordinate system) of the 3D scattered field for a four-layered dielectric cylinder of Fig. 4.8 under oblique TM plane wave illumination with $\theta^i = 40^\circ$ at 8 GHz. Solid line: analytical solution, dotted line: 2.5D simulation.

4.3. Comparison to fully three-dimensional forward solvers

In this section, simulation results for the 2.5D solver are compared to simulations from two full 3D solvers, one is based on a volume integral equation (VIE) approach, the other used a boundary integral equation (BIE) method. Both 3D solvers are developed at the Department of Information Technology. The VIE solver [1] uses, as the 2.5D forward solver, a Biconjugate Gradient method to iteratively solve a fully vectorial three-dimensional contrast source integral equation and accelerates single iterations with the FFT-method. The BIE solver [2] is intended for (piecewise) homogeneous objects and uses the Multilevel Fast Multipole method for acceleration and a TFQMR method (Transpose-Free Quasi-Minimal Residual method) for the iterative solution. It is a fully parallel simulation tool, which strongly reduces the computation time and allows for more memory to be allocated. With these 3D solvers, only a finite 3D object can be modeled, whereas the 2.5D solver only treats 2D objects. Consequently, the comparison between 2.5D and 3D solvers is only meaningful for configurations where the diffraction effects from the upper and lower sides of the finite cylinder are negligible. In the following examples we consider homogeneous cylinders with circular and rectangular cross-sections under plane wave and Gaussian beam illuminations, respectively.

4.3.1 Comparison to a 3D VIE solver for plane wave illumination

For a plane wave illumination, the comparison with the infinitely long cylinder used in the 2.5D forward solver is only meaningful when the length l of the finite cylinder is chosen sufficiently long with respect to its cross-sectional dimensions, and when the scattered field is calculated close enough to the cylinder. Therefore, its length is set to $l = 100\lambda_0$ and the detector consists of $N = 360$ points on small circle with radius $b = 2\lambda_0$.

The scattering object is a dielectric cylinder with permittivity $\varepsilon_{r,cyl} = 2$ and radius $a = \lambda_0$ (Fig. 4.1). The incident field is an oblique TM-polarized plane wave with a propagation vector $\mathbf{k}^{\mathrm{i}} = k_0\mathbf{u}_i$. The propagation direction makes an angle θ^{i} with the xy-plane, hence $k_z^{\mathrm{i}} = k_0 \sin\theta^{\mathrm{i}}$, see Fig. 4.5. Three different angles of incidence are simulated: $\theta^{\mathrm{i}} = 8^\circ$, $\theta^{\mathrm{i}} = 16^\circ$ and $\theta^{\mathrm{i}} = 30^\circ$.

For the incident angle $\theta^{\mathrm{i}} = 8^\circ$, the 3D simulation consists of more than 5 million unknowns, occupying 2.4 Gb of memory, and takes 16 simulation hours. The number of iterations has already been limited by choosing the BICGS threshold in the 3D simulation relatively high: at $10^{-2.5}$. On the other hand, the 2.5D simulation for $\theta^{\mathrm{i}} = 8^\circ$ only requires 13 068 unknowns, occupying 40.6 Mb of memory, and only lasts 6 seconds. Here, the BICGS tolerance is 10^{-3} and a discretization with 66 cells in both x- and y-directions is used, leading to a cell size $\Delta = \lambda_{cyl}/20$.

In Table 4.6 some other computational parameters are listed for the three different incident angles θ^{i}, as well as the NRMSE for component $p = x, y, z$ of the scattered

field, defined as:

$$NRMSE(E_p^s) = \frac{\sqrt{\sum_{k=1}^{K} |E_{2.5D,p}^s(k) - E_{3D,p}^s(k)|^2}}{\sqrt{\sum_{k=1}^{K} |E_{3D,p}^s(k)|^2}}. \tag{4.2}$$

Figure 4.11 shows the amplitude and phase of each component of the scattered field vector for the largest elevation, $\theta^i = 30^\circ$. There is a good agreement between the 2.5D (dotted lines) and the 3D (solid lines) solutions. Similar results were obtained for the angles $\theta^i = 8^\circ$ and $\theta^i = 16^\circ$.

Table 4.6: Comparison to a 3D VIE solver: parameters for the 2.5D simulations are incident angle, number of iterations, total computation time and NRMSE's for the *x*-, *y*- and *z*-components of the scattered field.

θ^i	# it.	CPU time	NRMSE E_1^s	NRMSE E_2^s	NRMSE E_3^s
8°	18	00' 06"	$5.1\ 10^{-2}$	$2.6\ 10^{-2}$	$2.3\ 10^{-2}$
16°	19	00' 06"	$7.1\ 10^{-2}$	$2.7\ 10^{-2}$	$2.4\ 10^{-2}$
30°	22	00' 06"	$4.9\ 10^{-2}$	$2.6\ 10^{-2}$	$2.5\ 10^{-2}$

4.3.2 Comparison to a 3D BIE solver for Gaussian beam illumination

Up to this point, all validations have been for plane waves as incident field. Now, an orthogonally incident three-dimensional Gaussian beam is used. In this case, only a spatially limited region of the object is illuminated. Therefore, a finite dielectric cylinder under Gaussian beam illumination can also be modeled with the 2.5D algorithm if it has invariant electromagnetic properties in the axial direction over a distance roughly corresponding to the spot size of the beam. In the following, such objects are referred to as *quasi-2D objects*. This approach is validated by comparing scattered fields from an *infinite* dielectric cuboid computed with the 2.5D solver to scattered fields from *finite* cuboids with increasing length, obtained with the 3D BIE solver.

Figure 4.12 presents the simulated configuration. The incident field is a 94 GHz (corresponding to a free space wavelength of $\lambda_0 = 3.2$ mm), normally incident, 3D Gaussian beam with beam waist radius $w_0 = 8.5$ mm. Its center is located at **O** and the distance d between the beam center and the cuboid surface is chosen half the collimation distance: $b_0/2 = 35.6$ mm. The electric field is parallel to the z-axis (TM polarization). The beam radius at the cuboid surface is $w_{cuboid} = 9.5$ mm and the corresponding spot size $a = 2w_{cuboid} = 19$ mm. The cross-sectional dimensions of the cuboid are equal to half the spot size ($b_1 = b_2 = a/2$) and its relative permittivity is $\varepsilon_{r,cuboid} = 2.0$. Note that the object's cross-section is completely located within the collimated region of the Gaussian beam.

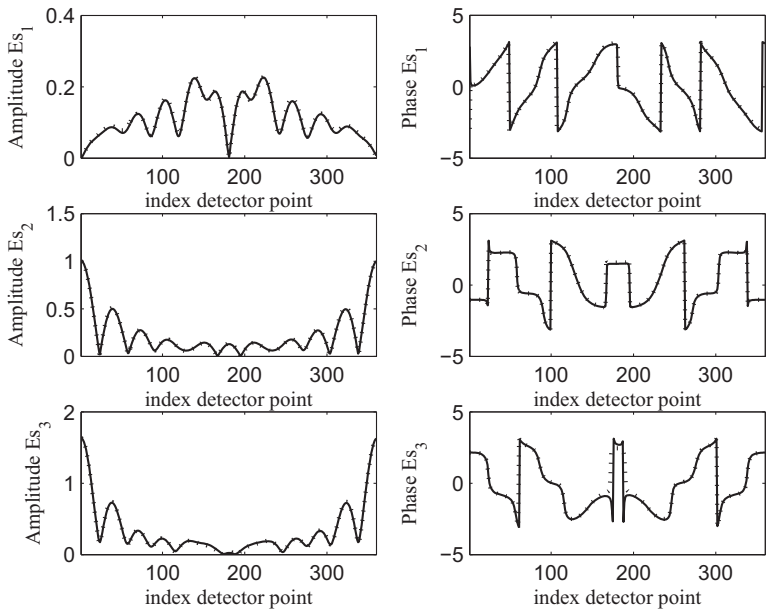

Figure 4.11: Amplitude (left) and phase (right) of the x- (top), y- (middle) and z- (bottom) components of the scattered field for a cylinder with radius λ_0 under oblique plane wave illumination with $\theta^{\mathrm{i}} = 30°$. Solid line: 3D simulation, dotted line: 2.5D simulation.

The scattered fields are computed in $N = 180$ points on a circle with radius $r_{detec} = a/2 = 9.5$ mm, located in the xy-plane.

Since the Gaussian beam is orthogonally incident, the different spectral components k_z of the 2.5D algorithm (3.15) are spread symmetrically around $k_z = 0$, hence symmetry is invoked to reduce the k_z-interval to half its size. The beam is further expanded in five different positive k_z values, which appear to be sufficient for the NRMSE on the incident field, defined as

$$NRMSE\ (E^{\mathrm{i}}) = \frac{\sqrt{\sum_{n=1}^{N} |E^{\mathrm{i}}_{2.5D,z}(n) - E^{\mathrm{i}}_{3D,z}(n)|^2}}{\sqrt{\sum_{n=1}^{N} |E^{\mathrm{i}}_{3D,z}(n)|^2}}, \tag{4.3}$$

to be lower than 10^{-3}. This is also illustrated by Fig. 4.13, showing the amplitude and phase of the z-component of the 2.5D ((3.17)-(3.18)) and 3D [4] incident field computed on the detector points.

In successive full 3D simulations, the length of the cuboid is increased, starting from $l = a/2$. It is expected that from a certain length on, further increasing the cuboid length will no longer change the scattered fields, since the incident and scattered fields

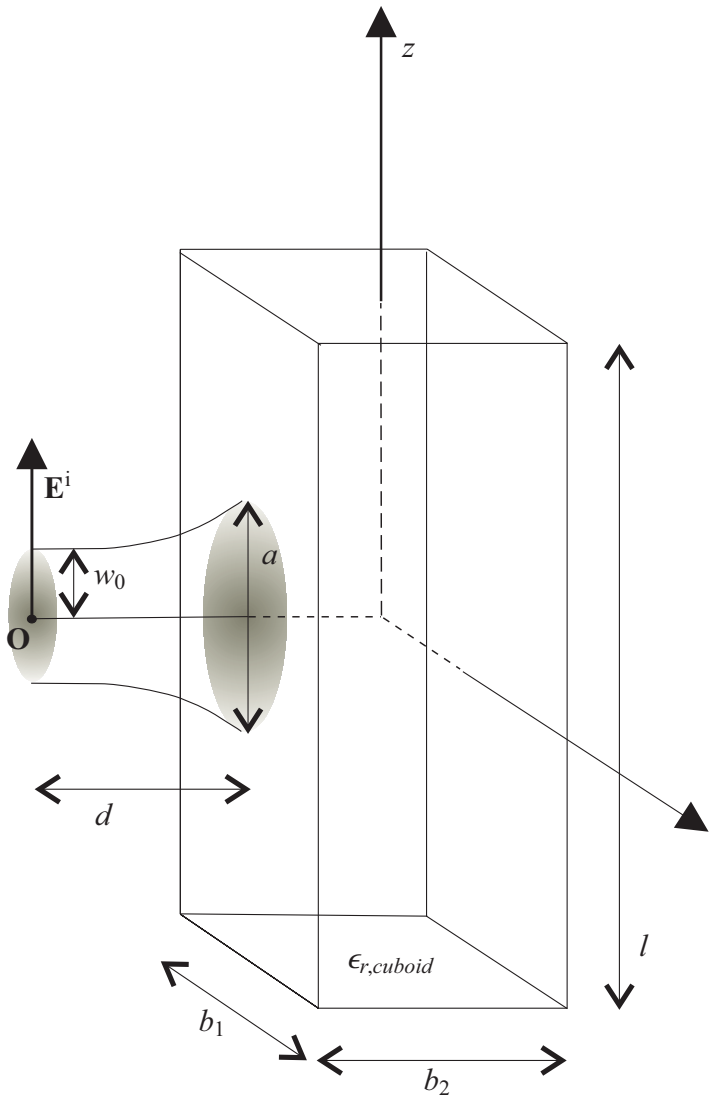

Figure 4.12: Configuration with normally incident 3D Gaussian beam on a finite dielectric cuboid.

on the top and bottom faces of the cuboid are negligible. Figure 4.14 shows the amplitude and phase of the z-component of the scattered fields, computed in the detector points, for different lengths of the cuboid. Fields for $l = 4a$ and $l = 8a$ do not differ from the scattered field for $l = 2a$ and are therefore not shown in the figure. It can be concluded that finite cuboids with length $l \geq 2a$ can be treated as quasi-2D objects when placed in the collimated region of the beam. When the object is placed

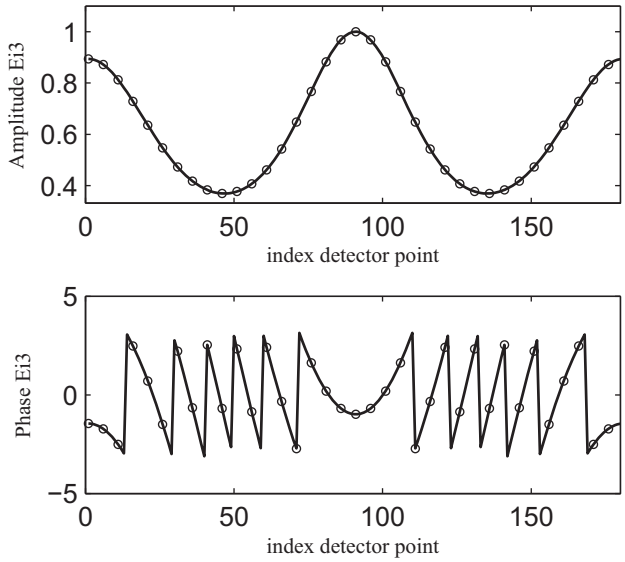

Figure 4.13: Amplitude (top) and phase (bottom) of the z-component of the incident field for the simulations of the (in)finite dielectric cuboid. Solid line: full 3D Gaussian beam, dotted line: 2.5D Gaussian beam with 5 positive discrete k_z values.

outside the collimated region, this minimum length will be larger, since the beam is expanding.

Since fields for longer cuboids do not differ from fields obtained for $l = 2a$, the comparison between the 2.5D and 3D solver results is performed for $l = 2a$. Figure 4.15 displays the amplitude and phase of the z-component of the scattered field for the 2.5D and 3D simulations, showing a very good agreement. The corresponding NRMSE for the scattered field, defined as

$$NRMSE\ (E_z^s) = \frac{\sqrt{\sum_{n=1}^{N} |E_{3D,z}^s(n) - E_{2.5D,z}^s(n)|^2}}{\sqrt{\sum_{n=1}^{N} |E_{2.5D,z}^s(n)|^2}}, \tag{4.4}$$

is only 1.1%. Table 4.7 presents the relevant simulation parameters: total number of unknowns, CPU time, memory usage and the number of CPU-cores used to compute the result. Whereas the 2.5D simulation only lasts 4 minutes and uses 55.6 MB of memory (on 1 CPU-core), the 3D simulation takes 3h 26 min, occupying 5 GB of memory on 14 CPU-cores. The very short simulation time and the small memory consumption, combined with the good precision, clearly proves the advantages of the 2.5D algorithm for simulating quasi-2D objects, illuminated with Gaussian beams.

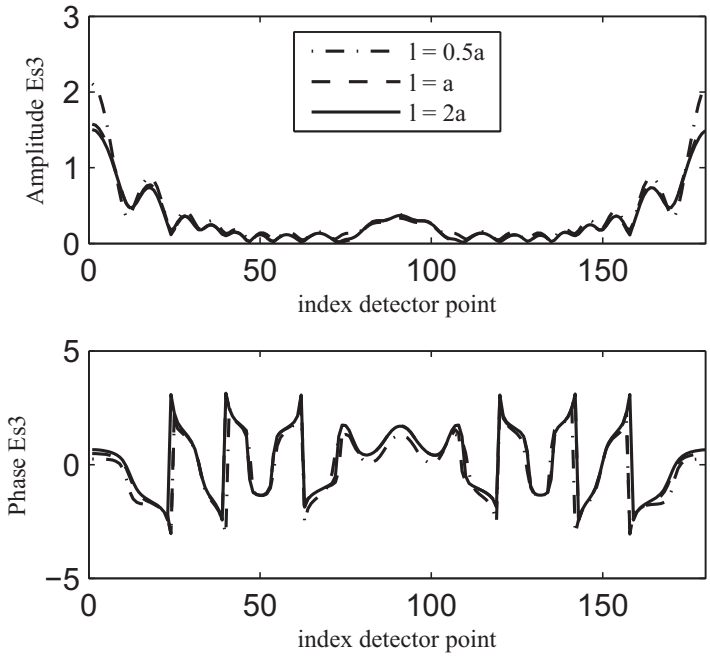

Figure 4.14: Amplitude (top) and phase (bottom) of the z-component of the scattered field as computed with the 3D BIE solver for the finite dielectric cuboid with lengths $l = a/2$, $l = a$ and $l = 2a$.

Table 4.7: Computational effort for the dielectric cuboid simulations.

	length (m)	# unkn.	CPU time	Mem. usage	# CPU-cores
2.5D	$l = \infty$	34 992	3 min 58 s	55.6 MB	1
3D	$l = 2a$	67 500	3h 26 min	5.0 GB	14

4.4. Scattering by objects on a human body

As the presented 2.5D scheme was shown to be accurate in the previous sections, the applicability is demonstrated for a typical configuration: the scattering of millimeter waves on the human body. Due to the relatively high frequency and the large dimensions of the human body compared to the wavelength, such simulations can hardly be done in full 3D. If we assume invariance of the electromagnetic properties of the human body (e.g. the abdomen) over a sufficient distance along the vertical direction, this configuration perfectly fits the quasi-two-dimensional approximation of the 2.5D algorithm. Due to the high number of unknowns, the computational speed is increased by distributing computationally demanding operations (e.g. DFT's) over all four CPU cores of the computing machine by applying multi-threaded commands [5].

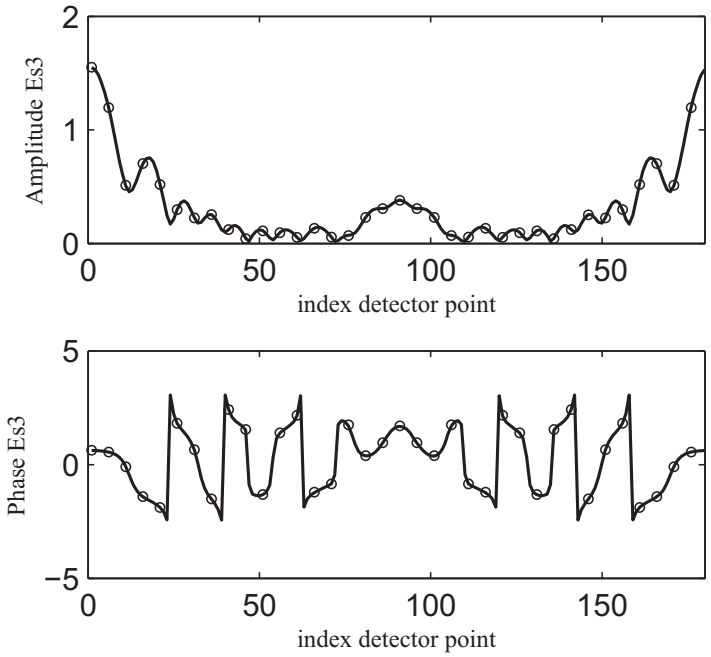

Figure 4.15: Amplitude (top) and phase (bottom) of the z-component of the scattered field as computed for the dielectric cuboid. Solid line: 2.5D simulation with infinite cuboid, dotted line: 3D simulation with finite cuboid: $l = 2a$.

In this section, the scattering from a simple, clothed abdomen model is studied, with and without a hidden quasi-2D (dielectric or conducting) object. Figure 4.16 (a) shows the model cross-section, consisting of the object underneath a layer of clothing on an elliptically shaped abdomen. The $z-$axis is chosen vertically for a standing person. The orthogonally incident 3D TM-polarized Gaussian beam has a frequency of 100 GHz and a waist $w_0 = 8$ mm. Its center is chosen at the exterior surface of the skin. Since the size of the illuminated body region is only a few cm in the z-direction, assuming invariance of the electromagnetic properties of the abdomen along this direction (i.e. the quasi-2D assumption) is a valid approach. The heterogeneity of the inner body tissues does not affect the scattering, due to the very limited penetration of mm-waves into the human body [6]. This limited penetration, as well as the finiteness of the illuminated region in the x-direction, furthermore allow to consider a strongly reduced computational domain, containing only a part of the abdomen as depicted in Fig. 4.16 (b). In this restricted domain, four layers can be distinguished: clothing, air, dry skin and fat. The thickness d and permittivity ε_r for each layer are chosen as follows: $d_{clothing} = 2$ mm and $\varepsilon_{r,clothing} = 4.0 + i\ 0.1$ for clothing [6], $d_{air} = 3$ mm and $\varepsilon_{r,air} = 1$ for air, $d_{skin} = 2$ mm and $\varepsilon_{r,skin} = 5.60 + i\ 7.09$ for dry skin [7] and $d_{fat} = 10$ mm and $\varepsilon_{r,fat} = 2.89 + i\ 0.64$ for fat [7]. A rectangular object with width 15 mm,

thickness 2.5mm and relative permittivity ε_{obj} is placed between clothing and skin. If such an object is to be detected using mm-waves, its introduction should lead to a significant change in the total field detected at the outside.

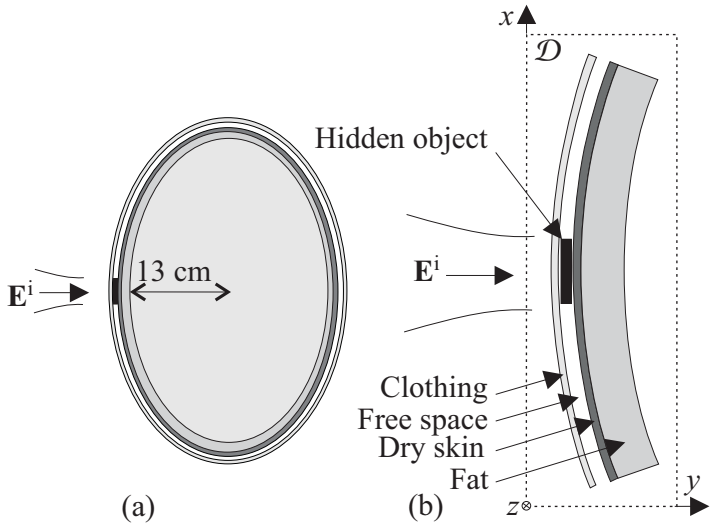

Figure 4.16: Configuration for the abdomen under 3D Gaussian beam illumination.

In all simulations the computational domain has dimensions of 110 mm in the x-direction and 40 mm in the y-direction. It is discretized into 1120×416 cells with size $\Delta = 0.1$ mm, yielding a total of 1 397 760 unknowns. The BICGS tolerance is set to 10^{-3}. The incident field is computed using the vectorial complex-source beam formula (3.14) for five different k_z values, see Table 4.8.

Table 4.8: Computational effort for the abdomen simulations.

	no object	conducting object	dielectric object
k_z/k_0	# it.	# it.	# it.
0.0122	535	882	548
0.0601	532	868	531
0.1302	529	919	605
0.2004	299	443	303
0.2482	340	398	323
CPU time	1h 43min	2h 42min	1h 47min

As mentioned in Chapter 2, a marching-on-in-k_z technique [8] is applied to reduce the number of BICGS iterations. For the first three k_z values the initial guess for the electric flux density is a zero field, whereas the initial guess for the fourth and fifth k_z

value is a combination of three previous solutions. This is clearly visible from Table 4.8: the number of BICGS iterations drop significantly from the fourth k_z value on. The left part of Fig. 4.17 shows the total field amplitude when no hidden object is present. Since the black color corresponds to a zero field amplitude, it is clear that there is no significant field penetration further than the skin and that there is no diffraction at the truncated edges. This proves that the selected part (Fig. 4.16 (b)) from the abdomen cross-section is chosen large enough. On the contrary, the clothing is almost transparent for the beam, which is mostly reflected by the skin towards the incident direction. Note that for illustrative purposes the size of the computational domain in the x-direction was in fact chosen larger than strictly necessary (see Fig. 4.17).

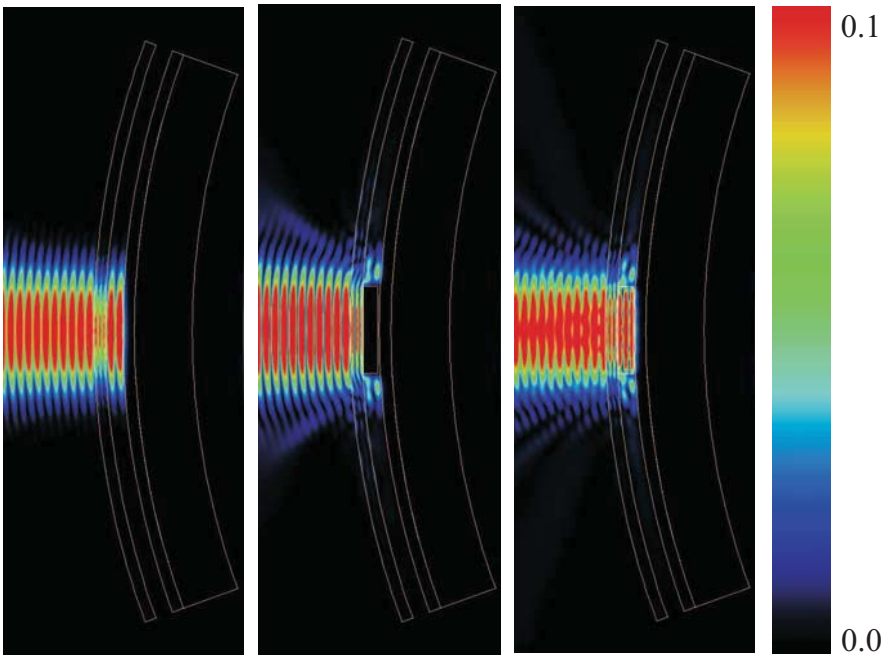

Figure 4.17: Total field amplitude for the simulation of the abdomen. Left: no hidden object, middle: hidden conducting object and right: hidden dielectric object.

Next, a strongly conducting object with $\varepsilon_{obj} = 1 + i100$, representing a small knife-like object, is inserted. The resulting total field amplitude is presented in the middle part of Fig. 4.17 and clearly reveals the scattering introduced by this object. Finally, a dielectric object with $\varepsilon_{obj} = 2$, representing certain explosives (for example $\varepsilon_{TNT} = 2.7$, $\varepsilon_{RDX} = 3.14$, $\varepsilon_{Semtex-H} = 3$ [9]) is considered. The scattering from this object is again clearly visible within and outside the main beam, as appears from the right part of Fig. 4.17. From Table 4.8 it follows that the simulation for the conducting object is computationally most expensive. The presence of the hidden objects is

furthermore illustrated in Fig. 4.18, which shows the amplitude of the difference between the total fields with and without hidden object (i.e. the change in the total field due to the insertion of the object) on a line left of the abdomen (19.7 mm left of the exterior surface of the skin) for the three different simulations. Although it is generally assumed that a dielectric object with a low permittivity will be more difficult to detect than a conducting object, this is contradicted by the field plots in Fig. 4.19, which, for each hidden object, show the amplitude of the difference between the total fields with and without object, revealing that both dielectric and conductive objects are clearly "visible".

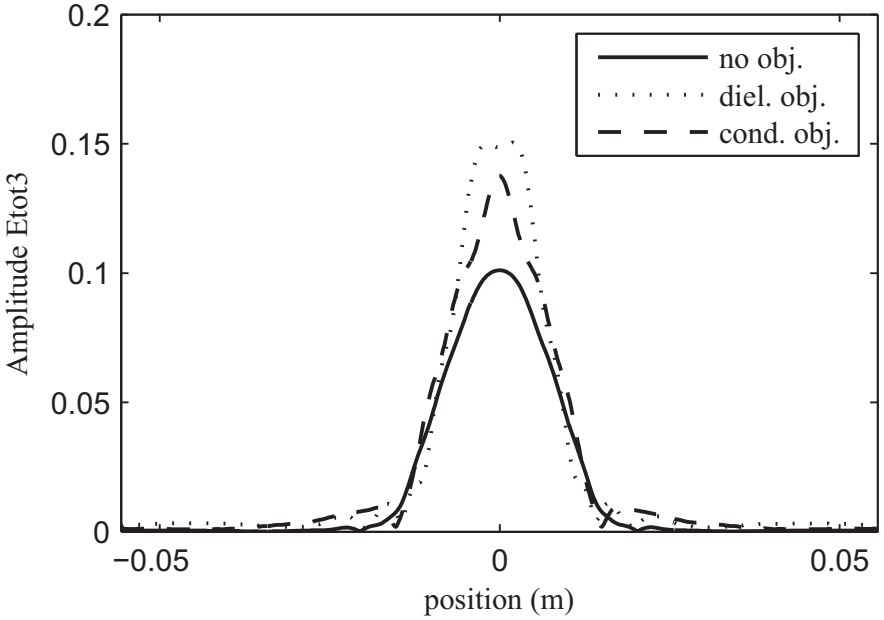

Figure 4.18: Total field amplitude for the simulation of the abdomen, on a line 19.7mm left to the skin surface. Solid line: no hidden object, dashed line: hidden conducting object, dotted line: hidden dielectric object.

4.5. Conclusion

In this chapter, the proposed 2.5D forward solver has been tested extensively, both for plane wave and Gaussian beam illumination. For plane wave illumination, simulated scattered fields have been compared to analytic solutions for: (i) a homogeneous cylinder illuminated by a purely two-dimensional TM-polarized orthogonally incident field, (ii) a homogeneous cylinder illuminated by a purely two-dimensional TE-polarized orthogonally incident field, (iii) a homogeneous cylinder illuminated by a

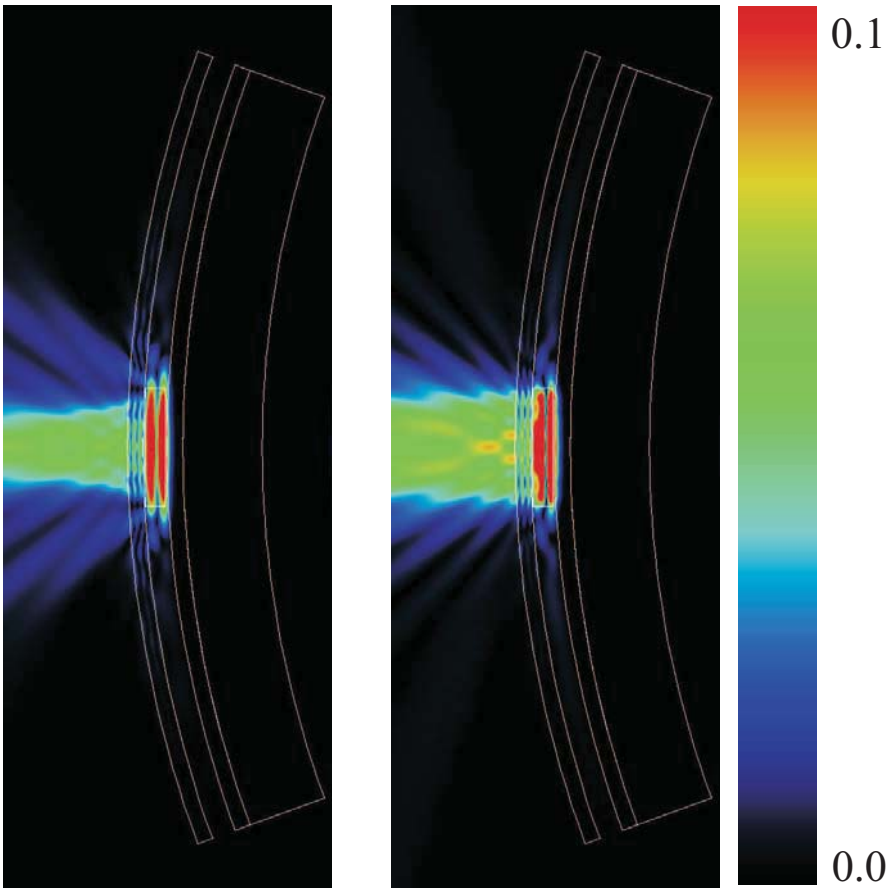

Figure 4.19: Amplitude of the difference between the total field with hidden object and the total field without hidden object for the simulation of the abdomen. Left: hidden conducting object, right: hidden dielectric object.

three-dimensional obliquely incident TM-polarized incident field and (iv) a piecewise-homogeneous multilayered cylinder illuminated by a three-dimensional obliquely incident TM-polarized incident field. For all configurations, the comparison to the corresponding analytic solution yielded excellent results.

Moreover, simulated fields have also been compared to scattered fields, obtained from fully three-dimensional forward solvers. The comparison to a 3D VIE-based forward solver with plane wave illumination illustrated the advantage of the 2.5D approach when simulating long dielectric cylinders: the 2.5 solver needs far less unknowns and much shorter computation times. A 3D BIE-based solver was used to study the 2.5D assumption under Gaussian beam illumination. Increasing the length

of a homogeneous dielectric cuboid has shown that the restriction to *infinitely long* cylinders in the 2.5D solver can be weakened to *long enough* cylinders in case of a Gaussian beam illumination. The scattered fields from the 2.5D and 3D solvers agreed perfectly.

As an illustration of the imaging applications for which this forward solver is intended, the scattering from the human body has been simulated. This test case considers a Gaussian beam illumination, orthogonally incident on a simplified model of a clothed human torso. A small metallic or dielectric object was hidden underneath the layer of clothing and the effect on the scattered fields was compared. The hidden object clearly influenced the scattered fields.

Bibliography

[1] P. Lewyllie, A. Franchois, C. Eyraud, and J.M. Geffrin, "Testing a 3D BCGS-FFT solver against experimental data," in *Proceedings of the 9th International Conference on Electromagnetics in Advanced Applications (ICEAA 2005)*, Torino, Italy, Sept. 2005, pp. 421–424.

[2] J. Peeters, J. Fostier, F. Olyslager, and D. De Zutter, "New parallel approaches for fast multipole solvers," in *Proceedings of the second European Conference on Antennas and Propagation*, Edinburgh, UK, 2007, pp. 1–5.

[3] Z. Peng and A. Tijhuis, "Transient scattering by a lossy dielectric cylinder: Marching-on-in-frequency approach," *Journal of Electromagnetic Waves and Applications*, vol. 7, no. 5, pp. 739–763, 1993.

[4] I. Lindell, *Advanced Field Theory*. Helsinki, Finland: Helsinki University of Technology, 2000.

[5] D. Butenhof, *Programming with POSIX(R) Threads*. Addison-Wesley Professional Computing Series, 1997.

[6] O. Gandhi and A. Riazi, "Absorption of millimeter waves by human beings and its biological implications," *IEEE Transactions on Microwave Theory and Techniques*, vol. 34, no. 2, pp. 228–235, Feb. 1986.

[7] Institute for Applied Physics. Italian National research Council. [Online]. Available: http://niremf.ifac.cnr.it/tissprop/htmlclie/htmlclie.htm

[8] A. Tijhuis, M. van Beurden, and P. Zwamborn, "Iterative solution of field problems with a varying physical parameter," *Elektrik, Turkish Journal of Electrical Engineering & Computer Sciences*, vol. 10, no. 2, pp. 163–183, 2002.

[9] Committee on Assessment of Security Technologies for Transportation, National Research Council, *Assessment of Millimeter-Wave and Terahertz Technology for Detection and Identification of Concealed Explosives and Weapons*. The National Academies Press, 2007.

CHAPTER 5

Comparison with experimental data

5.1. Introduction

When an inverse solver is used in practical applications, the data are real-life measurements. Therefore, it is useful to compare also forward solver results to experimentally measured scattered fields. However, different effects affect the comparison between simulated and scattered fields.
In an inverse problem, the position of the object is not known in advance, whereas in the forward problem, knowledge of the position and orientation of the scatterer is critical to achieve a good agreement between simulated and measured scattered field. The higher the frequency, the more these positioning errors make the comparison more difficult. This is even more the case, when not only the amplitude, but also the phase of the fields are compared.
Another major issue is the characterization of the incident field. If there is no proper characterization of the incident field, it makes no sense trying to invert the measured data. In an experimental environment, an incident field can not be a perfect plane wave. However, cylindrical and spherical waves emitted at a large distance from the scatterer can be approximated by a plane wave at the scatterer's position. Moreover, the distance between antenna and target has to be large enough to neglect the antenna to target coupling. For a Gaussian beam illumination, it is essential to know the beam waist radius and the location of the beam waist plane to characterize its propagating behavior, especially when the beam does not illuminate the target completely. It seems hard to extract these beam parameters from an incident field in an experimental set-up. Furthermore, the frequency itself also has an effect. The higher the frequency, the more complicated the measurement and hence the more expensive the necessary measurement facilities.

Another important issue when simulation results are compared to measurements, is the calibration, in which both simulated and measured incident fields are given the same power and reference plane by scaling one of them, as well as the corresponding scattered field, by a complex scaling factor.
In this chapter, two types of experiments are presented to compare the 2.5D forward solver with real measurement data. The first experiment was conducted in the bistatic polarimetric measurement facility of Institut Fresnel [1] and consists in measuring the scattered field in amplitude and phase of a long inhomogeneous dielectric cylinder under oblique quasi-plane wave illumination for microwave frequencies between 1 and 18 GHz. The quality of the data provided by this facility is much appreciated by the electromagnetic inversion community [2, 3, 4, 5].
The second experiment was performed with a millimeter wave measurement setup at the Vrije Universiteit Brussel (VUB) and yields measurements of the field amplitude at 94 GHz for the configuration of a 3D Gaussian beam normally incident on a homogenous teflon cylinder. In the time-span of this PhD work, this millimeter wave set-up only allowed for field amplitude measurements. This is why the comparison with amplitude *and* phase measurements is presented in the microwave regime for oblique plane wave incidences.
Results of both experiments are presented in [6, 7].

5.2. Plane wave scattering by an inhomogeneous cylinder

5.2.1 Measurement set-up at Institut Fresnel

Figure 5.1 shows the bistatic microwave measurement set-up in the large faradized anechoic chamber of Institut Fresnel in Marseille [1]. This facility operates in a continuous wave stepped frequency mode in the range 45 MHz - 26.5 GHz. A transmitting antenna is moved on a vertical arch with radius 1.796 m over 7 elevation angles $\theta_n^{\mathrm{i}}, n = 1...7$, in steps of 10° starting from $\theta_1^{\mathrm{i}} = 0^\circ$ with respect to the horizontal xy-plane (see Fig. 5.2). The field generated by the transmitting antenna can locally (i.e. at the location of the object) be assumed to be a plane wave, although it has a limited spatial extension. In this way, the incident field approximates a TM polarized plane wave propagating along $\mathbf{u}_n^{\mathrm{i}}$ (with the electrical field in a vertical plane through the z-axis, see Fig. 5.2, and with the magnetic field in the horizontal plane). For each transmitting position, a receiving antenna is moved on a horizontal arch with radius 1.795 m from -130° to $+130^\circ$ in steps of 1°. The 0° position corresponds to the location opposite to the vertical transmitter arch. The z-component of the field is measured in amplitude and phase. The scattered field is obtained as the difference between the measured fields with and without the cylinder for frequencies between 1 to 18 GHz, in steps of 1 GHz. The 1.5 m long scattering object is placed in the center of both source and receiver arches, see Fig. 5.2. The white cylinder in Fig. 5.1 that supports

the scattering target is made of PA6 tube (with a diameter of 0.1 m and $\varepsilon_r = 2.6$) and allows an accurate positioning of rather heavy objects [1].

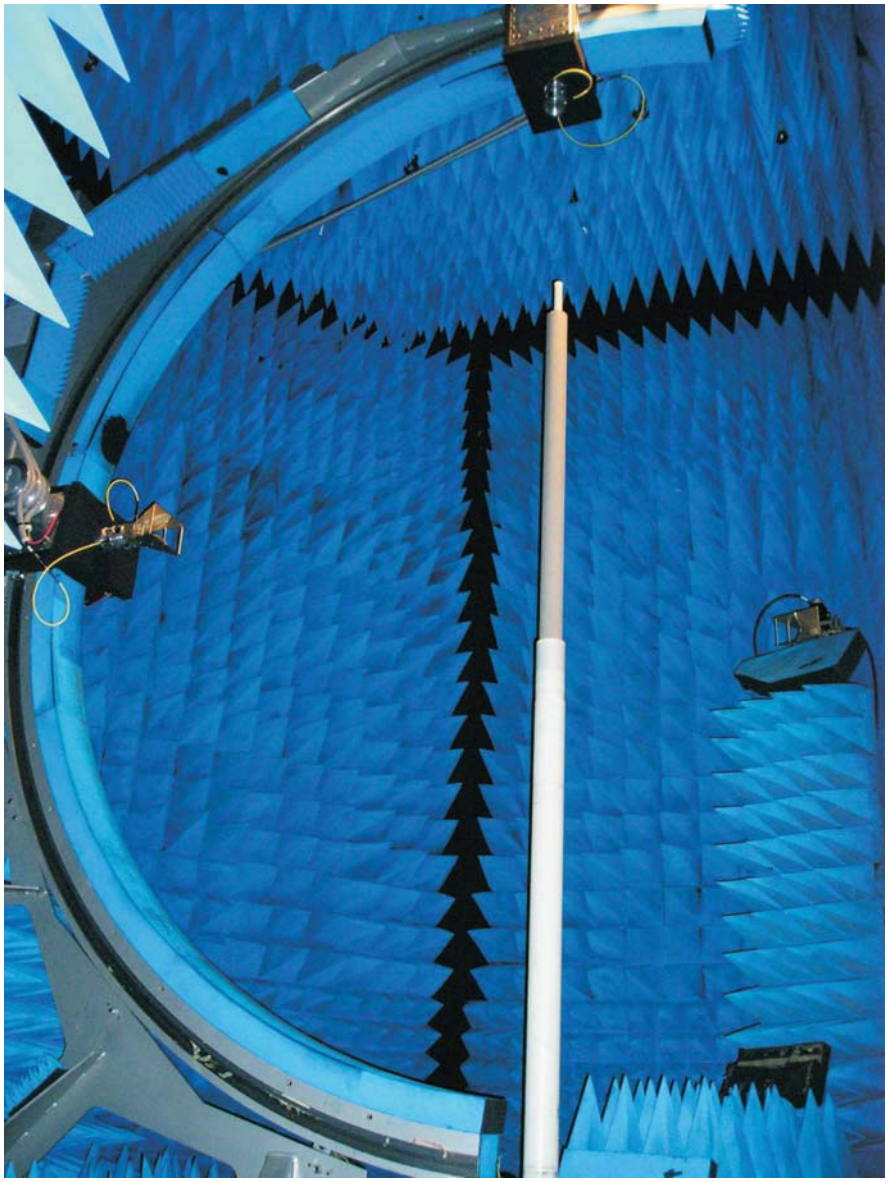

Figure 5.1: Microwave measurement set-up at Institut Fresnel: transmitting antenna (left), scattering cylinder (middle) and receiving antenna (right).

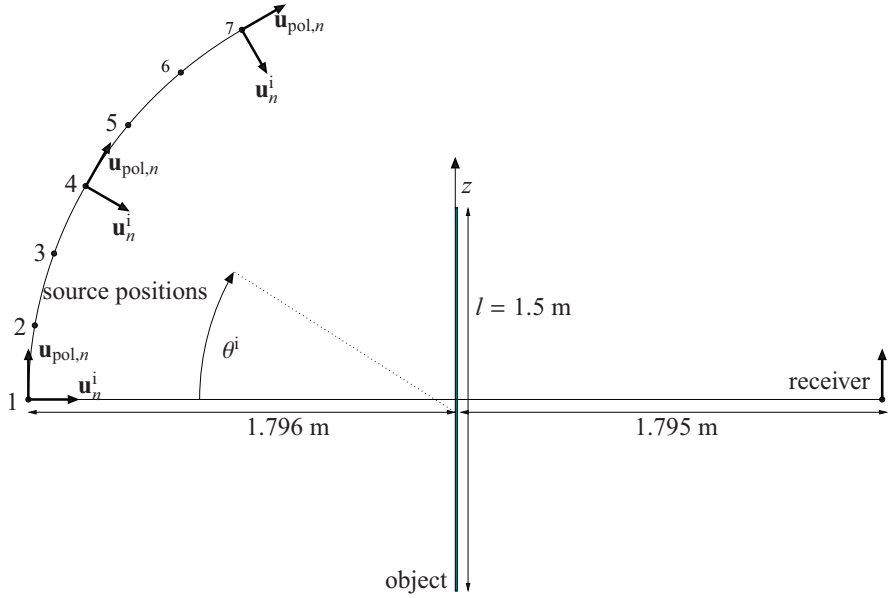

Figure 5.2: Antenna configurations for the microwave plane wave experiments.

5.2.2 Measured target at Institut Fresnel

The Institut Fresnel has different dielectric targets that are used to validate two-dimensional imaging techniques. These dielectric cylinders (with names as *FoamDielInt*, *FoamDielExt* and *TwinDiel* [1]) are 1.5 m long, which is long enough for use in purely two-dimensional forward and inverse solvers [1]. However, for this PhD work, the target is obliquely illuminated with plane waves. It can be expected that for increasing elevation angles (from orthogonal incidence to more and more oblique illumination) the upper and lower ends of the targets will contribute more to the scattered field on the receiver and hence will make the agreement worse.
In this chapter, the target under study is the inhomogeneous *FoamDielInt* target. This dielectric cylinder consists of a berylon plastic circular cylinder with radius $r_a = 15.5$ mm and relative permittivity $\varepsilon_{r,a} = 3 \pm 0.3$ which is off-centered enclosed in a foam (SAITEC SBF 300) circular cylinder with $r_b = 40$ mm and $\varepsilon_{r,b} = 1.45 \pm 0.15$ (see Fig. 5.3). The distance d between the centers of both cylinders is $d = 5$ mm.
In the 2.5D simulations, the relative permittivities for both constituents are set to $\varepsilon_{r,a} = 3$ and $\varepsilon_{r,b} = 1.45$.

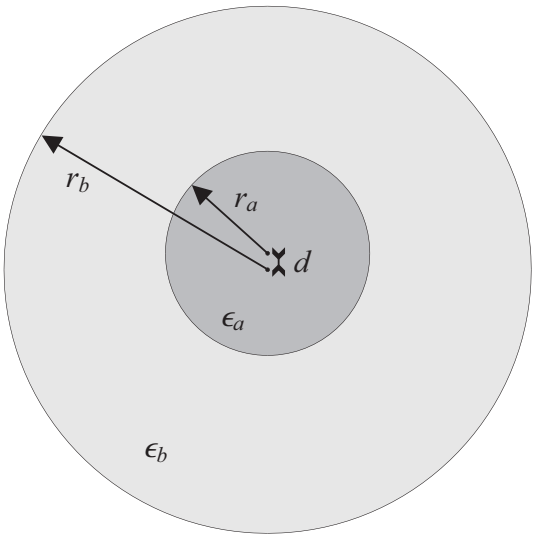

Figure 5.3: Plane wave scattering configuration: Cross-section of the piecewise homogeneous dielectric cylinder FoamDielInt.

5.2.3 Comparison of incident and scattered fields

Since the measured object is slightly misaligned, an optimization for its real position is made by trial and error by performing multiple simulations. Results shown in the following are for this optimized position of the cylinder. Furthermore, to compare measurements and simulations, a calibration procedure is applied. The simulated fields are multiplied by a complex scaling factor α, which is determined by minimizing the least-squares difference between the (scaled) simulated incident field and the measured one. If the simulated field values are collected in the data vector $\mathbf{e}^{\text{sim}}$ and the measured field values are collected in $\mathbf{e}^{\text{meas}}$, the least-squares difference between both is defined as:

$$||\alpha\, \mathbf{e}^{\text{sim}} - \mathbf{e}^{\text{meas}}||^2 = (\alpha\, \mathbf{e}^{\text{sim}} - \mathbf{e}^{\text{meas}})^H (\alpha\, \mathbf{e}^{\text{sim}} - \mathbf{e}^{\text{meas}}). \tag{5.1}$$

Minimizing the function with respect to the complex scaling factor α yields an adequate value for the scaling parameter:

$$\alpha = \frac{\mathbf{e}^{\text{sim}\,H}\mathbf{e}^{\text{meas}}}{\mathbf{e}^{\text{sim}\,H}\mathbf{e}^{\text{sim}}}. \tag{5.2}$$

Figure. 5.4 and Fig. 5.5 show the simulated and measured z-components of the scattered field, for the elevation angles $\theta_1^{\text{i}} = 0^o$ and $\theta_3^{\text{i}} = 20^o$ and for frequencies 3 GHz and 8 GHz. Figure 5.4(a) and Fig. 5.5(a) show that for an elevation angle $\theta_1^{\text{i}} = 0^o$ (normally incident field), there is a very good agreement in amplitude *and*

phase between the measured and simulated scattered fields. For an elevation angle $\theta_3^i = 20^o$, Fig. 5.4(b) and Fig. 5.5(b) again show a good agreement in amplitude, at both frequencies. At 3 GHz, the phases show a very good agreement whereas at 8 GHz, the phases are somewhat different for the outer negative detector angles.

For large elevation angles, see Fig. 5.6 and Fig. 5.7, deviations between the simulated and measured scattered field occur due to two different effects. First, there is the different nature of the measured and simulated incident field: a spatially confined plane wave approximation (measurements) against an infinite plane wave (simulations). Second, there are diffraction effects at the end faces of the cylinder, which are not accounted for by the 2.5D simulation tool but are present in the measurements. Since, for larger elevation angles, the top edge of the finite cylinder becomes more and more illuminated, the measured configuration no longer fits the 2.5D assumption. Table 5.1 presents the total number of unknowns and CPU-time for each simulation (these computations are all performed on one CPU-core).

Table 5.1: Computational effort for the microwave plane wave simulations.

frequency	elevation angle	# unknowns	CPU time
3 GHz	$\theta^i = 0^o$	4 563	5 s
3 GHz	$\theta^i = 20^o$	4 563	5 s
8 GHz	$\theta^i = 0^o$	24 843	31 s
8 GHz	$\theta^i = 20^o$	24 843	31 s

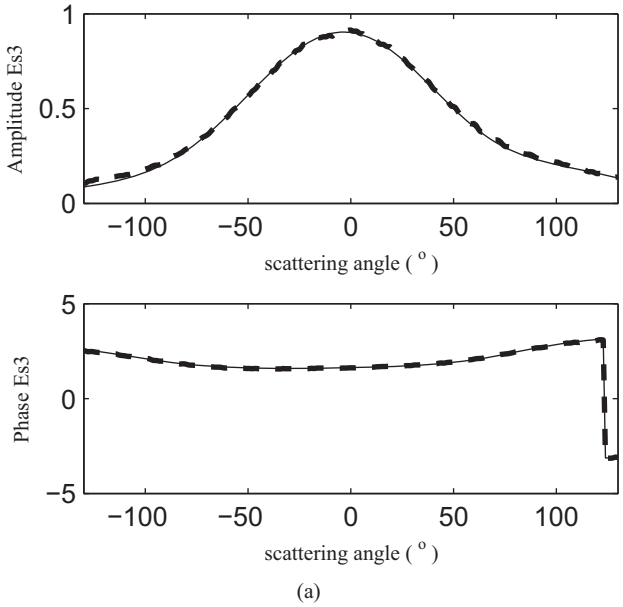

(a)

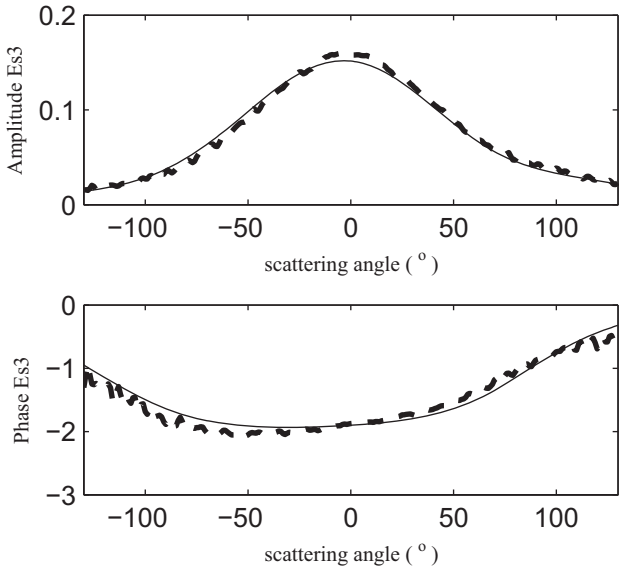

(b)

Figure 5.4: Amplitude and phase of the z-component of the scattered field from the FoamDielInt target under plane wave illumination at 3 GHz: (a) with elevation angle $\theta^{\mathrm{i}} = 0^o$, (b) with elevation angle $\theta^{\mathrm{i}} = 20^o$. Solid line: 2.5D simulation, dotted line: measurement.

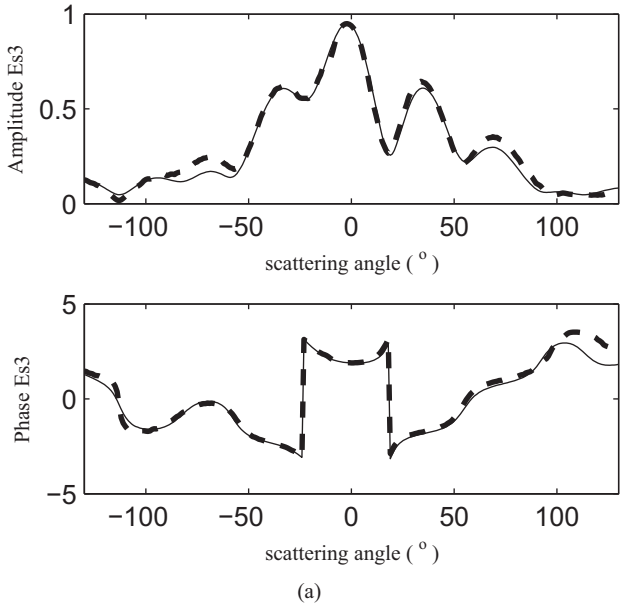

(a)

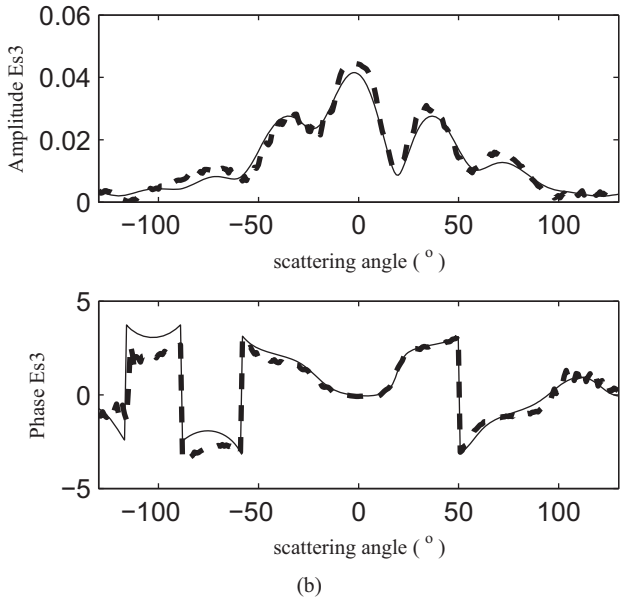

(b)

Figure 5.5: Amplitude and phase of the z-component of the scattered field from the FoamDielInt target under plane wave illumination at 8 GHz: (a) with elevation angle $\theta^{\mathrm{i}} = 0^o$, (b) with elevation angle $\theta^{\mathrm{i}} = 20^o$. Solid line: 2.5D simulation, dotted line: measurement.

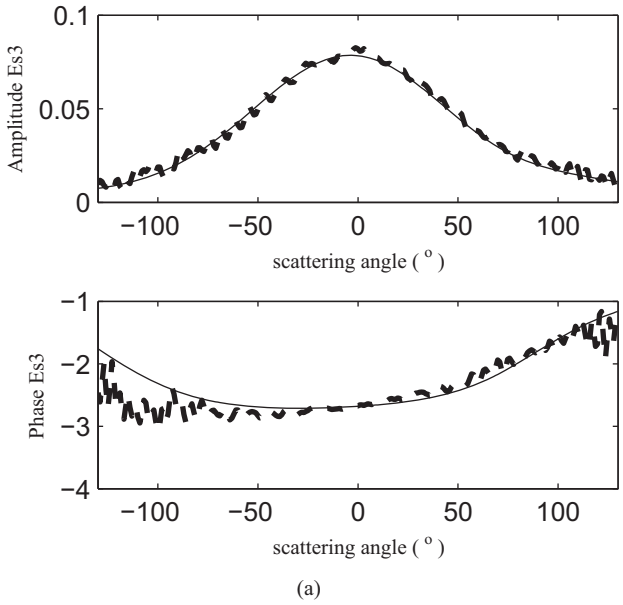

(a)

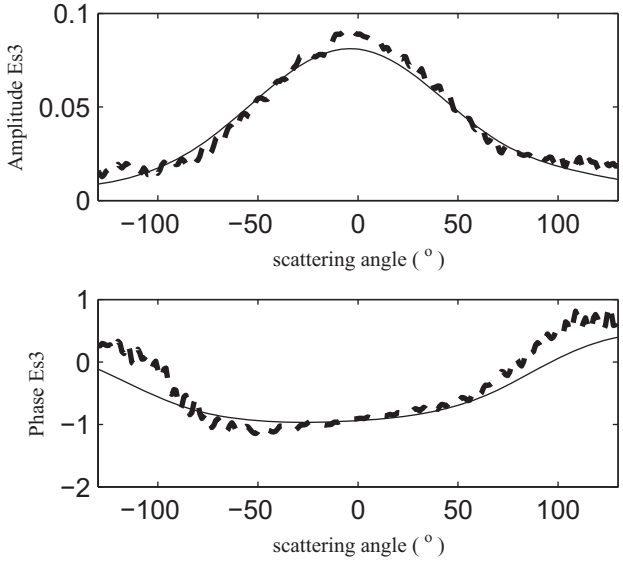

(b)

Figure 5.6: Amplitude and phase of the z-component of the scattered field from the FoamDielInt target under plane wave illumination at 3 GHz: (a) with elevation angle $\theta^{\mathrm{i}} = 30^o$, (b) with elevation angle $\theta^{\mathrm{i}} = 40^o$. Solid line: 2.5D simulation, dotted line: measurement.

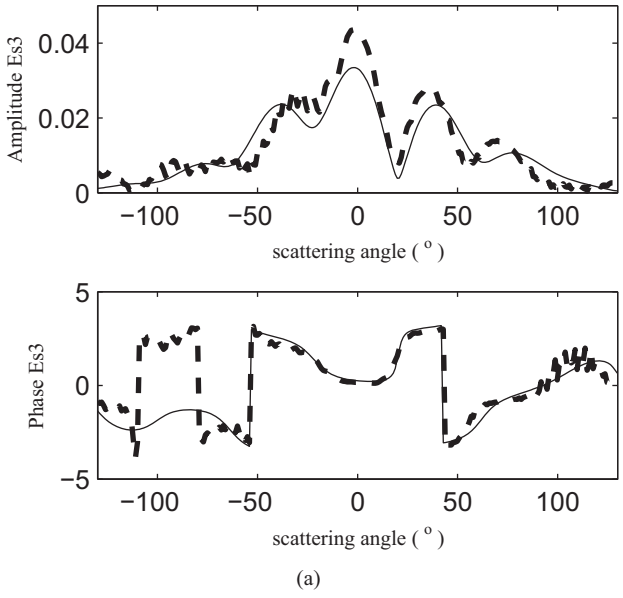

(a)

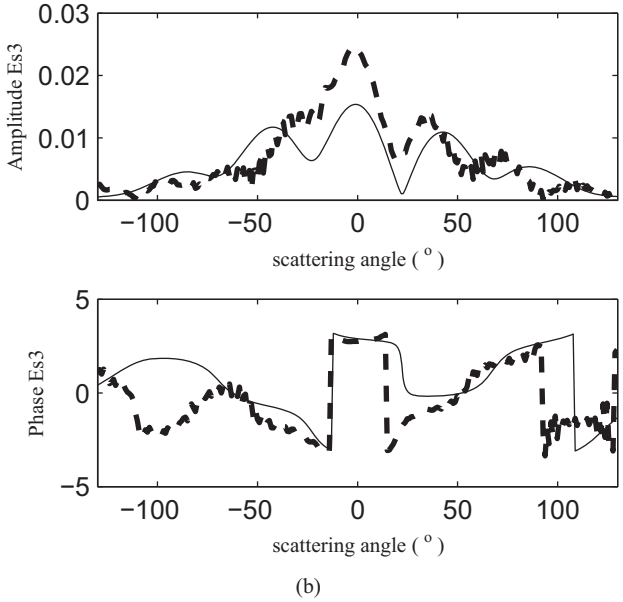

(b)

Figure 5.7: Amplitude and phase of the z-component of the scattered field from the FoamDielInt target under plane wave illumination at 8 GHz: (a) with elevation angle $\theta^i = 30^o$, (b) with elevation angle $\theta^i = 40^o$. Solid line: 2.5D simulation, dotted line: measurement.

5.3. Gaussian beam scattering by a homogeneous cylinder

5.3.1 Measurement set-up at the Vrije Universiteit Brussel

A picture and a sketch of the millimeter wave experimental set-up at the department LAMI-ETRO at the Vrije Universiteit Brussel (VUB) is shown in Fig. 5.8 and Fig. 5.9, respectively. A W-band (75 GHz to 110 GHz) Backward Wave Oscillator (BWO) emits a 94 GHz wave, which is focussed into a TM polarized (i. e. electric field directed along the z-axis) Gaussian beam with a beam waist $w_0 = 8.5 \pm 0.5$ mm by a lens-capped corrugated horn antenna.

At the detecting side, the receiving antenna is an open WR10 waveguide probe coupled to a zero biased Schottky diode detector. The detector has a sensitivity of 550 mV/mW and measures the relative power of the field, which is related to its amplitude. The probe and detector are mounted together on a two-axis scanner, which is able to move both parallel and perpendicular to the beam axis in a horizontal plane.

In this way, three different horizontal detector lines are obtained at $d_1 = 4.5$ cm, $d_2 = 6.5$ cm and $d_3 = 8.5$ cm from the cylinder's center (Fig. 5.10). Each line consists of $N = 81$, 1 mm spaced, detector points.

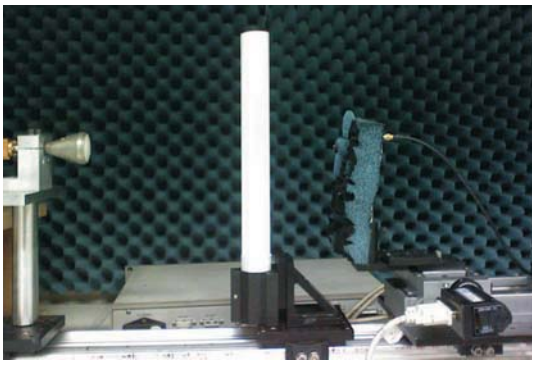

Figure 5.8: Photo of the Gaussian beam measurement set-up at 94 GHz.

5.3.2 Measured target at the Vrije Universiteit Brussel

The scatterer is a 30 cm long homogeneous teflon cylinder with radius $r = 1.75$ cm and relative permittivity $\varepsilon_r = 2.06 + 0.0015j$, positioned along the beam axis at $d_0 = 10.5 \pm 0.9$ cm from the source (see Fig. 5.10). Only a small central part of the cylinder is illuminated by the incident Gaussian beam (the diameter of the illuminated spot is approximately 3 cm) such that the cylinder can be treated as infinitely long. In the 2.5D simulation, the distance and the beam waist radius are chosen as $d_0 = 10.5$ cm

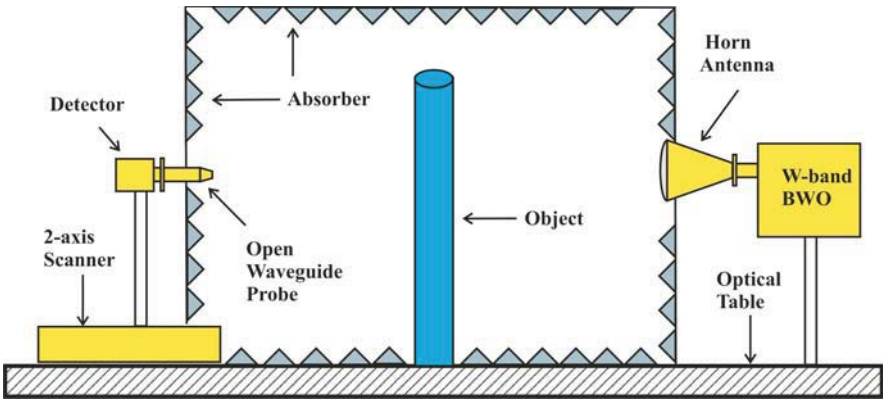

Figure 5.9: Schematic of the Gaussian beam measurement set-up at 94 GHz.

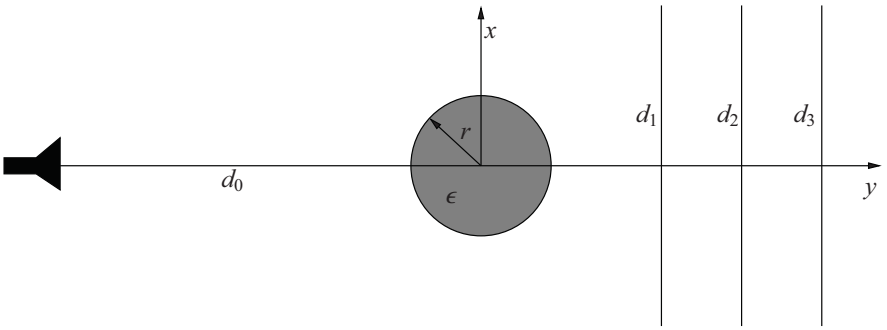

Figure 5.10: Configuration of the 94 GHz Gaussian beam scattering experiment.

and $w_0 = 8.5$ mm and the permittivity is set to $\varepsilon_r = 2.06 + 0.0015\,j$. The simulation needs 338 688 unknowns and takes 39 min 55 s on four CPU-cores.

5.3.3 Comparison of incident and scattered fields

A similar calibration as for the microwave experiment (5.2) is applied. However, only the field amplitude is measured. Therefore, the z-components of the simulated fields are multiplied with a *real* scaling factor α, given by

$$\alpha = \frac{\mathbf{e}^{\text{sim } T}\mathbf{e}^{\text{meas}}}{\mathbf{e}^{\text{sim } T}\mathbf{e}^{\text{sim}}}. \tag{5.3}$$

Here, the data vectors $\mathbf{e}^{\text{sim}}$ and $\mathbf{e}^{\text{meas}}$ contain the simulated and measured incident field amplitudes respectively.

Figure 5.11 and Fig. 5.12 show the amplitude of the incident and total electric fields on the three different detector lines, respectively. The simulated vectorial Gaussian beam agrees very well with the measured incident field. The corresponding simulated and measured total fields are also very similar. The remaining small differences are due to the uncertainty on the beam waist ($w_0 = 8.5 \pm 0.5$ mm) and the position of the source ($d_0 = 10.5 \pm 0.9$ cm).

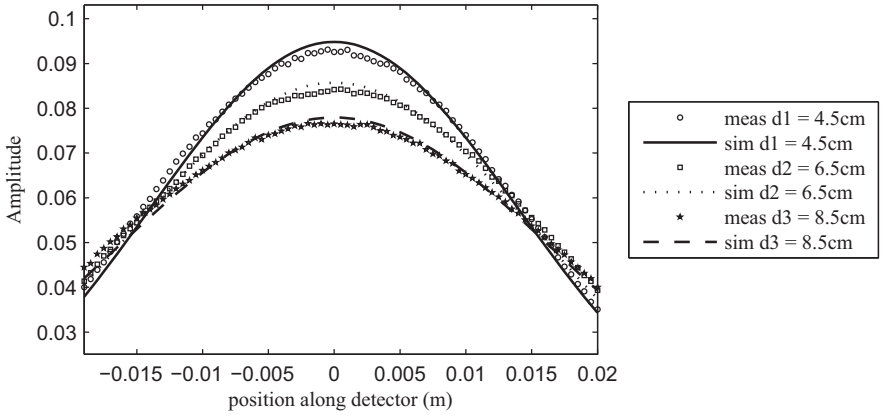

Figure 5.11: Amplitude of the z-component of the measured and simulated incident field, corresponding to the 94 GHz incident Gaussian beam for the configuration of Fig. 5.10.

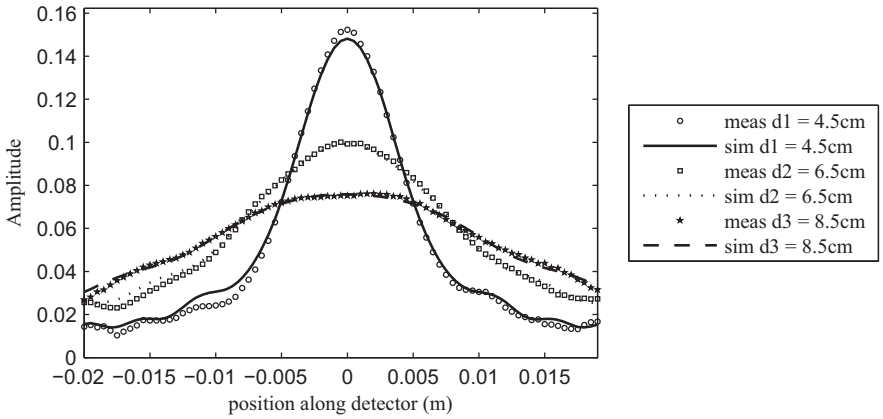

Figure 5.12: Amplitude of the z-component of the measured and simulated total field at 94 GHz, for the configuration of Fig. 5.10.

5.4. Conclusion

In this chapter, we have studied the correspondence between simulated scattered fields on the one hand and experimentally measured scattered fields on the other hand. At the LAMI-ETRO lab (VUB), amplitude-only scattering measurements are performed at 94 GHz for homogeneous teflon cylinders. At this high frequency, the incident field is a three-dimensional Gaussian beam. Although the beam could not be characterized precisely (there is some uncertainty on the beam waist location and beam waist radius), the simulated and measured fields agree quite well. No amplitude *and* phase measurements are yet available to us in the millimeter wave range.

A completely vectorial comparison to experimental fields is performed in the microwave range. The Institut Fresnel in Marseille is well known for high quality scattering experiments [1,2,5] and provided measured scattered fields from an inhomogeneous dielectric cylinder under oblique plane wave illumination at different frequencies. Also here, simulated and measured scattered fields are in good agreement.

Bibliography

[1] J. Geffrin, P. Sabouroux, and C. Eyraud, "Free space experimental scattering database continuation: experimental set-up and measurement precision," *Inverse Problems*, vol. 21, no. 6, pp. S117–S130, 2005.

[2] K. Belkebir and M. Saillard, "Testing inversion algorithms against experimental data: Inhomogeneous targets," *Inverse Problems*, vol. 21, no. 6, pp. S1–S3, 2005.

[3] J. De Zaeytijd and A. Franchois, "3D quantitative microwave imaging from measured data with multiplicative smoothing and value picking regularization," *Inverse Problems*, vol. 25, no. 2, p. 024004, Feb. 2009.

[4] J. De Zaeytijd, A. Franchois, C. Eyraud, and J. Geffrin, "Full-wave three-dimensional microwave imaging with a regularized gauss-newton method – theory and experiment," *IEEE Transactions on Antennas and Propagation*, vol. 55, no. 11, pp. 3279–3292, Nov. 2007.

[5] J. Geffrin and P. Sabouroux, "Continuing with the fresnel database: experimental set-up and improvements in 3D scattering measurements," *Inverse Problems*, vol. 25, no. 2, p. 024001, 2009.

[6] S. Van den Bulcke, L. Zhang, A. Franchois, J. Geffrin, and J. Stiens, "Plane wave and gaussian beam scattering by long dielectric cylinders: 2.5D simulations versus measurements," *International Journal of Infrared and Millimeter Waves*, vol. 29, no. 11, pp. 1038–1047, Nov. 2008.

[7] S. Van den Bulcke and A. Franchois, "Validation of a full-wave 2.5D VIE solver with millimeter-wave gaussian beam and microwave experiments," in *Proceedings of the URSI Forum*, Brussels, Belgium, May 2008, p. 41.

Part II

The Inverse problem

CHAPTER 6

The quantitative inverse scattering problem

6.1. Introduction

This chapter deals with the quantitative electromagnetic inverse scattering problem. The goal is to characterize an unknown object by reconstructing its complex permittivity profile from measured scattered fields. Therefore, the unknown object is sequentially illuminated with known, time-harmonic, electromagnetic fields from different directions and often also with different polarizations. This results in an active imaging technique.

Many different techniques to solve the inverse scattering problem have been developed for microwave imaging applications [1, 2, 3, 4, 5, 6, 7, 8, 9]. In this PhD, we apply this knowledge to the millimeter wave frequency range. We have extended the existing inverse scattering techniques in different ways. First, apart from the generally used plane wave illumination, also a Gaussian beam illumination is considered. Second, we have developed a new generally applicable regularization technique, called the stepwise relaxed object smoothed value picking regularization. Third, the proposed inversion scheme is made applicable to large scattering systems by introducing a *partial inverse problem grid* description, which restricts the inversion domain to a limited area surrounded by known background objects.

Due to the non-linearity of the inverse problem, it is solved in an iterative way, as shown in Fig. 6.1. From Fig. 6.1, four main components of the inverse problem can be distinguished:

1. The routine starts with an initial guess for the unknown permittivity profile $\boldsymbol{\varepsilon}_{init}$ (e.g. free space everywhere).
2. Then, the forward model computes the scattered fields $\mathbf{e}^{\text{scat}}(\boldsymbol{\varepsilon})$ that correspond to the current permittivity profile $\boldsymbol{\varepsilon}$ in the measurement points, for all illuminations.

3. In the *evaluation block*, an evaluation is made of how well the current permittivity profile satisfies some predefined quality standards (e.g. how large is the error between computed and measured scattered fields, how smooth is the current permittivity profile, etc.).
4. If the permittivity profile does not meet the above requirements, the *updating block* derives a new permittivity profile for the next iteration

We refer to the first part of this PhD work for a detailed overview of the forward model and focus in this chapter on the evaluation and updating blocks. The evaluation block is implemented by constructing a real-valued cost function that unites the different quality standards for the reconstruction. The cost function usually consists of a *data fit* part and a *regularization* part. The data fit part is a measure for the difference between the experimentally obtained scattered fields and the simulated ones, for the current iteration. Due to the ill-posedness of the inverse scattering problem, the use of only this data fit part does often not allow to obtain a solution. The regularization part contains additional a-priori information to the inverse problem (e.g. all objects are more or less smooth, the scatterer consists of a limited number of homogeneous regions, etc.).

The updating block contains a two-step procedure. First, an *update direction* $\mathbf{\Delta\varepsilon}_k$ for the current permittivity profile $\mathbf{\varepsilon}_k$ is computed from the cost function. Second, an approximate *line search* is performed yielding the step size β_k which (appoximately) minimizes the cost function along this direction. Hence, permittivity profiles are updated as

$$\mathbf{\varepsilon}_{k+1} = \mathbf{\varepsilon}_k + \beta_k \mathbf{\Delta\varepsilon}_k. \tag{6.1}$$

The update direction is obtained by applying a Newton method. In this PhD work a Gauss-Newton technique and a modified Gauss-Newton technique are applied. The approximate line search is performed as proposed by Fletcher in [10]. In the rest of this PhD work, the term *iteration* denotes one single loop in Fig. 6.1: the construction of a new, updated, permittivity profile by (i) computing an update direction for the permittivity profile and (ii) performing an approximate line search along this direction. Although the updating routine for the permittivity profile is based on the total cost function, the criterion to terminate the iterative routine is based on the data fit part only: the procedure is iterated until the data fit is smaller than a predefined threshold. The corresponding permittivity profile is denoted the *reconstruction*.

This chapter is organized as follows. The next section defines general scatterer, source and detector configurations and the organization of the data vectors. Afterwards, the effects of the ill-posedness of the electromagnetic inverse problem are discussed and the necessity of regularization is illustrated. The following sections deal with the evaluation and updating blocks of the inverse problem, respectively, for various types of regularization. In the updating block, derivatives of the forward model with respect to the permittivity unknowns are required. An analytical expression for these derivatives is derived in Section 6.6. Finally, the *partial inverse problem grid* approach is briefly illustrated.

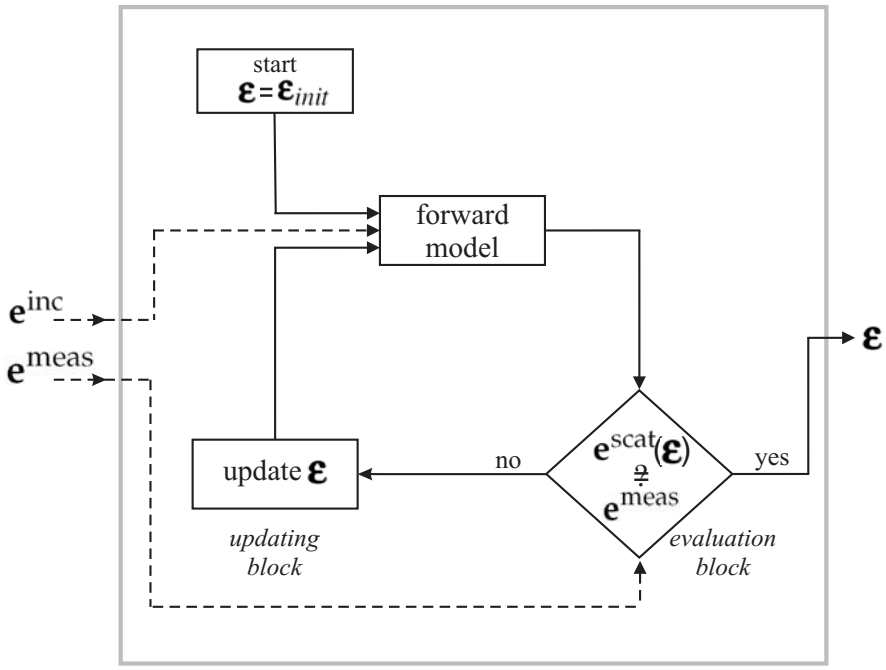

Figure 6.1: Iterative solution of the inverse scattering problem.

6.2. Scatterer, source and detector configurations

The reconstruction of the unknown permittivity profile is obtained by a pixel based inversion scheme. An investigation domain $\mathcal{D}$ is defined, which is known to contain the unknown scatterer. This investigation domain is subdivided in square cells, yielding a square grid that consists of N^{ε} cells with cell size Δ_{ε} and contains N^x and N^y cells in the x- and y- directions respectively. The center point of an inverse problem cell (k,l) is denoted by $\mathbf{r}_{k,l} = k\Delta_{\varepsilon}\mathbf{u}_x + l\Delta_{\varepsilon}\mathbf{u}_y$. Note that this inverse problem grid usually consists of larger cells than the forward problem grid (i.e. the grid employed to solve the forward scattering problem).

Over the investigation domain $\mathcal{D}$, the unknown complex permittivity function $\varepsilon(\mathbf{r})$ is approximated as a piecewise constant function with a unique value within each cell:

$$\varepsilon(\mathbf{r}) \approx \sum_{k=0}^{N^x-1} \sum_{l=0}^{N^y-1} \varepsilon_0 \varepsilon_{k,l} \Phi_{k,l}(\mathbf{r}) \qquad \mathbf{r} \in \mathcal{D}. \tag{6.2}$$

Here, $\Phi_{k,l}(\mathbf{r})$ is a 2D pulse function which is 1 inside cell (k,l) and zero elsewhere. The inverse problem thus consists of determining the unknown coefficients $\varepsilon_{k,l}$, which

are ordered in a N^{ε}-dimensional complex permittivity vector

$$\boldsymbol{\varepsilon} = [\varepsilon_{0,0} \ldots \varepsilon_{N^x-1,N^y-1}]^T = [\varepsilon_v]^T, \tag{6.3}$$

where $[.]^T$ stands for transpose.

Now suppose there are N^T transmitting antennas, see Fig. 6.2, positioned in $\mathbf{r}_t^A$ and producing incident fields (e.g. Gaussian beam, plane wave) with polarization $\mathbf{u}_{t,p}^A$ ($t = 1 \ldots N^T$). The total number of illuminations is $N^I = N^P N^T$, where $N^P = 1$ if only one incident field (being TE- or TM- polarized) originates from each transmitting antenna and $N^P = 2$ if two incident fields originate from each transmitting antenna (one being TE- polarized and the other being TM- polarized). We assume that the receiver configuration can be different for each transmitting antenna t: every transmitting antenna is linked to a set of N_t^R receiver locations, denoted as $\mathbf{r}_r^A$ ($r = 1 \ldots N_t^R$), which measure the scattered field along 3 polarization directions $\mathbf{u}_{r,p}^A$ (i.e. the x-, y- and z-components of the scattered field).

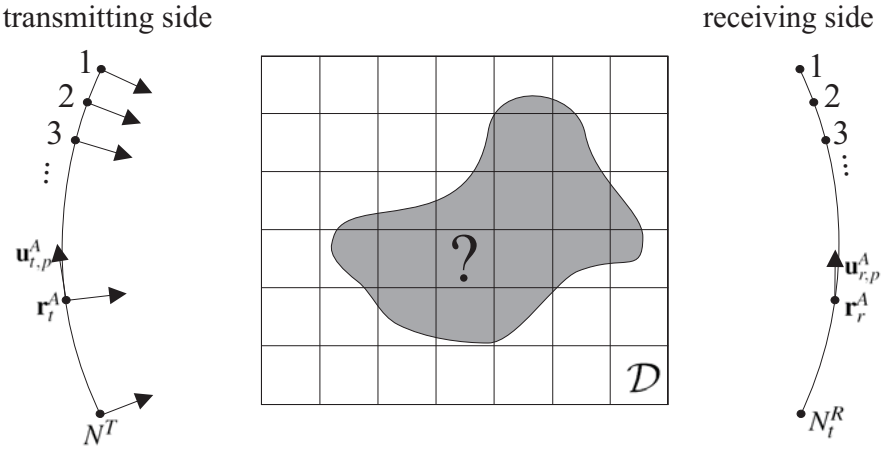

Figure 6.2: Definition of the position and polarization direction of the transmitting and receiving antennas in the inverse problem configuration. The propagation direction of the illuminations is also indicated.

All obtained scattered field data are organized in the data vector $\mathbf{e}^{\text{meas}}$, which has a length $N^D = N^P \sum_{t=1}^{N^T} 3N_t^R$. The elements of the data vector are $\mathbf{E}_{t,p}^{\text{meas}}(\mathbf{r}_r^A) \cdot \mathbf{u}_{r,p'}^A$, these are components of the scattered field, measured in points $\mathbf{r}_r^A$, along a polarization vector $\mathbf{u}_{r,p'}^A$ for an incident field generated in the source position $\mathbf{r}_t^A$ with polarization $\mathbf{u}_{t,p}^A$. Similarly, the vector containing the simulated scattered fields at all measurement positions for every illumination is represented as $\mathbf{e}^{scat}(\boldsymbol{\varepsilon})$.

6.3. Ill-posedness of the quantitative inverse scattering problem

The quantitative inverse scattering problem is ill-posed, which means that, as defined by Hadamard [11], existence of a solution, uniqueness of a solution and stability (convergence to the solution) are not guaranteed simultaneously.

If the solution of the inverse problem is defined as the permittivity profile for which the simulated scattered field exactly matches the measured fields (i.e. an exact *data fit*), then the inverse problem hardly ever has a solution since both measured and simulated scattered fields will be corrupted by noise (due to misalignment, unwanted reflections, ... in the measurement set-up and/or discretization errors, approximations and other numerical errors in the numerical implementation of the forward problem). The existence of a solution can be guaranteed by dropping the exact data fit requirement and reformulating the solution to an inverse problem as the permittivity profile that minimizes the least squares scattered field error

$$||\mathbf{e}^{\text{meas}} - \mathbf{e}^{\text{scat}}(\boldsymbol{\varepsilon})||^2. \tag{6.4}$$

This scattered field error (6.4) is denoted as the data fit. In practice, it is sufficient that the data fit is smaller than a predefined tolerance value to end the iterative procedure and call the current permittivity profile the solution.

Since scattered fields, measured on an arbitrary surface outside the source region, only have a limited number of degrees of freedom in finite precision [12], adding more illumination and measurement points to a measurement set-up does not increase the information content of the data vector $\mathbf{e}^{\text{meas}}$ from a certain point on. Therefore, it is possible that there exist more than one permittivity profile that minimizes the least squares data fit, since the number of degrees of freedom for the permittivity profile is usually (especially when a fine reconstruction grid is applied for a good resolution) larger than the number of degrees of freedom in the data. This uniqueness problem can be partly alleviated by providing as much *non-redundant* information as possible, i. e. maximizing the information content of the data.

The stability problem strongly influences the reconstruction process. Small fluctuations on the measured scattered field (e.g. caused by noise) can introduce relatively large changes in the permittivity profile. A *regularization* procedure adds extra, *a-priori*, information to the inverse problem, e.g. all scattering objects are more or less smooth. Consequently, the regularization suppresses the occurrence of unwanted permittivity fluctuations caused by noise and also mitigates the uniqueness problem since it reduces the number of degrees of freedom for the solution.

Many regularization strategies proposed in literature are based on the same principle: a regularization term is added to the data fit cost function. In this PhD work, three different regularization techniques are implemented, which are all developed at INTEC. The first type of regularization is the so-called multiplicative smoothing regularization [13, 14]. This technique penalizes strong local variations of the permittivity and hence smooths out edges in the reconstructed profile. Whereas the first type of

regularization penalizes spatial variations, the stepwise relaxed value picking regularization [15] penalizes deviations of the permittivity profile with respect to a number of (hitherto unknown) permittivity values. Hence, this regularization strategy is particularly suited for the reconstruction of piecewise (quasi-) homogeneous targets. It yields promising results for reconstructions of dielectric targets from 3D experimental data [13]. In this PhD, a new type of regularization is proposed, which is a combination of a spatially smoothing regularization and the stepwise relaxed value picking regularization. We have named it stepwise relaxed *object smoothed* value picking regularization. It is shown in Chapter 7 that this new regularization method significantly improves the reconstruction, in cases when applying the purely stepwise relaxed value picking regularization leads to artifacts in the reconstructed permittivity profile.

6.4. The evaluation block: Cost functions

For every permittivity profile, an evaluation is made of how well the computed scattered field fits the measurement data by evaluating a real-valued non-linear cost function. This is represented by the evaluation block in Fig. 6.1.

Due to the ill-posedness of the quantitative inverse scattering problem, its solution is defined as the permittivity profile that minimizes the least squares data fit cost function, in this PhD work denoted as $\mathcal{F}^{LS}(\boldsymbol{\varepsilon})$. Furthermore, a regularization strategy must be applied to the data fit cost function to improve its stability and to compensate for the loss of information due to noise. Generally, this is done by adding a regularization term $\mathcal{F}^{reg}$ to the data fit cost function $\mathcal{F}^{LS}$ with its weight given by the regularization parameter γ:

$$\mathcal{F}(\boldsymbol{\varepsilon}) = \mathcal{F}^{LS}(\boldsymbol{\varepsilon}) + \gamma \mathcal{F}^{reg}(\boldsymbol{\varepsilon}). \tag{6.5}$$

In the following, the data fit cost function $\mathcal{F}^{LS}$ is discussed, together with the cost functions $\mathcal{F}^{reg}$ that correspond to the three different types of regularization. Note that the regularization parameter (here denoted as γ) has different representations (α, γ and ζ) in the following sections, depending on the type of regularization that is applied.

6.4.1 The data fit cost function

The least squares data fit cost function is given by:

$$\mathcal{F}^{LS}(\boldsymbol{\varepsilon}) = \frac{1}{N^{LS}} ||\mathbf{e}^{\text{meas}} - \mathbf{e}^{\text{scat}}(\boldsymbol{\varepsilon})||^2, \tag{6.6}$$

where N^{LS} is a normalization constant such that $\mathcal{F}^{LS}(\boldsymbol{\varepsilon}) = 1$ when $\mathbf{e}^{\text{scat}}(\boldsymbol{\varepsilon}) = 0$, hence $N^{LS} = ||\mathbf{e}^{\text{meas}}||^2$. Since the electromagnetic inverse problem is ill-posed, the minimum of $\mathcal{F}^{LS}$ is not well defined. Scattered fields depend in a non-linear manner on the permittivity profile, hence this cost function is also non-linear in $\boldsymbol{\varepsilon}$.

The evaluation of the data fit cost function for a permittivity profile $\boldsymbol{\varepsilon}$ is a time demanding operation since the scattered field vector $\mathbf{e}^{\text{scat}}(\boldsymbol{\varepsilon})$ must be constructed by solving the corresponding forward problems for every illumination.

6.4.2 The multiplicative smoothing regularized cost function

The multiplicative smoothing (*MS*) regularization [14] penalizes strong local variations of the permittivity. It is ideally suited to reconstruct smooth objects since it softens sharp edges in the reconstructed profile. In the multiplicative approach, the total cost function, denoted as $\mathcal{F}^{\mathcal{MS}}(\boldsymbol{\varepsilon})$, becomes

$$\mathcal{F}^{\mathcal{MS}}(\boldsymbol{\varepsilon}) = \mathcal{F}^{\mathcal{LS}}(\boldsymbol{\varepsilon})[1+\alpha\mathcal{F}^{\mathcal{R}}(\boldsymbol{\varepsilon})] = \mathcal{F}^{\mathcal{LS}}(\boldsymbol{\varepsilon}) + \alpha\mathcal{F}^{\mathcal{LS}}(\boldsymbol{\varepsilon})\mathcal{F}^{\mathcal{R}}(\boldsymbol{\varepsilon}), \tag{6.7}$$

with α the regularization parameter, which is a small positive number. The smoothing function $\mathcal{F}^{\mathcal{R}}(\boldsymbol{\varepsilon})$ is defined as

$$\mathcal{F}^{\mathcal{R}}(\boldsymbol{\varepsilon}) = \frac{1}{\mathcal{N}^{\mathcal{R}}}\left[\sum_{k=0}^{N^x}\sum_{l=0}^{N^y-1}|\varepsilon_{k,l}-\varepsilon_{k-1,l}|^2 + \sum_{k=0}^{N^x-1}\sum_{l=0}^{N^y}|\varepsilon_{k,l}-\varepsilon_{k,l-1}|^2\right], \tag{6.8}$$

where $\mathcal{N}^{\mathcal{R}}$ is a normalization constant which accounts for the dimensions of the object and the size of a discretization cell. In fact, expression (6.8) is a discrete version of

$$\frac{1}{\varepsilon_0^2\mathcal{D}}\int_{\mathcal{D}}|\nabla\varepsilon(\mathbf{r})|^2\mathrm{d}\mathbf{r}. \tag{6.9}$$

The effect of the smoothing function $\mathcal{F}^{\mathcal{R}}$ is illustrated in Fig. 6.3 for permittivity variations in the k-direction only (the first term in (6.8)). Every permittivity jump between two horizontally (vertically) adjacent cells is once accounted for in the first (second) term of the smoothing function $\mathcal{F}^{\mathcal{R}}$, hence this term comprises for each cell (k,l) the squared permittivity difference with its left (lower) neighbor as indicated with the horizontal arrows in Fig. 6.3. Since all permittivity jumps contribute to $\mathcal{F}^{\mathcal{R}}$, smoothing is imposed all over the reconstruction domain.

The multiplicative nature of (6.7) makes the choice of the regularization parameter α less critical since the regularizing term in the cost function is proportional to the data fit. At the start of the optimization, the optimization domain is restricted to very smooth profiles since the regularization weight, given by $\alpha\mathcal{F}^{\mathcal{LS}}$ is still large. During the following iterations the regularization weight decreases, thus gradually enlarging the optimization domain to allow for more detail. Typically the data fit stagnates when the noise level is reached, thus yielding an estimate of the noise level.

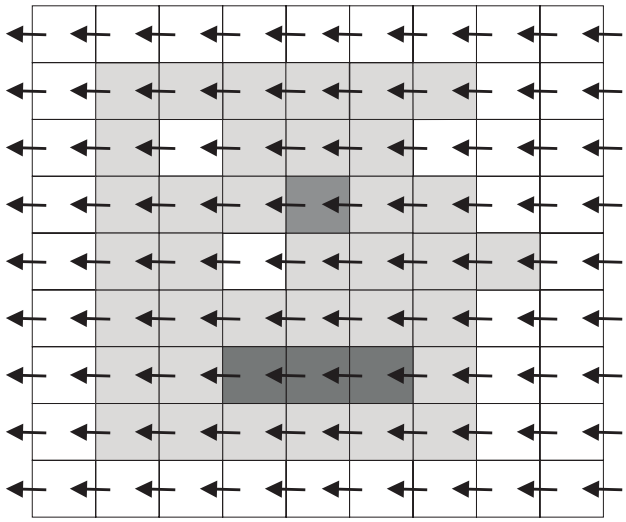

Figure 6.3: An illustration of the effect of the smoothing function $\mathcal{F}^{\mathcal{R}}$ for permittivity variations in the k- direction (the first term in (6.8)): every permittivity jump between two horizontally adjacent cells (represented as a horizontal arrow) is once accounted for. The different colors of the cells represent different permittivity values.

6.4.3 Cost function with stepwise relaxed value picking regularization

The recently developed value picking (*VP*) regularization [13, 15] is particularly suited for the reconstruction of piecewise (quasi-) homogeneous targets, consisting of $P \ll N^{\varepsilon}$ different permittivity values. This regularization technique does not introduce smoothing based on spatial information, as does the multiplicative smoothing regularization. In the method, an extra term is added to the data fit cost function, which penalizes permittivity profiles with more than P different values and hence clusters all permittivity values in the investigation domain around P reference values, named *VP values*. This clustering is achieved for each individual cell in a manner that is independent of the permittivity clustering of neighboring cells. The total cost function is given by

$$\mathcal{F}^{\mathcal{VP}}(\boldsymbol{\varepsilon},\mathbf{c}) = \mathcal{F}^{\mathcal{LS}}(\boldsymbol{\varepsilon}) + \gamma \mathcal{F}^{\mathcal{P}}(\boldsymbol{\varepsilon},\mathbf{c}), \tag{6.10}$$

with γ a positive regularization parameter and the vector $\mathbf{c}$ containing the VP values. The regularization function $\mathcal{F}^{\mathcal{P}}(\boldsymbol{\varepsilon},\mathbf{c})$ is defined as

$$\mathcal{F}^{\mathcal{P}}(\boldsymbol{\varepsilon},\mathbf{c}) = \frac{1}{N^{\varepsilon}} \sum_{n=1}^{N^{\varepsilon}} f^{P}(|\varepsilon_n - c_1|^2, \ldots, |\varepsilon_n - c_P|^2), \tag{6.11}$$

where f^P is the P-dimensional choice function. It is defined as

$$f^P(u_1,\ldots,u_P) = F^P(u_1,\ldots,u_P;0), \tag{6.12}$$

with $F^P(u_1,\ldots,u_P;x)$ defined and evaluated through the recursion formula

$$F^P(u_1,\ldots,u_P;x) = (u_P+x)\,\frac{F^{P-1}(u_1,\ldots,u_{P-1};x)}{F^{P-1}(u_1,\ldots,u_{P-1};u_P+x)} \tag{6.13}$$

with $F^1(u_1;x) = u_1 + x$. The particular form of this choice function is discussed in more detail in [1, 15].

The regularization function $\mathcal{F}^{\mathcal{P}}(\boldsymbol{\varepsilon},\mathbf{c})$ (6.11) can be reformulated in terms of a weighted sum of penalty functions $|\varepsilon_n - c_p|^2$ [1]:

$$\mathcal{F}^{\mathcal{P}}(\boldsymbol{\varepsilon},\mathbf{c}) = \frac{1}{N^{\varepsilon}}\sum_{n=1}^{N^{\varepsilon}}\sum_{p=1}^{P} b^P_{p,n}(\boldsymbol{\varepsilon},\mathbf{c})|\varepsilon_n - c_p|^2. \tag{6.14}$$

The behavior of the regularization function is as follows: (i) when the permittivity of a cell is close to a particular VP value, the choice function will try to enforce equality of the permittivity of that cell with this VP value (i.e. the corresponding weight of that term in (6.14) will be close to 1), (ii) when there is no clear preference of a permittivity cell for a particular VP value, no choice is made (the weight in (6.14) being somewhere intermediate between 0 and 1) and (iii) VP values that are clearly far away from the considered permittivity cell are neglected (the weight in (6.14) is almost zero). At the end of the optimization process, the reconstructed permittivity profile is obtained. Furthermore, a plot of the final weights $b^P_{p,n}(\boldsymbol{\varepsilon},\mathbf{c})$ for every permittivity pixel shows to which particular VP value it is most attracted, providing a good idea of the overall success of the reconstruction.

The VP values are not known in advance and are thus treated as extra variables in the optimization process. They are initialized randomly within some predefined upper and lower bounds on their real and imaginary part. One of these VP values, c_P, is kept fixed to the background permittivity, since this permittivity value appears definitely in the reconstruction domain.

In the value picking regularization method, every permittivity profile consisting of only P permittivity values, within the constraints on $\boldsymbol{\varepsilon}$ and $\mathbf{c}$, yields $\mathcal{F}^{\mathcal{V}\mathcal{P}}(\boldsymbol{\varepsilon},\mathbf{c}) = 0$. Consequently, the permittivity profile can be trapped in a local minimum above the noise level. Therefore, a stepwise relaxed value picking (*SRVP*) regularization scheme is introduced. The number of VP values is gradually increased, starting with only the background permittivity as a VP value. When the gradient of the cost function is small enough, indicating that a local minimum of the cost function is reached, an extra VP value is introduced to relax the optimization. A VP value is also added when the data fit increases again, indicating that the value picking regularization is making decisions which are not guided by the data fit. Ideally, the data fit reaches the noise level when the number of introduced VP values corresponds to the number of piecewise constant

objects with different permittivity. When the value of the regularization parameter γ is chosen too high, the relatively large weight of the regularization function is compensated by adding more VP values then necessary. To determine the ideal value for this parameter, the clustering of the permittivities is studied. Sufficient clustering should be achieved with as few VP values as possible and for the smallest value for γ yielding a proper clustering.

6.4.4 Cost function with stepwise relaxed object smoothed value picking regularization

This section presents the new stepwise relaxed object smoothed value picking (*SROSVP*) regularization, developed during this PhD work. It is a combination of the two previously mentioned regularization techniques and uses only slightly more a-priori information than the purely stepwise relaxed value picking regularization: i.e. we assume that all homogeneous objects in the permittivity profile have an extent in both x- and y- directions that is larger than the size of one inverse problem cell. This new regularization technique allows for edges in the reconstructed permittivity profile while penalizing unwanted permittivity fluctuations within homogeneous regions. It shows resemblanceto existing edge preserving techniques, originally developed for image processing applications (e.g. the Markov Random field approach [16]) and also used for the microwave inverse scattering problem [17, 18].

As stated in the Section 6.4.3, the weights $b^P_{p,n}(\boldsymbol{\varepsilon},\mathbf{c})$, that correspond to permittivity cell n and VP value c_p, give information on how well this particular cell "belongs" to one of the different homogeneous regions in the permittivity profile. This is because the weights $b^P_{p,n}(\boldsymbol{\varepsilon},\mathbf{c})$ indicate how close the permittivity of cell n lies to a particular VP value c_p. If neighboring cells have the same dominant weight, it can be expected that these cells belong to the same part of the scattering object. This spatial information is not used in the purely stepwise relaxed value picking regularization, but is exploited in this new type of regularization.

The regularizing part of the cost function is now two-fold: one term contains the previously presented stepwise relaxed value picking regularization term $\gamma\mathcal{F}^{\mathcal{P}}(\boldsymbol{\varepsilon},\mathbf{c})$ and added to this term there is now a smoothing term $\mathcal{F}^{OS}(\boldsymbol{\varepsilon},\mathbf{c})$ with weight ζ. Hence, the total cost function is in this case given by

$$\mathcal{F}^{\mathcal{SROSVP}}(\boldsymbol{\varepsilon},\mathbf{c}) = \mathcal{F}^{\mathcal{LS}}(\boldsymbol{\varepsilon}) + \gamma\mathcal{F}^{\mathcal{P}}(\boldsymbol{\varepsilon},\mathbf{c}) + \zeta\mathcal{F}^{OS}(\boldsymbol{\varepsilon},\mathbf{c}) \tag{6.15}$$

The smoothing term $\mathcal{F}^{OS}(\boldsymbol{\varepsilon},\mathbf{c})$ behaves as the multiplicative smoothing regularization term $\mathcal{F}^{\mathcal{R}}(\boldsymbol{\varepsilon})$. However, smoothing is only performed over cells that belong to the same homogeneous region in the permittivity profile.

In every iteration, the cost function $\mathcal{F}^{\mathcal{SROSVP}}(\boldsymbol{\varepsilon},\mathbf{c})$ is to be evaluated. Therefore, different preprocessing steps have to be performed: (i) the VP weights $b^P_{p,n}(\boldsymbol{\varepsilon},\mathbf{c})$ have to be determined for the current permittivity profile, (ii) for each pixel n in the reconstruction grid it must be decided to which homogeneous region it most probably

belongs, based on the knowledge of the VP weights $b^P_{p,n}(\boldsymbol{\varepsilon},\mathbf{c})$ and (iii) a set of smoothing areas is determined in which the smoothing will be performed.

We have chosen to name the second preprocessing step *group mapping* and call the different homogeneous regions *VP groups*. The group mapping is done by comparing all VP weights that correspond to a cell n. The largest and second largest weight are determined and if the difference between both is larger than a certain threshold value (the *grouping tolerance*, often chosen as 0.2), cell n is assigned to the VP group that corresponds with the largest weight. If the difference is not large enough, we conclude that we cannot determine to which VP group a cell belongs and the current cell is assigned to the *indefinite cells group*. Note that a VP group that is obtained in this way can consist of several spatially disconnected areas, while it is the purpose to apply the smoothing only within each separate area.

To detail the determination of smoothing areas from knowledge of the VP groups, we look back at the implementation of the smoothing function $\mathcal{F}^{\mathcal{R}}$ (6.8), where, for every cell (k,l) in the reconstruction grid $\mathcal{D}$, the differences in permittivity with the neighboring cells $(k-1,l)$ and $(k,l-1)$ are contributing to the smoothing. Hence, permittivity variations over all cell boundaries in the grid are penalized. For the stepwise relaxed object smoothed value picking regularization, these permittivity differences only contribute to the cost function if these neighboring cells belong to the same VP group. Hence, permittivity jumps over cell boundaries between different VP groups are not penalized. This spatial information is incorporated in two *smoothing direction matrices* $\mathbf{S}(\mathbf{c})$ that indicate for each cell boundary whether smoothing is allowed in the x- and y- directions respectively: if cell $(k-1,l)$ belongs to the same VP group as cell (k,l), smoothing is allowed and the $(k,l)-$th element of the first smoothing direction matrix $\mathbf{S}^1$ is set to $\mathbf{S}^1_{k,l}=1$, otherwise smoothing is not allowed and this element is zero. This is also illustrated in Fig. 6.4 (a) and (b), where cells having the same color are assumed to be assigned to the same VP group. Similarly, if cells $(k,l-1)$ and (k,l) belong to the same VP group, $\mathbf{S}^2_{k,l}=1$. Consequently, the smoothing term $\mathcal{F}^{OS}(\boldsymbol{\varepsilon},\mathbf{c})$ of the cost function is given by

$$\begin{aligned}\mathcal{F}^{OS}(\boldsymbol{\varepsilon},\mathbf{c}) \;=\; & \frac{1}{\mathcal{N}^{\mathcal{R}}}\sum_{k=0}^{N^x}\sum_{l=0}^{N^y-1}\mathbf{S}^1_{k,l}(\mathbf{c})\;|\varepsilon_{k,l}-\varepsilon_{k-1,l}|^2 \\ & +\frac{1}{\mathcal{N}^{\mathcal{R}}}\sum_{k=0}^{N^x-1}\sum_{l=0}^{N^y}\mathbf{S}^2_{k,l}(\mathbf{c})\;|\varepsilon_{k,l}-\varepsilon_{k,l-1}|^2,\end{aligned} \tag{6.16}$$

which only differs from the smoothing function $\mathcal{F}^{\mathcal{R}}$ (6.8) by the presence of smoothing direction matrices $\mathbf{S}$.

To smooth out unwanted local fluctuations (artifacts) in the permittivity profile, the second neighbor is also of importance. For example, if pixel (k,l) and his neighbor $(k-1,l)$ do not belong to the same VP group, the second neighbor in the same direction (i.e. cell $(k-2,l)$) is taken into account. If this neighbor does belong to the same VP group as cell (k,l), it is assumed that the intermediate pixel (cell $(k-1,l)$) is

attracted to the wrong VP value. In this case, it is also allowed to smooth towards cell $(k-1,l)$ and $\mathbf{S}^1_{k,l} = 1$. This is illustrated in Fig. 6.4 (c). Here, the additional a-priori information that all scatterers are supposed to be larger than one inversion cell in both (x- and y-) directions is incorporated.

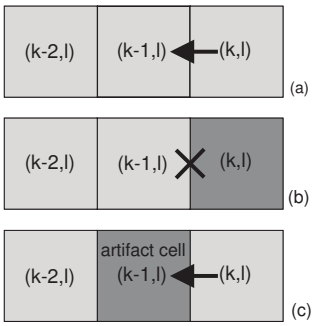

Figure 6.4: An illustration of the construction of the smoothing direction matrices **S**, where cells having the same color are assumed to be assigned to the same VP group. Allowed smoothing is represented as a horizontal arrow between cells, prohibited smoothing is represented as a cross between cells.

Finally, the effect of the smoothing function $\mathcal{F}^{OS}$ is illustrated in Fig. 6.5 for variations in the k-direction only (the first term in (6.16)). When this figure is compared to the corresponding figure in case of multiplicative smoothing regularization (Fig. 6.3), three effects can be recognized:

- Smoothing is imposed within homogeneous regions only.
- No smoothing is allowed over the boundaries between different homogeneous regions.
- Smoothing is allowed over boundaries of artifacts.

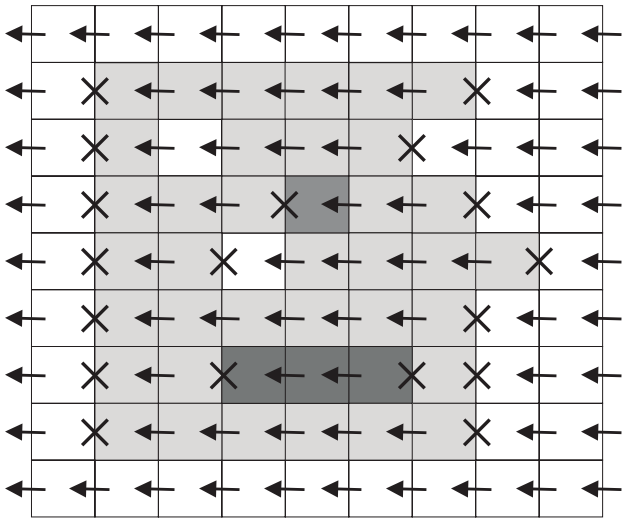

Figure 6.5: An illustration of the effect of the smoothing function $\mathcal{F}^{OS}$ for permittivity variations in the k- direction (the first term in (6.16)). Cells having the same color are assumed to be assigned to the same VP group. Allowed smoothing is represented as a horizontal arrow between cells, prohibited smoothing is represented as a cross between cells.

6.5. The updating block: The Gauss-Newton method with line search

Different types of cost functions have been proposed in the previous section. To determine whether a new update for the permittivity profile must be constructed or not, the data fit cost function is used. If its value is smaller than a predefined threshold, the current profile yields the reconstruction. If not, a new update is made.

A large body of literature on Newton-type techniques [2, 3, 4, 19, 20, 21] has been dedicated to the derivation of new updates. Classically, an update direction is derived for the permittivity profile and a fixed step size $\beta_k = 1$ is used along this direction, as in (6.1). Sometimes, this step size is too large, yielding convergence problems. Therefore, in this PhD, an approximate line search [10] is performed to determine an adequate step size.

The most common Newton-type methods used to determine an update direction for the permittivity are the quasi-Newton method [2, 19], the Levenberg-Marquardt method [3, 20] and the Gauss-Newton method [4, 19, 21]. In this PhD work, the Gauss-Newton method and a modified Gauss-Newton method [13, 14, 22] are used. An overview of these methods can be found in [10, 23]. The mentioned methods have in common that they are local optimization methods and hence require the computation of local derivatives. These methods can be trapped in local minima or can yield a non-physical solution (e.g. the real part of the relative permittivity of a cell is smaller than 1). Global optimization methods however are impractical since, usually, the number of unknowns is large and global methods require many cost function evaluations, which are computationally demanding. Examples of global methods are genetic algorithms [5, 6, 7], neural network techniques [8, 24] or the simulated annealing methods [9, 25]. Another type of local methods are the so-called conjugate gradient methods [26, 27, 28, 29]. These methods avoid the computationally demanding process of solving forward scattering problems but typically require a large amount of iterations.

This section is organized as follows. The first part introduces the Newton method used to determine an update direction for the permittivity profile. Note here that the term update direction does not refer to a normalized vector, but to a vector which will be used as a search direction in a line search. Since the derivation of the update direction is independent of the step size β_k, we set $\beta_k = 1$ and omit the step size in the following parts of this section. First, the general Newton method and the Gauss-Newton method are introduced for the special case when no regularization term is added to the cost function. Next, the Gauss-Newton method is extended to the multiplicative smoothing regularization case, introducing the modified Gauss-Newton method. Further, the Gauss-Newton method is formulated for the stepwise relaxed value picking regularization and stepwise relaxed object smoothed value picking regularization. The last part of this section introduces the concept of using an approximate line search in the updating routine.

6.5.1 Newton's method applied to the non-regularized cost function

In each iteration, Newton's method approximates the non-linear cost function with a quadratic model, derived from first and second order derivatives of the cost function. The stationary point of the quadratic model serves as update direction for the permittivity profile. Hence, to start iteration $k+1$, the complex permittivity vector is updated as

$$\boldsymbol{\varepsilon}_{k+1} = \boldsymbol{\varepsilon}_k + \boldsymbol{\Delta\varepsilon}_k, \tag{6.17}$$

where $\boldsymbol{\varepsilon}_k$ is the permittivity profile at iteration k and $\boldsymbol{\Delta\varepsilon}_k$ is the corresponding permittivity update direction. Instead of using the real and imaginary parts of all elements ε_ν of the permittivity vector as independent variables, the complex permittivity vector elements ε_ν and their complex conjugate ε_ν^* are considered as independent variables [30, 31, 32].

The Newton optimization scheme constructs the permittivity update direction $\boldsymbol{\Delta\varepsilon}_k$ as

$$\begin{bmatrix} \boldsymbol{\Delta\varepsilon}_k \\ \boldsymbol{\Delta\varepsilon}_k^* \end{bmatrix} = -\mathbf{H}_k^{-1}\mathbf{g}_k. \tag{6.18}$$

In (6.18), $\mathbf{g}_k$ denotes the gradient vector of the cost function for the k^{th} iteration and $\mathbf{H}_k$ denotes the corresponding Hessian matrix.

Newton's method has the fundamental property of superlinear convergence if the initial guess is close enough to the solution [10]. However, when the optimization process starts further away from the solution, the Newton correction may lead to an increase in the cost function and cause convergence problems. This behavior can be due to two reasons: (i) in the stationary point, the quadratic model is no longer a good approximation to the cost function or (ii) the Hessian matrix is not positive definite, indicating that the model has no positive curvature. Furthermore, there are second order derivatives required to construct the Hessian matrix, which is a highly computationally demanding operation, requiring many forward model evaluations.

For a general cost function $\mathcal{F}(\boldsymbol{\varepsilon})$, the gradient vector and the Hessian matrix are defined as

$$\mathbf{g}_k = \begin{bmatrix} \frac{\partial \mathcal{F}}{\partial \varepsilon_\nu} \\ \\ \frac{\partial \mathcal{F}}{\partial \varepsilon_\nu^*} \end{bmatrix}, \qquad \mathbf{H}_k = \begin{bmatrix} \frac{\partial^2 \mathcal{F}}{\partial \varepsilon_\nu \partial \varepsilon_\mu} & \frac{\partial^2 \mathcal{F}}{\partial \varepsilon_\nu \partial \varepsilon_\mu^*} \\ \\ \frac{\partial^2 \mathcal{F}}{\partial \varepsilon_\nu^* \partial \varepsilon_\mu} & \frac{\partial^2 \mathcal{F}}{\partial \varepsilon_\nu^* \partial \varepsilon_\mu^*} \end{bmatrix}. \tag{6.19}$$

For the data fit cost function (6.6), the gradient vector has the dimension $2N^\varepsilon \times 1$ and is given by

$$\mathbf{g}_k^{\mathcal{LS}} = \frac{1}{\mathcal{N}^{\mathcal{LS}}} \begin{bmatrix} \mathbf{J}_k^T [\mathbf{e}^{\text{scat}}(\boldsymbol{\varepsilon}_k) - \mathbf{e}^{\text{meas}}]^* \\ \mathbf{J}_k^H [\mathbf{e}^{\text{scat}}(\boldsymbol{\varepsilon}_k) - \mathbf{e}^{\text{meas}}] \end{bmatrix}, \tag{6.20}$$

where $\mathbf{J}$ is the $N^D \times N^\varepsilon$ Jacobian matrix, which contains the first order derivatives of the scattered fields: $J_{d,\nu} = \partial e_d^{\text{scat}} / \partial \varepsilon_\nu$. An expression for these first order derivatives of

$\mathbf{e}^{\text{scat}}(\boldsymbol{\varepsilon}_k)$ with respect to the complex permittivity coefficients ε_ν is derived in analytical form in section 6.6. The Hessian matrix, with dimension $2N^\varepsilon \times 2N^\varepsilon$, is represented as:

$$\mathbf{H}_k^{\mathcal{LS}} = \frac{1}{\mathcal{N}^{\mathcal{LS}}} \begin{bmatrix} \mathbf{B}_k & \mathbf{J}_k^T \mathbf{J}_k^* \\ \mathbf{J}_k^H \mathbf{J}_k & \mathbf{B}_k^* \end{bmatrix}, \tag{6.21}$$

where $\mathbf{B}$ is a $N^\varepsilon \times N^\varepsilon$ matrix with second order derivatives of the scattered field: $\mathbf{B}_{\nu,\mu} = (\partial^2 \mathbf{e}^{\text{scat}} / \partial\varepsilon_\nu \partial\varepsilon_\mu)^T [\mathbf{e}^{\text{scat}} - \mathbf{e}^{\text{meas}}]^*$.

6.5.2 The Gauss-Newton method applied to the non-regularized cost function

In the Gauss-Newton method, the scattered field $\mathbf{e}^{\text{scat}}$ is linearized as follows:

$$\Delta\mathbf{e}_k^{\text{scat}} = \mathbf{e}^{\text{scat}}(\boldsymbol{\varepsilon}_{k+1}) - \mathbf{e}^{\text{scat}}(\boldsymbol{\varepsilon}_k) = \mathbf{e}^{\text{scat}}(\boldsymbol{\varepsilon}_k + \Delta\boldsymbol{\varepsilon}_k) - \mathbf{e}^{\text{scat}}(\boldsymbol{\varepsilon}_k) \approx \mathbf{J}_k \Delta\boldsymbol{\varepsilon}_k. \tag{6.22}$$

This linearization is introduced in the data fit cost function, yielding

$$\begin{aligned} \mathcal{F}^{\mathcal{LS}}(\boldsymbol{\varepsilon}_{k+1}) &= \frac{1}{N^{\mathcal{LS}}} ||\mathbf{e}^{\text{scat}}(\boldsymbol{\varepsilon}_k + \Delta\boldsymbol{\varepsilon}_k) - \mathbf{e}^{\text{meas}}||^2 \\ &= \frac{1}{N^{\mathcal{LS}}} ||\mathbf{e}^{\text{scat}}(\boldsymbol{\varepsilon}_k) + \mathbf{J}_k \Delta\boldsymbol{\varepsilon}_k - \mathbf{e}^{\text{meas}}||^2. \end{aligned} \tag{6.23}$$

If this least squares data fit cost function is minimized with respect to $\Delta\boldsymbol{\varepsilon}_k$, the permittivity update direction is obtained as

$$\Delta\boldsymbol{\varepsilon}_k = -\left(\mathbf{J}_k^H \mathbf{J}_k\right)^{-1} \mathbf{J}_k^H [\mathbf{e}^{\text{scat}}(\boldsymbol{\varepsilon}_k) - \mathbf{e}^{\text{meas}}]. \tag{6.24}$$

Hence, no second order derivatives need to be computed, contrary to Newton's method. However, the condition number for $\mathbf{J}_k^H \mathbf{J}_k$ is typically large, which is a measure of the ill-posedness of the inverse problem. Applying a regularization strategy will improve the condition number.

The Gauss-Newton update direction is also obtained from the Newton optimization scheme (6.18) applied to the data fit $\mathcal{F}^{\mathcal{LS}}$:

$$-\mathbf{H}_k^{\mathcal{LS}} \begin{bmatrix} \Delta\boldsymbol{\varepsilon}_k \\ \Delta\boldsymbol{\varepsilon}_k^* \end{bmatrix} = \mathbf{g}_k^{\mathcal{LS}} \iff -\begin{bmatrix} \mathbf{B}_k \Delta\boldsymbol{\varepsilon}_k + \mathbf{J}_k^T \mathbf{J}_k^* \Delta\boldsymbol{\varepsilon}_k^* \\ \mathbf{J}_k^H \mathbf{J}_k \Delta\boldsymbol{\varepsilon}_k + \mathbf{B}_k^* \Delta\boldsymbol{\varepsilon}_k^* \end{bmatrix} = \begin{bmatrix} \mathbf{J}_k^T [\mathbf{e}_k^{\text{scat}} - \mathbf{e}^{\text{meas}}]^* \\ \mathbf{J}_k^H [\mathbf{e}_k^{\text{scat}} - \mathbf{e}^{\text{meas}}] \end{bmatrix}, \tag{6.25}$$

if the matrix $\mathbf{B}$, containing the second order derivatives of the scattered field, is neglected.

6.5.3 The modified Gauss-Newton method with MS regularization

Now, the update direction is formulated for the multiplicative smoothing regularized cost function (6.7):

$$\mathcal{F}^{\mathcal{MS}}(\boldsymbol{\varepsilon}_k) = \mathcal{F}^{\mathcal{LS}}(\boldsymbol{\varepsilon}_k)[1+\alpha\mathcal{F}^{\mathcal{R}}(\boldsymbol{\varepsilon}_k)].$$

Gradient vector and Hessian matrix of $\mathcal{F}^{\mathcal{R}}(\boldsymbol{\varepsilon}_k)$

The Newton optimization scheme requires the determination of the gradient vector and Hessian matrix of the regularizing part of the cost function $\mathcal{F}^{\mathcal{R}}(\boldsymbol{\varepsilon}_k)$ given by (6.8). The gradient vector, with dimension $2N^{\varepsilon}\times 1$, contains the first order derivatives of the regularizing function and is defined as

$$\mathbf{g}_k^{\mathcal{R}} = \begin{bmatrix} \frac{\partial \mathcal{F}^{\mathcal{R}}}{\partial \varepsilon_\nu} \\ \frac{\partial \mathcal{F}^{\mathcal{R}}}{\partial \varepsilon_\nu^*} \end{bmatrix} = \begin{bmatrix} \boldsymbol{\Omega}_k^{\mathcal{R}} \\ \boldsymbol{\Omega}_k^{\mathcal{R}*} \end{bmatrix}. \tag{6.26}$$

Derivatives with respect to ε_ν are collected in the vector $\boldsymbol{\Omega}_k^{\mathcal{R}}$, derivatives with respect to ε_ν^* are collected in $\boldsymbol{\Omega}_k^{\mathcal{R}*}$, e.g.

$$\Omega_{k;\nu}^{\mathcal{R}*} = \frac{\partial \mathcal{F}^{\mathcal{R}}}{\partial \varepsilon_\nu^*} = \frac{\partial \mathcal{F}^{\mathcal{R}}}{\partial \varepsilon_{i,j}^*} = \frac{2}{\mathcal{N}^{\mathcal{R}}}(4\varepsilon_{i,j} - \varepsilon_{i-1,j} - \varepsilon_{i,j-1} - \varepsilon_{i+1,j} - \varepsilon_{i,j+1}) \tag{6.27}$$

Similarly, the Hessian matrix is defined as

$$\mathbf{H}_k^{\mathcal{R}} = \begin{bmatrix} \frac{\partial^2 \mathcal{F}^{\mathcal{R}}}{\partial \varepsilon_\nu \partial \varepsilon_\mu} & \frac{\partial^2 \mathcal{F}^{\mathcal{R}}}{\partial \varepsilon_\nu \partial \varepsilon_\mu^*} \\ \frac{\partial^2 \mathcal{F}^{\mathcal{R}}}{\partial \varepsilon_\nu^* \partial \varepsilon_\mu} & \frac{\partial^2 \mathcal{F}^{\mathcal{R}}}{\partial \varepsilon_\nu^* \partial \varepsilon_\mu^*} \end{bmatrix} = \begin{bmatrix} 0 & \boldsymbol{\Sigma}_k^{\mathcal{R}} \\ \boldsymbol{\Sigma}_k^{\mathcal{R}} & 0 \end{bmatrix}. \tag{6.28}$$

The diagonal elements are zero due to the specific form of the multiplicative smoothing regularizing function (6.8), the other second order derivatives of the regularizing function are collected in the matrix $\boldsymbol{\Sigma}_k^{\mathcal{R}}$. The diagonal elements of $\boldsymbol{\Sigma}_k^{\mathcal{R}}$ are given by

$$\Sigma_{k;\nu,\nu}^{\mathcal{R}} = \frac{\partial^2 \mathcal{F}^{\mathcal{R}}}{\partial \varepsilon_\nu \partial \varepsilon_\nu^*} = \frac{\partial^2 \mathcal{F}^{\mathcal{R}}}{\partial \varepsilon_{i,j} \partial \varepsilon_{i,j}^*} = \frac{8}{\mathcal{N}^{\mathcal{R}}}. \tag{6.29}$$

Non-diagonal elements of $\boldsymbol{\Sigma}_k^{\mathcal{R}}$ ($\Sigma_{k;\nu,\mu}^{\mathcal{R}}$) are zero except if ν denotes a neighbor of μ, i.e. if (m,n) is a neighbor of (i,j): $m=i-1, n=j$ or $m=i, n=j-1$ or $m=i+1, n=j$ or $m=i, n=j+1$. Then,

$$\Sigma_{k;\nu,\mu}^{\mathcal{R}} = \frac{\partial^2 \mathcal{F}^{\mathcal{R}}}{\partial \varepsilon_\nu \partial \varepsilon_\mu^*} = \frac{\partial^2 \mathcal{F}^{\mathcal{R}}}{\partial \varepsilon_{m,n} \partial \varepsilon_{i,j}^*} = -\frac{2}{\mathcal{N}^{\mathcal{R}}}. \tag{6.30}$$

Gradient vector and Hessian matrix of the total cost function $\mathcal{F}^{\mathcal{MS}}(\boldsymbol{\varepsilon}_k)$

The gradient vector and Hessian matrix of the complete cost function are obtained by applying the chain rule. Hence,

$$\mathbf{g}_k = \mathbf{g}_k^{\mathcal{LS}}[1+\alpha\mathcal{F}^{\mathcal{R}}(\boldsymbol{\varepsilon}_k)] + \alpha\mathcal{F}^{\mathcal{LS}}(\boldsymbol{\varepsilon}_k)\mathbf{g}_k^{\mathcal{R}} \tag{6.31}$$

and

$$\mathbf{H}_k = \frac{1}{\mathcal{N}^{\mathcal{LS}}}\begin{bmatrix}\mathbf{B}_k' & \mathbf{A}_k^* \\ \mathbf{A}_k & \mathbf{B}_k^{*\prime}\end{bmatrix}, \tag{6.32}$$

with

$$\begin{aligned}\mathbf{B}_k' \;=\; & \mathbf{B}_k[1+\alpha\mathcal{F}^{\mathcal{R}}(\boldsymbol{\varepsilon}_k)] + \alpha\boldsymbol{\Omega}_k^{\mathcal{R}}[\mathbf{e}^{\text{scat}}(\boldsymbol{\varepsilon}_k)-\mathbf{e}^{\text{meas}}]^H\mathbf{J}_k \\ & +\alpha\mathbf{J}_k^T[\mathbf{e}^{\text{scat}}(\boldsymbol{\varepsilon}_k)-\mathbf{e}^{\text{meas}}]^*(\boldsymbol{\Omega}_k^{\mathcal{R})T}\end{aligned} \tag{6.33}$$

and

$$\begin{aligned}\mathbf{A}_k \;=\; & \mathbf{J}_k^H\mathbf{J}_k[1+\alpha\mathcal{F}^{\mathcal{R}}(\boldsymbol{\varepsilon}_k)] + \alpha\boldsymbol{\Omega}_k^{\mathcal{R}*}[\mathbf{e}^{\text{scat}}(\boldsymbol{\varepsilon}_k)-\mathbf{e}^{\text{meas}}]^H\mathbf{J}_k \\ & +\alpha\mathbf{J}_k^H[\mathbf{e}^{\text{scat}}(\boldsymbol{\varepsilon}_k)-\mathbf{e}^{\text{meas}}](\boldsymbol{\Omega}_k^{\mathcal{R}})^T + \alpha\mathcal{N}^{\mathcal{LS}}\mathcal{F}^{\mathcal{LS}}(\boldsymbol{\varepsilon}_k)\boldsymbol{\Sigma}_k^{\mathcal{R}}\end{aligned} \tag{6.34}$$

Update direction for the permittivity profile

Applying Newton's update formula (6.18) yields

$$\begin{aligned}\begin{bmatrix}\mathbf{B}_k'\Delta\boldsymbol{\varepsilon}_k + \mathbf{A}_k^*\Delta\boldsymbol{\varepsilon}_k^* \\ \mathbf{A}_k\Delta\boldsymbol{\varepsilon}_k + \mathbf{B}_k^{\prime *}\Delta\boldsymbol{\varepsilon}_k^*\end{bmatrix} \;=\; & -\begin{bmatrix}\mathbf{J}_k^T[\mathbf{e}^{\text{scat}}(\boldsymbol{\varepsilon}_k)-\mathbf{e}^{\text{meas}}]^* \\ \mathbf{J}_k^H[\mathbf{e}^{\text{scat}}(\boldsymbol{\varepsilon}_k)-\mathbf{e}^{\text{meas}}]\end{bmatrix}[1+\alpha\mathcal{F}^{\mathcal{R}}(\boldsymbol{\varepsilon}_k)] \\ & -\alpha\mathcal{N}^{\mathcal{LS}}\mathcal{F}^{\mathcal{LS}}(\boldsymbol{\varepsilon}_k)\begin{bmatrix}\boldsymbol{\Omega}_k^{\mathcal{R}} \\ \boldsymbol{\Omega}_k^{\mathcal{R}*}\end{bmatrix}.\end{aligned} \tag{6.35}$$

Now, the expressions for the matrices $\mathbf{A}_k$ (6.34) and $\mathbf{B}_k'$ (6.33) are introduced in the left hand side of the Newton update direction (6.35). Furthermore, the matrix $\mathbf{B}_k$, which contains the second order derivatives is neglected, as in (6.25). In this way, the linearization of the scattered field (6.22) is introduced in the Newton method, yielding a Gauss-Newton optimization scheme. The left hand side of the Newton update direction (6.35) transforms into:

$$\begin{aligned}\mathbf{A}_k\Delta\boldsymbol{\varepsilon}_k + \mathbf{B}_k^{\prime *}\Delta\boldsymbol{\varepsilon}_k^* \;=\; & \mathbf{J}_k^H\mathbf{J}_k(1+\alpha\mathcal{F}^{\mathcal{R}}(\boldsymbol{\varepsilon}_k))\Delta\boldsymbol{\varepsilon}_k \\ & +\alpha\mathcal{N}^{\mathcal{LS}}\mathcal{F}^{\mathcal{LS}}(\boldsymbol{\varepsilon}_k)\boldsymbol{\Sigma}_k^{\mathcal{R}}\Delta\boldsymbol{\varepsilon}_k \\ & +\alpha\mathbf{J}_k^H[\mathbf{e}^{\text{scat}}(\boldsymbol{\varepsilon}_k)-\mathbf{e}^{\text{meas}}]\left((\boldsymbol{\Omega}_k^{\mathcal{R}})^T\Delta\boldsymbol{\varepsilon}_k + (\boldsymbol{\Omega}_k^{\mathcal{R}})^H\Delta\boldsymbol{\varepsilon}_k^*\right) \\ & +\alpha\boldsymbol{\Omega}_k^{\mathcal{R}*}[\mathbf{e}^{\text{scat}}(\boldsymbol{\varepsilon}_k)-\mathbf{e}^{\text{meas}}]^H\Delta\mathbf{e}^{\text{scat}} \\ & +\alpha\boldsymbol{\Omega}_k^{\mathcal{R}*}[\mathbf{e}^{\text{scat}}(\boldsymbol{\varepsilon}_k)-\mathbf{e}^{\text{meas}}]^T\Delta\mathbf{e}^{\text{scat}*}.\end{aligned} \tag{6.36}$$

In (6.36) certain terms contribute more than others. In the first iteration, often all cells have the background permittivity assigned, which corresponds to $\mathcal{F}^{\mathcal{R}}(\boldsymbol{\varepsilon}_0) = 0$ and hence $\boldsymbol{\Omega}^{\mathcal{R}} = 0$. Therefore, the third, fourth and fifth term in (6.36) vanish or remain small in a few subsequent iterations. When approaching the last few iterations, the simulated scattered field is already close to the measured one, yielding a small data residue $[\mathbf{e}^{\text{scat}}(\boldsymbol{\varepsilon}_k) - \mathbf{e}^{\text{meas}}]$. Therefore, the same terms (3rd, 4th and 5th term) vanish at the end of the optimization process. Due to this behavior at the beginning and end op the optimization, these terms are omitted from (6.36) and therefore this method is denoted the *modified* Gauss-Newton method [14]. The update direction is then given by combining this approximate version of (6.36) with (6.35):

$$\left(\mathbf{J}_k^H \mathbf{J}_k + \lambda^2 \boldsymbol{\Sigma}_k^{\mathcal{R}}\right) \Delta\boldsymbol{\varepsilon}_k = -\left(\mathbf{J}_k^H [\mathbf{e}^{\text{scat}}(\boldsymbol{\varepsilon}_k) - \mathbf{e}^{\text{meas}}] + \lambda^2 \left(\boldsymbol{\Omega}_k^{\mathcal{R}}\right)^*\right), \tag{6.37}$$

where the trade-off parameter λ is given by

$$\lambda^2 = \frac{\alpha ||\mathbf{e}^{\text{meas}}||^2 \mathcal{F}^{\mathcal{LS}}}{1 + \alpha \mathcal{F}^{\mathcal{R}}}. \tag{6.38}$$

6.5.4 The Gauss-Newton method with SRVP regularization

In the value picking regularization scheme, the auxiliary variables $\{c_p\}$ (the VP values) are not fixed, but are also optimized for. However, the VP values are subject to upper and lower bounds on their real and imaginary part. Therefore, a *constrained* optimization scheme is needed to update the VP values. This constrained optimization is performed by an active set method [10] and will not be discussed here.

Every inverse iteration is a two-step procedure. First, an update direction is derived for the permittivity profile and a line search along this direction yields the next permittivity profile. During this first step, the VP values are kept fixed to their current value. Second, the permittivity vector is kept fixed while the VP values are being updated. Hence, the updating process for the VP values does not influence the data fit. Apart from this alternating optimization scheme, VP values are also updated when a new VP value is introduced in the SRVP regularization scheme.

For the value picking regularization, the cost function has the following form:

$$\mathcal{F}^{\mathcal{VP}}(\boldsymbol{\varepsilon}, \mathbf{c}) = \mathcal{F}^{\mathcal{LS}}(\boldsymbol{\varepsilon}) + \gamma \mathcal{F}^{\mathcal{P}}(\boldsymbol{\varepsilon}, \mathbf{c}),$$

with the regularizing part given by

$$\mathcal{F}^{\mathcal{P}}(\boldsymbol{\varepsilon}, \mathbf{c}) = \frac{1}{N^{\varepsilon}} \sum_{n=1}^{N^{\varepsilon}} \sum_{p=1}^{P} b_{p,n}^{P}(\boldsymbol{\varepsilon}, \mathbf{c}) |\varepsilon_n - c_p|^2.$$

To incorporate the regularizing term in the Gauss-Newton update scheme, gradient and Hessian matrices need to be determined for the regularizing part of the cost function $\mathcal{F}^{\mathcal{P}}(\boldsymbol{\varepsilon}, \mathbf{c})$. However, the weights $b_{p,n}^{P}(\boldsymbol{\varepsilon})$ also depend on $\boldsymbol{\varepsilon}$. Therefore, the updating

process for the permittivity profile is performed for a slightly modified cost function:

$$\mathcal{F}^{\mathcal{Q}}(\boldsymbol{\varepsilon},\mathbf{c};\boldsymbol{\varepsilon}_k,\mathbf{c}_k) = \mathcal{F}^{\mathcal{LS}}(\boldsymbol{\varepsilon}) + \gamma \mathcal{Q}^{\mathcal{P}}(\boldsymbol{\varepsilon},\mathbf{c};\boldsymbol{\varepsilon}_k,\mathbf{c}_k) \tag{6.39}$$

with

$$\mathcal{Q}^{\mathcal{P}}(\boldsymbol{\varepsilon},\mathbf{c};\boldsymbol{\varepsilon}_k,\mathbf{c}_k) = \frac{1}{N^{\varepsilon}} \sum_{n=1}^{N^{\varepsilon}} \sum_{p=1}^{P} b_{p,n}^{P}(\boldsymbol{\varepsilon}_k,\mathbf{c}_k)|\varepsilon_n - c_p|^2. \tag{6.40}$$

The difference with $\mathcal{F}^{\mathcal{VP}}(\boldsymbol{\varepsilon},\mathbf{c})$ lies in the fact that the weights are kept fixed to their current value while updating the permittivity profile from $\boldsymbol{\varepsilon}_k$ to $\boldsymbol{\varepsilon}_{k+1}$. Hence, the gradient vector and Hessian matrix must be determined for $\mathcal{Q}^{\mathcal{P}}(\boldsymbol{\varepsilon},\mathbf{c};\boldsymbol{\varepsilon}_k,\mathbf{c}_k)$.

Gradient vector and Hessian matrix of $\mathcal{Q}^{\mathcal{P}}(\boldsymbol{\varepsilon},\mathbf{c};\boldsymbol{\varepsilon}_k,\mathbf{c}_k)$

As in Section 6.5.3, first order derivatives of $\mathcal{Q}^{\mathcal{P}}(\boldsymbol{\varepsilon},\mathbf{c};\boldsymbol{\varepsilon}_k,\mathbf{c}_k)$ with respect to the permittivity are collected in the vector $\boldsymbol{\Omega}_k$ and the gradient vector is represented as

$$\mathbf{g}_k^{\mathcal{P}} = \begin{bmatrix} \frac{\partial \mathcal{Q}^{\mathcal{P}}(\boldsymbol{\varepsilon},\mathbf{c};\boldsymbol{\varepsilon}_k,\mathbf{c}_k)}{\partial \varepsilon_{\nu}} \\ \frac{\partial \mathcal{Q}^{\mathcal{P}}(\boldsymbol{\varepsilon},\mathbf{c};\boldsymbol{\varepsilon}_k,\mathbf{c}_k)}{\partial \varepsilon_{\nu}^*} \end{bmatrix} = \begin{bmatrix} \boldsymbol{\Omega}_k^{\mathcal{P}} \\ \boldsymbol{\Omega}_k^{\mathcal{P}*} \end{bmatrix}. \tag{6.41}$$

Elements of $\boldsymbol{\Omega}_k^{\mathcal{P}*}$ are obtained as

$$\Omega_{k;\nu}^{\mathcal{P}*} = \frac{\partial \mathcal{Q}^{\mathcal{P}}(\boldsymbol{\varepsilon},\mathbf{c};\boldsymbol{\varepsilon}_k,\mathbf{c}_k)}{\partial \varepsilon_{\nu}^*} = \frac{1}{N^{\varepsilon}} \sum_{p=1}^{P} b_{p,\nu}^{P}(\boldsymbol{\varepsilon}_k,\mathbf{c}_k)(\varepsilon_{\nu} - c_p), \tag{6.42}$$

Also here, diagonal elements of the Hessian matrix are zero and the other second order derivatives are collected in the matrix $\boldsymbol{\Sigma}_k^{\mathcal{P}}$:

$$\mathbf{H}_k^{\mathcal{P}} = \begin{bmatrix} \frac{\partial^2 \mathcal{Q}^{\mathcal{P}}(\boldsymbol{\varepsilon},\mathbf{c};\boldsymbol{\varepsilon}_k,\mathbf{c}_k)}{\partial \varepsilon_{\nu} \partial \varepsilon_{\mu}} & \frac{\partial^2 \mathcal{Q}^{\mathcal{P}}(\boldsymbol{\varepsilon},\mathbf{c};\boldsymbol{\varepsilon}_k,\mathbf{c}_k)}{\partial \varepsilon_{\nu} \partial \varepsilon_{\mu}^*} \\ \frac{\partial^2 \mathcal{Q}^{\mathcal{P}}(\boldsymbol{\varepsilon},\mathbf{c};\boldsymbol{\varepsilon}_k,\mathbf{c}_k)}{\partial \varepsilon_{\nu}^* \partial \varepsilon_{\mu}} & \frac{\partial^2 \mathcal{Q}^{\mathcal{P}}(\boldsymbol{\varepsilon},\mathbf{c};\boldsymbol{\varepsilon}_k,\mathbf{c}_k)}{\partial \varepsilon_{\nu}^* \partial \varepsilon_{\mu}^*} \end{bmatrix} = \begin{bmatrix} 0 & \boldsymbol{\Sigma}_k^{\mathcal{P}} \\ \boldsymbol{\Sigma}_k^{\mathcal{P}} & 0 \end{bmatrix}. \tag{6.43}$$

Elements of $\boldsymbol{\Sigma}_k^{\mathcal{P}}$ are given by

$$\Sigma_{k;\nu,\mu}^{\mathcal{P}} = \frac{\partial^2 \mathcal{Q}^{\mathcal{P}}(\boldsymbol{\varepsilon},\mathbf{c};\boldsymbol{\varepsilon}_k,\mathbf{c}_k)}{\partial \varepsilon_{\nu} \partial \varepsilon_{\mu}^*} = \delta_{\nu,\mu} \frac{1}{N^{\varepsilon}} \sum_{p=1}^{P} b_{p,\nu}^{P}(\boldsymbol{\varepsilon}_k,\mathbf{c}_k). \tag{6.44}$$

Gradient vector and Hessian matrix of total cost function $\mathcal{F}^{\mathcal{Q}}(\boldsymbol{\varepsilon},\mathbf{c};\boldsymbol{\varepsilon}_k,\mathbf{c}_k)$

The gradient of the complete cost function is a combination of the data fit gradient $\mathbf{g}_k^{\mathcal{LS}}$ and the gradient $\mathbf{g}_k^{\mathcal{P}}$:

$$\mathbf{g}_k = \mathbf{g}_k^{\mathcal{LS}} + \gamma \mathbf{g}_k^{\mathcal{P}} \tag{6.45}$$

Similarly, the total Hessian is given by

$$\mathbf{H}_k = \mathbf{H}_k^{\mathcal{LS}} + \gamma \mathbf{H}_k^{\mathcal{P}}. \tag{6.46}$$

Update direction for permittivity

Also here, a Gauss-Newton scheme is used, hence the matrix $\mathbf{B}$ in the data fit Hessian (6.21) is omitted as a consequence of the linearization of the scattered field around the current iteration. The Gauss-Newton update direction is obtained as

$$\mathbf{H}_k \begin{bmatrix} \Delta\boldsymbol{\varepsilon}_k \\ \Delta\boldsymbol{\varepsilon}_k^* \end{bmatrix} = -\mathbf{g}_k. \tag{6.47}$$

Substituting the expression for the gradient vectors and Hessian matrices finally yields the update direction:

$$\left(\mathbf{J}_k^H \mathbf{J}_k + \lambda^2 \boldsymbol{\Sigma}_k^{\mathcal{P}}\right) \Delta\boldsymbol{\varepsilon}_k = -\left(\mathbf{J}_k^H [\mathbf{e}^{\text{scat}}(\boldsymbol{\varepsilon}_k) - \mathbf{e}^{\text{meas}}] + \lambda^2 \left(\boldsymbol{\Omega}_k^{\mathcal{P}}\right)^*\right), \tag{6.48}$$

Here, the trade-off parameter λ is given by $\lambda^2 = \gamma ||\mathbf{e}^{\text{meas}}||^2$.

6.5.5 The Gauss-Newton method with SROSVP regularization

Finally, the update direction is formulated for the stepwise relaxed object smoothed value picking regularization, for which the cost function takes the following form (6.15):

$$\mathcal{F}^{\mathcal{SROSVP}}(\boldsymbol{\varepsilon}, \mathbf{c}) = \mathcal{F}^{\mathcal{LS}}(\boldsymbol{\varepsilon}) + \gamma \mathcal{F}^{\mathcal{P}}(\boldsymbol{\varepsilon}, \mathbf{c}) + \zeta \mathcal{F}^{\mathcal{OS}}(\boldsymbol{\varepsilon}, \mathbf{c}), \tag{6.49}$$

in which the VP part $\mathcal{F}^{\mathcal{P}}(\boldsymbol{\varepsilon}, \mathbf{c})$ is given by

$$\mathcal{F}^{\mathcal{P}}(\boldsymbol{\varepsilon}, \mathbf{c}) = \frac{1}{N^{\varepsilon}} \sum_{n=1}^{N^{\varepsilon}} \sum_{p=1}^{P} b_{p,n}^{P}(\boldsymbol{\varepsilon}, \mathbf{c}) |\varepsilon_n - c_p|^2 \tag{6.50}$$

and the smoothing part $\mathcal{F}^{\mathcal{OS}}(\boldsymbol{\varepsilon}, \mathbf{c})$ is given by

$$\begin{aligned} \mathcal{F}^{\mathcal{OS}}(\boldsymbol{\varepsilon}, \mathbf{c}) \;=\; & \frac{1}{\mathcal{N}^{\mathcal{R}}} \sum_{k=0}^{N^x} \sum_{l=0}^{N^y-1} \mathbf{S}_{k,l}^1(\mathbf{c}) \; |\varepsilon_{k,l} - \varepsilon_{k-1,l}|^2 \\ & + \frac{1}{\mathcal{N}^{\mathcal{R}}} \sum_{k=0}^{N^x-1} \sum_{l=0}^{N^y} \mathbf{S}_{k,l}^2(\mathbf{c}) \; |\varepsilon_{k,l} - \varepsilon_{k,l-1}|^2. \end{aligned} \tag{6.51}$$

Since this type of regularization is also based on the concept of VP values, a two step optimization is applied in every iteration step. First, the permittivity profile is updated by constructing an update direction along which a line search is performed. Second, the VP values are updated by applying a constrained optimization scheme (i.e. an active set method [10]) on the cost function in case of purely stepwise relaxed value

picking regularization (6.10). Similarly as for the case of purely stepwise relaxed value picking regularization, VP values are also updated when a new VP value is introduced. After every update of the VP values, the smoothing direction matrices $\mathbf{S}^1(\mathbf{c})$ and $\mathbf{S}^2(\mathbf{c})$ are also updated.

Also for this new type of regularization, gradient and Hessian matrices are needed of all contributing terms in the total cost function. However, since the VP part of the cost function $\mathcal{F}^{\mathcal{P}}(\boldsymbol{\varepsilon},\mathbf{c})$ does not differ from the regularizing part of the cost function for the purely stepwise relaxed value picking regularization (6.14), the gradient and Hessian matrices for $\mathcal{F}^{\mathcal{P}}(\boldsymbol{\varepsilon},\mathbf{c})$ are identical to the ones given in Section 6.5.4. The VP weights are kept fixed to their current value while the permittivity profile is being updated from $\boldsymbol{\varepsilon}_k$ to $\boldsymbol{\varepsilon}_{k+1}$. Hence, the gradient vector and Hessian matrix that correspond to the VP term $\mathcal{F}^{\mathcal{P}}(\boldsymbol{\varepsilon},\mathbf{c})$, are in fact determined for the slightly modified VP term $Q^{\mathcal{P}}(\boldsymbol{\varepsilon},\mathbf{c};\boldsymbol{\varepsilon}_k,\mathbf{c}_k)$, given by

$$Q^{\mathcal{P}}(\boldsymbol{\varepsilon},\mathbf{c};\boldsymbol{\varepsilon}_k,\mathbf{c}_k)=\frac{1}{N^{\varepsilon}}\sum_{n=1}^{N^{\varepsilon}}\sum_{p=1}^{P}b_{p,n}^{P}(\boldsymbol{\varepsilon}_k,\mathbf{c}_k)|\varepsilon_n-c_p|^2. \tag{6.52}$$

The only gradient vector and Hessian matrix that still need to be determined are the ones that correspond to the smoothing part of the cost function $\mathcal{F}^{OS}(\boldsymbol{\varepsilon},\mathbf{c})$.

Gradient vector and Hessian matrix of $\mathcal{F}^{OS}(\boldsymbol{\varepsilon}_k)$

The gradient vector contains the first order derivatives of $\mathcal{F}^{OS}(\boldsymbol{\varepsilon}_k)$ with respect to the permittivity (collected in the vector $\boldsymbol{\Omega}_k^{OS}$) and with respect to its complex conjugate part (collected in the vector $\boldsymbol{\Omega}_k^{OS*}$). Hence,

$$\mathbf{g}_k^{OS}=\begin{bmatrix}\frac{\partial\mathcal{F}^{OS}}{\partial\varepsilon_{\nu}}\\ \frac{\partial\mathcal{F}^{OS}}{\partial\varepsilon_{\nu}^{*}}\end{bmatrix}=\begin{bmatrix}\boldsymbol{\Omega}_k^{OS}\\ \boldsymbol{\Omega}_k^{OS*}\end{bmatrix}. \tag{6.53}$$

Here, elements of $\boldsymbol{\Omega}_k^{OS*}$ are obtained as

$$\begin{aligned}\Omega_{k;\nu}^{OS*} &= \frac{\partial\mathcal{F}^{OS}}{\partial\varepsilon_{\nu}^{*}}=\frac{\partial\mathcal{F}^{OS}}{\partial\varepsilon_{i,j}^{*}}\\ &= \frac{2}{\mathcal{N}_{\mathcal{R}}}\left[\mathbf{S}_{i,j}^{1}(\varepsilon_{i,j}-\varepsilon_{i-1,j})+\mathbf{S}_{i,j}^{2}(\varepsilon_{i,j}-\varepsilon_{i,j-1})\right.\\ &\quad\left.+\mathbf{S}_{i,j}^{3}(\varepsilon_{i,j}-\varepsilon_{i+1,j})+\mathbf{S}_{i,j}^{4}(\varepsilon_{i,j}-\varepsilon_{i,j+1})\right].\end{aligned} \tag{6.54}$$

Note that two additional smoothing direction matrices $\mathbf{S}^3$ and $\mathbf{S}^4$ are introduced to account for cells above and to the right of the current cell.

The Hessian matrix $\mathbf{H}_k^{\mathcal{OS}}$ is constructed as follows:

$$\mathbf{H}_k^{\mathcal{OS}} = \begin{bmatrix} \frac{\partial^2 \mathcal{F}^{\mathcal{OS}}}{\partial \varepsilon_\nu \partial \varepsilon_\mu} & \frac{\partial^2 \mathcal{F}^{\mathcal{OS}}}{\partial \varepsilon_\nu \partial \varepsilon_\mu^*} \\ \frac{\partial^2 \mathcal{F}^{\mathcal{OS}}}{\partial \varepsilon_\nu^* \partial \varepsilon_\mu} & \frac{\partial^2 \mathcal{F}^{\mathcal{OS}}}{\partial \varepsilon_\nu^* \partial \varepsilon_\mu^*} \end{bmatrix} = \begin{bmatrix} 0 & \mathbf{\Sigma}_k^{\mathcal{OS}} \\ \mathbf{\Sigma}_k^{\mathcal{OS}} & 0 \end{bmatrix}. \tag{6.55}$$

The diagonal elements of $\mathbf{\Sigma}_k^{\mathcal{OS}}$ are given by

$$\Sigma_{k;\nu,\nu}^{\mathcal{OS}} = \frac{\partial^2 \mathcal{F}^{\mathcal{OS}}}{\partial \varepsilon_\nu \partial \varepsilon_\nu^*} = \frac{\partial^2 \mathcal{F}^{\mathcal{OS}}}{\partial \varepsilon_{i,j} \partial \varepsilon_{i,j}^*} = \frac{2}{\mathcal{NR}} \left[\mathbf{S}_{k,l}^1 + \mathbf{S}_{k,l}^2 + \mathbf{S}_{k,l}^3 + \mathbf{S}_{k,l}^4 \right]. \tag{6.56}$$

Non-diagonal elements of $\mathbf{\Sigma}_k^{\mathcal{OS}}$ ($\Sigma_{k;\nu,\mu}^{\mathcal{OS}}$) are zero except if ν denotes a neighbor of μ, i.e. if (m,n) is a neighbor of (i,j):

$$\begin{aligned} \Sigma_{k;\nu,\mu}^{\mathcal{OS}} &= \frac{\partial^2 \mathcal{F}^{\mathcal{OS}}}{\partial \varepsilon_\nu \partial \varepsilon_\mu^*} = \frac{\partial^2 \mathcal{F}^{\mathcal{OS}}}{\partial \varepsilon_{m,n} \partial \varepsilon_{i,j}^*} \\ &= \begin{cases} -\frac{2}{\mathcal{NR}} \mathbf{S}_{i,j}^1 : & m = i-1, n = j \\ -\frac{2}{\mathcal{NR}} \mathbf{S}_{i,j}^2 : & m = i, n = j-1 \\ -\frac{2}{\mathcal{NR}} \mathbf{S}_{i,j}^3 : & m = i+1, n = j \\ -\frac{2}{\mathcal{NR}} \mathbf{S}_{i,j}^4 : & m = i, n = j+1 \end{cases} \end{aligned} \tag{6.57}$$

Gradient vector and Hessian matrix of the total cost function $\mathcal{F}^{\mathcal{SROSVP}}(\boldsymbol{\varepsilon}_k)$

By applying linearity, the gradient and Hessian matrix of the complete cost function (6.15) are obtained as

$$\mathbf{g}_k = \mathbf{g}_k^{\mathcal{LS}} + \gamma \mathbf{g}_k^{\mathcal{P}} + \zeta \mathbf{g}_k^{\mathcal{OS}} \tag{6.58}$$

and

$$\mathbf{H}_k = \mathbf{H}_k^{\mathcal{LS}} + \gamma \mathbf{H}_k^{\mathcal{P}} + \zeta \mathbf{H}_k^{\mathcal{OS}}. \tag{6.59}$$

Update direction for the permittivity profile

We also use a Gauss-Newton scheme to derive an update direction for the permittivity for this type of regularization. Hence, the matrix $\mathbf{B}$ in the data fit Hessian $\mathbf{H}_k^{\mathcal{LS}}$ (6.21) is omitted. This yields a total Hessian matrix given by

$$\mathbf{H}_k = \begin{bmatrix} \mathbf{0} & \frac{1}{\mathcal{N}^{\mathcal{LS}}} \mathbf{J}_k^T \mathbf{J}_k^* + \gamma \mathbf{\Sigma}_k^{\mathcal{P}} + \zeta \mathbf{\Sigma}_k^{\mathcal{OS}} \\ \frac{1}{\mathcal{N}^{\mathcal{LS}}} \mathbf{J}_k^H \mathbf{J}_k + \gamma \mathbf{\Sigma}_k^{\mathcal{P}} + \zeta \mathbf{\Sigma}_k^{\mathcal{OS}} & \mathbf{0} \end{bmatrix}. \tag{6.60}$$

Replacing all expressions of the contributing terms in the formula for the total gradient yields

$$\mathbf{g}_k = \begin{bmatrix} \frac{1}{\mathcal{N}^{\mathcal{LS}}} \mathbf{J}_k^T [\mathbf{e}^{\text{scat}}(\boldsymbol{\varepsilon}_k) - \mathbf{e}^{\text{meas}}]^* + \gamma \mathbf{\Omega}_k^{\mathcal{P}} + \zeta \mathbf{\Omega}_k^{\mathcal{OS}} \\ \frac{1}{\mathcal{N}^{\mathcal{LS}}} \mathbf{J}_k^H [\mathbf{e}^{\text{scat}}(\boldsymbol{\varepsilon}_k) - \mathbf{e}^{\text{meas}}] + \gamma \mathbf{\Omega}_k^{\mathcal{P}*} + \zeta \mathbf{\Omega}_k^{\mathcal{OS}*} \end{bmatrix} \tag{6.61}$$

Substituting expressions (6.60) and (6.61) in the Gauss-Newton update direction (6.18) yields the update direction:

$$\left(\frac{1}{\mathcal{N}^{\mathcal{LS}}}\mathbf{J}_k^H\mathbf{J}_k+\gamma\boldsymbol{\Sigma}_k^{\mathcal{P}}+\zeta\boldsymbol{\Sigma}_k^{\mathcal{OS}}\right)\boldsymbol{\Delta\varepsilon}_k= -\left(\frac{1}{\mathcal{N}^{\mathcal{LS}}}\mathbf{J}_k^H[\mathbf{e}^{\text{scat}}(\boldsymbol{\varepsilon}_k)-\mathbf{e}^{\text{meas}}]+\gamma\boldsymbol{\Omega}_k^{\mathcal{P}*}+\zeta\boldsymbol{\Omega}_k^{\mathcal{OS}*}\right). \quad (6.62)$$

To obtain a formulation for the update direction in the same form as (6.37) and (6.48), we define two matrices $\boldsymbol{\Sigma}_k$ and $\boldsymbol{\Omega}_k$ as follows:

$$\boldsymbol{\Sigma}_k=\gamma\,\boldsymbol{\Sigma}_k^{\mathcal{P}}+\zeta\,\boldsymbol{\Sigma}_k^{\mathcal{OS}} \quad (6.63)$$

and

$$\boldsymbol{\Omega}_k=\gamma\,\boldsymbol{\Omega}_k^{\mathcal{P}}+\zeta\,\boldsymbol{\Omega}_k^{\mathcal{OS}}. \quad (6.64)$$

Hence, the update direction for the permittivity profile can we written as

$$\left(\mathbf{J}_k^H\mathbf{J}_k+\lambda^2\boldsymbol{\Sigma}_k\right)\boldsymbol{\Delta\varepsilon}_k=-\left(\mathbf{J}_k^H[\mathbf{e}^{\text{scat}}(\boldsymbol{\varepsilon}_k)-\mathbf{e}^{\text{meas}}]+\lambda^2\boldsymbol{\Omega}_k^*\right), \quad (6.65)$$

with the trade-off parameter λ in this formulation given by $\lambda^2=||\mathbf{e}^{\text{meas}}||^2=\mathcal{N}^{\mathcal{LS}}$.

6.5.6 Approximate line search to determine the permittivity step size

Once the update direction for the permittivity is constructed, an approximate line search is performed along this direction. This routine provides the step size β_k that yields the next permittivity guess $\boldsymbol{\varepsilon}_{k+1}=\boldsymbol{\varepsilon}_k+\beta_k\boldsymbol{\Delta\varepsilon}_k$. The step size β_k is such that $\mathcal{F}(\beta_k)=\mathcal{F}(\boldsymbol{\varepsilon}_k+\beta_k\boldsymbol{\Delta\varepsilon}_k)$ lies close to a local minimum of $\mathcal{F}$ along the update direction $\boldsymbol{\Delta\varepsilon}_k$. In case of the multiplicative smoothing regularization, the cost function $\mathcal{F}$ in the line search is the same as for the construction of the update direction, namely $\mathcal{F}^{\mathcal{MS}}$. In case of the value picking regularization, the update direction is determined from a modified cost function $\mathcal{F}^{\mathcal{Q}}$, whereas in the line search the actual cost function $\mathcal{F}^{\mathcal{VP}}$ is used. We refer to [10] for detailed information on the implementation of an approximate line search.

The advantage of incorporating a line search routine is that it improves the convergence. However, the line search routine requires that the search direction is a *descent* direction or that

$$\left.\frac{\partial\mathcal{F}}{\partial\beta_k}\right|_{\beta_k=0}<0. \quad (6.66)$$

This restriction is equal to

$$\left.\sum_{\nu=1}^{N^{\varepsilon}}\frac{\partial\mathcal{F}}{\partial\varepsilon_\nu}\boldsymbol{\Delta\varepsilon}_{k,\nu}+\frac{\partial\mathcal{F}}{\partial\varepsilon_\nu^*}\boldsymbol{\Delta\varepsilon}_{k,\nu}^*\right|_{\beta_k=0}=[\boldsymbol{\Delta\varepsilon}_k^T\boldsymbol{\Delta\varepsilon}_k^H]\mathbf{g}_k<0, \quad (6.67)$$

with $\mathbf{g}_k$ the gradient of the cost function $\mathcal{F}$ as computed for iteration k. In [10], it is demonstrated that an optimization method that searches successively along different descent paths using an approximate line search, converges to a (local) minimizer provided that the search directions are uniformly bounded away from orthogonality with the steepest descent direction, given by $-\mathbf{g}_k$. In the following, we will check this requirement in case of the Gauss-Newton method as applied in the various subsections of Section 6.5.

Approximate line search with the Gauss-Newton method

For Gauss-Newton optimization without regularization, the update direction is given by (6.24). Since the hermitian matrix $\mathbf{J}_k^H \mathbf{J}_k$ is at least positive semi-definite, the update direction is never uphill. If the gradient vector $\mathbf{g}_k$ is split in two

$$\mathbf{g}_k = \begin{bmatrix} \mathbf{g}_k^a \\ \mathbf{g}_k^b \end{bmatrix}, \tag{6.68}$$

the update direction can be written as

$$\Delta\boldsymbol{\varepsilon}_k = -\left(\mathbf{J}_k^H \mathbf{J}_k\right)^{-1} \mathbf{g}_k^b = -\left(\mathbf{J}_k^H \mathbf{J}_k\right)^{-1} \mathbf{g}_k^{a*} = -\mathbf{A}\mathbf{g}_k^{a*}. \tag{6.69}$$

By construction, $\mathbf{A}$ is hermitian and positive semi-definite. Hence,

$$\begin{aligned} \Delta\boldsymbol{\varepsilon}_k^T \mathbf{g}_k^a &= -\left[\mathbf{A}\mathbf{g}_k^{a*}\right]^T \mathbf{g}_k^a \\ &= -\mathbf{g}_k^{aH} \mathbf{A}^T \mathbf{g}_k^a \\ &\leq 0. \end{aligned} \tag{6.70}$$

Therefore, the update direction $\Delta\boldsymbol{\varepsilon}_k$ either lies along a level contour of the cost function or is a descent direction.

Approximate line search with the modified Gauss-Newton method with MS regularization

If the multiplicative smoothing regularization is applied, the modified Gauss-Newton direction is given by (6.37). In (6.37), the right hand side is proportional to the total gradient $\mathbf{g}_k^{a*}$. In the left hand side, $\left(\mathbf{J}_k^H \mathbf{J}_k + \lambda^2 \boldsymbol{\Sigma}_k^{\mathcal{R}}\right)$ is always positive definite (provided $\lambda \neq 0$) since $\mathbf{J}_k^H \mathbf{J}_k$ is positive semi-definite and $\boldsymbol{\Sigma}_k^{\mathcal{R}}$ is strictly positive definite. To illustrate that $\boldsymbol{\Sigma}_k^{\mathcal{R}}$ ((6.29)-(6.30)) is strictly positive, we make the following considerations [33]: (i) $\boldsymbol{\Sigma}_k^{\mathcal{R}}$ is a real and symmetric matrix, consequently it is also hermitian, (ii) $\boldsymbol{\Sigma}_k^{\mathcal{R}}$ is a constant matrix, i.e. independent of the permittivity profile, since $\mathcal{F}^{\mathcal{R}}(\boldsymbol{\varepsilon}, \boldsymbol{\varepsilon}^*)$ is a quadratic function, and (iii) $\mathcal{F}^{\mathcal{R}}(\boldsymbol{\varepsilon}, \boldsymbol{\varepsilon}^*) \geq 0$, $\forall \boldsymbol{\varepsilon}$ and $\mathcal{F}^{\mathcal{R}}(\boldsymbol{\varepsilon}, \boldsymbol{\varepsilon}^*) = 0$ if and only if all $\varepsilon_{k,l} = 1$, due to the condition that $\varepsilon(\mathbf{r}) = \varepsilon_0$ outside the reconstruction domain. Consequently, $\mathcal{F}^{\mathcal{R}}$ has a unique minimizer, which for a quadratic function means that

its curvature must be strictly positive. Hence, for every non-zero N^{ε}-dimensional complex vector $\mathbf{s}$ the following must hold:

$$\begin{bmatrix}\mathbf{s}^T & \mathbf{s}^H\end{bmatrix}\mathbf{H}_k^{\mathcal{R}}\begin{bmatrix}\mathbf{s}\\ \mathbf{s}^*\end{bmatrix} = \begin{bmatrix}\mathbf{s}^T & \mathbf{s}^H\end{bmatrix}\begin{bmatrix}0 & \boldsymbol{\Sigma}_k^{\mathcal{R}}\\ \boldsymbol{\Sigma}_k^{\mathcal{R}} & 0\end{bmatrix}\begin{bmatrix}\mathbf{s}\\ \mathbf{s}^*\end{bmatrix} = 2\mathbf{s}^H\boldsymbol{\Sigma}_k^{\mathcal{R}}\mathbf{s} > 0 \tag{6.71}$$

Thus $\boldsymbol{\Sigma}_k^{\mathcal{R}}$ must be positive definite.

The presence of the regularization term $\lambda^2\boldsymbol{\Sigma}_k^{\mathcal{R}}$ ensures that $\boldsymbol{\Delta\varepsilon}_k$ is a strictly descent direction. Hence, the optimization will converge to a minimum of the MS regularized cost function.

Approximate line search with the Gauss-Newton method with SRVP regularization

Checking the descent property for the update direction for the SRVP regularization, is very similar to the previous case. Now, the update direction is given by (6.48). The right hand side of (6.48) is again proportional to the total gradient, whereas in the left hand side $\left(\mathbf{J}_k^H\mathbf{J}_k + \lambda^2\boldsymbol{\Sigma}_k^{\mathcal{P}}\right)$ is always positive definite for $\lambda \neq 0$ since $\boldsymbol{\Sigma}_k^{\mathcal{P}}$ is a diagonal matrix with strictly positive diagonal elements. Therefore, the update direction is always a descent direction. Towards the end op the optimization, VP values have been assigned to every permittivity unknown. Hence,

$$\boldsymbol{\Sigma}_k^{\mathcal{P}} \rightarrow \frac{1}{N^{\varepsilon}}\mathbf{I}, \tag{6.72}$$

where $\mathbf{I}$ denotes a $N^{\varepsilon} \times N^{\varepsilon}$ unity matrix.

Approximate line search with the Gauss-Newton method with SROSVP regularization

The formulation for the update direction for the stepwise relaxed object smoothed value picking regularization (6.65) is very similar to the update directions for the other types of regularization ((6.37) and (6.48)). Also here, the right hand side of (6.65) is proportional to the total gradient and the term $\left(\mathbf{J}_k^H\mathbf{J}_k + \lambda^2\boldsymbol{\Sigma}_k\right)$ in the left hand side is positive definite for $\lambda \neq 0$. The matrix $\boldsymbol{\Sigma}_k$ is by construction positive definite ($\boldsymbol{\Sigma}_k = \gamma\,\boldsymbol{\Sigma}_k^{\mathcal{P}} + \zeta\,\boldsymbol{\Sigma}_k^{OS}$, with γ and ζ not simultaneously zero) since $\boldsymbol{\Sigma}_k^{\mathcal{P}}$ and $\boldsymbol{\Sigma}_k^{OS}$ are positive definite matrices. By consequence, the update direction based on stepwise relaxed value picking regularization is always a descent direction.

6.6. Derivatives of the forward model

For the construction of the gradient vector (6.20) and the Hessian matrix (6.21) of the data fit cost function in each iteration, the derivatives of the scattered field with respect

to the permittivity unknowns $\partial \mathbf{E}^{\mathrm{s}}(\mathbf{r},z)/\partial\varepsilon_{\nu}$ are required. In this section, an analytical expression for these derivatives is determined.

Measurement data are three-dimensional electromagnetic fields, whereas in the forward solver the three-dimensional simulated fields are Fourier transformed along the invariant (z-) direction. Hence, the derivatives of the scattered field with respect to the permittivity unknowns are obtained as

$$\frac{\partial \mathbf{E}^{\mathrm{s}}(\mathbf{r},z)}{\partial\varepsilon_{\nu}} = \frac{1}{2\pi}\sum_{k_z}\frac{\partial \widehat{\mathbf{E}}^{\mathrm{s}}(\mathbf{r},k_z)}{\partial\varepsilon_{\nu}}e^{jk_z z}. \tag{6.73}$$

To derive an expression for $\partial \widehat{\mathbf{E}}^{\mathrm{s}}(\mathbf{r},k_z)/\partial\varepsilon_{\nu}$, an operator $\mathcal{G}^{\mathcal{V}}$, acting on a vector function $\mathbf{p}$ with support $\mathcal{V}$, is defined as

$$[\mathcal{G}^{\mathcal{V}}(\mathbf{p})](\mathbf{r}) = j\omega\mu_0\left(\mathbf{I}+\frac{1}{k_0^2}\widehat{\nabla}\widehat{\nabla}\right)\cdot\int_{\mathcal{V}}\widehat{G}(\mathbf{r},\mathbf{r}';k_z)\mathbf{p}(\mathbf{r}')\mathrm{d}\mathbf{r}'. \tag{6.74}$$

In this way, the CSIE (2.26) for the total electric field $\widehat{\mathbf{E}}(\mathbf{r},k_z)$ can be formulated as

$$\begin{aligned}\widehat{\mathbf{E}}(\mathbf{r},k_z) &= [\mathcal{G}^{\mathcal{S}}(\widehat{\mathbf{J}}^{\mathrm{i}})](\mathbf{r})+[\mathcal{G}^{\mathcal{D}}(\widehat{\mathbf{J}}^{\mathrm{s}})](\mathbf{r})\\ &= [\mathcal{G}^{\mathcal{S}}(\widehat{\mathbf{J}}^{\mathrm{i}})](\mathbf{r})+[\mathcal{G}^{\mathcal{D}}(-j\omega[\varepsilon-\varepsilon_0]\widehat{\mathbf{E}})](\mathbf{r}).\end{aligned} \tag{6.75}$$

Since the incident field does not depend on the permittivity, the derivative with respect to the permittivity of the scattered field is equal to the derivative of the total field:

$$\begin{aligned}\frac{\partial \widehat{\mathbf{E}}^{\mathrm{s}}(\mathbf{r},k_z)}{\partial\varepsilon_{\nu}} &= \frac{\partial \widehat{\mathbf{E}}(\mathbf{r},k_z)}{\partial\varepsilon_{\nu}}\\ &= \frac{\partial}{\partial\varepsilon_{\nu}}\left([\mathcal{G}^{\mathcal{S}}(\widehat{\mathbf{J}}^{\mathrm{i}})](\mathbf{r})+[\mathcal{G}^{\mathcal{D}}(-j\omega[\varepsilon-\varepsilon_0]\widehat{\mathbf{E}})](\mathbf{r})\right)\\ &= [\mathcal{G}^{\mathcal{D}}(-j\omega\varepsilon_0\Phi_{\nu}\widehat{\mathbf{E}})](\mathbf{r})+[\mathcal{G}^{\mathcal{D}}(-j\omega[\varepsilon-\varepsilon_0]\frac{\partial \widehat{\mathbf{E}}^{\mathrm{s}}(\mathbf{r},k_z)}{\partial\varepsilon_{\nu}})](\mathbf{r}),\end{aligned} \tag{6.76}$$

where Φ_{ν} is defined in (6.2). When this equation is compared to (6.75), it is clear that $\partial \widehat{\mathbf{E}}^{\mathrm{s}}(\mathbf{r},k_z)/\partial\varepsilon_{\nu}$ satisfies a similar CSIE equation, where $\widehat{\mathbf{J}}^{\mathrm{i}}$ is replaced by a current density $-j\omega\varepsilon_0\Phi_{\nu}\widehat{\mathbf{E}}$ in cell ν.

We will now formulate the total field in terms of the applied current density $\widehat{\mathbf{J}}^{\mathrm{i}}$ since it will be sufficient to replace $\widehat{\mathbf{J}}^{\mathrm{i}}$ by $-j\omega\varepsilon_0\Phi_{\nu}\widehat{\mathbf{E}}$ in this expression to obtain an expression for the scattered field derivatives $\partial \widehat{\mathbf{E}}^{\mathrm{s}}(\mathbf{r},k_z)/\partial\varepsilon_{\nu}$. This is done in the following.

First, two different 3×3 dyadic Green's functions are defined: $\widehat{\mathbf{G}}(\mathbf{r},\mathbf{r}';k_z)$ for free space and $\widehat{\mathbf{G}}_{\mathrm{inh}}(\mathbf{r},\mathbf{r}';k_z)$ for inhomogeneous space (i.e. in presence of the scatterer). The different columns of the dyadic Green's function of free-space $\widehat{\mathbf{G}}(\mathbf{r},\mathbf{r}';k_z)$ can be constructed by applying a 2D current density along a unit vector $\mathbf{u}$ in a point $\mathbf{r}$" for the

three orthogonal directions $\mathbf{u} = \mathbf{u}_x$, $\mathbf{u} = \mathbf{u}_y$ and $\mathbf{u} = \mathbf{u}_z$ with current density

$$\widehat{\mathbf{J}}_\delta(\mathbf{r}) = \frac{1}{j\omega\mu_0}\delta(\mathbf{r}-\mathbf{r}")\mathbf{u} \tag{6.77}$$

in free space. The dyadic Green's function of inhomogeneous space $\widehat{\mathbf{G}}_{\text{inh}}(\mathbf{r},\mathbf{r}';k_z)$ is constructed in a similar way: by using the same 2D current densities (in points $\mathbf{r}"$ along a unit vector $\mathbf{u}$ with current density $\widehat{\mathbf{J}}_\delta(\mathbf{r})$), but now generating incident fields on the scattering objects. The corresponding total fields yield the different columns of the inhomogeneous dyadic Green's function:

$$\widehat{\mathbf{E}}(\mathbf{r},k_z) = j\omega\mu_0 \int_{\mathcal{D}} \widehat{\mathbf{G}}_{\text{inh}}(\mathbf{r},\mathbf{r}';k_z)\cdot\widehat{\mathbf{J}}_\delta(\mathbf{r}')\mathrm{d}\mathbf{r}' = \widehat{\mathbf{G}}_{\text{inh}}(\mathbf{r},\mathbf{r}";k_z)\cdot\mathbf{u}. \tag{6.78}$$

Hence, the total electric field, resulting from any applied current $\widehat{\mathbf{J}}^{\text{i}}(\mathbf{r},k_z)$ in presence of the scatterer can now be expressed in terms of $\widehat{\mathbf{G}}_{\text{inh}}$ as

$$\widehat{\mathbf{E}}(\mathbf{r},k_z) = j\omega\mu_0 \int_{\mathcal{D}} \widehat{\mathbf{G}}_{\text{inh}}(\mathbf{r},\mathbf{r}';k_z)\cdot\widehat{\mathbf{J}}^{\text{i}}(\mathbf{r}',k_z)\mathrm{d}\mathbf{r}'. \tag{6.79}$$

As a result, by replacing $\widehat{\mathbf{J}}^{\text{i}}(\mathbf{r},k_z)$ with $-j\omega\varepsilon_0\Phi_\nu\widehat{\mathbf{E}}$ in the above expression, the derivatives of the scattered field with respect to the permittivity unknowns are given by

$$\begin{aligned}\frac{\partial\widehat{\mathbf{E}}^{\text{s}}(\mathbf{r},k_z)}{\partial\varepsilon_\nu} &= j\omega\mu_0\int_{\mathcal{D}}\widehat{\mathbf{G}}_{\text{inh}}(\mathbf{r},\mathbf{r}';k_z)\cdot\Big(-j\omega\varepsilon_0\Phi_\nu(\mathbf{r}')\widehat{\mathbf{E}}(\mathbf{r}',k_z)\Big)\,\mathrm{d}\mathbf{r}' \\ &= k_0^2\int_{\mathcal{D}}\Phi_\nu(\mathbf{r}')\widehat{\mathbf{G}}_{\text{inh}}(\mathbf{r},\mathbf{r}';k_z)\cdot\widehat{\mathbf{E}}(\mathbf{r}',k_z)\mathrm{d}\mathbf{r}'.\end{aligned} \tag{6.80}$$

As mentioned in Section 6.2, the data vector $\mathbf{e}^{\text{meas}}$ contains the elements $\mathbf{E}^{\text{meas}}_{t,p}(\mathbf{r}_r^A,z_r^A)\cdot\mathbf{u}^A_{r,p'}$ and the simulated scattered field vector $\mathbf{e}^{\text{scat}}$ consists of elements $\mathbf{E}^{\text{s}}_{t,p}(\mathbf{r}_r^A,z_r^A)\cdot\mathbf{u}^A_{r,p'}$. These respectively correspond to measured and simulated scattered fields in receiver points $(\mathbf{r}_r^A,z_r^A)$, directed along $\mathbf{u}^A_{r,p'}$, resulting from an illumination with excitation in $(\mathbf{r}_t^A,z_t^A)$ and polarized along $\mathbf{u}^A_{t,p}$. Following (6.73), the derivatives of the simulated scattered field with respect to ε_ν are thus given by

$$\frac{\partial\mathbf{E}^{\text{s}}_{t,p}}{\partial\varepsilon_\nu}(\mathbf{r}_r^A,z_r^A)\cdot\mathbf{u}^A_{r,p'} = \frac{1}{2\pi}\sum_{k_z}\frac{\partial\widehat{\mathbf{E}}^{\text{s}}_{t,p}}{\partial\varepsilon_\nu}(\mathbf{r}_r^A,k_z)\cdot\mathbf{u}^A_{r,p'}e^{jk_zz_r^A} \tag{6.81}$$

where, based on (6.80), each spectral component is given by

$$\frac{\partial\widehat{\mathbf{E}}^{\text{s}}_{t,p}}{\partial\varepsilon_\nu}(\mathbf{r}_r^A,k_z)\cdot\mathbf{u}^A_{r,p'} = k_0^2\int_{\mathcal{D}}\Phi_\nu(\mathbf{r}')\;\mathbf{u}^A_{r,p'}\cdot\widehat{\mathbf{G}}_{\text{inh}}(\mathbf{r}_r^A,\mathbf{r}';k_z)\cdot\widehat{\mathbf{E}}_{t,p}(\mathbf{r}',k_z)\mathrm{d}\mathbf{r}'. \tag{6.82}$$

Due to reciprocity $\widehat{\mathbf{G}}_{\text{inh}}(\mathbf{r}_r^A,\mathbf{r}';k_z) = \widehat{\mathbf{G}}^{\text{T}}_{\text{inh}}(\mathbf{r}',\mathbf{r}_r^A;k_z)$ and since the columns of the dyadic Green's function can be constructed by using 2D dipoles as incident fields (6.78), the

term $\mathbf{u}^A_{r,p'} \cdot \widehat{\mathbf{G}}_{\text{inh}}(\mathbf{r}^A_r, \mathbf{r}'; k_z)$ in (6.82) can be replaced by

$$\mathbf{u}^A_{r,p'} \cdot \widehat{\mathbf{G}}_{\text{inh}}(\mathbf{r}^A_r, \mathbf{r}'; k_z) = \widehat{\mathbf{G}}_{\text{inh}}(\mathbf{r}', \mathbf{r}^A_r; k_z) \cdot \mathbf{u}^A_{r,p'} = \widehat{\mathbf{E}}^{\text{dipole}}_{r,p'}(\mathbf{r}', k_z). \tag{6.83}$$

Here, $\widehat{\mathbf{E}}^{\text{dipole}}_{r,p'}(\mathbf{r}', k_z)$ is the total field generated by a 2D dipole in the point $\mathbf{r}^A_r$, polarized along $\mathbf{u}^A_{r,p'}$ in presence of the scatterer. Introducing (6.83) into (6.82) finally yields the searched expression:

$$\frac{\partial \widehat{\mathbf{E}}^{\text{s}}_{t,p}}{\partial \varepsilon_\nu}(\mathbf{r}^A_r, k_z) \cdot \mathbf{u}^A_{r,p'} = k_0^2 \int_{\mathcal{D}} \Phi_\nu(\mathbf{r}')\, \widehat{\mathbf{E}}_{t,p}(\mathbf{r}', k_z) \cdot \widehat{\mathbf{E}}^{\text{dipole}}_{r,p'}(\mathbf{r}', k_z) \mathrm{d}\mathbf{r}'. \tag{6.84}$$

For the computation of the derivatives of the simulated scattered field with respect to the current permittivity profile, two groups of forward problems must be solved:

- *regular* forward problems: to construct $\widehat{\mathbf{E}}_{t,p}(\mathbf{r}', k_z)$, there is a forward problem for each spectral component k_z of the incident field (e.g. a Gaussian Beam), for each incidence direction and for all N^P_t polarizations.
- *dipole* forward problems: to construct $\widehat{\mathbf{E}}^{\text{dipole}}_{r,p'}(\mathbf{r}', k_z)$, there is a forward problem for each spectral component k_z of the incident field, for each receiver position $\mathbf{r}^A_r$, now considered as an excitation point, and for all N^P_r receiver polarizations.

Consequently, in total, there are $\#k_z\,(N^T\,N^P_t + N^R\,N^P_t)$ forward problems which have to be solved for constructing the derivatives of the simulated scattered field with respect to the current permittivity profile. Of course, the regular forward problems with the real incident fields already have been solved to determine the scattered fields and cost function, hence only the dipole forward problems yield an extra computational cost.

6.7. The partial inverse problem grid approach

The proposed inverse scattering method naturally allows for a forward problem grid that extends the inverse problem grid. Hence, it is possible to account for known objects in the immediate neighborhood of the unknown scatterer, as illustrated in Fig. 6.6. The dimensions and positioning of the inverse problem grid are chosen to cover only the expected area of the unknown scatterer. All known background objects (e.g. having permittivities ε_1 and ε_2 in Fig. 6.6) are located inside the forward problem grid, but outside the unknown scatterer area. Only cells inside the inverse problem grid are optimized for their respective permittivities. In this approach, it is even possible to have multiple separate inverse problem grids inside one larger forward problem grid. The total number of permittivity unknowns then equals the total number of cells in all inverse problem grids. To indicate that an inverse problem grid is part of a larger forward problem grid, we call the inverse problem grid in this case the *partial inverse problem grid*.

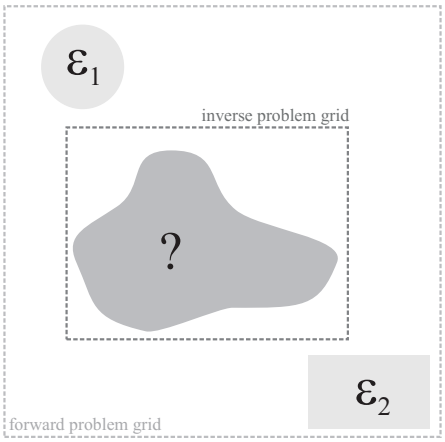

Figure 6.6: Incorporation of the inverse problem grid inside a larger forward problem grid.

For the cost function evaluation in the inverse scattering method, a mapping is necessary between the partial inverse problem grid (usually with the coarser cells) and the surrounding (overlapping) forward problem grid (usually with the finer cells). This mapping is performed at two levels, see Fig. 6.7:

1. To evaluate the data fit part of the cost function, the partial inverse problem grid is subdivided in smaller cells with the same cell size Δ as the forward problem grid.

2. To evaluate the regularizing part of the cost function for the multiplicative smoothing or stepwise relaxed object smoothed value picking regularization, it is sometimes necessary to step outside the partial inverse problem grid with cell size Δ_ε. This is the case when the permittivity of a coarse cell adjacent to a border cell is needed, which now no longer can be assumed to be free space. Therefore, the permittivities of all forward problem cells within this coarse cell are averaged, yielding one permittivity value for the corresponding coarse grid cell, see Fig. 6.7.

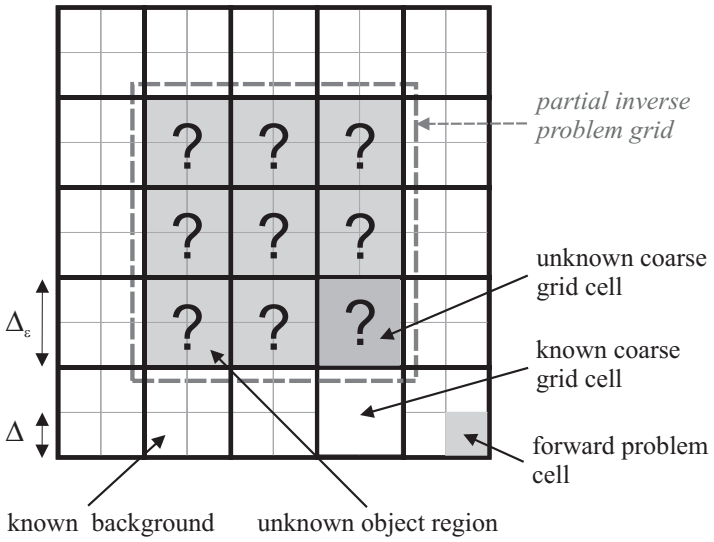

Figure 6.7: The different types of cells in the partial inverse problem grid approach.

6.8. Conclusion

In this chapter, we have detailed the theoretical aspects and the implementation of the proposed inverse scattering method. Iterative techniques to solve the non-linear quantitative inverse scattering problem, as known for microwave imaging, have been adapted and applied to the millimeter wave range for plane wave and Gaussian beam illuminations.

Two regularization techniques –both developed at the department of Information Technology– have been implemented: the multiplicative smoothing regularization (a spatial regularization method) and the stepwise relaxed value picking regularization (a non-spatial technique). In this PhD work, we have combined both methods into a new regularization method, denoted as the stepwise relaxed object smoothed value picking regularization. As the value picking regularization, this new regularization method favors permittivity profiles consisting of few distinct permittivity values and is ideally suited to reconstruct piecewise homogeneous objects. It differs from the value picking method by imposing smoothness within the homogeneous regions, deduced from the VP weights in each iteration.

It is outlined how the different regularization strategies are embedded in the updating scheme for the permittivity profile. First, an update direction is derived by applying a Gauss-Newton method. Afterwards, an approximate line search is performed along this direction, yielding the next permittivity profile. The gradient vector and the Hessian matrix of the data fit cost function depend on the derivatives of the scattered

field with respect to the permittivity unknowns. In this PhD work, we have formulated analytical expressions for these derivatives for the 2.5D case.

Finally, to account for large scattering systems, a partial inverse problem grid description is introduced within the proposed inversion scheme. This approach restricts the inversion domain to a limited area surrounded by known background objects and hence strongly reduces the number of permittivity unknowns.

Bibliography

[1] J. De Zaeytijd, "On the 3D electromagnetic quantitative inverse scattering problem: algorithms and regularization," Ph.D. dissertation, Ghent University, 2008.

[2] A. Franchois and A. Tijhuis, "A quasi-newton reconstruction algorithm for a complex microwave imaging scanner environment," *Radio Science*, vol. 38, no. 2, January 2003.

[3] A. Franchois and C. Pichot, "Microwave imaging - complex permittivity reconstruction with a levenberg-marquardt method," *IEEE Transactions on Antennas and Propagation*, vol. 45, no. 2, pp. 203–215, Feb. 1997.

[4] P. Mojabi and J. LoVetri, "Microwave biomedical imaging using the multiplicative regularized gauss-newton inversion," *IEEE Antennas and Wireless Propagation Letters*, vol. 8, pp. 645–648, 2009.

[5] S. Caorsi and M. Pastorino, "Two-dimensional microwave imaging approach based on a genetic algorithm," *IEEE Transactions on Antennas and Propagation*, vol. 48, no. 3, pp. 370–373, March 2000.

[6] S. Caorsi, A. Massa, and M. Pastorino, "A computational technique based on a real-coded genetic algorithm for microwave imaging purposes," *IEEE Transactions on Geoscience and Remote Sensing*, vol. 38, no. 4, pp. 1697–1708, July 2000.

[7] M. Pastorino, A. Massa, and S. Caorsi, "A microwave inverse scattering technique for image reconstruction based on a genetic algorithm," *IEEE Transactions on Instrumentation and Measurement*, vol. 49, no. 3, pp. 573–578, June 2000.

[8] E. Bermani, S. Caorsi, and M. Raffetto, "Microwave detection and dielectric characterization of cylindrical objects from amplitude-only data by means of neural networks," *IEEE Transactions on Antennas and Propagation*, vol. 50, no. 9, pp. 1309–1314, September 2002.

[9] L. Garnero, A. Franchois, J. Hugonin, C. Pichot, and N. Joachimowicz, "Microwave imaging - complex permittivity reconstruction by simulated annealing," *IEEE Transactions on Microwave Theory and Techniques*, vol. 39, no. 11, pp. 1801–1807, November 1991.

[10] R. Fletcher, *Practical Methods of Optimization*. New York: John Wiley, 1990.

[11] J. Hadamard, "Sur les problèmes aux derivéés partielles et leur signification physique," *Princeton University Bulletin*, 1902.

[12] O. Bucci, C. Gennarelli, and C. Savarese, "Representation of electromagnetic fields over arbitrary surfaces by a finite and nonredundant number of samples,"

IEEE Transactions on Antennas and Propagation, vol. 46, no. 3, pp. 351–359, March 1998.

[13] J. De Zaeytijd and A. Franchois, "3D quantitative microwave imaging from measured data with multiplicative smoothing and value picking regularization," *Inverse Problems*, vol. 25, no. 2, p. 024004, Feb. 2009.

[14] J. De Zaeytijd, A. Franchois, C. Eyraud, and J. Geffrin, "Full-wave three-dimensional microwave imaging with a regularized gauss-newton method – theory and experiment," *IEEE Transactions on Antennas and Propagation*, vol. 55, no. 11, pp. 3279–3292, Nov. 2007.

[15] J. De Zaeytijd, A. Franchois, and J. Geffrin, "A new value picking regularization strategy – application to the 3D electromagnetic inverse scattering problem," *IEEE Transactions on Antennas and Propagation*, vol. 57, no. 4, pp. 1133–1149, April 2009.

[16] S. Geman and D. Geman, "Stochastic relaxation, gibbs distributions and the bayesian restoration of images," *IEEE Transactions on Pattern Analysis and Machine Intelligence*, vol. 6, no. 6, pp. 721–741, 1984.

[17] P. Lobel, C. Pichot, L. Blanc-Féraud, and M. Barlaud, "Microwave imaging: Reconstructions from experimental data using conjugate gradient and enhancement by edge-preserving regularization," *International Journal of Imaging Systems and Technology*, vol. 8, no. 4, pp. 337–342, 1997.

[18] ——, "Conjugate-gradient algorithm with edge-preserving regularization for image reconstruction from ipswich data for mystery objects," *IEEE Antennas and Propagation Magazine*, vol. 39, no. 2, pp. 12–14, 1997.

[19] M. Loke and T. Dahlin, "A comparison of the gauss-newton and quasi-newton methods in resistivity imaging inversion," *Journal of Applied Geophysics*, vol. 49, no. 3, pp. 149–162, March 2002.

[20] J. Pujol, "The solution of nonlinear inverse problems and the levenberg-marquardt method," *Geophysics*, vol. 72, no. 4, pp. W1–W16, July-August 2007.

[21] R. Pratt, C. Shin, and G. Hicks, "Gauss-newton and full newton methods in frequency-space seismic waveform inversion," *Geophysical Journal International*, vol. 133, no. 2, pp. 341–362, May 1998.

[22] J. De Zaeytijd and A. Franchois, "3D quantitative microwave imaging with a regularized gauss-newton method for breast cancer detection," in *The 24rd Annual Review of Progress in Applied Computational Electromagnetics (ACES 2008)*, Niagara Falls, Canada, 2008, pp. 467–472.

[23] C. Vogel, *Computational Methods for Inverse Problems*. Philadelphia: Society for Industrial and Applied Mathematics (SIAM), Frontiers in Applied Mathematics Series, 2002.

[24] E. Bermani, S. Caorsi, and M. Raffetto, "An inverse scattering approach based on a neural network technique for the detection of dielectric cylinders buried in a lossy half-space," *Journal of Electromagnetic Waves and Applications*, vol. 14, no. 3, pp. 323–324, 2000.

[25] S. Sharma and P. Kaikkonen, "Two-dimensional non-linear inversion of VLF-R data using simulated annealing," *Geophysical Journal International*, vol. 133, no. 3, pp. 649–668, June 1998.

[26] P. Chaumet and K. Belkebir, "Three-dimensional reconstruction from real data using a conjugate gradient-coupled dipole method," *Inverse Problems*, vol. 25, no. 2, p. 024003 (17 pp.), February 2009.

[27] A. Abubakar, P. van den Berg, and B. Kooij, "A conjugate gradient contrast source technique for 3D profile inversion," *IEICE Transactions on Electronics*, vol. E83C, no. 12, pp. 1864–1874, December 2000.

[28] H. Harada, D. Wall, T. Takenaka, and M. Tanaka, "Conjugate-gradient method applied to inverse scattering problem," *IEEE Transactions on Antennas and Propagation*, vol. 43, no. 8, pp. 784–792, August 1995.

[29] P. Lobel, R. Kleinman, C. Pichot, L. Blanc-Feraud, and M. Barlaud, "Conjugate-gradient method for solving inverse scattering with experimental data," *IEEE Antennas and Propagation Magazine*, vol. 38, no. 3, pp. 48–51, June 1996.

[30] A. Van den Bos, "Complex gradient and hessian," *Vision, Image and Signal Processing, IEE Proceedings*, vol. 141, no. 6, pp. 380–383, 1994.

[31] W. Rudin, *Real and complex analysis*. New-Delhi: Tata Mc. Graw - Hill, 1974.

[32] G. Crosta, *Direct and inverse halfspace scalar diffraction: some models and problems*. W. M. Boerner et. al. Eds., D. Reidel publishing company, 1985.

[33] J. De Zaeytijd, Private Communication.

CHAPTER 7

Reconstructions based on experimental data

7.1. Introduction

This chapter covers the most challenging reconstruction examples: reconstructions from experimentally measured scattered fields. These are challenging due to different reasons: measurement noise distorts the results, incident fields are not exactly the same in the measurement set-up and the simulation, discretization noise and numerical errors influence the simulated scattered fields, etc. Moreover, using experimental data prevents *inverse crime* [1], when synthetic scattering data is generated by the same forward solver that is used in the inversion routine. Obtaining accurate amplitude *and* phase data of measured scattered fields at millimeter wave frequencies requires a highly sophisticated measurement set-up and we are not aware of any such data yet being made available to the inversion community. Therefore, we validate the presented inversion procedure in a lower frequency range.

Many different inverse scattering algorithms have been proposed in the past. However, it was hard to validate and compare these methods without having benchmark cases. This problem was first alleviated in 1996 by the US Air Force, which provided experimental scattering data, known as the *Ipswich Data*. These are based on a measurement set-up described in [2]. Several special issues of the *IEEE Antennas and Propagation Magazine* were devoted to reconstructions based on these *Ipswich Data* [3, 4, 5]. In 2001, scattering measurements of homogeneous targets at the Institut Fresnel gave rise to a special section on inversion algorithms in *Inverse Problems* [6]. This database was extended in 2005 with scattering data for inhomogeneous targets [7, 8]. This purely two-dimensional database contains scattered fields that correspond to elongated (1.5 m long) objects and an orthogonally incident illumination. In 2009, a special section in *Inverse Problems* was devoted to a fully three-dimensional version of the Institut Fresnel scattering database [9]. In this case, cubes and spheres

are illuminated by orthogonally *and* obliquely incident fields. Since the 3D-database objects do not have a longitudinal shape and are fully illuminated from different directions by each of the incident fields, they do not fit the quasi 2D assumption of this PhD work, see Section 4.3.2. Hence, we here validate the proposed inversion technique on the 2D Fresnel data, for which both TE- and TM- polarizations are available.

In the presented PhD work, we have chosen to perform single frequency reconstructions of the inhomogeneous dielectric Fresnel targets, named *FoamDielInt*, *FoamDielExt* and *TwinDiel*. These targets were the subject of the 2005 special issue in *Inverse Problems* [7, 8].

Although we now have a benchmark case available, it is still hard to compare our results to the different reconstructions presented in [7], due to different reasons. First, scattering data are available at different frequencies (2 - 10 GHz). Some authors use different frequency data simultaneously to obtain a detailed reconstruction (i.e. *multifrequency* techniques) [10, 11, 12, 13]. When such a multifrequency approach is to be used within the presented inverse scattering method, this would be at the expense of larger simulation times and more memory requirements. Other authors gradually increase the working frequency and use the reconstruction at a lower frequency as an initial guess for the next frequency, which gradually allows for more detail (i.e. *frequency hopping* techniques) [14, 15]. This technique can easily be incorporated in the presented inverse scattering method with acceptable memory requirements, but with much larger simulation times. The *single frequency* approach [16, 17, 18, 19], which we also apply, uses fewer input data to reconstruct the targets, making it harder to obtain a reconstruction of similar quality as in the multifrequency cases but resulting in an optimal combination of memory consumption and simulation times.

For this experimental validation, we have chosen a working frequency of 4 GHz. At this frequency, the inverse problems are still moderately sized (as the discretization cell size scales with the wavelength), resulting in small memory consumptions and fast simulation times. Moreover, this relatively low working frequency already gives rise to accurate reconstruction results.

Second, both TE- and TM- polarizations are available from the database. Almost all authors only use the TM data for the reconstruction [11,12,13,14,15,16,17,18,19]. Some also perform a reconstruction from the TE polarized data only [10,15], but none use, as we do, both TM- and TE-polarized data simultaneously. This is a consequence of the fact that the presented techniques in [7] all are purely two-dimensional ones, which requires a different implementation for each polarization case. Our 2.5D implementation is able to simulate both polarizations simultaneously as well as each one of them separately. The use of both TM and TE data increases the quality of the single frequency reconstructions.

A third factor that complicates the comparison is that some techniques only reconstruct the shape, dimensions and position of the objects, not the complex permittivity [16,17].

Finally, there is a purely technical complication: There is no quantity defined which represents the correctness of a reconstruction. Therefore, most authors revert to figures to show the quality of a reconstruction. Some figures however have poor resolution and/or are only available with grayscales. Therefore, we have detailed our reconstructions by providing color figures and cross-section plots of the reconstructed profiles.

Despite the aforementioned complications when comparing results, we can state that our reconstructions are comparable to the best ones presented in [7]. Our method significantly outperforms the two quantitative single frequency methods [18, 19] for all three measured targets.

Different regularization methods are applied and their influence on the reconstruction is studied. For all targets, the multiplicative smoothing regularization and the stepwise relaxed value picking regularization are used. The advantages of the newly proposed stepwise relaxed object smoothed value picking regularization are illustrated by applying it for the reconstructions of the *FoamDielExt* and *TwinDiel* targets, since in these cases the purely stepwise relaxed value picking regularization leads to artifacts in the reconstructed images.

7.2. Measurement set-up at Institut Fresnel

As in Section 5.2, the measurements of the 2005 Fresnel database were performed in the anechoic chamber of Institut Fresnel in Marseille. Scattered fields for different dielectric objects (all embedded in free space) are collected in an open-source database. The illumination - receiver configuration is as follows. All antenna (transmitting and receiving) positions lie equally spaced (with a maximum offset of 1°) in the azimuthal plane on a circle with radius 1.67 m. The scattering object is positioned at the center of this circle. Only a subset of T (equally spaced) positions is used to position the transmitting antenna ($T = 8$ for the *FoamDielInt* and *FoamDielExt* target and $T = 18$ for the *TwinDiel* target, see further). Instead of rotating the transmitting antenna, the scatterer itself is rotated and the source remains fixed. The number of receiving antenna positions is $R = 241$. Due to technical limitations, only a part of the receiving positions along the circle can be reached, e.g. for a transmitting antenna at 0°, the receiving antenna is positioned from 60° to 300°, see Fig. 7.1. The fields emitted by the source antenna are treated as plane waves, which is a common procedure for reconstructing the targets in the Fresnel database [11, 17, 19, 20, 21]. More details about the set-up and methodology are presented in [8].

Measurements have been performed for frequencies ranging from 2 to 10 GHz (exceptionally 18 GHz for the most complicated object). In this PhD work, all reconstructions are performed on single frequency data, for which we have chosen 4 GHz ($\lambda_0 = 0.0749$ m). At this intermediate frequency, the objects are moderately sized in terms of wavelengths and by consequence, all accelerating techniques from Chapter 2 can be applied without reaching the memory limit.

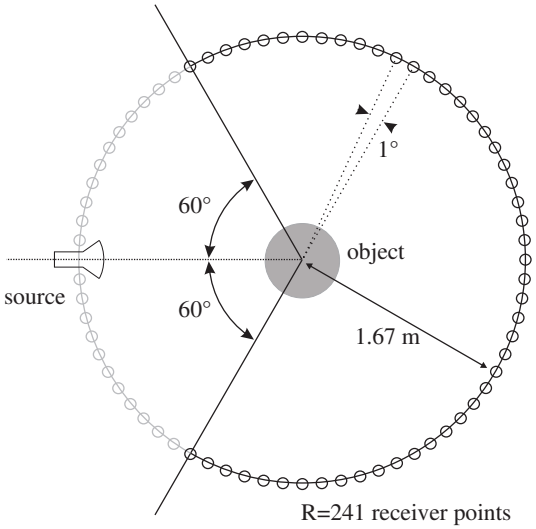

Figure 7.1: Antenna configuration for the measurement set-up at Institut Fresnel.

As proposed in [8], a simple calibration procedure is applied to avoid an overall phase and energy mismatch between measured and simulated fields. Therefore, all measured *scattered* field values are multiplied by one complex factor. This complex factor is obtained as the ratio of the simulated and measured *incident* field, at the receiver location opposite to the source (for a source at 0°, the opposite receiver is at 180°).

7.3. General settings for the inverse solver

All targets measured in the 2D Fresnel database are guaranteed to lie in a $0.15 \times 0.15\ m^2$ square. This square is chosen as the reconstruction domain in the inverse solver and is discretized in 30×30 square inverse problem cells, yielding a total of 900 permittivity unknowns. The edge size of an inverse problem cell is 5 mm, which roughly corresponds to 15 inverse problem cells per wavelength λ_0. This relatively small size of an inverse problem cell should facilitate to reconstruct the curved shapes of the measured targets. To solve the forward problems, each inverse problem cell is subdivided in $2 \times 2 = 4$ forward problem cells, which have the same permittivity. The tolerance for the BICGSTAB iterative routine is set to 10^{-3}. For all reconstructions, the initial guess for the permittivity profile is set to free space and no constraints on the permittivity are applied.

All simulations are performed on a machine with two AMD Opteron 270 Quad core processors, occupying all 8 CPU cores. Each of the cores solves its own set of

forward problems, hence the acceleration scheme of Fig. 2.6(b) is applied. Furthermore, the marching-on-in-incident-fields approach is applied, based on three previous solutions. The marching parameter is in this case the angular position of the transmitting antenna.

Two noise factors complicate the reconstruction. On the one hand, the unavoidable measurement noise corrupts the data vector $\mathbf{e}^{\text{meas}}$, on the other hand, the discretization noise and numerical errors in the forward problem influence $\mathbf{e}^{\text{scat}}(\boldsymbol{\varepsilon})$. The noise level (further denoted as T^N) can be estimated by applying the multiplicative smoothing regularization, since this type of regularization typically stagnates when approaching T^N (see [22]). Reconstructions with stepwise relaxed value picking regularization and stepwise relaxed object smoothed value picking regularization show no such stagnation behavior at the noise level. Hence, in these cases, the iterative procedure is stopped when the data fit reaches T^N, estimated by a reconstruction with multiplicative smoothing regularization. As shown further, the reconstruction for the *TwinDiel* target has the highest stagnation level, i.e. at $2.4\ 10^{-3}$, therefore we have set the noise level to $T^N = 5\ 10^{-3}$. This value is larger but illustrates that a good reconstruction is already possible for this value of T^N. Furthermore, for the stepwise relaxed (object smoothed) value picking regularization, the simulation is also terminated as soon as a sixth extra VP value is to be introduced.

7.4. Reconstruction of the FoamDielInt target

The first real world target that is reconstructed from the Fresnel database is the FoamDielInt target, shown in Fig. 7.2. This target was also discussed in Section 5.2.2. A homogeneous plastic cylinder is embedded in a second homogeneous foam cylinder. The inner plastic cylinder has a radius $r_a = 15.5$ mm $\approx 0.2\lambda_0$ and relative permittivity $\varepsilon_{r,a} = 3 \pm 0.3$. The outer foam cylinder has $r_b = 40$ mm $\approx 0.5\lambda_0$ and $\varepsilon_{r,b} = 1.45 \pm 0.15$. The distance d between the centers of both cylinders is $d = 5$ mm. Within the uncertainty introduced by the positioning errors, the outer cylinder is positioned in the center of the antenna circle, which is also the center of the reconstruction grid. For this experimental set-up, data for 8 source positions are available with TE and TM polarization. Hence, the dimension of the data vector $\mathbf{e}^{\text{meas}}$, containing the x-, y- and z-components of the measured scattered field, is $N^D = 11568$.

7.4.1 Reconstruction using Multiplicative Smoothing regularization

First, the FoamDielInt target is reconstructed by applying the multiplicative smoothing regularization, with the regularizing parameter α in (6.7) set to $\alpha = 10^{-3}$. The reconstructed profile is shown in Fig. 7.3, with the white lines representing the actual boundaries of both cylinders. The shape of the inner cylinder is clearly visible. However, due to the imposed smoothness, the dimensions of the objects as well as their permittivities cannot be accurately determined. A swarm plot of the reconstructed pro-

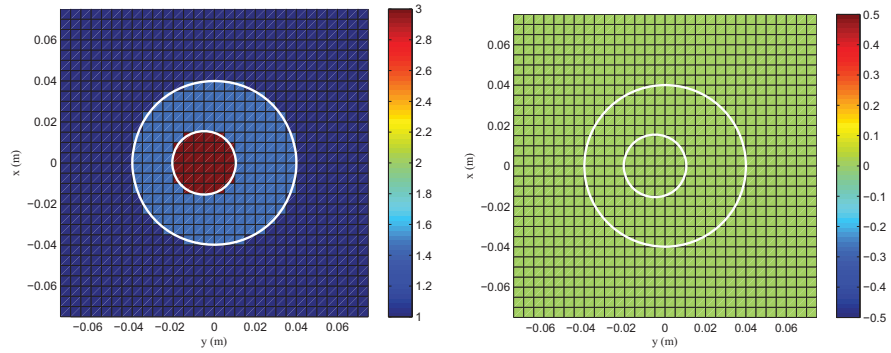

(a) (b)

Figure 7.2: (a) Real part and (b) imaginary part of the permittivity profile, corresponding to the FoamDielInt target. The white lines indicate the actual object boundaries.

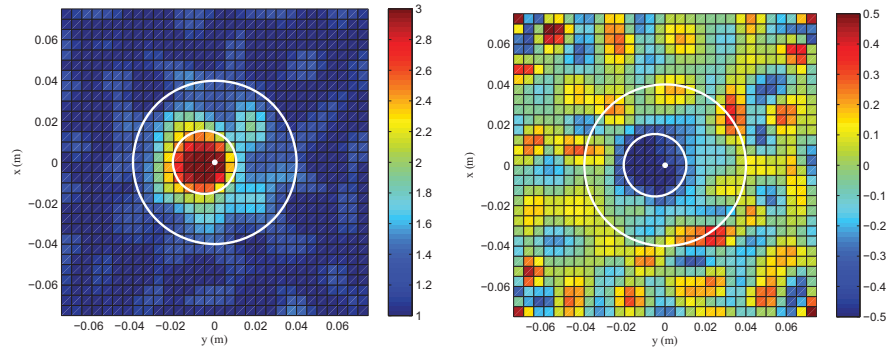

(a) (b)

Figure 7.3: (a) Real part and (b) imaginary part of the reconstructed permittivity profile of the FoamDielInt target, based on the multiplicative smoothing regularized cost function. The white lines indicate the actual object boundaries.

file (i.e. the permittivity of each pixel, represented as a dot in the complex permittivity plane) is shown in Fig. 7.4. The cross-sections of the horizontal and vertical solid lines represent the actual permittivity values of the FoamDielInt target (including free space as background). There is few clustering of the permittivity pixels around the cross-sections due to the inherent smoothing procedure and the imaginary parts are spread out relatively far away from the real axis. From Fig. 7.5, it is clear that the data fit stagnates after 11 iterations around $\mathcal{F}^{LS} \approx 1.6\ 10^{-3}$.

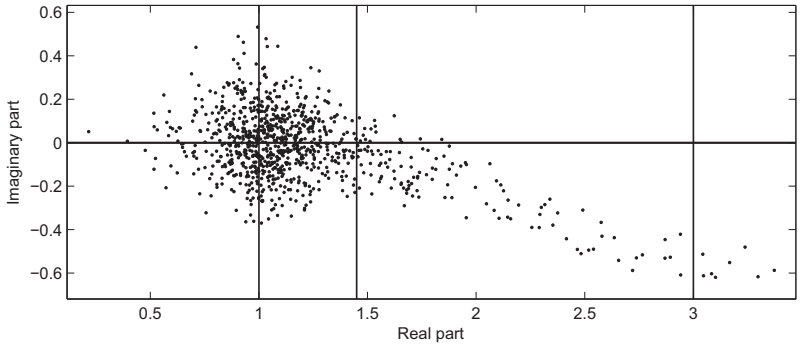

Figure 7.4: Swarm plot of the reconstructed FoamDielInt permittivity profile with multiplicative smoothing regularization. Each permittivity pixel is represented as a dot in the complex plane, the intersections of the solid lines represent the actual permittivity values, including free space as background.

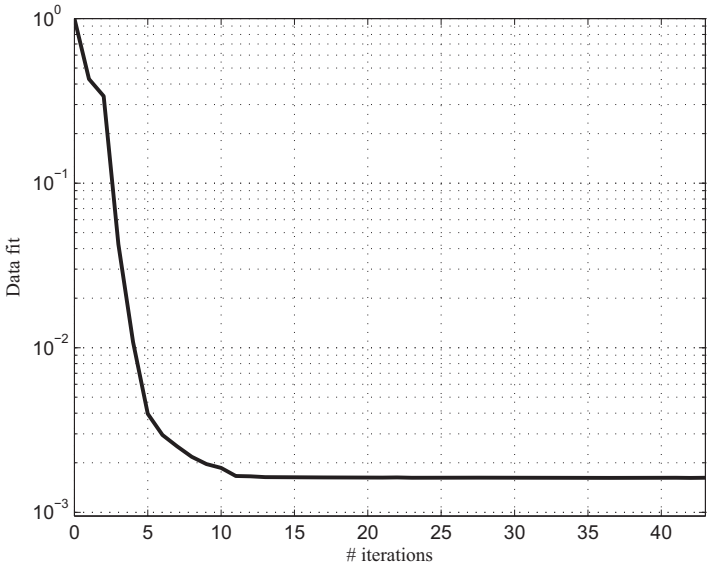

Figure 7.5: The data fit while reconstructing the FoamDielInt target, based on the multiplicative smoothing regularized cost function.

7.4.2 Reconstruction using Stepwise Relaxed Value Picking regularization

Second, the stepwise relaxed value picking regularization is applied. In the updating procedure for the VP values c_p ($p = 1 \ldots P$), we have imposed the following constraints on all added VP values: (i) $1.1 < \Re(c_p) < 5$, $\forall c_p$ and (ii) $-0.001 < \Im(c_p) < 0.001$, $\forall c_p$, taking into account the a-priori knowledge that the object permittivities do not have a significant imaginary part.

In the case of stepwise relaxed value picking regularization, the choice of the regularization parameter in (6.10) is more critical when compared to the multiplicative smoothing regularization. Therefore, simulations are performed for three different regularization parameters: $\gamma = 1$, $\gamma = 3$ and $\gamma = 5$. Figure 7.6 shows the decrease of the data fit as a function of the iteration number for these three cases. Vertical lines in the same line style as the different data fit curves, stand for the iterations in which a VP value is added in the stepwise relaxed VP regularization scheme. When the weight is chosen too large (e.g. $\gamma = 5$), the data fit is prevented to reach the noise level and the simulation stagnates. When the weight is too small, the data fit reaches the noise level easily, without using much of the a-priori knowledge, incorporated in the regularizing function. This results in a very weak clustering of the permittivity values in the complex plane. This is the case for $\gamma = 1$, where the noise level is already reached after 5 iterations but only 1 VP value ($c_1 = 2.62$) is introduced. From Fig. 7.6, the choice $\gamma = 3$ seems most adequate. However, when reaching the estimated noise level at iteration 18, there are 3 added VP values, $c_1 = 2.98$, $c_2 = 1.38$ and $c_3 = 2.72$. Hence, one superfluous VP value is added, since there are only two non-background permittivities. Here, the two VP values c_1 and c_3 lie close to each other. Figure 7.7 presents, for every pixel in the reconstruction domain, the VP weights (see Section 6.4.3) that correspond to the three added VP values at iteration number 18. Cells at the left side of the inner cylinder tend more towards c_1, whereas the right half of the inner cylinder tends more towards c_3. However, for the majority of cells in the inner cylinder, the weights corresponding with c_1 and the weights corresponding with c_3 are similar in magnitude. From these weights-plots, it is quite reasonable to conclude that the actual permittivity of this inner cylinder will lie between c_1 and c_3, both already lying within the uncertainty bounds on the permittivity of the inner cylinder ($\varepsilon_{r,a} = 3 \pm 0.3$).

Figure 7.8 shows two orthogonal cross-sections along the real part of the reconstructed profile at iteration number 18, parallel to the coordinate axes and through the center of the reconstruction grid. The solid lines represent the original profile, the dashed lines correspond to $\gamma = 1$ and $\gamma = 3$. The result for $\gamma = 5$ is not shown since this simulation converged too slowly and was terminated. The simulation with a small regularization weight ($\gamma = 1$) results in a relatively smooth profile since, until the last but one iteration, the only active VP value is the one kept fixed to the background medium. The profile that corresponds to $\gamma = 3$ yields a fairly good reconstruction: the size of the outer cylinder is exactly reconstructed, the deviation in size for the inner

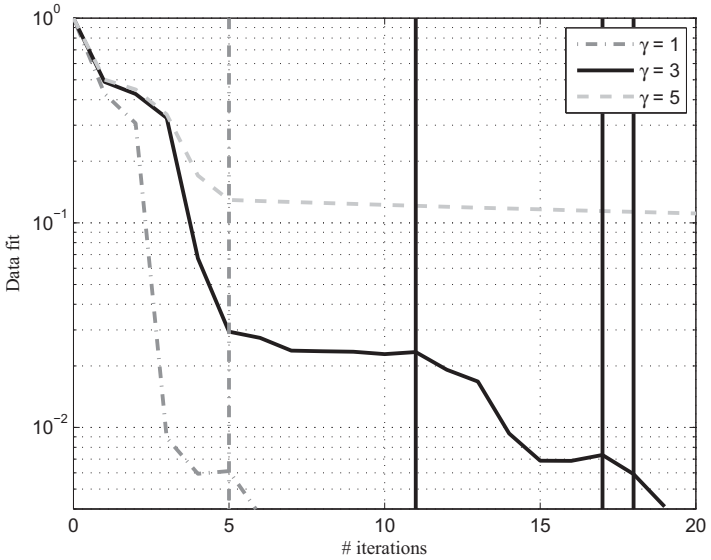

Figure 7.6: The data fit as a function of the iteration number, for the reconstruction of the FoamDielInt target with stepwise relaxed value picking regularization. The vertical lines indicate the iterations in which a VP value was added, their corresponding line styles are identical to the data fit curves they are related to.

cylinder is of the order of a reconstruction cell. The permittivity of the outer cylinder is very well estimated. Due to the fact that the permittivity of the inner cylinder is slightly underestimated, its size is somewhat too large. Also from this figure, it is clear that $\gamma = 3$ is the best choice.

The reconstructed permittivity profile, for $\gamma = 3$ at iteration number 18, is presented in Fig. 7.9. Again, the solid white lines indicate the contours of the actual target. The final VP values are $c_1 = 2.98$, $c_2 = 1.38$ and $c_3 = 2.72$. From Fig. 7.7, we already concluded that the actual permittivity of the inner cylinder lies somewhere between $c_1 = 2.98$ and $c_3 = 2.72$, the permittivity of the outer cylinder can be fixed to $c_2 = 1.38$, which is also within the uncertainty bounds $\varepsilon_{r,b} = 1.45 \pm 0.15$. A swarm plot of the reconstructed permittivity profile, for $\gamma = 3$, is shown in Fig. 7.10. The dots in the complex plane represent the different pixel permittivities, cross-sections of solid lines denote the actual permittivities and cross-sections of dashed lines denote the optimized VP values. When this swarm plot is compared to the one for multiplicative smoothing regularization (Fig. 7.4), it is clear that a substantially better clustering of the permittivities is achieved. The total simulation time for the reconstruction with stepwise relaxed value picking regularization (with $\gamma = 3$) of the FoamDielInt target is 1h 57 min.

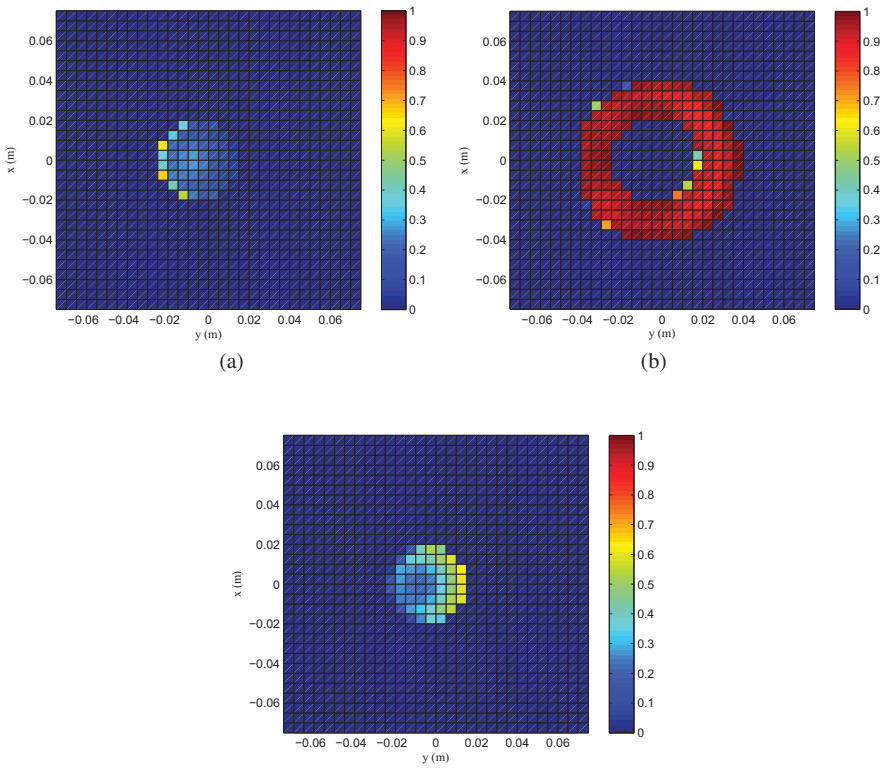

Figure 7.7: A plot of the VP weights $b^P_{p,n}$ for every reconstruction cell n at iteration number 18 (for $\gamma = 3$). (a) weight $b^P_{1,n}$ corresponding to the first added VP value $c_1 = 2.98$, (b) weight $b^P_{2,n}$ corresponding to the second added VP value $c_2 = 1.38$ and (c) weight $b^P_{3,n}$ corresponding to the last added VP value $c_3 = 2.720$.

Since the reconstructed cylinders already show a smooth permittivity profile inside the different permittivity regions, no extra improvement is expected when the stepwise relaxed object smoothed value picking regularization technique is applied.

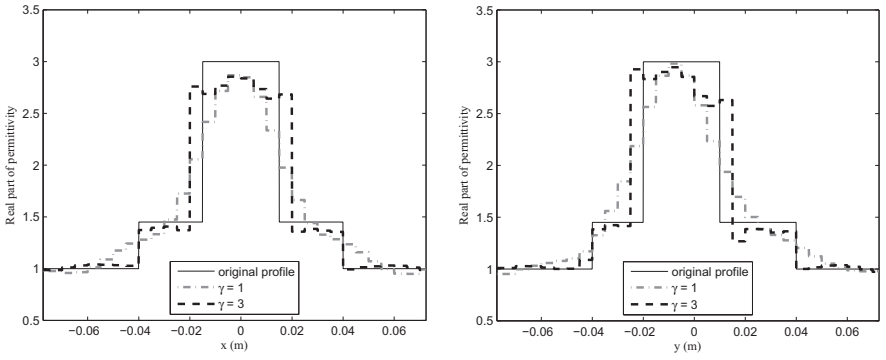

(a) (b)

Figure 7.8: Cross-section through the real part of the reconstructed permittivity profile along the $x-$axis (a) and along the y-axis (b) and through the center of the reconstruction grid, for a reconstruction of the FoamDielInt target with stepwise relaxed value picking regularization. The solid lines correspond to the actual profile, the dashed ones to reconstructed profiles with different values for the regularization parameter γ.

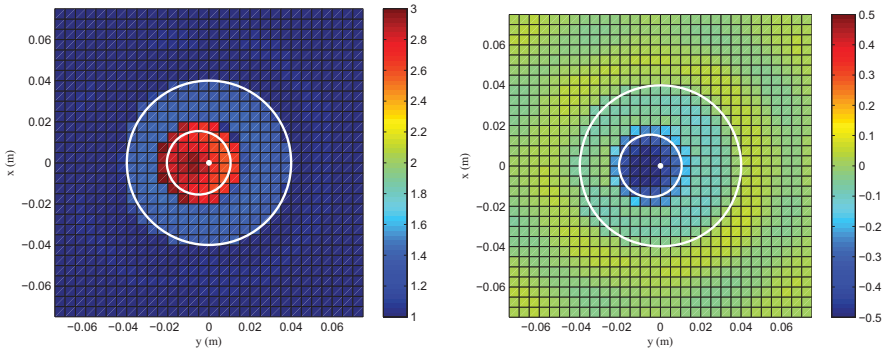

(a) (b)

Figure 7.9: (a) Real part and (b) imaginary part of the reconstructed permittivity profile of the FoamDielInt target after 18 iterations, based on a stepwise relaxed value picking regularized cost function. The white lines indicate the actual object boundaries.

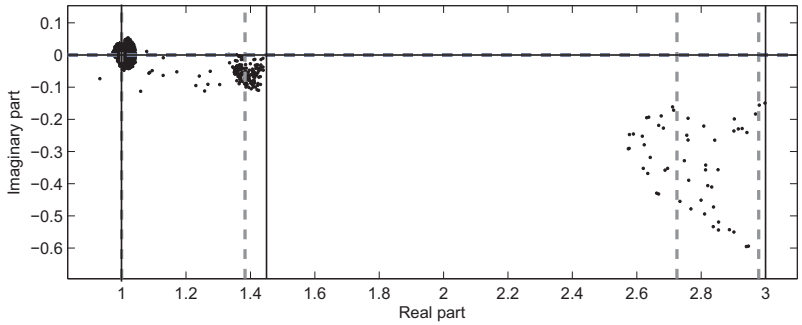

Figure 7.10: Swarm plot of the reconstructed FoamDielInt permittivity profile with stepwise relaxed value picking regularization. Each permittivity pixel is represented as a dot in the complex plane, the intersections of the solid lines represent the actual permittivity values, intersections of dashed lines represent optimized VP values.

7.5. Reconstruction of the FoamDielExt target

The second target that is reconstructed from the Fresnel database is named FoamDielExt. It consists of the same two cylinders as the FoamDielInt target, where the small plastic cylinder is now positioned outside the larger foam cylinder, as shown in Fig. 7.11. The material properties for the small cylinder are: radius $r_a = 15.5$ mm $\approx 0.2\lambda_0$ and relative permittivity $\varepsilon_{r,a} = 3 \pm 0.3$. The foam cylinder has $r_b = 40$ mm $\approx 0.5\lambda_0$ and $\varepsilon_{r,b} = 1.45 \pm 0.15$. Also here, the foam cylinder is positioned in the center of the antenna circle (within the uncertainty introduced by the positioning errors). The source configuration is the same as for the FoamDielInt target: $T = 8$ source positions with TM and TE polarization resulting in a data vector $\mathbf{e}^{\text{meas}}$ of length $N^D = 11568$.

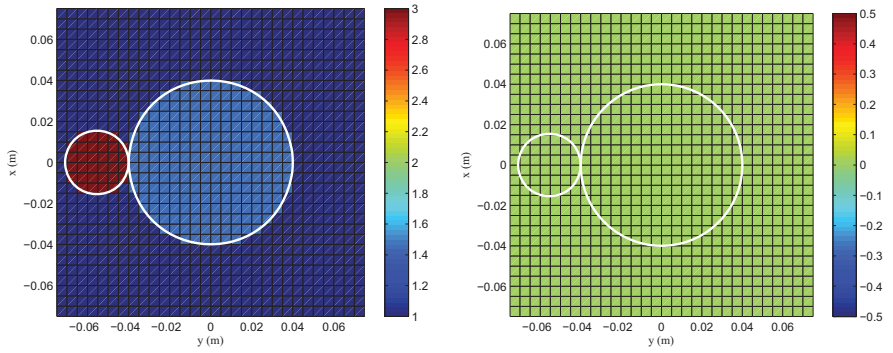

(a) (b)

Figure 7.11: (a) Real part and (b) imaginary part of the FoamDielExt target of Institut Fresnel.

7.5.1 Reconstruction using Multiplicative Smoothing regularization

As a benchmark case, a reconstruction is performed with the multiplicative smoothing regularization with the weight of the regularizing part of the cost function set to $\alpha = 10^{-3}$. The result is presented in Fig. 7.12. The small plastic cylinder is clearly visible and its permittivity is well estimated. The larger foam cylinder however, is only revealed as a blurry area to the right of the plastic cylinder. Its shape and permittivity are not well resolved. Furthermore, around both cylinders artifacts are present where free space is supposed. Still, one could come to the conclusion that there are two objects next to each other, one having a permittivity of approximately 3 and one having a permittivity of approximately 1.7. Figure 7.13 contains the swarm plot of the reconstructed profile. Due to the imposed smoothness, few clustering of permittivity values is visible. Many pixels have an imaginary part relatively far away from the real axis and a real part of the permittivity smaller than 1. The data fit as a function of the iteration number is shown in Fig. 7.14 and stagnates after 16 iterations around $\mathcal{F}^{LS} \approx 1.4\ 10^{-3}$.

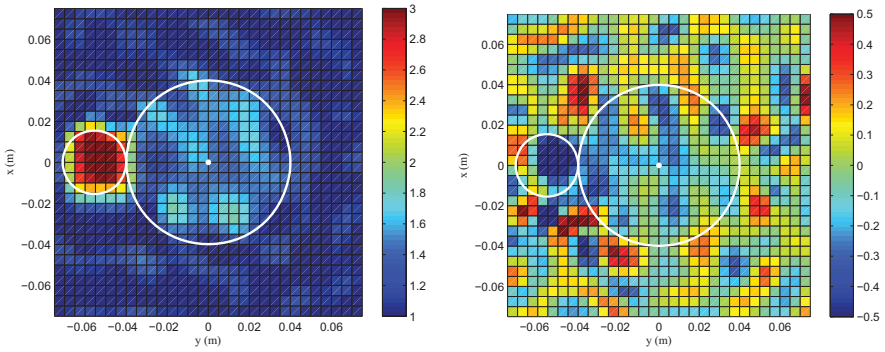

(a) (b)

Figure 7.12: (a) Real part and (b) imaginary part of the reconstructed permittivity profile of the FoamDielExt target, based on the multiplicative smoothing regularized cost function. The white lines indicate the actual object boundaries.

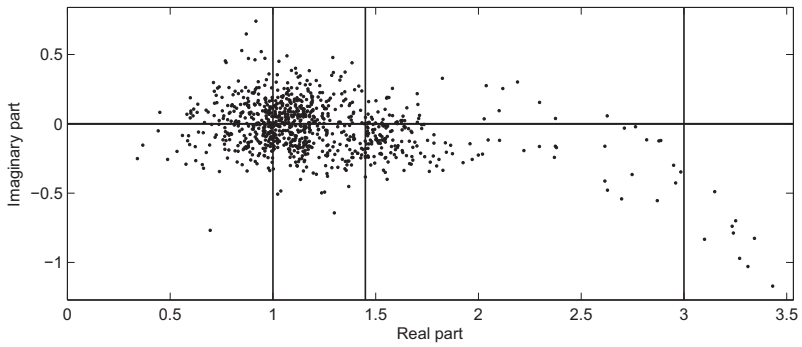

Figure 7.13: Swarm plot of the reconstructed FoamDielExt permittivity profile with multiplicative smoothing regularization. Each permittivity pixel is represented as a dot in the complex plane, the intersections of the solid lines represent the actual permittivity values, including free space as background.

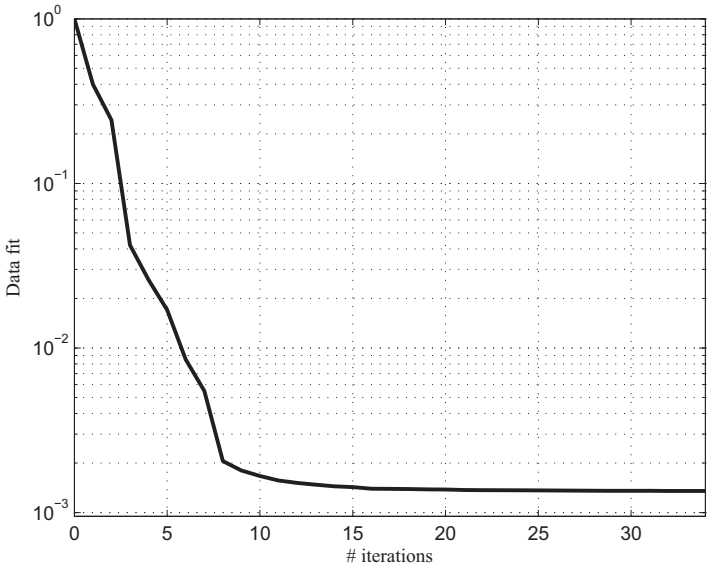

Figure 7.14: The data fit while reconstructing the FoamDielExt target, based on the multiplicative smoothing regularized cost function.

7.5.2 Reconstruction using Stepwise Relaxed Value Picking regularization

The previous result is now compared to a reconstruction, based on the stepwise relaxed value picking regularization. We have imposed the same constraints on the VP values as in Section 7.4.2: (i) $1.1 < \Re(c_p) < 5$, $\forall c_p$ and (ii) $-0.001 < \Im(c_p) < 0.001$, $\forall c_p$, taking into account the a-priori knowledge that the object permittivities do not have a significant imaginary part. Also for this object, simulations have been performed for different values of the regularization parameter γ. The data fit is shown in Fig. 7.15. Due to the large difference in the number of iterations for the cases $\gamma = 1$ and $\gamma = 3$, an additional simulation is done for $\gamma = 2$. The case $\gamma = 1$ corresponds to very weak regularization and it can be seen that the data fit easily reaches the noise level. In case of a really strong regularization ($\gamma = 5$), the data fit decreases really slowly, boosting the iteration number. Therefore this simulation was terminated and is no longer considered in what follows. For $\gamma = 2$ and $\gamma = 3$, the data fit decreases steadily, but the optimization process adds too many VP values (in the last few iterations a VP value is added in every step). The results for $\gamma = 2$ (after 21 iterations) do not differ substantially from those for $\gamma = 3$ (after 32 iterations), but we will focus on $\gamma = 3$ since this value was also chosen in Section 7.4.2. In that case, the final (after 32 iterations) VP values are $c_1 = 2.99$, $c_2 = 1.39$, $c_3 = c_4 = 2.70$ and $c_5 = 2.8$. Here, c_3 and c_4 were initially different but merged during the optimization process.

Figure 7.16 presents, for every pixel in the reconstruction domain, the VP weights that correspond to the five added VP values and the VP value that is kept fixed to the background permittivity. In Fig. 7.16(a), (c), (d) en (e), the presence of the small cylinder at the left is revealed. However, the difference in weight for these four VP values is negligible. No dominant VP value can be selected, which suggest that the actual permittivity of the small cylinder at the left lies somewhere in between the VP values c_1, c_3, c_4 and c_5. The pixels are slightly more attracted towards $c_3 = c_4 = 2.70$, than towards $c_1 = 2.99$ and $c_5 = 2.8$. Since the permittivity $c_3 = c_4 = 2.70$ is slightly too small, the cylinder dimensions are overestimated. From these weight plots, we can conclude that there is (probably) a small cylinder at the left side with a permittivity somewhere between 2.70 and 2.99 and a larger cylinder with circular shape and an estimated permittivity of $c_2 = 1.39$. These reconstructed permittivities all lie within the specified uncertainties on the object properties ($\varepsilon_{r,a} = 3 \pm 0.3$ and $\varepsilon_{r,b} = 1.45 \pm 0.15$). However, in the three different distinguished permittivity regions some artifacts are clearly visible. For instance, pixels in the small cylinder region take the VP value corresponding to the large cylinder and vice versa. The same exchange of VP values also takes place between the background and the large cylinder, see Fig. 7.16(b) and (f).

The occurring artifacts also appear in Fig. 7.17, which shows the real part of the reconstructed permittivity profile along the *x*- and *y*- axis of the reconstruction grid for $\gamma = 1$, $\gamma = 2$ and $\gamma = 3$. The presence of artifacts is clearly visible for the case $\gamma = 1$ in

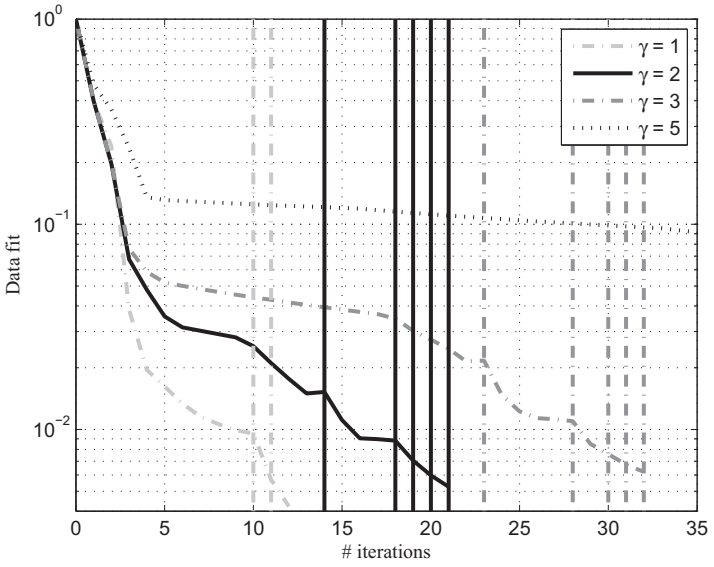

Figure 7.15: The data fit as a function of the iteration number, for the reconstruction of the FoamDielExt target with stepwise relaxed value picking regularization. The vertical lines denote the iterations in which a VP value was added, their corresponding line styles are identical to the data fit curves they are related to.

Fig. 7.17(a) and for all cases in Fig. 7.17(b). The complete reconstructed permittivity profile, for $\gamma = 3$, is presented in Fig. 7.18.

Fig. 7.19 shows the swarm plot of the reconstructed permittivity profile, for $\gamma = 3$. There is a good clustering of the permittivities around the background permittivity and around $c_2 = 1.39$, whereas the higher permittivities are more spread out. This was also the case in the reconstruction of the FoamDielInt target with VP regularization. Compared to the swarm plot when multiplicative smoothing regularization (Fig. 7.13) is applied, the clustering effect is apparent. A total simulation time of 3h 40 min was necessary to obtain this reconstruction of the FoamDielExt target with stepwise relaxed value picking regularization (with $\gamma = 3$).

Contrary to the reconstruction of the FoamDielInt target, we still have room for improvement after the application of the stepwise relaxed value picking regularization technique. It is expected that applying the stepwise relaxed object smoothed value picking regularization technique will lead to a further improvement of the reconstruction.

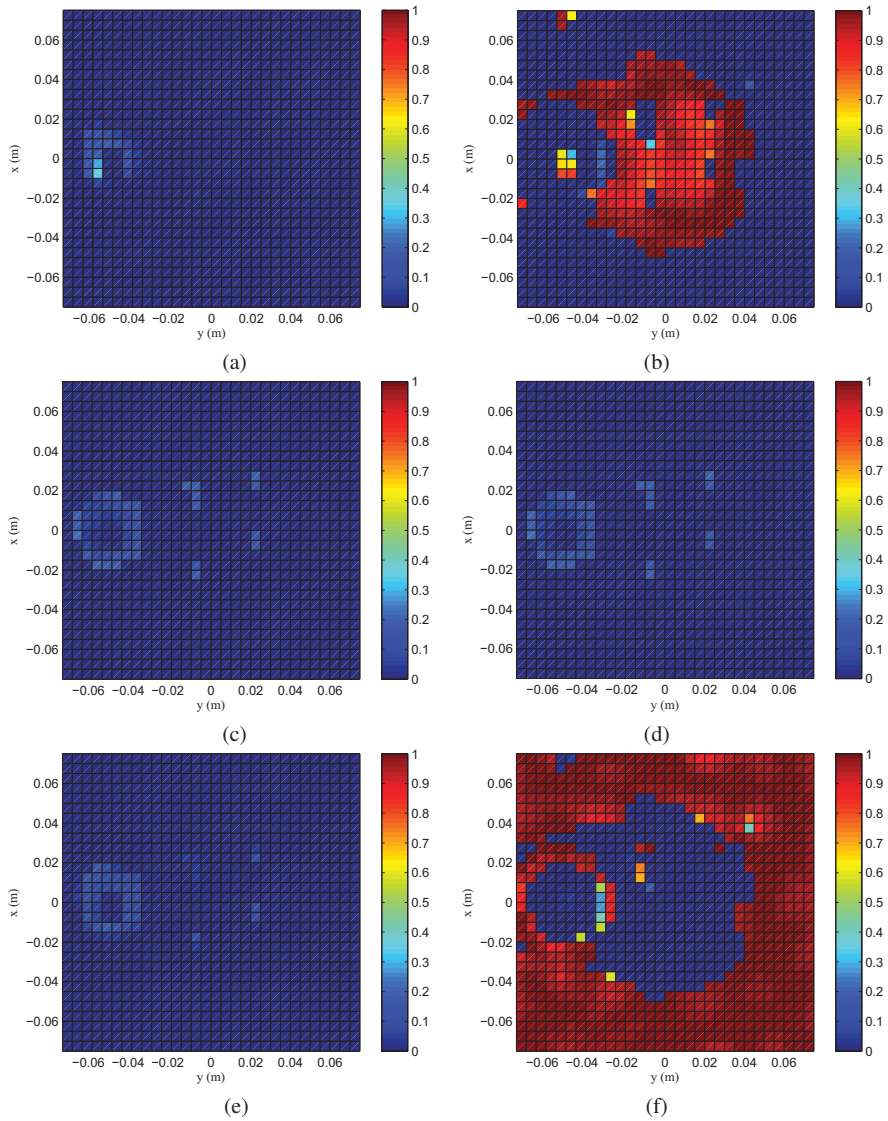

Figure 7.16: A plot of the VP weights $b^P_{p,n}$ for every reconstruction cell n corresponding to $\gamma = 3$. (a) weight $b^P_{1,n}$ corresponding to $c_1 = 2.99$, (b) weight $b^P_{2,n}$ corresponding to $c_2 = 1.39$, (c) weight $b^P_{3,n}$ corresponding to $c_3 = 2.70$, (d) weight $b^P_{4,n}$ corresponding to $c_4 = 2.70$, (e) weight $b^P_{5,n}$ corresponding to $c_5 = 2.8$ and (f) weight $b^P_{6,n}$ corresponding to the VP value that is kept fixed to the background permittivity ($c_6 = 1$).

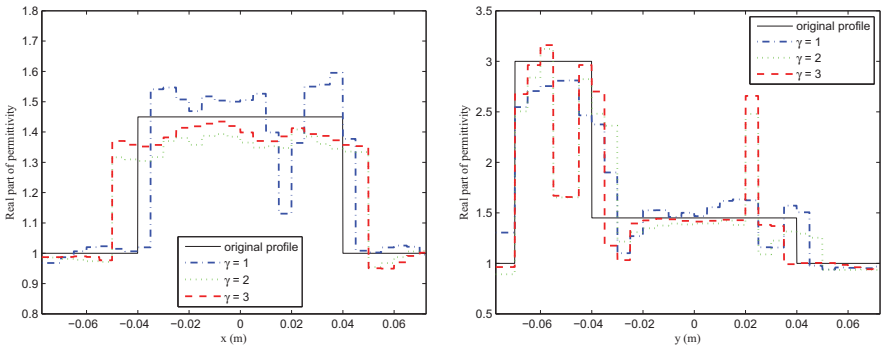

(a) (b)

Figure 7.17: Cross-section through the real part of the reconstructed permittivity profile along the $x-$ axis (a) and along the y-axis (b) and through the center of the reconstruction grid, for a reconstruction of the FoamDielExt target with stepwise relaxed value picking regularization. The solid lines correspond to the actual profile, the dashed ones to reconstructed profiles for different values of the regularization parameter γ.

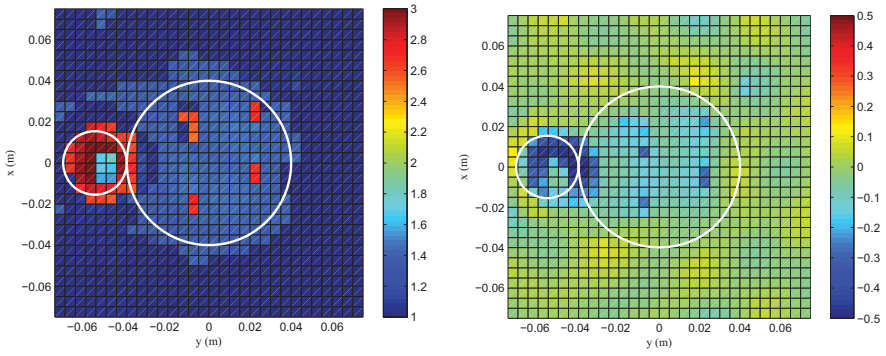

(a) (b)

Figure 7.18: (a) Real part and (b) imaginary part of the reconstructed permittivity profile of the FoamDielExt target, after 32 iterations and based on a stepwise relaxed value picking regularized cost function. The white lines indicate the actual object boundaries.

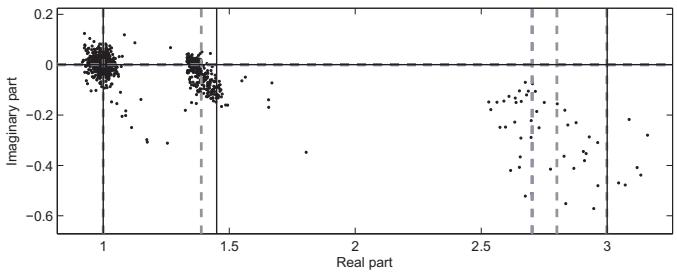

Figure 7.19: Swarm plot of the reconstructed FoamDielExt permittivity profile with stepwise relaxed value picking regularization. Each permittivity pixel is represented as a dot in the complex plane, the intersections of the solid lines represent the actual permittivity values, intersections of dashed lines represent optimized VP values.

7.5.3 Reconstruction using Stepwise Relaxed Object Smoothed Value Picking regularization

The FoamDielExt target is an ideal example to illustrate the performance of the proposed stepwise relaxed object smoothed VP regularization. This type of regularization spatially smooths over neighboring cells that are attracted to the same VP value, including over isolated cells that are attracted towards another VP value. The VP values are subject to the same constraints as in the case of purely stepwise relaxed value picking regularization: $1.1 < \Re(c_p) < 5,\ \forall c_p$ and $-0.001 < \Im(c_p) < 0.001,\ \forall c_p$. Furthermore, VP values are added once the criterion to add an new VP value in the stepwise relaxed VP regularization scheme is fulfilled.

The object smoothing regularization term is additive to the VP regularized part of the cost function and the corresponding weight is set to $\zeta = 10^{-3}$. The weight of the VP part of the cost function is kept to $\gamma = 3$. Since an additional term is added to the cost function, the total weight of the regularizing part, when compared to the data fit term, has increased. This results in a stronger regularization and a slower decrease of the data fit. Consequently, VP values are added later in the optimization process. This is clearly visible in Fig. 7.20, showing the data fit with stepwise relaxed VP regularization and with stepwise relaxed object smoothed VP regularization. The final VP values are $c_1 = 3.00$, $c_2 = 1.48$ and $c_3 = c_4 = c_5 = 2.75$, where c_3, c_4 and c_5 merged during the optimization. Whereas the total simulation time for this target with purely stepwise relaxed value picking regularization and $\gamma = 3$ is 3h 40 min, the reconstruction with the new stepwise relaxed object smoothed value picking regularization needs almost the double in computation time (6h 23 min) due to the stronger regularization.

As explained in Section 6.4.4, a group mapping of the pixels into VP groups has to be performed. This mapping, at different iteration numbers, is illustrated in Fig. 7.21. First, only the fixed background VP value (here denoted as c_0) is present, see Fig. 7.21(a). Consequently, all pixels are assigned to the background group and the object smoothing part of the cost function behaves as the multiplicative smoothing regularization with a fixed weight. After the first added VP value (at that stage $c_1 = 2.74$ at iteration 44), the small cylinder starts to appear in the group mapping, see Fig. 7.21(b). The inner cells at the location of the small cylinder are assigned to the newly added VP group, whereas the border cells at this location are assigned to the indefinite cells group. At this stage, object smoothing is performed within the three different VP groups. Once, the second VP value is introduced (at iteration 48, $c_2 = 1.40$, see Fig. 7.21(c)), all cells at the location of the small cylinder are assigned to the same VP group and to the right the larger foam cylinder starts to appear. Also here, the inner cells are assigned to the new VP group, whereas the outer cells are now mapped to the indefinite cells group. A third VP value is added ($c_3 = 2.77$ in iteration 51) in Fig. 7.21(d). Some cells of the small cylinder switch groups to the newly added VP group, which causes the other cells to join the indefinite cells group. For the foam cylinder, all cells are now assigned to the correct group. In Fig. 7.21(e), another VP value is

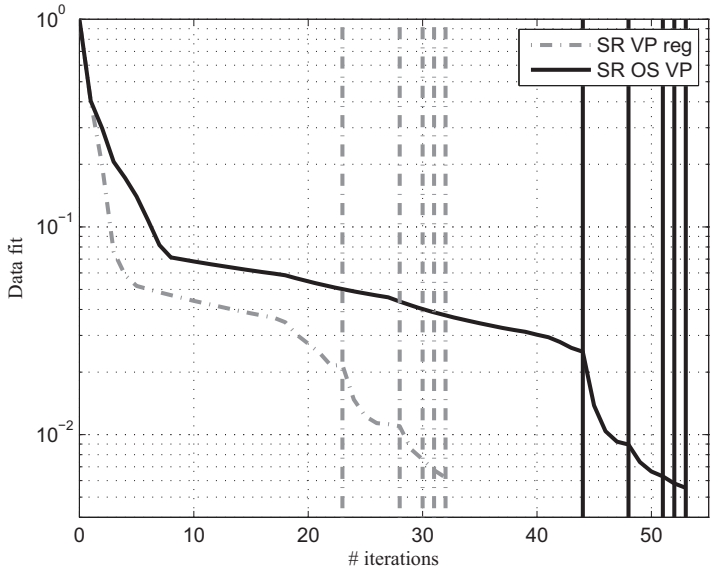

Figure 7.20: The data fit as a function of the iteration number, for the reconstruction of the FoamDielExt target. Dashed curve: with stepwise relaxed value picking regularization, solid curve: with stepwise relaxed object smoothed value picking regularization. The vertical lines denote the iterations in which a VP value was added, their corresponding line styles are identical to the data fit curves they are related to.

added in iteration 52 but immediately merges with c_3 ($c_4 = c_3 = 2.75$). Because none of the VP values are dominant, the corresponding weights only slightly differ and all cells of the small cylinder end up in the indefinite cells group. Consequently, the smoothing is performed over the complete left cylinder. All pixels at the location of the foam cylinder still belong to the same VP group. Also for this object, the smoothing is performed over almost the exact object location. The situation in the last iteration (after adding $c_5 = c_4 = c_3 = 2.75$, see Fig. 7.21(f)) does not differ from the one in Fig. 7.21(e), since c_5 also merges with the other VP values. We can conclude that the object smoothing is performed exactly in the regions that we wanted.

Figure 7.22 shows cross-sections of the real part of the permittivity profile. The cross-sections are still along the x- (a) and y- (b) axis, but now pass through the regions in which artifacts are present when using the purely stepwise relaxed value picking regularization ($y = 0.005$ m and $x = 0.005$ m respectively). Fig. 7.22(a) shows that the artifacts have disappeared when the object smoothing is applied. The permittivity of the larger cylinder is correctly estimated while the size of the larger cylinder is only slightly overestimated. In Fig. 7.22(b), the artifacts also disappeared. The permittivity of the small cylinder is somewhat underestimated and its location is shifted slightly to the right, but the dimension is exactly estimated. The permittivity of the larger cylinder is correctly estimated and its dimensions are a little bit too small.

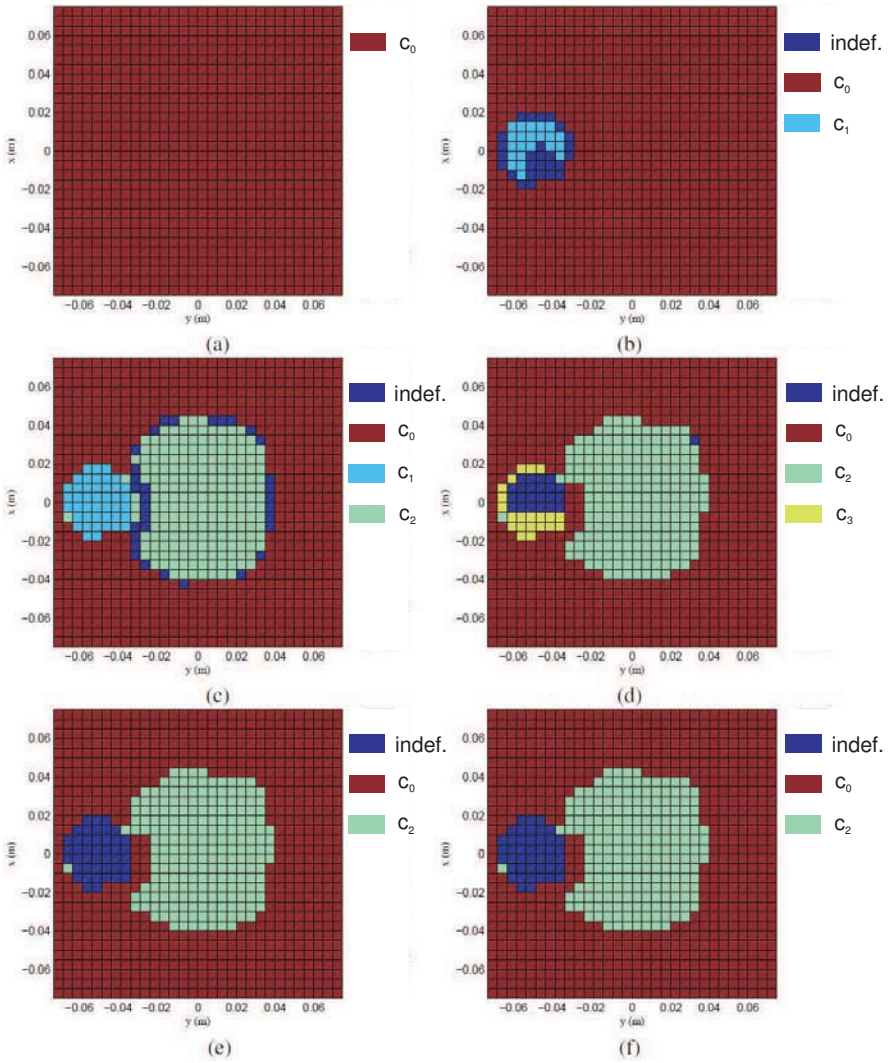

Figure 7.21: A plot of the mapping of permittivity cells into VP groups for FoamDielExt. The indefinite cells group is denoted as *indef.*, the other VP groups are represented by their VP value, where c_0 denotes the VP value that is kept fixed to the background medium. (a) group mapping when $c_1 = 2.74$ is added, (b) group mapping after the introduction of $c_2 = 1.40$, (c) group mapping after adding $c_3 = 2.77$, (d) group mapping after adding $c_4 = c_3 = 2.75$, (e) group mapping in last but one iteration, after introduction of $c_5 = c_4 = c_3 = 2.75$ and (f) final group mapping.

The complete reconstructed permittivity profile, for $\gamma = 3$, is presented in Fig. 7.23. The circular shape, dimensions and center positions of both cylinders are correctly reconstructed. The only deviations appear where both cylinders touch. The permittivity of the small cylinder is estimated to be 2.75 and the permittivity of the larger cylinder is estimated to be 1.48, which both lie within the uncertainty bounds on the objects ($\varepsilon_{r,a} = 3 \pm 0.3$, $\varepsilon_{r,b} = 1.45 \pm 0.15$).

Fig. 7.24 shows the swarm plot of the reconstructed permittivity profile, for $\gamma = 3$. The clustering of the permittivities around the background and object permittivities is even better than in case of the purely stepwise relaxed value picking regularization (Fig. 7.19).

We can conclude that the stepwise relaxed object smoothed value picking regularization is indeed a valuable approach to deal with artifacts that can appear when purely stepwise relaxed value picking regularization is applied to scatterers with a limited number of (quasi-) homogeneous regions.

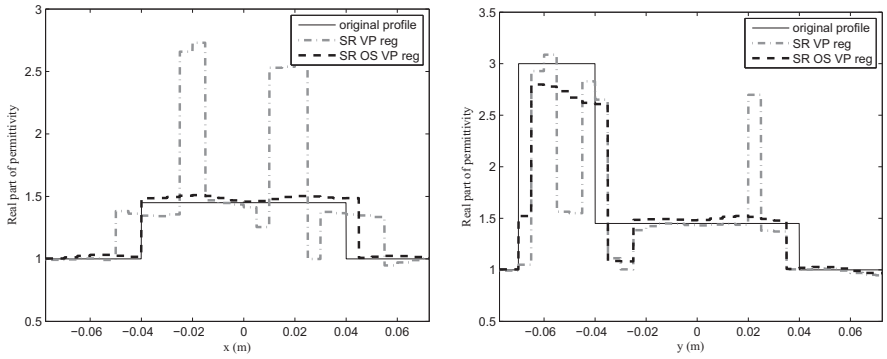

Figure 7.22: Cross-section through the real part of the reconstructed permittivity profile along the $x-$ axis (a) and along the y-axis (b) and cutting through the location of the artifacts, for a reconstruction of the FoamDielExt target with stepwise relaxed object smoothed value picking regularization and purely stepwise relaxed value picking regularization. The solid lines correspond to the actual profile, the dashed ones to reconstructed profiles.

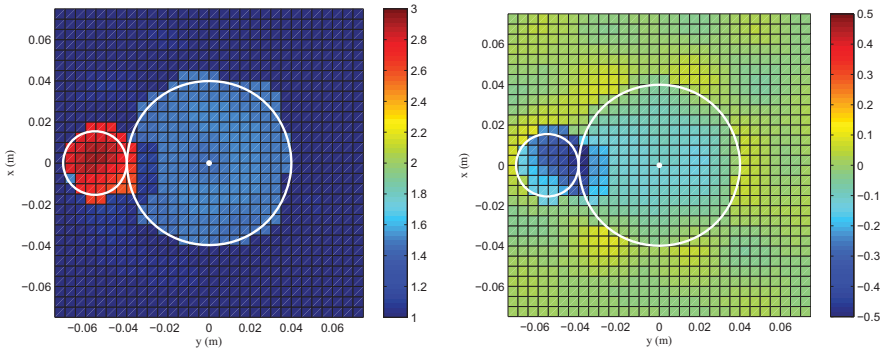

(a) (b)

Figure 7.23: (a) Real part and (b) imaginary part of the reconstructed permittivity profile of the FoamDielExt target, based on a stepwise relaxed object smoothed value picking regularized cost function. The white lines indicate the actual object boundaries.

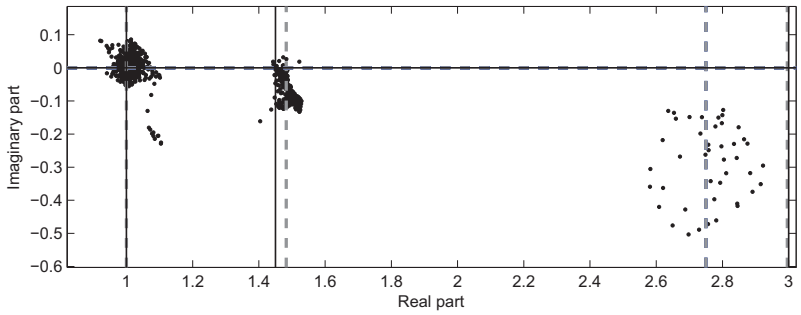

Figure 7.24: Swarm plot of the reconstructed FoamDielExt permittivity profile with stepwise relaxed object smoothed value picking regularization. Each permittivity pixel is represented as a dot in the complex plane, the intersections of the solid lines represent the actual permittivity values, intersections of dashed lines represent optimized VP values.

7.6. Reconstruction of the TwinDiel target

The last target, also the most complicated one, is a combination of the two previous targets and is named TwinDiel. It consists of the same cylinders as the FoamDielInt and FoamDielExt target and contains twice the smallest plastic cylinder, once positioned outside the larger foam cylinder and once inside it, as shown in Fig. 7.25. The material properties for the smallest cylinders are: radius $r_a = 15.5$ mm $\approx 0.2\lambda_0$ and relative permittivity $\varepsilon_{r,a} = 3 \pm 0.3$. The larger foam cylinder has $r_b = 40$ mm $\approx 0.5\lambda_0$ and $\varepsilon_{r,b} = 1.45 \pm 0.15$. Also here, the foam cylinder is positioned in the center of the antenna circle (within the uncertainty introduced by the positioning errors). The source configuration is slightly different than before: $T = 18$ source positions with TM and TE polarization resulting in a data vector $\mathbf{e}^{\text{meas}}$ of length $N^D = 26028$.

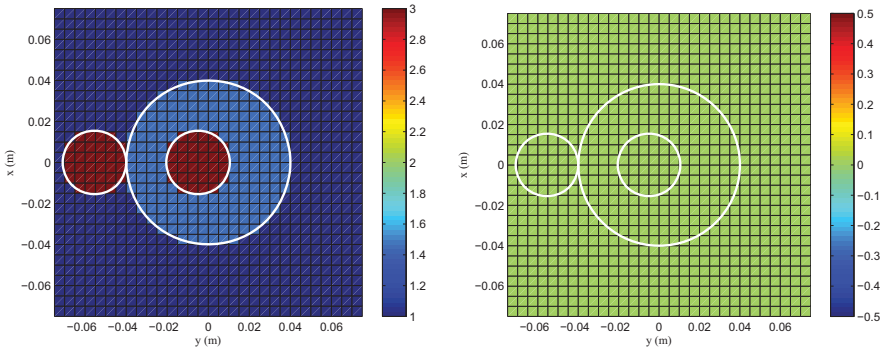

(a) (b)

Figure 7.25: (a) Real part and (b) imaginary part of the TwinDiel target of Institut Fresnel.

7.6.1 Reconstruction using Multiplicative Smoothing regularization

We start with a reconstruction based on multiplicative smoothing regularization. Also here, the regularization parameter of the cost function is set to $\alpha = 10^{-3}$. Figure 7.26 shows the reconstructed permittivity profile. The presence of the two small plastic cylinders is clearly visible, although their shape is harder to determine. Their relatively large permittivity (when compared to the background and foam cylinder) can be distinguished. The larger foam cylinder is less perceptible, due to the fluctuations in permittivity of the background medium. With regard to the permittivity of the foam cylinder, one can only conclude that it lies somewhere between the high permittivity of the small cylinders and the background permittivity. A swarm plot of the reconstructed profile is shown in Fig. 7.27. As could be expected from this type of regularization, no clustering of permittivities is visible. Furthermore, permittivities are spread out relatively far to the left (real part smaller than 1) and towards high imaginary parts. The

decrease of the data fit as a function of the iteration number is presented in Fig. 7.28, showing a stagnation after ± 22 iterations around $\mathcal{F}^{LS} \approx 2.4\ 10^{-3}$.

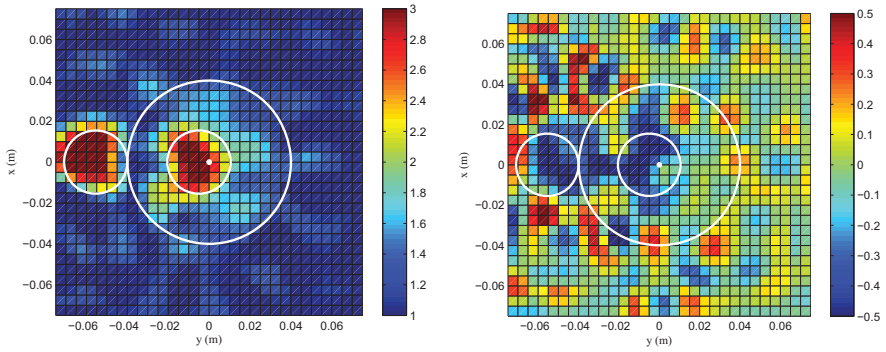

(a) (b)

Figure 7.26: (a) Real part and (b) imaginary part of the reconstructed permittivity profile of the TwinDiel target, based on the multiplicative smoothing regularized cost function. The white lines indicate the actual object boundaries.

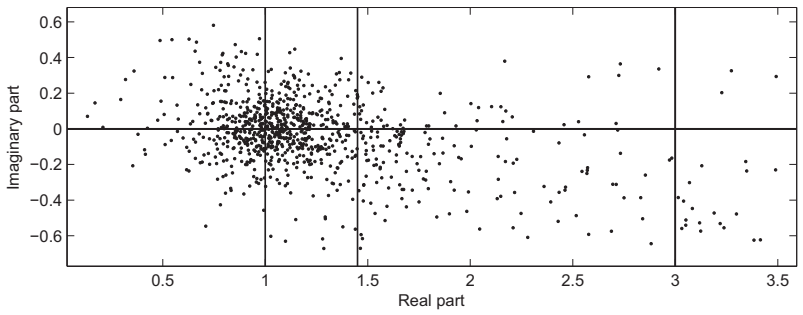

Figure 7.27: Swarm plot of the reconstructed TwinDiel permittivity profile with multiplicative smoothing regularization. Each permittivity pixel is represented as a dot in the complex plane, the intersections of the solid lines represent the actual permittivity values, including free space as background.

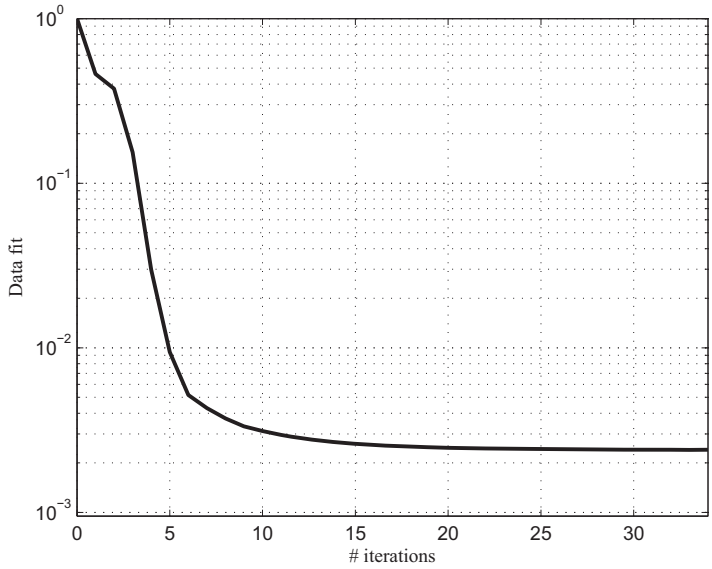

Figure 7.28: The data fit while reconstructing the TwinDiel target, based on the multiplicative smoothing regularized cost function.

7.6.2 Reconstruction using Stepwise Relaxed Value Picking regularization

In the previous sections, the reconstructions based on the stepwise relaxed value picking regularization yielded a more detailed image of the target, when compared to the reconstruction with the multiplicative smoothing regularization. We will show that this is also the case for this more complicated target.

Since the measurement set-up for this target consists of many more illuminations than the previous ones (resulting in many more forward problems that need to be solved and hence much longer simulation times), we choose not to start from free-space as initial guess, but from a permittivity profile that is obtained during the multiplicative smoothing regularized optimization. However, we cannot use the final result as initial guess since this profile already corresponds to a data fit on the noise level and leaves no extra space for further optimization. Therefore, the permittivity profile that corresponds to a data fit of $\mathcal{F}^{LS} = 9.5\ 10^{-3}$ (achieved in iteration 5 in the multiplicative smoothed reconstruction after approximately 2.5 hours) is taken as initial guess for this reconstruction. This permittivity profile is shown in Fig. 7.29.

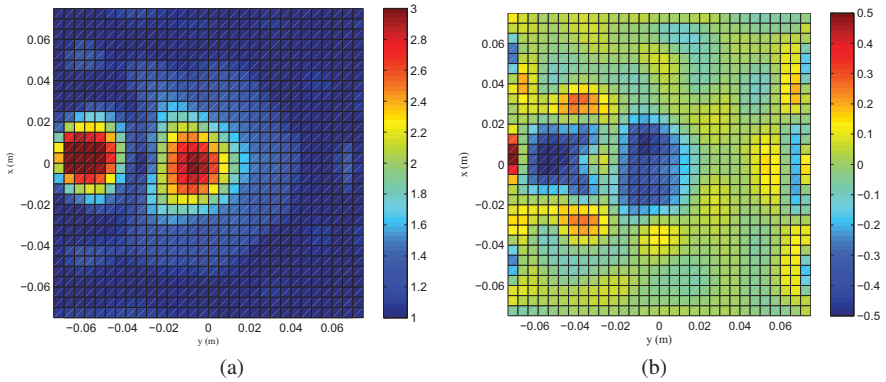

(a) (b)

Figure 7.29: (a) Real part and (b) imaginary part of the initial permittivity profile for the reconstruction of the TwinDiel target.

The same constraints are imposed on the VP values as in the previous sections: (i) $1.1 < \Re(c_p) < 5,\ \forall c_p$ and (ii) $-0.001 < \Im(c_p) < 0.001,\ \forall c_p$. Since a regularization weight of $\gamma = 3$ proved to be a good choice for the other targets, we choose to use the same regularization parameter for this target.

Figure 7.30 presents the decreasing data fit during the optimization with the stepwise relaxed value picking regularization. In the first iteration (the switching between multiplicative smoothing and stepwise relaxed value picking regularization), the data fit slightly increases, but decreases steadily afterwards. The total simulation time in this case is 3h 35 min.

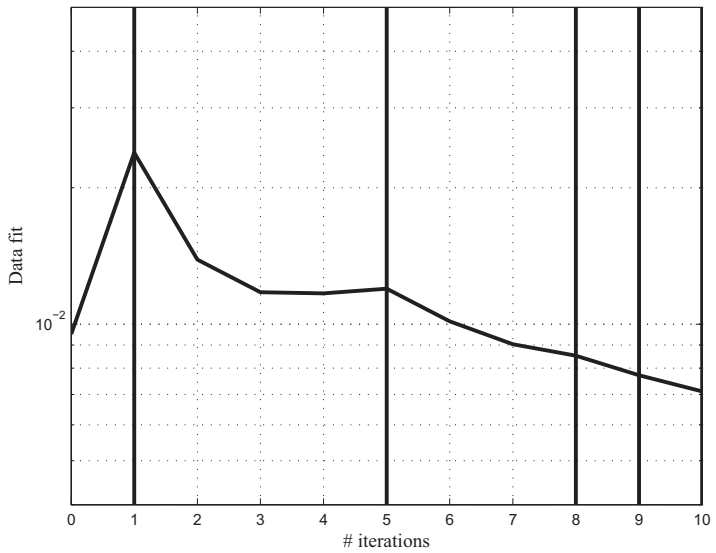

Figure 7.30: The data fit as a function of the iteration number, for the reconstruction of the FoamDielExt target with stepwise relaxed value picking regularization. The vertical lines denote the iterations in which a VP value was added.

Five VP values are added during the optimization process (after iteration 10): $c_1 = 3.00$, $c_2 = 1.39$ and c_3, c_4 and c_5 merged during the optimization process into $c_3 = c_4 = c_5 = 2.59$. The corresponding VP weights for every pixel in the reconstruction domain are shown in Fig. 7.31. Since the VP's c_3, c_4 and c_5 merged, their corresponding weight plots are identical, as can be seen from Fig. 7.31(c), (d) en (e). The small cylinder at the left side of the reconstruction grid and the small cylinder inside the foam one are visible, although their inner parts (especially that of the left one) are more drawn towards $c_1 = 3.00$, see Fig. 7.31(a). Figure 7.31(b) reveals the outer foam cylinder and Fig. 7.31(f) shows which cells are attracted to the background VP. Based on these weight plots, we can conclude that the scatterers are probably: (i) a large cylinder in the center of the grid with permittivity $c_2 = 1.39$ ($\varepsilon_{r,b} = 1.45 \pm 0.15$), (ii) a small cylinder inside the large one with permittivity $c_3 = c_4 = c_5 = 2.59$ (slightly too low, $\varepsilon_{r,a} = 3 \pm 0.3$), (iii) a small cylinder left of the large one with permittivity $c_3 = c_4 = c_5 = 2.59$ (again slightly too low, $\varepsilon_{r,a} = 3 \pm 0.3$) and possibly (iv) a very small cylinder inside the left one with permittivity $c_1 = 3.00$. Hence, from these VP weights, the left cylinder is not expected to be a homogeneous object. Furthermore, artifacts are present in the reconstructed profile: there is an exchange of VP values between the background and the large cylinder, see 7.31(b) and Fig. 7.31(f). This was also the case when reconstructing the FoamDielExt target, see Section 7.5.2.

Figure 7.32 shows cross-sections through the real part of the reconstructed permittivity profile along the x- and y- axis and through the center of the reconstruction

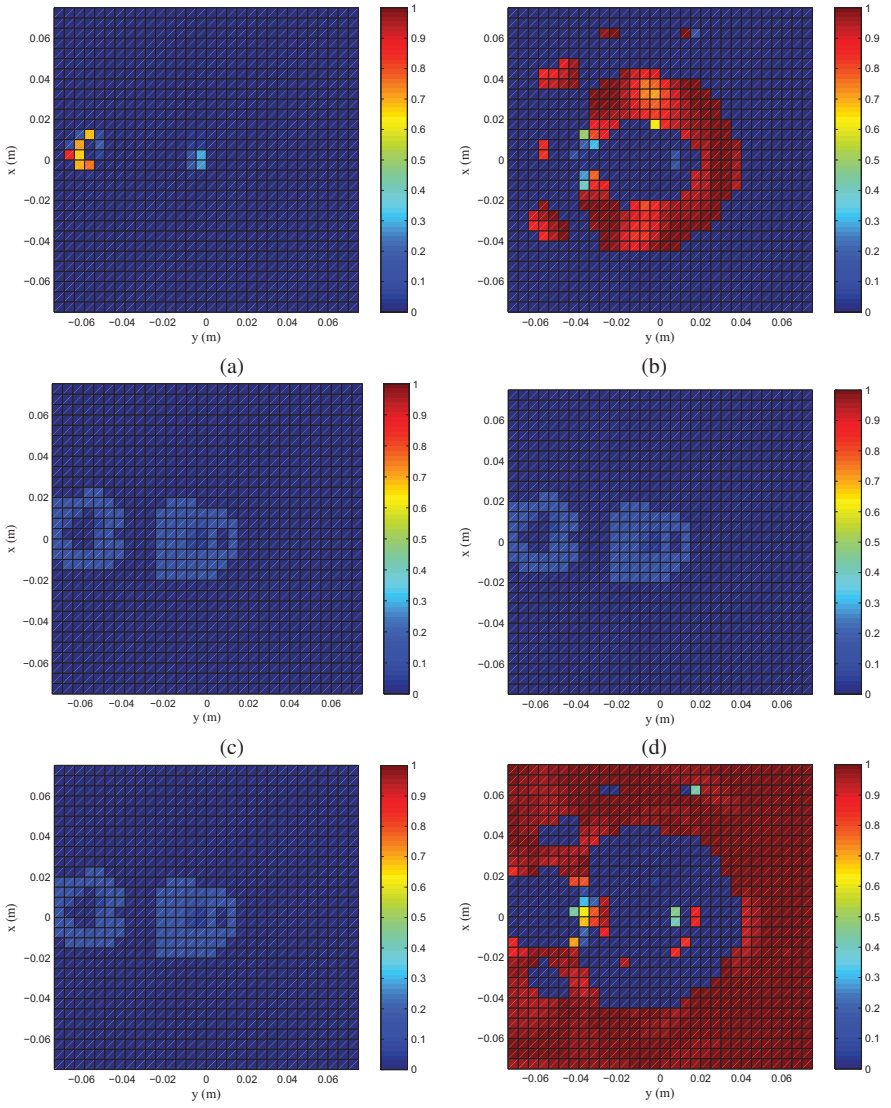

Figure 7.31: A plot of the VP weights $b^P_{p,n}$ for every reconstruction cell n. (a) weight $b^P_{1,n}$ corresponding to $c_1 = 3.00$, (b) weight $b^P_{2,n}$ corresponding to $c_2 = 1.39$, (c) weight $b^P_{3,n}$ corresponding to $c_3 = 2.59$, (d) weight $b^P_{4,n}$ corresponding to $c_4 = 2.59$, (e) weight $b^P_{5,n}$ corresponding to $c_5 = 2.59$ and (f) weight $b^P_{6,n}$ corresponding to the VP value that is kept fixed to the background permittivity ($c_6 = 1$).

grid. The reconstruction in Fig. 7.32(a) is rather good, whereas Fig. 7.32(b) reveals the artifacts inside all cylinders and the background medium. The complete reconstructed permittivity profile, for $\gamma = 3$, is presented in Fig. 7.33.

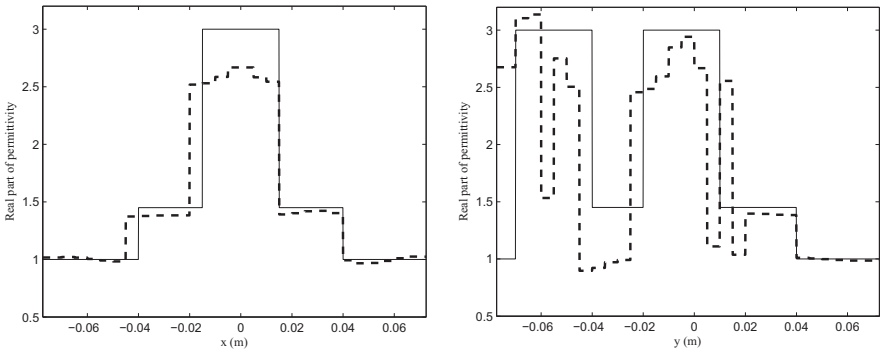

(a) (b)

Figure 7.32: Cross-section through the real part of the reconstructed permittivity profile along the $x-$ axis (a) and along the y-axis (b) and through the center of the reconstruction grid, for a reconstruction of the TwinDiel target with stepwise relaxed value picking regularization. The solid lines correspond to the actual profile, the dashed ones to reconstructed profiles.

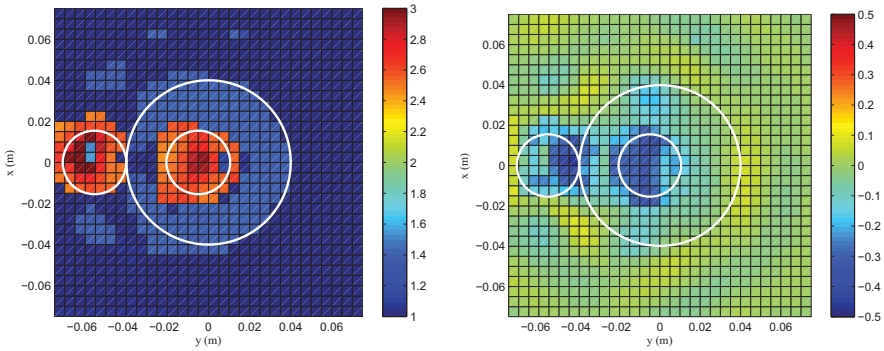

(a) (b)

Figure 7.33: (a) Real part and (b) imaginary part of the reconstructed permittivity profile of the TwinDiel target, based on the stepwise relaxed value picking regularized cost function. The white lines indicate the actual object boundaries.

Fig. 7.34 shows the swarm plot of the reconstructed permittivity profile, for $\gamma = 3$. A good clustering of the permittivities is visible around the background permittivity and around $c_2 = 1.39$, the assumed permittivity of the large foam cylinder. The reconstructed permittivities for the small plastic cylinders are more spread out around

$c_3 = c_4 = c_5 = 2.59$ and spread towards negative imaginary parts. A few permittivity dots appear with a real part larger then 3. However, when compared to the swarm plot when multiplicative smoothing regularization (Fig. 7.27) is applied, the clustering effect is apparent. This behavior was also present in the reconstructions of the FoamDielInt and FoamDielExt targets with stepwise relaxed value picking regularization (see Fig. 7.10 and Fig. 7.19).

Section 7.5.3 already proved that the newly proposed stepwise relaxed object smoothed value picking regularization technique is capable of strongly reducing the artifacts that can appear when purely stepwise relaxed value picking regularization is applied. It is expected that also for this target, this new regularization technique will lead to a further improvement of the reconstruction.

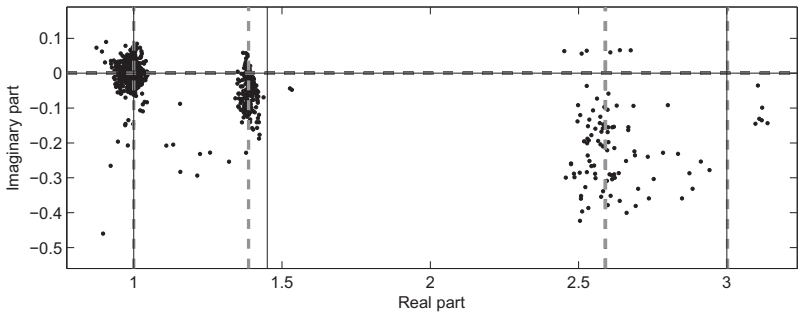

Figure 7.34: Swarm plot of the reconstructed TwinDiel permittivity profile with stepwise relaxed value picking regularization. Each permittivity pixel is represented as a dot in the complex plane, the intersections of the solid lines represent the actual permittivity values, intersections of dashed lines represent optimized VP values.

7.6.3 Reconstruction using Stepwise Relaxed Object Smoothed Value Picking regularization

Finally, the stepwise relaxed object smoothed VP regularization is applied to the TwinDiel target. Also here, the constraints on the VP values are $1.1 < \Re(c_p) < 5$, $\forall c_p$ and $-0.001 < \Im(c_p) < 0.001$, $\forall c_p$, and VP values are added once the criterion to add an new VP value in the stepwise relaxed VP regularization scheme is fulfilled. The weight of the object smoothing regularization term is set to $\zeta = 10^{-3}$, whereas the weight of the VP part of the cost function is still $\gamma = 3$. Due to the stronger regularization (when compared to the purely stepwise relaxed value picking regularization), the data fit decreases more slowly, as can be seen from Fig. 7.35. Furthermore, the total simulation time (i.e. 6h 53 min) is much larger, compared to the purely stepwise relaxed value picking regularized reconstruction (3h 35 min). The final VP values (at iteration nr. 12) are $c_1 = 3.50$, $c_2 = 1.40$ and c_3, c_4 and c_5 merged during the optimization into $c_3 = c_4 = c_5 = 2.88$. It can be expected that the two largest VP values correspond to the small plastic cylinders and that their actual real part of the permittivity lies somewhere in between these values. However, if the final VP weights are studied in Fig. 7.36, it is clear that no cells are attracted towards $c_1 = 3.50$ (see Fig. 7.36(a)) and hence, all cells at the locations of the small cylinders take the VP value $c_3 = c_4 = c_5 = 2.88$ (see Fig. 7.36(c), (d) and (e)). Therefore, the permittivity of the small cylinders can be estimated as 2.88, which lies again within the uncertainty bounds on the actual permittivity ($\varepsilon_{r,a} = 3 \pm 0.3$). All cells at the location of the larger foam cylinder are attracted towards $c_2 = 1.40$ (see Fig. 7.36(b)) and, by consequence, this foam cylinder permittivity is estimated as 1.40, lying within the uncertainty bounds on the permittivity ($\varepsilon_{r,b} = 1.45 \pm 0.15$).

Although none of the cells are finally attracted towards $c_1 = 3.50$, this VP value has not been useless during the optimization. This is illustrated in the group mapping plot of Fig. 7.37, showing the result of the group mapping step at different iteration numbers. Figure 7.37(a) shows the different VP groups after the first iteration. Here, only the background VP value (denoted as c_0) is present and all pixels are assigned to the background group. In Fig. 7.37(b), a first VP value is added (at that stage $c_1 = 3.03$) and the two plastic cylinders start to appear at the correct locations. The same behavior as for the reconstruction of the FoamDielExt target appears here: the inner cells of the appearing small cylinders are assigned to the newly added VP value, the outer cells are still assigned to the indefinite cells group. Once the second VP value is introduced ($c_2 = 1.34$, see Fig. 7.37(c)), the larger foam cylinder appears at the correct position. Also here, its inner cells are immediately assigned to the new VP group, whereas the outer cells end up in the indefinite cells group. At the same time, all cells at the location of the small cylinders have switched to the VP group corresponding to c_1. In Fig. 7.37(d), a third VP value is added ($c_3 = 2.92$). All cells at the small cylinder positions immediately switch to the newly added VP group, since c_1 has moved away at that stage towards $c_1 = 3.49$. Almost all cells that correspond to the foam cylinder

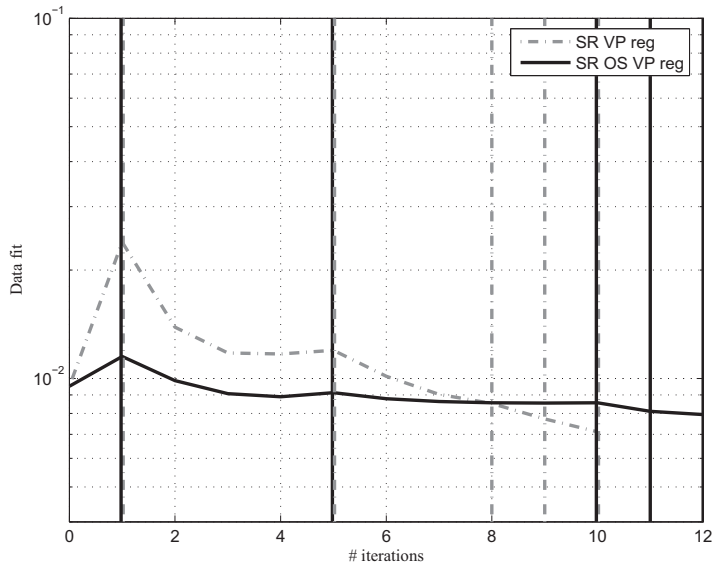

Figure 7.35: The data fit as a function of the iteration number, for the reconstruction of the TwinDiel target. Dashed curve: with stepwise relaxed value picking regularization, solid curve: with stepwise relaxed object smoothed value picking regularization. The vertical lines denote the iterations in which a VP value was added, their corresponding line styles are identical to the data fit curves they are related to.

are now assigned to the correct VP group ($c_2 = 1.38$). In the last but one iteration (Fig. 7.37(e)), another VP value is added but immediately merges with c_3 ($c_4 = c_3 = 2.88$). Since the weight that should correspond to a VP value equal to 2.88 is distributed over two identical VP values, none of these two VP values are dominant. Consequently, all cells that belong to the small plastic cylinders are moved towards the indefinite cells group. At this stage, smoothing is performed over four different regions: (i) an area corresponding with the location of the small plastic cylinder at the left, (ii) an equally sized area corresponding with the location of the small plastic cylinder inside the foam one, (iii) a larger area that corresponds with the support of the foam cylinder and finally (iv) the background medium. In the last iteration (see Fig. 7.37(f)), c_5 is added and also merges ($c_5 = c_4 = c_3 = 2.88$). Therefore, the final situation does not differ from the one in Fig. 7.37(e). Also for this target, we can conclude that the object smoothing is performed exactly on the regions that we wanted.

Cross-sections of the reconstructed permittivity profile are presented in Fig. 7.38, with cross-sections along the x- (a) and y- (b) axis and through the center of the reconstruction grid. From Fig. 7.38(a), we conclude that the dimensions of the large foam cylinder and its inner small plastic cylinder are exactly reconstructed. The permittivity of the large foam cylinder is almost exactly reconstructed (estimated to be 1.40), the permittivity of the small plastic cylinder is somewhat underestimated as 2.88,

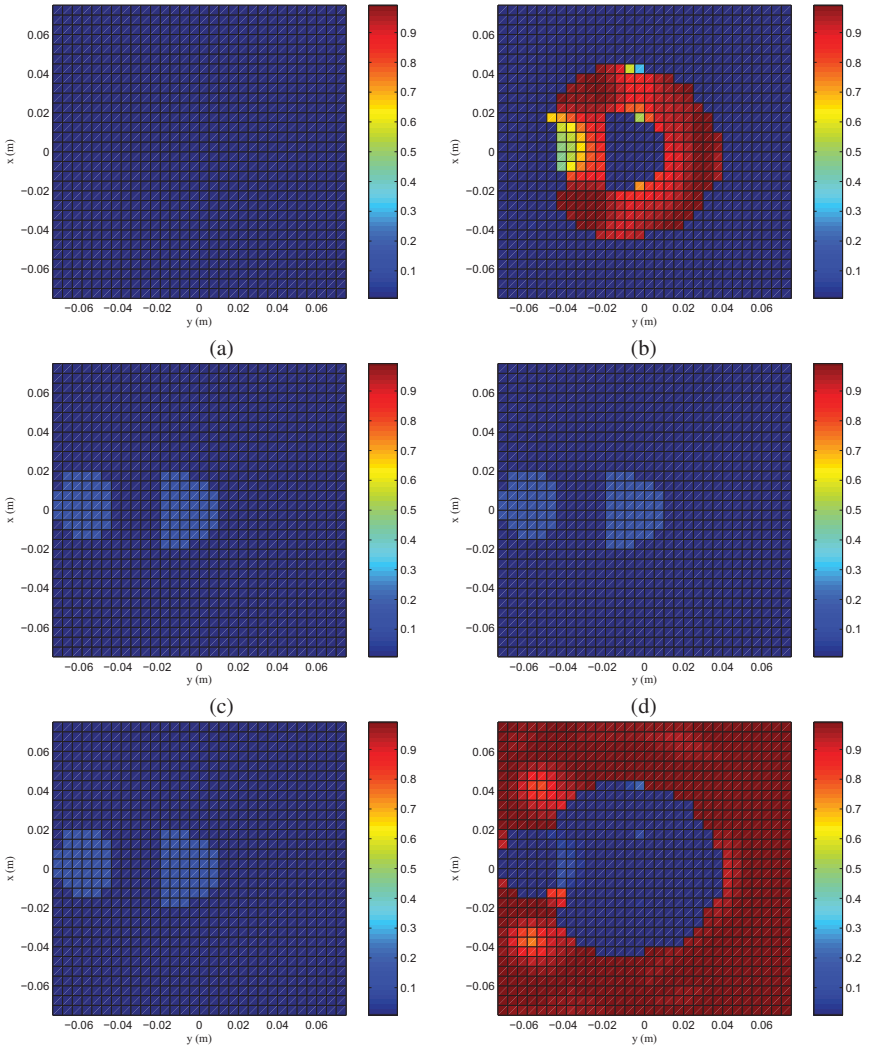

Figure 7.36: A plot of the VP weights $b^P_{p,n}$ for every reconstruction cell n. (a) weight $b^P_{1,n}$ corresponding to $c_1 = 3.50$, (b) weight $b^P_{2,n}$ corresponding to $c_2 = 1.40$, (c) weight $b^P_{3,n}$ corresponding to $c_3 = 2.88$, (d) weight $b^P_{4,n}$ corresponding to $c_4 = 2.88$, (e) weight $b^P_{5,n}$ corresponding to $c_5 = 2.88$ and (f) weight $b^P_{6,n}$ corresponding to the VP value that is kept fixed to the background permittivity ($c_6 = 1$).

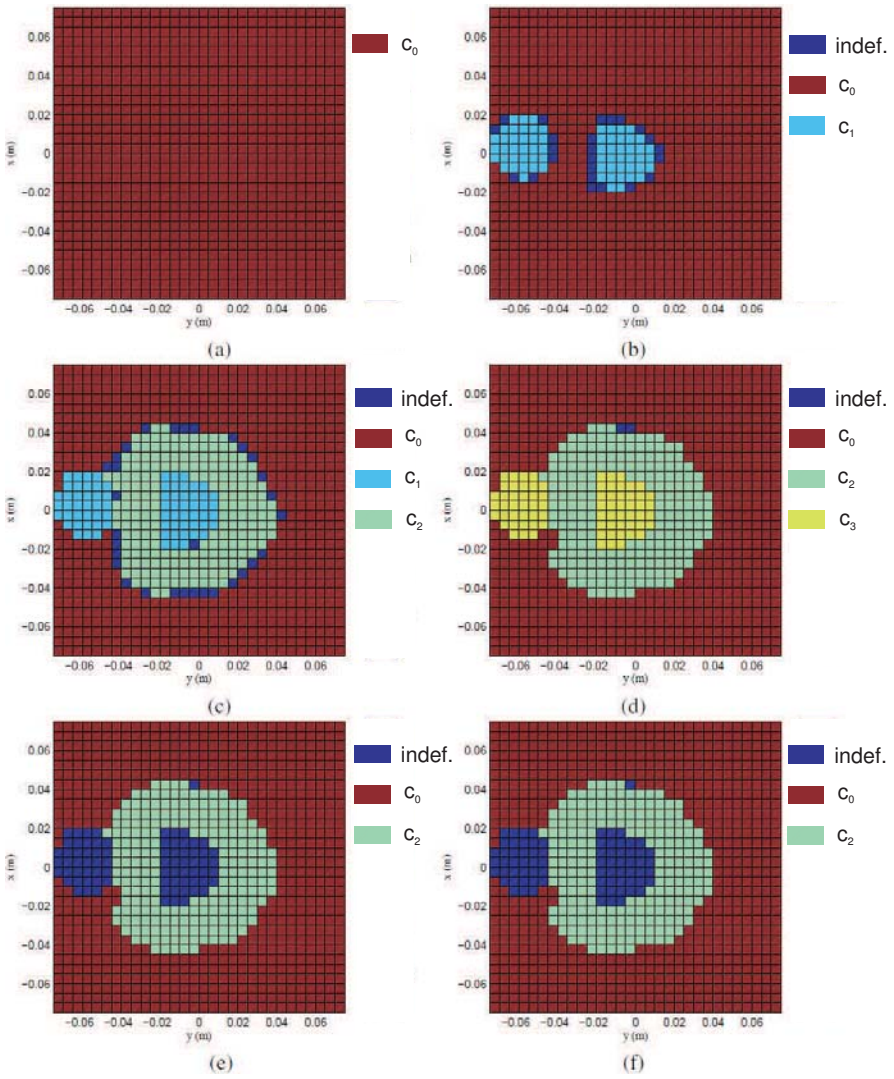

Figure 7.37: A plot of the mapping of permittivity cells into VP groups. The indefinite cells group is denoted as *indef.*, the other VP groups are represented by their VP value, where c_0 denotes the VP value that is kept fixed to the background medium. (a) group mapping before any VP is added (first iteration), (b) group mapping after the introduction of $c_1 = 3.03$, (c) group mapping after adding $c_2 = 1.34$, (d) group mapping after adding $c_3 = 2.92$, (e) group mapping in last but one iteration, after introduction of $c_4 = c_3 = 2.88$ and (f) final group mapping after introduction of $c_5 = c_4 = c_3 = 2.88$.

but all reconstructed permittivities lie within the uncertainty bounds ($\varepsilon_{r,a} = 3 \pm 0.3$, $\varepsilon_{r,b} = 1.45 \pm 0.15$). Figure 7.38(b) shows that the artifacts that appear when the purely stepwise relaxed value picking regularization is applied, have completely disappeared. The dimensions of the small plastic cylinder at the left are very little underestimated, the deviation being smaller than the size of a permittivity pixel. The dimensions of the outer foam cylinder and the inner plastic cylinder are exactly reconstructed, and their permittivities are very well estimated.

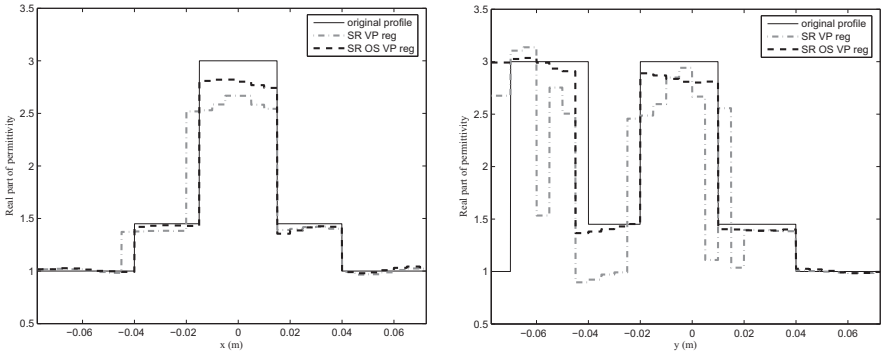

(a) (b)

Figure 7.38: Cross-section through the real part of the reconstructed permittivity profile along the $x-$ axis (a) and along the y-axis (b) and through the center of the reconstruction grid, for a reconstruction of the TwinDiel target with stepwise relaxed object smoothed value picking regularization and purely stepwise relaxed value picking regularization. The solid lines correspond to the actual profile, the dashed ones to reconstructed profiles.

Finally, the complete reconstructed permittivity profile is presented in Fig. 7.39. The quality of the reconstruction with stepwise relaxed object smoothed value picking regularization is comparable to the reconstruction of the FoamDielExt target (Fig. 7.23): the circular shape, dimensions and center positions of all cylinders are correctly reconstructed. There is only one small deviation: the large foam cylinder extends somewhat (approx. the size of two permittivity pixels) too far to the left. The swarm plot of the reconstructed permittivity profile is shown in Fig. 7.40.

From these results we again conclude that the stepwise relaxed object smoothed value picking regularization is a valuable approach to deal with artifacts that can appear when purely stepwise relaxed value picking regularization is applied.

7.7. Conclusion

In this chapter, we have validated the proposed inverse scattering method for the microwave frequency range by reconstructing real world targets from experimental data. The scattering data are part of the 2D Institut Fresnel database and consist of TM- and TE- polarized measured scattered fields for long inhomogeneous dielectric cylinders.

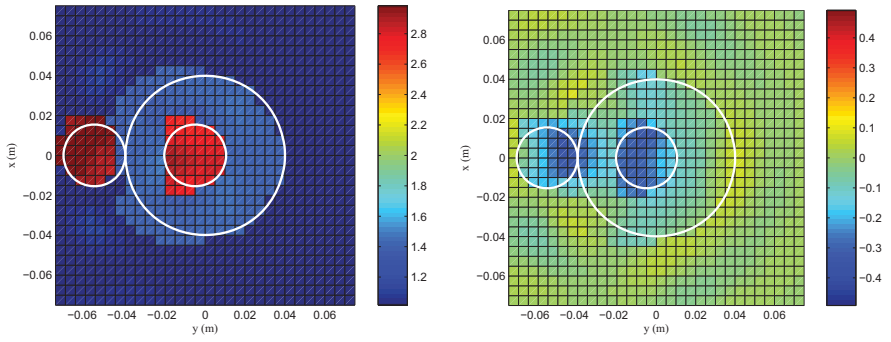

(a) (b)

Figure 7.39: (a) Real part and (b) imaginary part of the reconstructed permittivity profile of the TwinDiel target, based on the stepwise relaxed object smoothed value picking regularized cost function. The white lines indicate the actual object boundaries.

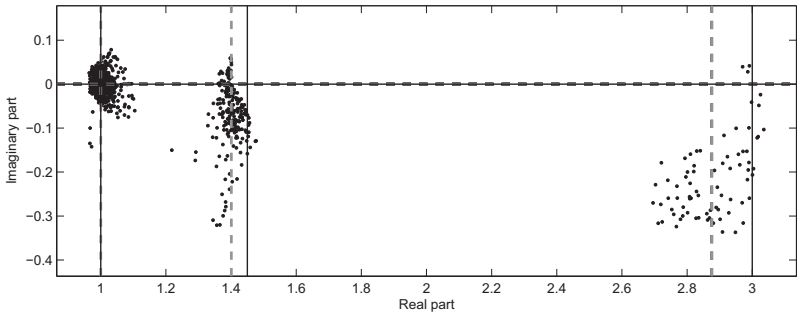

Figure 7.40: Swarm plot of the reconstructed TwinDiel permittivity profile with stepwise relaxed object smoothed value picking regularization. Each permittivity pixel is represented as a dot in the complex plane, the intersections of the solid lines represent the actual permittivity values, intersections of dashed lines represent optimized VP values.

We have obtained very accurate reconstructions of three different Fresnel targets by using single-frequency data only. Furthermore, it is demonstrated that the newly proposed stepwise relaxed object smoothed value picking regularization method leads to a perfectly piecewise homogeneous reconstruction where the stepwise relaxed value picking regularization method suffers from artifacts while reconstructing the FoamDielExt and TwinDiel targets.

Bibliography

[1] D. Colton and R. Kress, *Inverse acoustic and electromagnetic scattering theory*. New York: Springer, 1992.

[2] M. Cote, "Automated swept-angle bistatic scattering measurement using continuous wave radar," *IEEE Transactions on Instrumentation and Measurement*, vol. 41, pp. 185–192, 1992.

[3] R. Mc. Gahan and R. Kleinman, "Special session on image reconstruction using real data," *IEEE Antennas and Propagation Magazine*, vol. 38, pp. 39–40, 1996.

[4] ——, "Second annual special session on image reconstruction using real data," *IEEE Antennas and Propagation Magazine*, vol. 39, pp. 7–9, 1997.

[5] ——, "Third annual special session on image reconstruction using real data, part 1," *IEEE Antennas and Propagation Magazine*, vol. 41, pp. 34–36, 1999.

[6] K. Belkebir and M. Saillard, "Guest editors' introduction. special section: Testing inversion algorithms against experimental data," *Inverse Problems*, vol. 17, pp. 1565–1571, 2001.

[7] K. Belkebir and M. Saillard, "Testing inversion algorithms against experimental data: Inhomogeneous targets," *Inverse Problems*, vol. 21, no. 6, pp. S1–S3, 2005.

[8] J. Geffrin, P. Sabouroux, and C. Eyraud, "Free space experimental scattering database continuation: experimental set-up and measurement precision," *Inverse Problems*, vol. 21, no. 6, pp. S117–S130, 2005.

[9] J. Geffrin and P. Sabouroux, "Continuing with the fresnel database: experimental set-up and improvements in 3D scattering measurements," *Inverse Problems*, vol. 25, no. 2, p. 024001, 2009.

[10] A. Abubakar, P. van den Berg, and T. Habashy, "Application of the multiplicative regularized contrast source inversion method on TM- and TE- polarized experimental fresnel data," *Inverse Problems*, vol. 21, no. 6, pp. S5–S13, 2005.

[11] O. Feron, B. Duchene, and A. Mohammad-Djafari, "Microwave imaging of inhomogeneous objects made of a finite number of dielectric and conductive materials from experimental data," *Inverse Problems*, vol. 21, no. 6, pp. S95–S115, 2005.

[12] A. Baussard, "Inversion of multi-frequency experimental data using an adaptive multiscale approach," *Inverse Problems*, vol. 21, no. 6, pp. S15–S31, 2005.

[13] A. Dubois, K. Belkebir, and M. Saillard, "Retrieval of inhomogeneous targets from experimental frequency diversity data," *Inverse Problems*, vol. 21, no. 6, pp. S65–S79, 2005.

[14] L. Crocco, M. D'Urso, and T. Isernia, "Testing the contrast source extended born inversion method against real data: the TM case," *Inverse Problems*, vol. 21, no. 6, pp. S33–S50, 2005.

[15] C. Yu, L. Song, and Q. Liu, "Inversion of multi-frequency experimental data for imaging complex objects by a DTA-CSI method," *Inverse Problems*, vol. 21, no. 6, pp. S165–S178, 2005.

[16] A. Litman, "Reconstruction by level sets of *n*-ary scattering obstacles," *Inverse Problems*, vol. 21, no. 6, pp. S131–S152, 2005.

[17] U. Shahid, M. Testorf, and M. Fiddy, "Minimum-phase-based inverse scattering algorithm applied to institut fresnel data," *Inverse Problems*, vol. 21, no. 6, pp. S153–S164, 2005.

[18] C. Estatico, M. P. G. Bozza, A. Massa, and A. Randazzo, "A two-stepiterative inexact -newton method for electromagnetic imaging of dielectric structures from real data," *Inverse Problems*, vol. 21, no. 6, pp. S81–S94, 2005.

[19] M. Donelli, M. P. D. Franceschini, A. Massa, and A. Zanetti, "Multi-resolution iterative inversion of real inhomogeneous targets," *Inverse Problems*, vol. 21, no. 6, pp. S51–S63, 2005.

[20] J. De Zaeytijd, A. Franchois, C. Eyraud, and J. Geffrin, "Full-wave three-dimensional microwave imaging with a regularized gauss-newton method – theory and experiment," *IEEE Transactions on Antennas and Propagation*, vol. 55, no. 11, pp. 3279–3292, Nov. 2007.

[21] J. De Zaeytijd, "On the 3D electromagnetic quantitative inverse scattering problem: algorithms and regularization," Ph.D. dissertation, Ghent University, 2008.

[22] J. De Zaeytijd and A. Franchois, "3D quantitative microwave imaging from measured data with multiplicative smoothing and value picking regularization," *Inverse Problems*, vol. 25, no. 2, p. 024004, Feb. 2009.

CHAPTER 8

Reconstructions at millimeter wave frequencies from synthetic data

8.1. Introduction

The previous chapter offered an extensive validation study for the proposed inverse scattering method. These validation cases are all performed at microwave frequencies. The proposed method was developed in the framework of a millimeter wave joint research project [1]. Therefore, this chapter presents some reconstruction results at these high frequencies. By consequence, we are restricted to *synthetic* scattering data. The term *synthetic* denotes that the scattered field input data are generated by a forward scattering method instead of obtained by real measurements. All synthetic data in this chapter are produced by the forward scattering solver presented in the first part of this PhD work.

To fully exploit the acceleration techniques presented in Chapter 2, the marching-on-in-source-position and marching-on-in-spectral-component techniques are applied, where three previous forward problem solutions are combined into an initial guess for the current forward problem solution. All simulations are performed on a machine containing two quadcore AMD Opteron 2350 processors, allowing a multi-threaded implementation using all 8 CPU cores.

This chapter contains two sections. The first one deals with the influence of the type of incident field on the reconstruction process. A comparison is made between reconstructions obtained with plane wave illumination and reconstructions obtained with Gaussian beam illumination and this for different types of polarization of the incident field. The second section covers the largest reconstruction example of this PhD work: the reconstruction of a small object hidden underneath a layer of clothing on

a human body model. The configuration for this simulation is based on the human body simulation of Section 4.4 and is challenging due to different reasons. First, the permittivity of the skin layer is relatively large, which demands a fine discretization when solving the forward scattering problem. Combined with the relatively large dimensions of the body compared to the free space wavelength (order of millimeters), the number of cells in the forward scattering problem is very large. Second, the illumination is not realized over 360° around the target, since it is physically not possible to realize source positions inside the human body. Therefore the number of different incidence angles is limited, which worsens the *in-depth resolution*, i.e. the position between the clothing and skin layer and the thickness of the hidden object are hard to determine. Third, the human body model is illuminated with Gaussian beams, which requires the solution of forward scattering problems for different spectral components. Therefore, larger simulation times are expected compared to a plane wave illumination. Consequently, the number of antenna and detector positions must be strongly restricted and the human body model of Section 4.4 has to be further simplified.

8.2. Influence of the incident field type on the reconstruction

In this section, we study the influence of the type of incident field (plane wave versus Gaussian beam) and the polarization of the incident field (TM- or TE- only or combined TE-TM polarization) on the reconstruction process of a moderately sized target.

All simulations are performed at 300 GHz ($\lambda_0 = 1$ mm) and the multiplicative smoothing regularization technique (with a regularization parameter $\alpha = 0.005$) is used . The initial guess for the permittivity profile is free space. Furthermore, 30 dB of white Gaussian noise is added to the synthetic data. The target consists of three concentric dielectric squares, surrounded with air, see Fig. 8.1. The respective relative permittivities are $\varepsilon_{outer} = 1.2$, $\varepsilon_{middle} = 1.3$ and $\varepsilon_{inner} = 1.4$ and the edge lengths of the squares are $d_{outer} = 2\ \lambda_0 = 2.0$ mm, $d_{middle} = 1.2\ \lambda_0 = 1.2$ mm and $d_{inner} = 0.4\ \lambda_0 = 0.4$ mm. The size of a permittivity cell in the reconstruction grid is $\Delta_{inv} = 0.2\ \lambda_0 = 0.2$ mm, yielding 12×12 unknowns.

Plane waves and Gaussian beams are used as incident fields. The Gaussian beams have a beam waist radius of $8\lambda_0 = 8$ mm and the beam waist planes located at the center of the reconstruction grid.

The scatterer is illuminated from 40 directions, equally spaced 9°, see Fig. 8.2. All Gaussian beams completely illuminate the target. We test the effect on the reconstruction of three types of polarization for the incident field: TM, TE and combined TE-TM polarization. In Fig. 8.2, the black square represents the reconstruction grid, the horizontal dark blue arrows indicate the propagation direction for each illumination, and the vertical light blue arrows represent the direction of the electric field for TM polarization. The scattered fields are measured in 40 detector points, distributed along a circle of radius $5\lambda_0$, see Fig. 8.2.

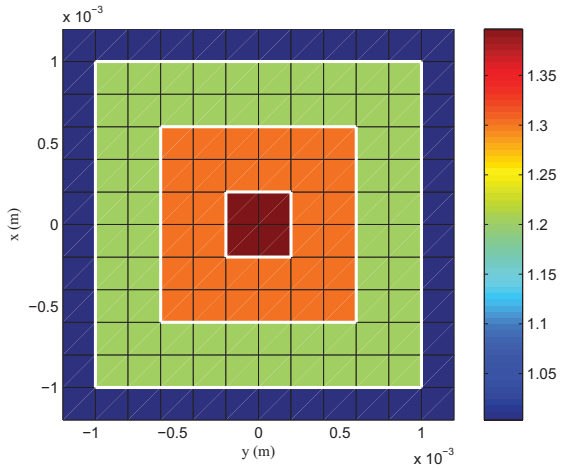

Figure 8.1: Real part of the actual permittivity profile when comparing the influence on the reconstruction of the incident field type.

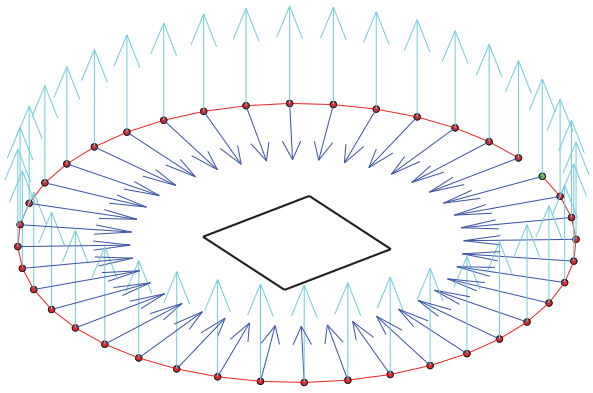

Figure 8.2: Illumination configuration for the reconstruction of the target of Fig. 8.1. All 40 source and detector positions are distributed along a circle of radius $5\lambda_0$. The black square represents the reconstruction grid. The horizontal dark blue arrows indicate the propagation directions of all incident fields, the vertical light blue arrows represent the TM polarization direction.

Figure 8.3 presents the real part of the reconstructed profile for the simulations with TM-polarized incident fields. Fig. 8.3(a) corresponds to a plane wave illumination, whereas Fig. 8.3(b) corresponds to an illumination with Gaussian beams. The solid white lines indicate the contours of the actual target. For both types of incident fields, the simulations result in relatively smooth objects. The permittivity of the smallest inner square is slightly underestimated: the permittivity of the 4 inner cells is estimated as 1.36, 1.36, 1.34 and 1.36 for the plane wave case and 1.36, 1.36, 1.35 and

1.35 for the Gaussian beam case. Figure 8.4 shows the real part of the reconstructed profile, for a TE-polarized illumination. Here, a larger difference exists between the reconstruction with plane wave illumination (Fig. 8.4(a)) and the reconstruction with Gaussian beam illumination (Fig. 8.4(b)) since there are slightly more local oscillations in the permittivity profile for the Gaussian beam case. The permittivity of the 4 inner cells is estimated as 1.37, 1.39, 1.39 and 1.38 for the plane wave case and 1.45, 1.41, 1.37 and 1.42 for the Gaussian beam case. The reconstruction for combined TE-TM- polarization, presented in Fig. 8.5, is almost perfect. For the plane wave illumination (Fig. 8.5(a)), the largest (outer) cylinder is very smooth, whereas the middle cylinder has more local oscillations in permittivity. The reverse situation is visible in the Gaussian beam case: the middle cylinder is relatively smooth and the outer cylinder has more local oscillations. For both types of incident field, the permittivity of the 4 inner cells is exactly estimated as $\varepsilon_{inner} = 1.4$. We conclude that a similar reconstruction quality is obtained for both types of incident fields, although the TE- reconstruction with Gaussian beams is slightly worse.

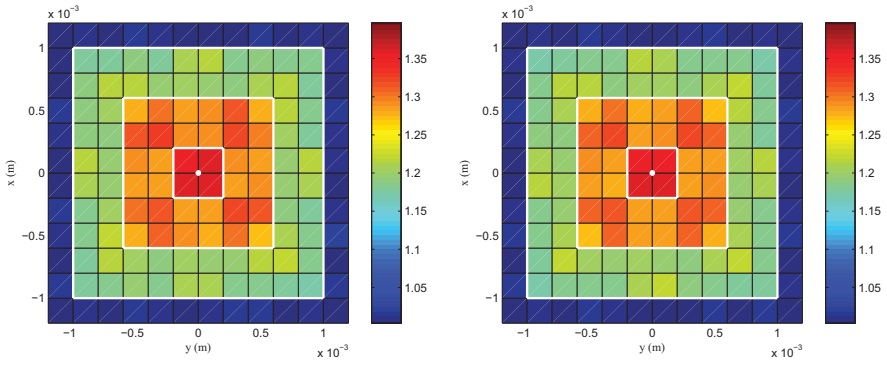

Figure 8.3: Reconstructed real part of the permittivity profile of Fig. 8.1 using a TM polarized illumination with (a) plane waves and (b) Gaussian beams as incident fields. The solid white lines indicate the contours of the actual target.

Table 8.1 shows some other reconstruction parameters for both types of incident fields and all three polarization cases. From the second column, it is clear that the type of incident field does not influence the number of iterations in the reconstruction process. However, the type of incident field is a determining factor when the total simulation times are compared. Since a factor five more forward problems need to be solved for the Gaussian beam case than for the plane wave case (five spectral components instead of one), the total simulation times are much larger. Another way to compare reconstructed permittivity profiles is to define a relative error as

$$\text{rel. error}(\boldsymbol{\varepsilon}) = \frac{||\boldsymbol{\varepsilon} - \boldsymbol{\varepsilon}^0||}{||\boldsymbol{\varepsilon}^0||}, \tag{8.1}$$

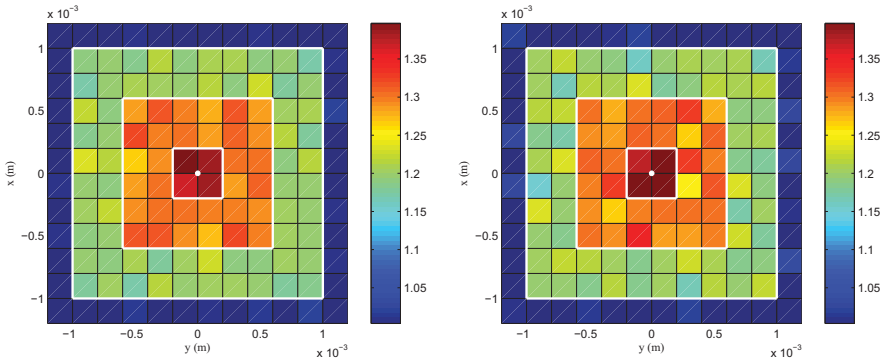

Figure 8.4: Reconstructed real part of the permittivity profile of Fig. 8.1 using a TE polarized illumination with (a) plane waves and (b) Gaussian beams as incident fields. The solid white lines indicate the contours of the actual target.

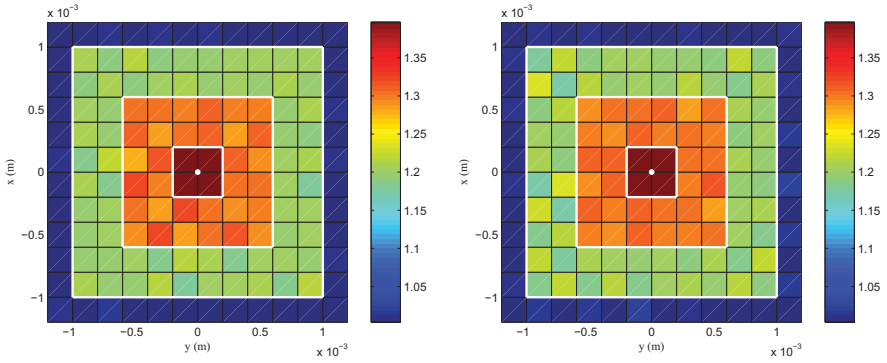

Figure 8.5: Reconstructed real part of the permittivity profile of Fig. 8.1 using a TE- and TM-polarized illumination with (a) plane waves and (b) Gaussian beams as incident fields. The solid white lines indicate the contours of the actual target.

where $\boldsymbol{\varepsilon}^0$ denotes the actual (correct) permittivity profile. The reconstructed profiles for TM polarization both have the largest relative error of only 1.5%. The plane wave TE-polarized case yields an error of 0.95%, whereas the Gaussian beam TE-polarized case corresponds to a larger error of 1.4%. The best reconstructions (obtained with combined TE-TM- polarization) have a relative error of 0.73% for the plane wave case and 0.98% for the Gaussian beam case. Another comparison parameter is the mean permittivity of a square. This mean permittivity is computed by averaging all permittivity cells that lie within the actual (correct) bounds of that object. If we compare these parameters, the difference between results of plane wave illumination and Gaus-

sian beam illumination is negligible, the only deviation appears for the TE-polarized reconstructions where the permittivity of the inner square is slightly underestimated ($\varepsilon_{inner}^{mean} = 1.38$) for plane wave illumination and slightly overestimated ($\varepsilon_{inner}^{mean} = 1.41$) for Gaussian beam illumination. From these data it is clear that in all cases almost perfect reconstructions are obtained.

The decrease of the data fit is shown in Fig. 8.6 for all polarization cases and both types of incident fields. All simulations give rise to a similar behavior, for plane wave and Gaussian beam illuminations.

Finally, we conclude that the largest implication of changing the incident fields from plane waves to Gaussian beams is the increased simulation time. The number of iterations remains unaltered and the mean permittivities do not remarkably change. There is a small effect on the reconstructed profiles, illustrated by the slightly larger relative errors on the permittivity.

Table 8.1: Results of the reconstructions with plane wave (PW) and Gaussian beam (GB) illumination for TM-, TE- and combined TE-TM polarization: number of iterations, total simulation time, relative error and mean permittivities of objects within their actual bounds.

	# it.	CPU time	rel. error($\boldsymbol{\varepsilon}$)	mean perm.
TM PW	4	1'24"	1.5%	1.196 1.294 1.358
TE PW	5	1' 54"	0.95%	1.199 1.297 1.383
TE-TM PW	5	2' 50"	0.73%	1.200 1.301 1.399
TM GB	4	8' 48"	1.5%	1.196 1.294 1.355
TE GB	5	10' 38"	1.4%	1.200 1.299 1.413
TE-TM GB	5	15' 35"	0.98%	1.201 1.301 1.403

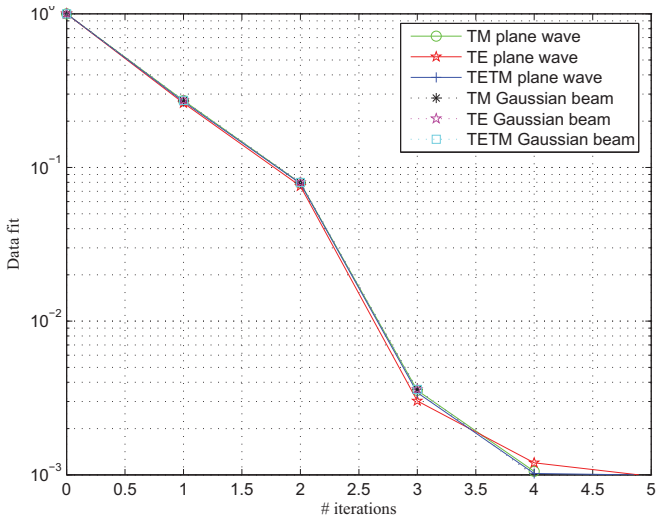

Figure 8.6: The data fit as a function of the iteration number, corresponding to the reconstructions of the target of Fig. 8.1 for plane wave and Gaussian beam illumination with TM-, TE- or combined TE-TM polarization.

8.3. A millimeter wave reconstruction of a simplified human body model

This section presents a reconstruction result for the clothed human body model (see Section 3.5) with a hidden object underneath the clothing. The working frequency is 94 GHz, which corresponds to a free space wavelength of about $\lambda_0 = 3$ mm. The illumination consists of Gaussian beams with a beam waist radius of $w_0 = 2.67\lambda_0 = 8$ mm, the beam waist plane is located at the exterior surface of the clothing layer.

This section illustrates the possibility to image hidden objects on a clothed human body with millimeter waves. Since we are restricted in memory consumption and computation time, we assume that the positions, thicknesses, shapes and permittivities of the clothing layer and the human body layers are known. It is not our aim to reconstruct these layers, we only hope to reveal the presence of the hidden object. Therefore, the *partial inverse problem grid* approach of Chapter 6 is used. All layers of the human body model are assumed to be part of the background and their corresponding permittivity cells are not optimized for. Only cells at the assumed location of a possible hidden object (i.e. between the clothing and skin layer) are treated as inverse problem unknowns.

As already mentioned in the introduction, this type of reconstruction is challenging due to the large size of the involved forward problems, the aspect-limited data and the Gaussian beam illumination. We will now focus on each of these aspects in detail.

We start the analysis by inspecting the number of forward problems that needs to be solved in every iteration. Each iteration consists of different steps. First, for the current permittivity profile, the corresponding scattered field is determined by solving the *regular forward problems* (see Section 6.6). A regular forward problem is to be solved for:

- every source position
- every polarization of the incident field (TM-, TE- or both)
- every spectral component k_z of the incident field.

Second, to determine the Jacobian matrix $\mathbf{J}$ (containing the derivatives of the scattered field with respect to the permittivity profile), we need to compute the inhomogeneous Green's function $\widehat{\mathbf{G}}_{\text{inh}}$ (6.83). This is done by solving the set of *dipole forward problems* (see Section 6.6). There is a dipole forward problem for:

- every receiver position
- all three receiver polarization directions ($x-$, y- and z-direction)
- every spectral component k_z of the incident field

Once the scattered field and Jacobian matrix are determined for the current permittivity profile ($\boldsymbol{\varepsilon}_k$), the update direction for the permittivity profile ($\Delta\boldsymbol{\varepsilon}_k$) can be determined, along which a line search is performed to find an adequate step size β_k. Hence, the next permittivity profile is given by $\boldsymbol{\varepsilon}_{k+1} = \boldsymbol{\varepsilon}_k + \beta_k \Delta\boldsymbol{\varepsilon}_k$.

Each step of the line search routine itself also contains several forward problems: (i) to evaluate $\mathcal{F}(\beta_k)$, all regular forward problems (for every k_z, every source position and every polarization) must be solved for $\boldsymbol{\varepsilon}_k + \beta_k \boldsymbol{\Delta\varepsilon}_k$, (ii) to evaluate $\partial\mathcal{F}(\beta_k)/\partial\beta_k$, the total gradient of the cost function $\mathbf{g}_k$ must be constructed, involving the evaluation of the Jacobian matrix $\mathbf{J}$. Hence, this also requires the solution of all dipole forward problems for $\boldsymbol{\varepsilon}_k + \beta_k \boldsymbol{\Delta\varepsilon}_k$ (for every k_z, every receiver position and 3 polarizations).

We can conclude that it is essential to restrict the number of regular forward problems and dipole forward problems as much as possible by an adequate choice of the number of spectral components and of the number of source and detector positions. Although the standard number of spectral components in this PhD work was previously chosen to be 5, we reduce this to three for this large reconstruction example. This still corresponds to an acceptable error on the incident field of the order of 1% for an orthogonally incident Gaussian beam (see Section 3.5).

The choice of an adequate number of beam directions and detector points cannot be made without considering the aspect-limited character of the source-receiver configuration. Due to the presence of the human body, a 360° illumination of the hidden object is not feasible. Hence, we are restricted to use source and detector positions at one side of the clothed human body model only, as shown in Fig. 8.7. Consequently, it is hard to get a good *in-depth* resolution (i.e. along the y-direction in Fig. 8.7). Therefore, it is advisable to maintain a good spatial distribution of the transmitting antennas along the x-axis to preserve the lateral resolution of the reconstruction. In this way, we hope to reveal the presence of the hidden object at the correct position along the x-axis, whereas its position along the y-axis will be much harder to determine. Since the number of regular forward problems relates directly to the number of incident fields, only 5 beam directions are used for the reconstruction (both a TE- and TM-polarizations are used). Blue arrows in Fig. 8.8 indicate the propagation direction of the incident Gaussian beams, which pass through the red dots that are equally spaced $4\lambda_0 = 12$ mm on a line at $33.3\lambda_0 = 10$ cm from the clothing layer. The pink arrows indicate the direction of the electric field for TE- polarization. The TM polarization direction is not shown since it points outwards of the figure. The black square represents the location of the clothed human body model. For the detector configuration, we have chosen a line of 41 receiver positions with a spacing of $\lambda_0/3 = 1$ mm and place the detector line very close (at $1.5\lambda_0 = 4.5$ mm) to the clothing layer. The detector positions are indicated as green dots in Fig. 8.8.

We will now focus on the forward and inverse problem grids. Since the partial inverse problem grid approach is used, the unknown grid cells at the assumed location of the hidden object have to fit in the larger background grid. To make this fitting easier, we neglect the curvature of the human body and model the clothing layer and the human body layers as rectangular objects, see Fig. 8.9.

The human body model of Fig. 8.7, used in Section 4.4, consists of approximately 1.4 million unknowns in the forward problem and corresponds to a simulation time of approximately two hours for a single illumination. Neglecting the curvature of all lay-

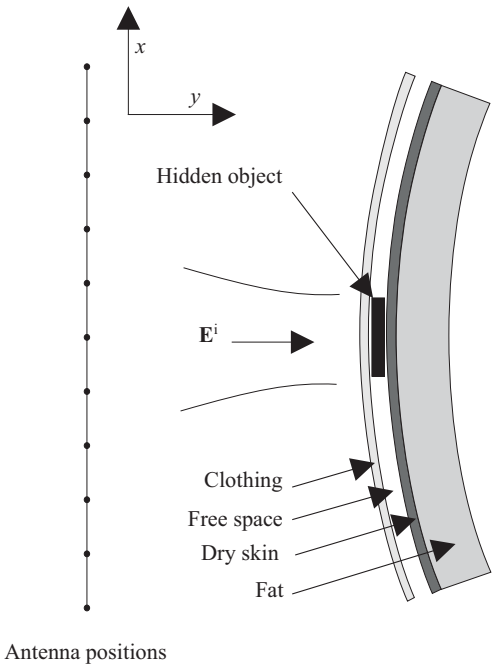

Figure 8.7: Human body model of Section 3.5 with antenna configuration.

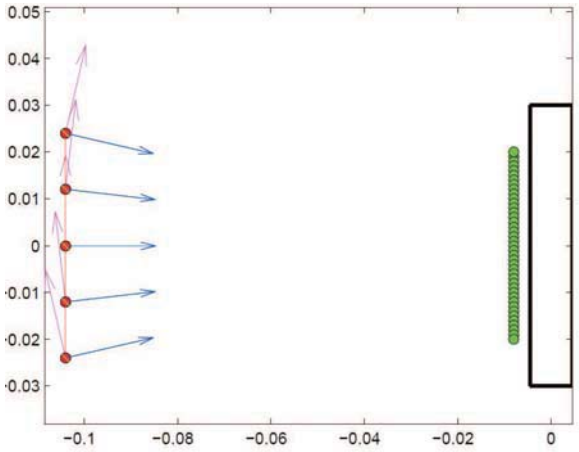

Figure 8.8: Sources and detector configuration for the reconstruction of the hidden object on a clothed human body.

ers will only slightly reduce the dimensions of a single forward problem. Therefore, more simplifications are required to obtain a model for which a single forward problem can be solved in a reasonable amount of time. A first necessary step is reducing the dimensions of the model along the x-axis. Since all incident Gaussian beams (with a beam diameter of approximately 1.6 cm) are directed towards the expected location of the hidden object, the outer parts of the rectangular clothing and human body layers are not illuminated and can therefore be further neglected. We have reduced the dimensions of all layers along the x-axis to 5.8 cm (in the original model of Fig. 8.7, this length was 10 cm). A second step to make the solution time of a forward problem acceptable is omitting the layer of fat in the human body model. Since the thickness of this layer (1cm) is large compared to the 2 mm thickness of the clothing and skin layer, omitting the fat will significantly reduce the number of forward problem cells in the y-direction. We expect that this necessary simplification will not strongly influence the fields since there is no substantial field penetration further than the skin layer (see Fig. 4.17). The permittivity profile of the simplified human body model is shown in Fig. 8.9. The layer at the left side represents the clothing layer, the layer at the right is the skin layer. The intermediate rectangular solid blue box denotes the positions of the unknown permittivity cells. The ultimate number of unknowns in the forward problem of the considered simplified human body model is 174 528 and corresponds to a forward problem cell size of $\lambda_0/30 = 0.1$ mm.

Now, the partial inverse problem grid is discussed. This is a coarser grid compared to the forward problem grid and it is restricted to a rectangle that includes the expected location of the hidden scatterer, as indicated by the light blue box in Fig. 8.9. Hence, only the cells within this partial inverse problem grid are optimized for. The dimensions of the partial inverse problem grid are 1 cell along the y-axis and 20 cells along the x-axis, yielding a total number of 20 permittivity unknowns. The cells have a cell size of $\lambda_0/3 = 1$ mm.

The rectangular hidden object is 1 mm wide and 14 mm long, which corresponds to one coarse grid cell along the y-axis and 14 cells along the $x-axis$. It is positioned in the center of the partial inverse problem grid and has a relative permittivity of $\varepsilon_{r,obj} = 2$, see Fig. 8.9. Note that the hidden object is less elongated than the partial inverse problem grid. Hence, we hope to reconstruct both permittivity and longitudinal dimension of this hidden object. The properties of the clothing and skin layer are (see Section 4.4): thickness $d_{clothing} = 2$ mm with a relative permittivity of $\varepsilon_{r,clothing} = 4.0 + i\ 0.1$ [2] and thickness $d_{skin} = 2$ mm with a relative permittivity of $\varepsilon_{r,skin} = 5.60 + i\ 7.09$ [3].

This configuration is very challenging in computation effort, but is relatively small in terms of memory consumption. Hence, all accelerating techniques of Chapter 2 are applied: (i) all forward problems are distributed over the 8 available CPU cores, (ii) a marching-on-in-source-position technique is applied which recycles three previous solutions and (iii) a marching-on-in-spectral-component technique is applied,

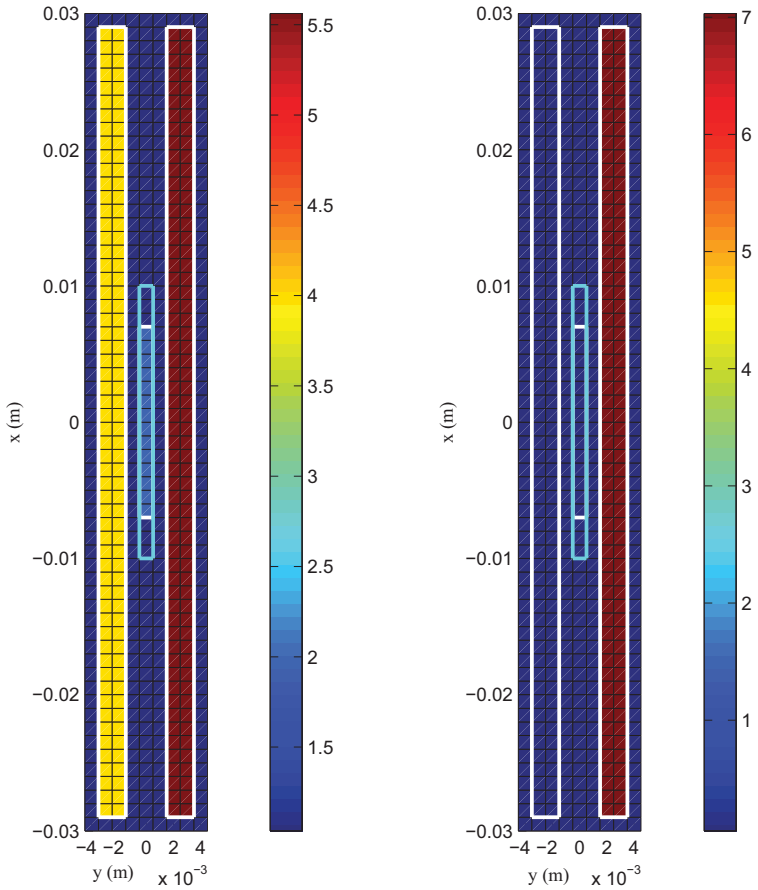

Figure 8.9: (a) Real part and (b) imaginary part of the coarse grid permittivity cells for the reconstruction of a hidden object underneath clothing on a human body. The solid white lines indicate the contours of the actual objects, the solid blue lines surround the positions of the unknown permittivity cells (i.e. the partial grid).

also reusing three previous solutions. All these implementation details lead to a total memory consumption of approximately 2 Gb (32 Gb available).

The reconstruction parameters are as follows. Since this configuration is already a highly demanding inverse scattering problem, no noise is added to the synthetic data. The tolerance for the BICGS routine in the forward problem is set to 10^{-3}. We have applied the stepwise relaxed value picking regularization technique with the regularization parameter $\gamma = 1$, since the computation time with purely stepwise relaxed value picking regularization is smaller compared to the stepwise relaxed ob-

ject smoothed value picking regularization. The bounds on the VP values c_p are (i) $1.1 < \Re(c_p) < 5$, $\forall c_p$ and (ii) $-0.001 < \Im(c_p) < 0.001$, $\forall c_p$.

Figure 8.10 shows the reconstructed permittivity profile, obtained after only 6 iterations. The hidden object is clearly visible inside the partial inverse problem grid and its dimensions are correctly estimated. Figure 8.11 shows a cross-sectional plot of the reconstructed permittivity values through the partial inverse problem grid. The solid lines correspond to the actual profile, whereas the dash-dot curve corresponds to the reconstructed permittivities inside the partial inverse problem grid. The longitudinal dimension of the hidden object is exactly determined, the permittivity is a little underestimated ($\varepsilon_{r,obj} = 1.8$ instead of $\varepsilon_{r,obj} = 2$). The vertical dashed lines represent the boundaries of the partial inverse problem grid. The decrease of the data fit is shown in Fig. 8.12. One VP value is added in the reconstruction process and its value at iteration 6 is $c_1 = 1.99$, which is exactly the actual permittivity of the hidden object.

The computation times for each iteration and the current value for c_1 are presented in Table 8.2. These computation times clearly illustrate the computational effort of this reconstruction example. More complex and/or realistic configurations in the millimeter wave range can be simulated if a fully parallel version of the presented methods is available, which allows to distribute the forward problems over more CPU cores. If the volume integral equation approach, presented in this PhD work, is combined with a boundary integral approach [4, 5] a computationally more efficient hybrid method might be obtained to cope with the influence of the surrounding background media. Here, the partial grid approach is an effective manner to avoid the inclusion of the known surrounding environment into the inverse problem unknowns. For future research, it may be of interest to look for more efficient ways to solve the forward problem in case of a changing object in a non-changing environment [6].

Table 8.2: Computation times and current value for the VP value c_1 as a function of the iteration number, corresponding to the reconstruction of an object hidden underneath clothing on u human body.

# it.	CPU time	c_1
init	0h 0’ 54”	-
1	15h 22’ 2”	-
2	15h 51’ 49”	-
3	16h 9’ 42”	-
4	14h 33’ 27”	-
5	26h 54’ 59”	1.73
6	24h 18’ 48”	1.99

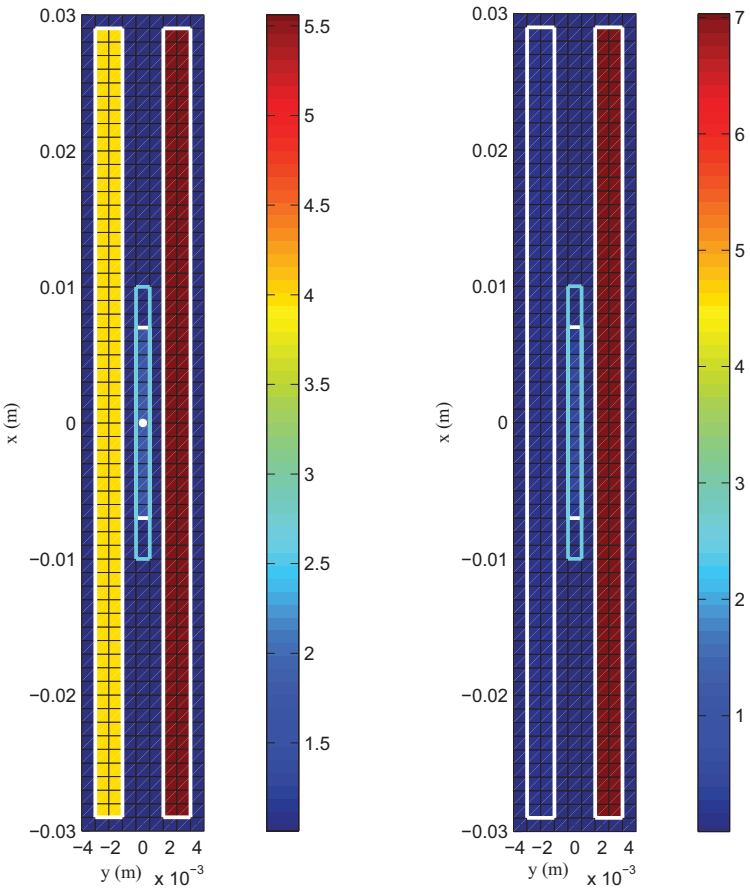

(a) (b)

Figure 8.10: (a) Real part and (b) imaginary part of the reconstructed permittivity profile inside the partial inverse problem grid, embedded in the coarse grid. This reconstruction corresponds to the configuration of an object hidden under clothing on a human body. The solid white lines indicate the contours of the actual objects, the solid blue lines surround the positions of the unknown permittivity cells (i.e. the partial inverse problem grid).

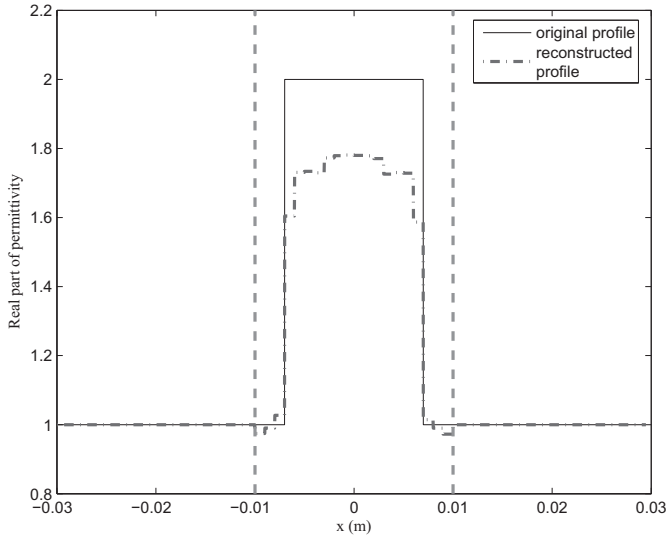

Figure 8.11: Real part of the permittivity profile along a vertical cross-section in the coarse grid and through the partial inverse problem grid. The solid line corresponds to the actual profile, the dashed curve corresponds to the reconstructed profile inside the partial inverse problem grid. The vertical dashed lines represent the boundaries of the partial inverse problem grid.

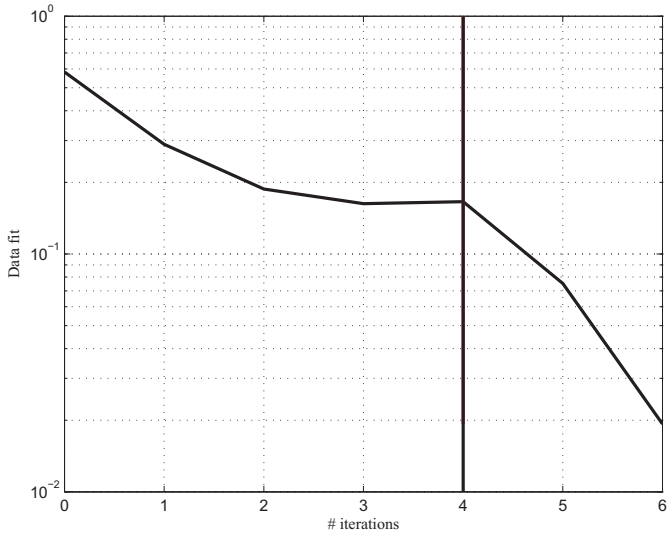

Figure 8.12: The data fit as a function of the iteration number, corresponding to the reconstruction of an object hidden underneath clothing on a human body. The vertical solid line denotes the iteration number in which a VP value is added.

8.4. Conclusion

In this Chapter, reconstructions are performed based on synthetic data in the millimeter wave range. First, the influence of the type of incident field on the reconstruction is investigated by comparing reconstructions with Gaussian beam illumination to reconstructions with plane wave illumination. Reconstructions with Gaussian beam illumination require much longer computation times due to the larger number of spectral components, while the number of iterations in the inversion scheme is similar to the plane wave illumination case. The quality of the reconstruction is slightly worse.

The second part of this chapter dealt with the reconstruction of a hidden object on the clothed human body model of Chapter 4, illuminated by a millimeter wave Gaussian beam. Due to the extremely large dimensions of this scattering example, we were obliged to adopt different model simplifications and reduce the number of spectral components to describe the Gaussian beam. Due to the presence of the human body, illuminations could not be realized over 360° around the hidden object, causing the scattering data to be aspect limited. Furthermore, a relatively small number of source and detector points was chosen to allow for a computation time of a single iteration to be less than or equal to one day. After only 6 iterations, the reconstructed permittivity profile revealed the hidden scatterer, at the correct location and with the correct dimensions. Its permittivity was slightly underestimated but the corresponding VP value converged to the exact permittivity value. This human body scattering example has clearly illustrated the limitations as well as the possibilities of the presented inverse scattering method. A fully parallel version is expected to be able to detect hidden objects on more realistic human body models within a more realistic millimeter wave imaging set-up.

Bibliography

[1] Visualisation of concealed objects using millimeter waves. [Online]. Available: http://www.etro.vub.ac.be/SBOMMW

[2] O. Gandhi and A. Riazi, "Absorption of millimeter waves by human beings and its biological implications," *IEEE Transactions on Microwave Theory and Techniques*, vol. 34, no. 2, pp. 228–235, Feb. 1986.

[3] Institute for Applied Physics. Italian National research Council. [Online]. Available: http://niremf.ifac.cnr.it/tissprop/htmlclie/htmlclie.htm

[4] J. Fostier, "Parallel techniques for fast multipole algorithms," Ph.D. dissertation, Ghent University, 2009.

[5] J. Peeters, J. Fostier, F. Olyslager, and D. De Zutter, "New parallel approaches for fast multipole solvers," in *Proceedings of the second European Conference on Antennas and Propagation*, Edinburgh, UK, 2007, pp. 1–5.

[6] A. Franchois and A. Tijhuis, "A quasi-newton reconstruction algorithm for a complex microwave imaging scanner environment," *Radio Science*, vol. 38, no. 2, January 2003.

Conclusions and further research

In this PhD work, we proposed a full-wave forward and inverse scattering algorithm for the millimeter wave frequency range. The consequences of such high frequencies are twofold. On the one hand, incident fields are typically Gaussian beams, which have a fully three-dimensional nature. On the other hand, realistic objects tend to be very large with respect to the wavelength, which makes a fully three-dimensional implementation hardly feasible. Consequently, we adopted a so-called two-and-a-half-dimensional implementation by assuming that all scatterers are two-dimensional (being infinitely long cylinders with an arbitrary cross-section) while maintaining the three-dimensional nature of the incident fields.

In a first part of this dissertation, we described the implementation of the forward solver. Since the forward solver is developed to be part of the quantitative inverse scattering scheme, special attention was paid to a fast and efficient implementation. A volume integral equation scheme was selected to allow the forward solver to simulate strongly inhomogeneous objects, which is required by the pixel-based inversion method. Therefore, we reformulated the well-known contrast source integral approach to fit the 2.5D description by applying a spatial Fourier transform of the electromagnetic fields along the invariant direction of the scattering cylinder. Hence, the longitudinal coordinate dependency of the electromagnetic fields was replaced by a spectral component dependency. Consequently, a set of two-dimensional contrast source integral equations was obtained: one for every spectral component. In this way, a 2D spatial discretization in a cross-sectional plane of the object could be applied. The set of discretized equations is iteratively solved by applying a biconjugate gradient FFT method.

Three different models for the 3D Gaussian beam illumination were implemented. These can be classified in two groups. The first two models are based on a scalar beam formulation, where a polarization vector is added to the scalar beam to obtain a vectorial illumination. Consequently, these models are only valid under the paraxial approximation. The third model is valid both inside and outside the well collimated region of the beam and yields the most accurate and efficient description of a Gaussian beam. In this model, the Gaussian beam is obtained as the field generated by a dipole source in complex space. This approach was inspired on the three-dimensional complex source beam formulation of Heyman and Felsen [1], which we have reformulated

for the two-and-a-half-dimensional case. This fully vectorial model was chosen as the standard implementation for a Gaussian beam within the presented PhD work.

An extensive validation of the proposed 2.5D forward solver was provided in Chapter 4, both for plane wave and Gaussian beam illumination. First, an excellent agreement was achieved between simulated scattered fields and analytic solutions for orthogonally and obliquely incident plane waves, being TE- or TM-polarized, incident on a homogeneous cylinder or a a piecewise-homogeneous multilayered cylinder. Second, a comparison of simulated scattered fields to fields obtained with a fully three-dimensional VIE-based forward solver [2] demonstrated the computational advantages of the 2.5D approach when simulating long dielectric cylinders. Third, for an orthogonally incident Gaussian beam illumination, we successfully matched simulated scattered fields to scattered fields obtained from a fully three-dimensional BIE-based forward solver [3]. Furthermore, we proved that the restriction to *infinitely long* cylinders in the 2.5D solver (i.e. the 2.5D assumption) can be weakened to *long enough* cylinders in case of a Gaussian beam illumination.

Since the presented forward solver is intended for millimeter wave imaging applications that visualize hidden objects under clothing [4], we showed a scattering example for a human body configuration, consisting of an orthogonally incident Gaussian beam that illuminates a simplified model of a clothed human torso. The effect on the total field of a small metallic or dielectric object, hidden underneath the clothing, was clearly visible.

We have also studied the correspondence between simulated scattered fields on the one hand and experimentally measured scattered fields on the other hand. The LAMI-ETRO lab of the Vrije Universiteit Brussel provided us amplitude-only scattering measurements of a homogeneous teflon cylinder, in the millimeter wave range and thus for a Gaussian beam illumination. The simulated and measured fields agreed quite well, even though the incident beam could not be characterized precisely. Fully vectorial scattering measurements in the microwave range were provided by the Institut Fresnel in Marseille for an obliquely illuminated long inhomogeneous dielectric cylinder. Also in this case, a good match was obtained between simulated and measured fields.

In the second part of this dissertation we described the quantitative inverse scattering algorithm. The iterative implementation is based on existing techniques for microwave imaging, which we adapted and applied to the millimeter wave range. Therefore, we reformulated the analytical expression for the derivatives of the scattered field with respect to the permittivity unknowns for the two-and-a-half-dimensional case. A two-step strategy is applied to update the permittivity profiles. First, an update direction is derived by applying a Gauss-Newton method. Afterwards, an approximate line search is performed along this direction, yielding the next permittivity profile. Furthermore, we proposed a partial inverse problem grid description to account for large

scattering systems, restricting the inversion domain to a limited investigation area surrounded by known background objects.

Both a spatial and a non-spatial regularization technique were implemented: the multiplicative smoothing regularization and the stepwise relaxed value picking regularization respectively. These existing methods inspired us to develop a new type of regularization, which we denoted the stepwise relaxed object smoothed value picking regularization. Its behavior is similar to that of the stepwise relaxed value picking regularization: it favors permittivity profiles consisting of few distinct permittivity values, which makes it ideally suited to reconstruct piecewise homogeneous objects. The novelty lies in the fact that smoothing is imposed within the different homogeneous regions, deduced from the VP weights in each iteration.

The proposed inverse scattering method was validated by reconstructing real world targets from TM- and TE- polarized experimental data for long inhomogeneous dielectric cylinders, provided by the 2D Institut Fresnel database. Only using single frequency data, we obtained very accurate reconstructions of different Fresnel targets. In some cases, the stepwise relaxed value picking regularization led to artifacts in the reconstructed profile. Since the targets are piecewise constant, these configurations were ideally suited to test the newly proposed stepwise relaxed object smoothed value picking regularization method. The results were excellent: perfectly piecewise homogeneous reconstructions with a good estimation of the positions, dimensions and permittivities of the objects were obtained.

To present some reconstruction results at millimeter wave frequencies, we were obliged to use synthetic data. A preliminary study was made of how the type of incident field (plane wave or Gaussian beam) influences the reconstruction process. This test case consisted of a relatively small multilayered square scatterer, completely illuminated by the incident fields. Whereas the number of iterations in the inversion scheme is similar for both types of illumination, the computation time for a reconstruction with Gaussian beam illumination is larger. These longer computation times are inherent to the Gaussian beam implementation, due to the larger number of spectral components. The quality of both reconstructions was very good, with a slight advantage for the plane wave illumination. This example shows that quantitative millimeter wave imaging could be promising for specific non-destructive testing applications, e.g. for material characterization of small samples that are opaque to light.

Finally, we came back to the millimeter wave imaging of concealed objects on the human body by trying to reconstruct a small hidden object on the clothed human body model of Chapter 4, which is a very challenging configuration due to its extremely large dimensions. We were obliged to further simplify this human body model and to reduce the number of spectral components in the description of the Gaussian beam. In order to simulate a configuration that could be realized experimentally, we had to omit the 360° illumination of the target and used aspect limited scattered field data. Although the number of source and detector points was already relatively small, this still resulted in a computation time of the order of one day for a single iteration in the

inverse scheme. After approximately five days and six iterations, the hidden scatterer was revealed at the correct location and with the correct dimensions. Its permittivity was slightly underestimated but the corresponding VP value converged to the exact permittivity value. This body scattering example clearly illustrates the present limitations as well as the possibilities of the presented inverse scattering method.

To be able to reconstruct more challenging configurations (e.g. detect hidden objects on more realistic human body models within a more realistic millimeter wave imaging set-up), further research is necessary and could include the following:

- The presented method uses a multithreaded implementation, which makes it, to some extent, already a parallelized simulation tool. However, we are restricted to run simulations on multiple processors on a *single* machine, all accessing the same common memory. A fully parallel implementation [5] would allow to spread out the computations over multiple processors on *multiple* machines, each having their own memory to store results. Hence, the simulation times could be strongly reduced, while the available memory increases. This parallelization should pose few difficulties since the parallelized version of the inverse problem is very similar to its multithreaded version.
- To speed up single forward problems, the conditioning of the set of CSIE's could be improved by implementing an appropriate preconditioner or by improving the routine to compute initial guesses (now the marching-on scheme).
- To better account for known and unchanging objects in the surroundings of the unknown scatterer, a hybrid solver which combines a BIE approach for the known objects with a VIE approach or a finite elements approach for the unknown objects might be an advantage.
- The choice of the regularization parameter in case of stepwise relaxed value picking and stepwise relaxed object smoothed value picking is still done by trial and error. More research should be done to obtain an a-priori or adaptive value for this regularization parameter.
- A more extensive study on the influence of the type of incident field on the reconstruction might provide more insight. Furthermore, it needs to be studied how the reconstruction process behaves when the object is only partially illuminated by a Gaussian beam.

Bibliography

[1] E. Heyman and L. Felsen, "Gaussian beam and pulsed beam dynamics: complex-source and complex-spectrum formulations within and beyond paraxial asymptotics," *Journal of the Optical Society of America A*, vol. 18, no. 7, pp. 1588–1611, July 2001.

[2] P. Lewyllie, A. Franchois, C. Eyraud, and J.M. Geffrin, "Testing a 3D BCGS-FFT solver against experimental data," in *Proceedings of the 9th International Conference on Electromagnetics in Advanced Applications (ICEAA 2005)*, Torino, Italy, Sept. 2005, pp. 421–424.

[3] J. Peeters, J. Fostier, F. Olyslager, and D. De Zutter, "New parallel approaches for fast multipole solvers," in *Proceedings of the second European Conference on Antennas and Propagation*, Edinburgh, UK, 2007, pp. 1–5.

[4] Visualisation of concealed objects using millimeter waves. [Online]. Available: http://www.etro.vub.ac.be/SBOMMW

[5] J. Fostier, "Parallel techniques for fast multipole algorithms," Ph.D. dissertation, Ghent University, 2009.

Appendices

APPENDIX A

Analytic solutions for an obliquely incident TM polarized plane wave on an infinitely long dielectric circular cylinder

1.1. Homogeneous cylinder

In this section we present a brief sketch of the construction of the analytic solution for the scattered field that results from a plane wave obliquely incident on a circular homogeneous cylinder with radius a_1 and relative permittivity ε'_{r1}.

We start from the Fourier transformed Maxwell equations ((2.7a)-(2.7b)):

$$\widehat{\nabla} \times \widehat{\mathbf{E}}(\mathbf{r}, k_z) = j\omega\mu_0 \widehat{\mathbf{H}}(\mathbf{r}, k_z) \tag{A.1a}$$

$$\widehat{\nabla} \times \widehat{\mathbf{H}}(\mathbf{r}, k_z) = \widehat{\mathbf{J}}^{\mathrm{i}}(\mathbf{r}, k_z) - j\omega\varepsilon(\mathbf{r})\widehat{\mathbf{E}}(\mathbf{r}, k_z), \tag{A.1b}$$

where, in case of a plane wave illumination, k_z corresponds to the projection of the propagation vector $\mathbf{k}^{\mathrm{i}} = k_0\mathbf{u}^{\mathrm{i}}$ of the obliquely incident plane wave on the z-axis, hence $k_z = k_0\mathbf{u}^{\mathrm{i}} \cdot \mathbf{u}_z$. The complex permittivity $\varepsilon(\mathbf{r})$ is equal to $\varepsilon_1 = \varepsilon_0\varepsilon'_{r1}$ inside the cylinder and equal to ε_0 outside the cylinder.

We will formulate all fields in a cylindrical coordinate system with origin ($\rho = 0$) in the center of the cylinder, hence $\mathbf{r} + z\mathbf{u}_z = \rho\mathbf{u}_\rho + \phi\mathbf{u}_\phi + z\mathbf{u}_z$. Consequently, the incident electric and magnetic fields are denoted as $\widehat{\mathbf{E}}^{\mathrm{i}}(\rho, \phi, k_z) = \widehat{E}^{\mathrm{i}}_\rho(\rho, \phi, k_z)\mathbf{u}_\rho + \widehat{E}^{\mathrm{i}}_\phi(\rho, \phi, k_z)\mathbf{u}_\phi + \widehat{E}^{\mathrm{i}}_z(\rho, \phi, k_z)\mathbf{u}_z$ and $\widehat{\mathbf{H}}^{\mathrm{i}}(\rho, \phi, k_z)$, respectively. Similarly, the scattered electric and magnetic fields outside the cylinder are represented as $\widehat{\mathbf{E}}^{\mathrm{s}}(\rho, \phi, k_z)$ and

$\widehat{\mathbf{H}}^{\mathrm{s}}(\rho,\phi,k_z)$, respectively, and the total electric and magnetic fields inside the cylinder are represented as $\widehat{\mathbf{E}}^{\mathrm{tot1}}(\rho,\phi,k_z)$ and $\widehat{\mathbf{H}}^{\mathrm{tot1}}(\rho,\phi,k_z)$, respectively.

At the surface of the cylinder (for $\rho = a_1$) the electromagnetic fields satisfy:

$$\widehat{E}_z^{\mathrm{i}}(a_1,\phi,k_z) + \widehat{E}_z^{\mathrm{s}}(a_1,\phi,k_z) = \widehat{E}_z^{\mathrm{tot1}}(a_1,\phi,k_z) \tag{A.2a}$$
$$\widehat{H}_z^{\mathrm{i}}(a_1,\phi,k_z) + \widehat{H}_z^{\mathrm{s}}(a_1,\phi,k_z) = \widehat{H}_z^{\mathrm{tot1}}(a_1,\phi,k_z) \tag{A.2b}$$
$$\widehat{E}_\phi^{\mathrm{i}}(a_1,\phi,k_z) + \widehat{E}_\phi^{\mathrm{s}}(a_1,\phi,k_z) = \widehat{E}_\phi^{\mathrm{tot1}}(a_1,\phi,k_z) \tag{A.2c}$$
$$\widehat{H}_\phi^{\mathrm{i}}(a_1,\phi,k_z) + \widehat{H}_\phi^{\mathrm{s}}(a_1,\phi,k_z) = \widehat{H}_\phi^{\mathrm{tot1}}(a_1,\phi,k_z). \tag{A.2d}$$

In the following subsections, we derive expressions for the $z-$ and $\phi-$ field components.

1.1.1 Expressions for the $z-$ and $\phi-$ components of the incident fields

Due to the TM polarization of the incident plane wave, the z-component of the incident magnetic field is zero:

$$\widehat{H}_z^{\mathrm{i}}(\rho,\phi,k_z) = 0. \tag{A.3}$$

The z-component of the incident electric field is expanded as

$$\widehat{E}_z^{\mathrm{i}}(\rho,\phi,k_z) = \sum_{n=-\infty}^{+\infty} A(-j)^n J_n(\gamma_0\rho) e^{jn\phi}, \tag{A.4}$$

where A represents the amplitude of the incident plane wave and $\gamma_0 = \sqrt{k_0^2 - k_z^2}$.

The corresponding ϕ- components of the incident electric and magnetic fields are obtained from

$$\widehat{\nabla} \times \widehat{\mathbf{E}}^{\mathrm{i}}(\rho,\phi,k_z) = j\omega\mu_0 \widehat{\mathbf{H}}^{\mathrm{i}}(\rho,\phi,k_z) \tag{A.5a}$$
$$\widehat{\nabla} \times \widehat{\mathbf{H}}^{\mathrm{i}}(\rho,\phi,k_z) = -j\omega\varepsilon_0 \widehat{\mathbf{E}}^{\mathrm{i}}(\rho,\phi,k_z). \tag{A.5b}$$

Since all field components are derived in a cylindrical coordinate system, we have to reformulate $\widehat{\nabla} \times \mathbf{a}$ (with $\mathbf{a}$ equal to $\widehat{\mathbf{E}}^{\mathrm{i}}(\rho,\phi,k_z)$ or $\widehat{\mathbf{H}}^{\mathrm{i}}(\rho,\phi,k_z)$ and $\widehat{\nabla} = \frac{\partial}{\partial x}\mathbf{u}_x + \frac{\partial}{\partial y}\mathbf{u}_y + jk_z\mathbf{u}_z$) to cylindrical coordinates (ρ,ϕ,z). Hence,

$$\begin{aligned}\widehat{\nabla} \times \mathbf{a} = & \left[\frac{1}{\rho}\frac{\partial}{\partial\phi}a_z - jk_z a_\phi\right]\mathbf{u}_\rho + \left[jk_z a_\rho - \frac{\partial}{\partial\rho}a_z\right]\mathbf{u}_\phi \\ & + \left[\frac{1}{\rho}\frac{\partial}{\partial\rho}(\rho a_\phi) - \frac{1}{\rho}\frac{\partial}{\partial\phi}a_\rho\right]\mathbf{u}_z\end{aligned} \tag{A.6}$$

By introducing (A.6) into (A.5) and by identifying the $\mathbf{u}_\rho$- and the $\mathbf{u}_\phi$- components, the following set of equations is obtained:

$$\frac{1}{\rho}\frac{\partial}{\partial\phi}\widehat{E}_z^{\mathrm{i}}(\rho,\phi,k_z) - jk_z\widehat{E}_\phi^{\mathrm{i}}(\rho,\phi,k_z) = j\omega\mu_0\widehat{H}_\rho^{\mathrm{i}}(\rho,\phi,k_z) \tag{A.7a}$$

$$jk_z\widehat{E}_\rho^{\mathrm{i}}(\rho,\phi,k_z) - \frac{\partial}{\partial\rho}\widehat{E}_z^{\mathrm{i}}(\rho,\phi,k_z) = j\omega\mu_0\widehat{H}_\phi^{\mathrm{i}}(\rho,\phi,k_z) \tag{A.7b}$$

$$-jk_z\widehat{H}_\phi^{\mathrm{i}}(\rho,\phi,k_z) = -j\omega\varepsilon_0\widehat{E}_\rho^{\mathrm{i}}(\rho,\phi,k_z) \tag{A.7c}$$

$$jk_z\widehat{H}_\rho^{\mathrm{i}}(\rho,\phi,k_z) = -j\omega\varepsilon_0\widehat{E}_\phi^{\mathrm{i}}(\rho,\phi,k_z). \tag{A.7d}$$

After elimination of $\widehat{E}_\rho^{\mathrm{i}}$ and $\widehat{H}_\rho^{\mathrm{i}}$, the ϕ- components of the incident fields are obtained as a function of the z- component of the incident electric field as

$$\widehat{E}_\phi^{\mathrm{i}}(\rho,\phi,k_z) = \frac{jk_z}{\gamma_0^2}\frac{1}{\rho}\frac{\partial}{\partial\phi}\widehat{E}_z^{\mathrm{i}}(\rho,\phi,k_z) \tag{A.8a}$$

$$\widehat{H}_\phi^{\mathrm{i}}(\rho,\phi,k_z) = \frac{j\omega\varepsilon_0}{\gamma_0^2}\frac{\partial}{\partial\rho}\widehat{E}_z^{\mathrm{i}}(\rho,\phi,k_z). \tag{A.8b}$$

1.1.2 Expressions for the $z-$ and $\phi-$ components of the scattered fields outside the cylinder

For $\rho \geq a_1$, the z-components of the scattered electric and magnetic fields are expanded as

$$\widehat{E}_z^{\mathrm{s}}(\rho,\phi,k_z) = \sum_{n=-\infty}^{+\infty} A_n H_n^{(1)}(\gamma_0\rho)e^{jn\phi} \tag{A.9a}$$

$$\widehat{H}_z^{\mathrm{s}}(\rho,\phi,k_z) = \sum_{n=-\infty}^{+\infty} B_n H_n^{(1)}(\gamma_0\rho)e^{jn\phi}, \tag{A.9b}$$

where A_n and B_n are unknown coefficients to be determined from the boundary equations (A.2).

The corresponding ϕ- components of the scattered electric and magnetic fields are obtained from

$$\widehat{\nabla}\times\widehat{\mathbf{E}}^{\mathrm{s}}(\rho,\phi,k_z) = j\omega\mu_0\widehat{\mathbf{H}}^{\mathrm{s}}(\rho,\phi,k_z) \tag{A.10a}$$

$$\widehat{\nabla}\times\widehat{\mathbf{H}}^{\mathrm{s}}(\rho,\phi,k_z) = -j\omega\varepsilon_0\widehat{\mathbf{E}}^{\mathrm{s}}(\rho,\phi,k_z). \tag{A.10b}$$

By introducing (A.6) into (A.10) and by identifying the $\mathbf{u}_\rho$- and the $\mathbf{u}_\phi$- components, the following set of equations is obtained:

$$\frac{1}{\rho}\frac{\partial}{\partial\phi}\widehat{E}_z^s(\rho,\phi,k_z) - jk_z\widehat{E}_\phi^s(\rho,\phi,k_z) = j\omega\mu_0\widehat{H}_\rho^s(\rho,\phi,k_z) \tag{A.11a}$$

$$jk_z\widehat{E}_\rho^s(\rho,\phi,k_z) - \frac{\partial}{\partial\rho}\widehat{E}_z^s(\rho,\phi,k_z) = j\omega\mu_0\widehat{H}_\phi^s(\rho,\phi,k_z) \tag{A.11b}$$

$$\frac{1}{\rho}\frac{\partial}{\partial\phi}\widehat{H}_z^s(\rho,\phi,k_z) - jk_z\widehat{H}_\phi^s(\rho,\phi,k_z) = -j\omega\varepsilon_0\widehat{E}_\rho^s(\rho,\phi,k_z) \tag{A.11c}$$

$$jk_z\widehat{H}_\rho^s(\rho,\phi,k_z) - \frac{\partial}{\partial\rho}\widehat{H}_z^s(\rho,\phi,k_z) = -j\omega\varepsilon_0\widehat{E}_\phi^s(\rho,\phi,k_z). \tag{A.11d}$$

From (A.11), the ϕ- components of the scattered fields are obtained as a function of the z- components of the scattered fields as

$$\widehat{E}_\phi^s(\rho,\phi,k_z) = \frac{jk_z}{\gamma_0^2}\frac{1}{\rho}\frac{\partial}{\partial\phi}\widehat{E}_z^s(\rho,\phi,k_z) - \frac{j\omega\mu_0}{\gamma_0^2}\frac{\partial}{\partial\rho}\widehat{H}_z^s(\rho,\phi,k_z) \tag{A.12a}$$

$$\widehat{H}_\phi^s(\rho,\phi,k_z) = \frac{jk_z}{\gamma_0^2}\frac{1}{\rho}\frac{\partial}{\partial\phi}\widehat{H}_z^s(\rho,\phi,k_z) + \frac{j\omega\varepsilon_0}{\gamma_0^2}\frac{\partial}{\partial\rho}\widehat{E}_z^s(\rho,\phi,k_z). \tag{A.12b}$$

1.1.3 Expressions for the $z-$ and $\phi-$ components of the total fields inside the cylinder

For $\rho \leq a_1$, the z-components of the total electric and magnetic fields are expanded as

$$\widehat{E}_z^{\text{tot1}}(\rho,\phi,k_z) = \sum_{n=-\infty}^{+\infty} C_n J_n(\gamma_1\rho)e^{jn\phi} \tag{A.13a}$$

$$\widehat{H}_z^{\text{tot1}}(\rho,\phi,k_z) = \sum_{n=-\infty}^{+\infty} D_n J_n(\gamma_1\rho)e^{jn\phi}, \tag{A.13b}$$

where C_n and D_n are unknown coefficients to be determined from the boundary equations (A.2) and $\gamma_1 = \sqrt{k_0^2\varepsilon'_{r1} - k_z^2}$.

The corresponding ϕ- components of the total magnetic and electric fields are obtained from

$$\widehat{\nabla}\times\widehat{\mathbf{E}}^{\text{tot1}}(\rho,\phi,k_z) = j\omega\mu_0\widehat{\mathbf{H}}^{\text{tot1}}(\rho,\phi,k_z) \tag{A.14a}$$

$$\widehat{\nabla}\times\widehat{\mathbf{H}}^{\text{tot1}}(\rho,\phi,k_z) = -j\omega\varepsilon_1\widehat{\mathbf{E}}^{\text{tot1}}(\rho,\phi,k_z). \tag{A.14b}$$

By introducing (A.6) into (A.14) and by identifying the $\mathbf{u}_\rho$- and the $\mathbf{u}_\phi$- components, the following set of equations is obtained:

$$\frac{1}{\rho}\frac{\partial}{\partial\phi}\widehat{E}_z^{\text{tot1}}(\rho,\phi,k_z) - jk_z\widehat{E}_\phi^{\text{tot1}}(\rho,\phi,k_z) = j\omega\mu_0\widehat{H}_\rho^{\text{tot1}}(\rho,\phi,k_z) \tag{A.15a}$$

$$jk_z\widehat{E}_\rho^{\text{tot1}}(\rho,\phi,k_z) - \frac{\partial}{\partial\rho}\widehat{E}_z^{\text{tot1}}(\rho,\phi,k_z) = j\omega\mu_0\widehat{H}_\phi^{\text{tot1}}(\rho,\phi,k_z) \tag{A.15b}$$

$$\frac{1}{\rho}\frac{\partial}{\partial\phi}\widehat{H}_z^{\text{tot1}}(\rho,\phi,k_z) - jk_z\widehat{H}_\phi^{\text{tot1}}(\rho,\phi,k_z) = -j\omega\varepsilon_1\widehat{E}_\rho^{\text{tot1}}(\rho,\phi,k_z) \tag{A.15c}$$

$$jk_z\widehat{H}_\rho^{\text{tot1}}(\rho,\phi,k_z) - \frac{\partial}{\partial\rho}\widehat{H}_z^{\text{tot1}}(\rho,\phi,k_z) = -j\omega\varepsilon_1\widehat{E}_\phi^{\text{tot1}}(\rho,\phi,k_z). \tag{A.15d}$$

From (A.15), the ϕ- components of the scattered fields are obtained as a function of the z- components of the scattered fields as

$$\widehat{E}_\phi^{\text{tot1}}(\rho,\phi,k_z) = \frac{jk_z}{\gamma_1^2}\frac{1}{\rho}\frac{\partial}{\partial\phi}\widehat{E}_z^{\text{tot1}}(\rho,\phi,k_z) - \frac{j\omega\mu_0}{\gamma_1^2}\frac{\partial}{\partial\rho}\widehat{H}_z^{\text{tot1}}(\rho,\phi,k_z) \tag{A.16a}$$

$$\widehat{H}_\phi^{\text{tot1}}(\rho,\phi,k_z) = \frac{jk_z}{\gamma_1^2}\frac{1}{\rho}\frac{\partial}{\partial\phi}\widehat{H}_z^{\text{tot1}}(\rho,\phi,k_z) + \frac{j\omega\varepsilon_1}{\gamma_1^2}\frac{\partial}{\partial\rho}\widehat{E}_z^{\text{tot1}}(\rho,\phi,k_z). \tag{A.16b}$$

1.1.4 Analytical solution

From the previous sections, we have obtained expressions for both the z- and ϕ-components of the incident and scattered fields outside the cylinder and of the total fields inside the cylinder. The expressions for the z-components of the scattered fields outside the cylinder contain 2 unknown coefficients (A_n and B_n, for each n). Similarly, the expressions for the z-components of the total fields inside the cylinder contain 2 unknown coefficients (C_n and D_n, for each n). All ϕ-components can be written as a function of the corresponding z- components. Consequently, the total number of unknowns to characterize all fields (for each n) is 4. The boundary equations at the surface of the cylinder (A.2) offer four independent equations. Hence, the system of equations (A.2) is sufficient to characterize all unknown coefficients and consequently all unknown fields.

1.2. Two-layered cylinder

The previous approach for a homogeneous cylinder can easily be extended towards the case of a two-layered homogeneous cylinder. Suppose the outer cylinder (denoted as cylinder 1) has a radius a_1 and relative permittivity ε'_{r1} (corresponding to a complex permittivity ε_1) and the inner cylinder (denoted as cylinder 2) has a radius a_2 and relative permittivity ε'_{r2} (corresponding to a complex permittivity ε_2). The total electric and magnetic fields inside cylinder 1 are now denoted as $\widehat{\mathbf{E}}^{\text{tot1}}(\rho,\phi,k_z)$ and

$\widehat{\mathbf{H}}^{\text{tot1}}(\rho,\phi,k_z)$, respectively, and the total electric and magnetic fields inside cylinder 2 are represented as $\widehat{\mathbf{E}}^{\text{tot2}}(\rho,\phi,k_z)$ and $\widehat{\mathbf{H}}^{\text{tot2}}(\rho,\phi,k_z)$, respectively.

At the exterior surface of cylinder 1 (for $\rho = a_1$, being the interface free space - cylinder 1) the electromagnetic fields satisfy

$$\widehat{E}_z^{\text{i}}(a_1,\phi,k_z) + \widehat{E}_z^{\text{s}}(a_1,\phi,k_z) = \widehat{E}_z^{\text{tot1}}(a_1,\phi,k_z) \tag{A.17a}$$
$$\widehat{H}_z^{\text{i}}(a_1,\phi,k_z) + \widehat{H}_z^{\text{s}}(a_1,\phi,k_z) = \widehat{H}_z^{\text{tot1}}(a_1,\phi,k_z) \tag{A.17b}$$
$$\widehat{E}_\phi^{\text{i}}(a_1,\phi,k_z) + \widehat{E}_\phi^{\text{s}}(a_1,\phi,k_z) = \widehat{E}_\phi^{\text{tot1}}(a_1,\phi,k_z) \tag{A.17c}$$
$$\widehat{H}_\phi^{\text{i}}(a_1,\phi,k_z) + \widehat{H}_\phi^{\text{s}}(a_1,\phi,k_z) = \widehat{H}_\phi^{\text{tot1}}(a_1,\phi,k_z), \tag{A.17d}$$

whereas, at the interface cylinder 1 - cylinder 2 (for $\rho = a_2$), the electromagnetic fields satisfy

$$\widehat{E}_z^{\text{tot1}}(a_2,\phi,k_z) = \widehat{E}_z^{\text{tot2}}(a_2,\phi,k_z) \tag{A.18a}$$
$$\widehat{H}_z^{\text{tot1}}(a_2,\phi,k_z) = \widehat{H}_z^{\text{tot2}}(a_2,\phi,k_z) \tag{A.18b}$$
$$\widehat{E}_\phi^{\text{tot1}}(a_2,\phi,k_z) = \widehat{E}_\phi^{\text{tot2}}(a_2,\phi,k_z) \tag{A.18c}$$
$$\widehat{H}_\phi^{\text{tot1}}(a_2,\phi,k_z) = \widehat{H}_\phi^{\text{tot2}}(a_2,\phi,k_z). \tag{A.18d}$$

Similarly as in the previous section, the z- components of the incident fields are characterized as

$$\widehat{H}_z^{\text{i}}(\rho,\phi,k_z) = 0 \tag{A.19a}$$
$$\widehat{E}_z^{\text{i}}(\rho,\phi,k_z) = \sum_{n=-\infty}^{+\infty} A(-j)^n J_n(\gamma_0\rho)e^{jn\phi} \tag{A.19b}$$

and the z- components of the scattered fields outside the cylinders are characterized as

$$\widehat{E}_z^{\text{s}}(\rho,\phi,k_z) = \sum_{n=-\infty}^{+\infty} A_n H_n^{(1)}(\gamma_0\rho)e^{jn\phi} \tag{A.20a}$$
$$\widehat{H}_z^{\text{s}}(\rho,\phi,k_z) = \sum_{n=-\infty}^{+\infty} B_n H_n^{(1)}(\gamma_0\rho)e^{jn\phi}. \tag{A.20b}$$

The Fourier series expansions for the z- components of the total fields inside cylinder 1 now contain four (instead of 2) unknown coefficients:

$$\widehat{E}_z^{\text{tot1}}(\rho,\phi,k_z) = \sum_{n=-\infty}^{+\infty} C_n J_n(\gamma_1\rho)e^{jn\phi} + D_n Y_n(\gamma_1\rho)e^{jn\phi} \tag{A.21a}$$
$$\widehat{H}_z^{\text{tot1}}(\rho,\phi,k_z) = \sum_{n=-\infty}^{+\infty} E_n J_n(\gamma_1\rho)e^{jn\phi} + F_n Y_n(\gamma_1\rho)e^{jn\phi}, \tag{A.21b}$$

where $\gamma_1 = \sqrt{k_0^2 \varepsilon'_{r1} - k_z^2}$. The Fourier series expansions for the z- components of the total fields inside cylinder 2 are similar to those in the homogeneous cylinder case:

$$\widehat{E}_z^{\text{tot2}}(\rho, \phi, k_z) = \sum_{n=-\infty}^{+\infty} G_n J_n(\gamma_2 \rho) e^{jn\phi} \tag{A.22a}$$

$$\widehat{H}_z^{\text{tot2}}(\rho, \phi, k_z) = \sum_{n=-\infty}^{+\infty} H_n J_n(\gamma_2 \rho) e^{jn\phi}, \tag{A.22b}$$

where $\gamma_2 = \sqrt{k_0^2 \varepsilon'_{r2} - k_z^2}$.

All ϕ- components of the incident, scattered and total fields can be derived from the corresponding z- components as in the previous section.

Consequently, the total number of unknowns to characterize all fields is eight (A_n to H_n) and the two sets of boundary equations at the surfaces of the cylinders ((A.17) and (A.18)) offer eight independent equations. Hence, the system of equations ((A.17) - (A.18)) is sufficient to characterize all unknown coefficients and consequently all unknown fields.

This approach can be easily extended towards the case of a N-layered cylinder by introducing extra boundary conditions of the type (A.18) for the extra interior interfaces and by introducing extra Fourier series expansions for the z-components of the total fields in the different layers as (A.22) for the inner part and as (A.21) for the other layers.

Research funded by a PhD grant of the Institute for the Promotion of Innovation through Science and Technology in Flanders (IWT-Vlaanderen).